Department of Mechanical Engineering

An Investigation of Gear Meshing Behaviour of Planetary Gear Systems for Improved Fault Diagnosis

Song Xue

This thesis is presented for the Degree of
Doctor of Philosophy
of
Curtin University

September 2016

Declaration

To the best of my knowledge and belief this thesis contains no material previously published by any other person except where due acknowledgment has been made.

This thesis contains no material which has been accepted for the award of any other degree or diploma in any university.

Signature: Song Xue

Date: 24/08/2016

Abstract

This research has presented gear dynamic models and associated simulations aiming to improve gear fault detection methods for vibration-based condition monitoring systems. These models include the use of finite element and lumped parameter methods for both fixed axis and planetary gear systems. It was found that these dynamic models could reveal the gear fault mechanism and further provide helpful guidelines for early fault detection, which can be used to assist proper scheduled shutdowns, prevent catastrophic failure and consequently provide a safer operation environment and reduction in maintenance costs.

The tooth mesh stiffness variations and the resulting transmission errors are the main internal vibration generation mechanism for the gear systems. The finite element (FE) method has been used to evaluate the mesh stiffness for fixed axis and planetary gears. In the fixed axis gear system, special effort has been taken on the analysis of flexibly supported gear sets which could result in a large operating gear centre distance variation. It was found that the gear centre distance could potentially change the behaviour of the gear mesh stiffness significantly in terms of the stiffness value and the ratio between the single and double contact zones. In the planetary gear system, a planetary gear model with three planet gears and its subsystem models was developed to study the subsystem and overall torsional stiffnesses. Based on the analysis of the torsional mesh stiffness, predictive models for the single branch sun-planet-ring and overall planetary gear torsional stiffnesses have been proposed. The effect of the ring gear boundary conditions on the ring-planet mesh stiffness has also been investigated and some modulation effects can be observed in the resultant mesh stiffness due to the pin support structure.

The gear dynamic equations have been solved by numerical simulation. A special numerical procedure was developed to solve the flexibly supported gear dynamics using an iterative calculation of the gear mesh stiffness. In the procedure, the gear centre distance, which varies over a significant range for the flexibly supported gear, has been selected as the iteration criteria to ensure the system convergence at each time step. As one of the purposes was to investigate the effectiveness of using the torsional vibration as a diagnostic aid for the

planetary gear condition monitoring, a 20 degree of freedom planetary gear model, which includes the input and output motor, one sun gear, one ring gear, one carrier arm and three planet gears, was created to obtain the faulted vibration signal. The transverse vibration signal from the ring gear rim was also obtained by treating the ring gear as a flexible beam and solving the response by treating the moving planet gear contact forces as a moving load problem.

Some advanced signal processing techniques were utilized to analyse the faulted vibration signals in the time domain, frequency domain and time-frequency domain. In the flexibly supported gear analysis, comparisons were made to investigate the difference in the diagnostic results between the new model and the traditional fixed centre distance model. In the planetary gear system, the torsional vibration signal was examined using these signal processing techniques and it was found that the torsional vibration was an effective way to monitor the planetary gear system as the torsional vibration is naturally free of the carrier arm modulation.

In conclusion, the findings in this research provide an improved understanding of the gear fault mechanism and advance the gear fault detection capability of the whole drive train system. It also provides an improved fundamental understanding of the planetary gear torsional vibration behaviour and suggests further effective ways of monitoring the planetary gear system.

Acknowledgement

First and foremost, I would like to express my deepest gratitude to Prof. Ian Howard for all his invaluable guidance and support throughout my study. I feel very fortunate to have had his guidance throughout my Ph.D. study. Prof. Ian Howard has been a great advisor who was always available to discuss and support all the technical problems and he provides a very pleasant research environment in the vibration group. His patience in examining and commenting on the thesis draft is greatly appreciated. His support and encouragement to attend the conference and to submit the manuscripts to the journals is also greatly appreciated. I benefitted a lot from his guidance not only in the academic life but also in the common everyday life.

I would like to express my sincere appreciation to Dr. Rodney Entwistle and Dr. Ilyas Mazhar, who are the associate supervisors of my Ph.D. thesis. Their discussions, supports and encouragement, especially the advices on the manuscripts, are greatly appreciated. I would also like to express my appreciation to the other members in the vibration group, Dr. Kistoffer McKee, Dr. Dirk Lutschinger, Dr. Mikail Lumentut and all the other Ph.D. students. Their presentations and discussions in the vibration research seminar have always been helpful and insightful. Special thanks are owed to Dr. Rodney Entwistle and Dr. Kistoffer McKee, who have offered valuable opportunities to be tutors in their classes. This tutoring experience has been a treasure for my life.

I would like to extend my appreciation to all the members of the Mechanical Engineering Department for their help during my study.

I would like to offer thanks to the Government of People's Republic of China for awarding me China Scholarship Council Scholarship (CSC) and Curtin University for awarding me Curtin International Postgraduate Research Scholarship (CIPRS).

Finally, I would like to express my dearest gratitude to my parents for their love and understanding to my oversea study. Special thanks to my beautiful wife, Qian Wang, for always supporting me.

Contents

List of Tables

List of Figures

Chapter 1 Introduction

1.1 Overview

Gears have long been a fundamental machine element of power transmission systems and various types of gears have been developed during its long history, such as spur gears, helical gears, bevel gears and so on (Stephen, 2012). All these gears have their own characteristics and are commonly used in many industrial applications including automotive, aerospace, and wind turbine gearboxes for example. However, noise and vibration, reliability assessment and early detection of damage of the gear system remain major concerns in their applications.

Gear condition monitoring is able to monitor the current gear system condition and predict its future condition while in operation (Randall, 2011; Smith, 2003). Gears can generate vibration even in good condition and once a fault occurs, it can change the vibration signature in a way that can be related to the fault. As a result, the vibration analysis has been recognized as the most prevalent method for gear condition monitoring as it reacts immediately to the faults and it is more likely to point to the actual faulty component (Randall, 2011). Most importantly, many powerful signal processing techniques can be applied to vibration signals to extract even very weak fault indications from noise and other masking signals (Randall, 2011).

Planetary gears, also known as epicyclic gear sets, commonly includes several planet gears meshing simultaneously to split the torque and power. The planet gear can not only rotate around its own axis, but also around the planetary gear common axis. However, this rotating mechanism poses a big challenge for planetary gear condition monitoring compared to that of the parallel shaft gear. Additionally, the vibration level of the planetary gear is also typically lower than the parallel shaft gear because of the self-centering capability of central members (sun gear, ring gear and the carrier) (Inalpotat, 2009).

The traditional approach for condition monitoring of the planetary gear is using a stationary transducer mounted on the ring gear casing to record all the vibration data when the planet

gear passes by (Mark & Hines, 2009). Various window functions could be used to capture the vibration data from the individual planet gear tooth as it was observed that the vibration level reached its peak when the corresponding planet gear was closest to the transducer (Howard, 1991). By this way, the measured vibration data exhibited a modulation effect caused by the carrier arm rotation. On the other hand, torsional vibration, measured from the gear shaft, also carries diagnostic information (Randall, 2011). It would be an advantage to measure the torsional vibration directly to naturally separate the signal from the modulation effect. As a result, measuring the torsional vibration could be treated as an alternative way for condition monitoring of the planetary gear system.

However, in spite of the wide application of planetary gears as well as the emerging gear diagnostic theories, there is still a general lack of understanding of planetary gear torsional vibration and currently no off-the-shelf sensors are available for measuring and utilizing the torsional vibration inside the gearbox as a diagnostic aid for planetary gear condition monitoring. Also, the research on fixed axis gear fault detection has been subjected to continuous research by many research groups as it provides the foundation to understand the planetary gear dynamic behavior. However, a number of research topics for fixed axis gears have not yet been covered and understood completely. These aspects form the main motivation for this study.

1.2 Research objective and scope

The main objective of the current thesis is to improve gear fault diagnostics using dynamic modelling and simulation. With this overall goal, the emphasis will be focussed on (i) bringing a fundamental understanding to the planetary gear torsional vibration, (ii) studying the gear faults and their effect on the torsional vibration and (iii) examining the signal processing techniques to diagnose gear faults in planetary gear systems via torsional vibration. The following can be listed as the main technical objectives of this research,

1) Develop FEA models to evaluate the planetary gear torsional mesh stiffness;

2) Improve the fault diagnostics methods for the fixed axis gears with flexible support;

3) Study the planetary gear boundary effects on the planetary gear dynamic behaviour;

4) Develop planetary gear dynamic models to incorporate the gear mesh stiffness;

5) Examine signal processing techniques appropriate for planetary gear fault diagnosis.

As the focus of this study is to improve the planetary gear fault diagnostic methods, any modal analysis and gear design guideline aspects will not be included in this dissertation. To keep the focus on simplicity and efficiency, spur gears were chosen for this study. The study of other types of gears such as helical gears is kept outside the scope of this thesis. It was not considered realistic to examine every possible parameter or variable with the tooth fault because there are such a large variety of options for the gear parameters. As a result, a planetary gear system with one particular set of gear parameters was used in this study. Moreover, the type of gear tooth fault in the research was limited to a tooth root crack as it can lead to catastrophic failure of the whole drive train system.

1.3 Research methodology

The gear fault detection analysis can be achieved by performing either experimental vibration measurements or dynamic simulations (Endo, 2005). The advantage of experimental measurements is that they are based on a real system, but the measurements could also be associated with some issues, for example, the difficulties in accessing the desired vibration measurement (Inalpotat, 2009; Endo, 2005). Most importantly, it is both time-consuming and cost-consuming to carry out the experiments, especially when producing multiple crack situations. Dynamic modelling and simulation can overcome many of these issues and can be a good alternative approach to study the dynamic behaviour of the cracked gear system (Endo, 2005). Dynamic modelling and simulation also has the advantage that it can increase the understanding of the system behaviour before the initiation of a measurement campaign. As a result, the dynamic modelling method will be used in this research with some reasonable trade-off between reality and simplicity. The methods used can be described as follows,

1. Mesh stiffness evaluation and crack modeling: The variation of the gear mesh stiffness is the main internal excitation mechanism for the gear system and once the tooth crack occurs, the gear mesh stiffness will change accordingly. The planetary gear system includes sun-planet mesh stiffness and ring-planet mesh stiffness, which could be evaluated by the finite element method. ANSYS is a popular finite element software, which could be used in the areas of structure analysis, fluid flow, heat transfer, magnetic field analysis and so on (Kohnme, 2003). With the availability of powerful nonlinear analysis capability, ANSYS can easily handle the nonlinear geometrical analysis, the nonlinear material behaviour and especially the ability to handle the nonlinear contact analysis as the gear teeth mesh with each other. APDL (ANSYS parametric design language) could be used to develop a computer program which could automatically generate the gear geometry and further calculate the gear mesh stiffness in ANSYS (Kohnme, 2003). Different crack scenarios could also be created by using the singular crack element and then its effect on the gear mesh stiffness could be obtained.

2. Dynamic modeling and numerical simulation: Dynamic modeling was used to represent the behaviour of a gear system over time. Newton's Second Law could then be used to develop the gear differential equations. As gear dynamic behaviour is a complex phenomenon, some reasonable assumptions must be used to simplify the system equations, like the lumped mass assumption. The support bearing could be simplified by using an isotropic stiffness. The interaction between gear teeth could be represented by a time varying spring, whose stiffness is equivalent to the gear mesh stiffness evaluated above. MATLAB is a high performance numeric computation and visualization software product developed by The Math Works Inc and it involves the use of an iterative environment containing numeric computation, matrix computation, signal processing and graphics capabilities (MathWorks, 2005). MATLAB has several different functions for the numerical solution of ordinary differential equations, such as ode45, ode23, ode15s, ode23s and so on (MathWorks, 2005). For example, the ode45 solver is based on an explicit Runge-Kutta formula and is suitable for nonstiff problems. The ode15s uses the backward differentiation formulas (also known as Gear's method) and is suitable for solving stiff problems. Besides, users could also use

MATLAB to program their own solvers as they need to, which could be based on the theory of Newmark or Wilson methods.

3. Signal processing techniques: For fault detection analysis, signal processing techniques could be used to extract the signal fault features. With the impact from the gear tooth fault, the gear system will produce abnormal dynamic responses compared with responses from a healthy gear system. However, these abnormal responses tend to be transient, weak and are mixed with the other normal responses and noise. Some advanced signal processing techniques, like amplitude demodulation, phase demodulation, narrow band envelope and so on are used in this research. MATLAB has a range of in-built functions such as Fast Fourier Transforms (FFT), cubic interpolations and digital filters (MathWorks, 2005). The color graphics included also provides a sophisticated visualization capability for the more advanced signal processing techniques. Besides, MATLAB also has a Signal Processing Toolbox, which could be used to analyze and compare signals in time, frequency, and time-frequency domains, identify patterns and trends, extract features, and gain insight into gear dynamic behaviour (MathWorks, 2005).

1.4 Organization of the thesis

The current thesis is organized into 8 chapters.

Chapter 1 presents an overview, the research objectives and scope, and the methodology employed in the gear fault simulation and analysis.

Chapter 2 performs a critical literature review to examine the recent gear fault analysis research frontier and identifies gaps in the field of gear tooth crack detection.

Chapter 3 presents detailed gear mesh stiffness evaluation procedures for the planetary gear system based on the FE method. The method of modeling the gear mesh stiffness with the tooth crack is also presented in this chapter.

Chapter 4 presents a study to improve the gear fault detection in a flexibly supported gear system using iterative convergence of tooth mesh stiffness.

Chapter 5 presents detailed analysis of a ring-planet mesh stiffness study with different ring gear boundary conditions and crack locations.

Chapter 6 presents the method of modeling planetary gear systems with a flexible ring gear.

Chapter 7 evaluates and analyses the planetary gear fault detection results using some advanced signal processing techniques.

Chapter 8 summaries and discusses the important findings and conclusions in this research. Further research is also recommended for future work.

Chapter 2 Literature review

2.1 Introduction

Vibration characteristics of cracked gear systems are able to provide essential information for maintenance engineers to detect the faults in the early stage of development. Gearbox condition monitoring and fault diagnosis has attracted considerable attention for both fixed-axis gears and planetary gears over the past decades. This chapter aims to review the research and development of condition monitoring and fault diagnosis of gearboxes, especially focussing on the dynamics of cracked planetary gear systems. There have been various types of gear faults, which were usually caused by inappropriate operating conditions, manufacturing errors or other reasons. Tooth cracks, as one of the most severe gear faults, often propagate along either the gear width direction or the gear thickness direction or both depending on the gear tooth parameters and the gear loading condition. Due to the propagation of the crack, the corresponding gear mesh stiffness will then be changed and therefore it will result in abnormal dynamic responses, such as transient impacts and the associated high frequency components. Thereafter, the signal processing techniques can be further used for the purpose of gearbox condition monitoring and fault diagnosis. This chapter presents a literature review of the relevant literature as follows,

Section 2.2: the summary of the gear failure modes;

Section 2.3: the review of the gear crack propagation paths;

Section 2.4: the review of methods calculating the shaft-variant mesh stiffness with cracks;

Section 2.5: the review of dynamic modelling methods of the gear systems;

Section 2.6: the review of signal processing methods for gear condition monitoring.

2.2 The summary of the gear failure modes

According to Neale, the gear failure modes mainly include four different types, which are surface fatigue, scuffing, wear, and tooth root cracks (Neale, 1995). These faults could be

induced by various reasons and this section mainly reviews the characteristics and the reasons for these faults. Of course, the other faults in the gear system accessories would also deteriorate the normal operation of the gear system, but these will be discussed in the future.

Surface fatigue or pitting occurs when the Hertzian contact stresses are higher than the surface can stand and it can be divided into initial pitting and progressive pitting. Initial pitting can be randomly distributed over the whole tooth flank, but more often is found around the pitch line or in the dedendum (Endo et al., 2009). Progressive pitting occurs when the load redistribution associated with the initial pitting is not sufficient to reduce stresses below the fatigue limit and the new high spots are continuously removed by fresh craters (Neale, 1995). A particular form of pitting is spalling which removes relatively large sections of the gear tooth surface around the pitch line. It can be caused by the abrupt transition between a hard case and the relatively soft materials underneath or may be due to local metallurgical defects (Smith, 2003).

The lack of a lubricant film caused by overheating or absence could induce scuffing (Neale, 1995). The scuffing characteristic may range from a lightly etched appearance to even severe welding and tearing of engaging teeth (Neale, 1995). There were two identified mechanisms which give oil film breakdown. Failure of the oil film at very low speed is caused by insufficient hydrodynamic bearing action to keep the surfaces apart and this form of scuffing is known as cold scuffing (Smith, 2003). The normal type of warm-scuffing generates oil film breakdown by raising the temperature of the oil film locally to the point where the oil film can no longer maintain the surface apart (Smith, 2003).

Wear involves steady removal of metal from the gear flank usually over the whole face and may either give the appearance of a lapped surface or may give a surface which is grooved in the sliding direction (Neale, 1995). The form of the wear includes abrasive wear and chemical wear. The abrasive wear was caused by abrasive particles dimensionally larger than the film thickness and both tooth flanks will be affected in the direction of sliding (Neale, 1995; Smith, 2003). If nothing was done to remove the abrasive particles, the gears can lose surprisingly large amounts of metal. Chemical wear can occur when the gear experiences

extreme pressure oil and high temperatures under sustained heavy loads (Smith, 2003). High pressure and high temperature can cause the chemical reaction between the gear material and the contaminations in the oil and then the corrosion would be removed under the gear mesh action.

The incidents of whole tooth breakage are very uncommon and in some cases, part of the tooth may be lost while the gear tooth could still bear the load. More often, the crack starts from the root of the tooth as the gear tooth acts like a cantilever beam and the root of the tooth experienced high cyclic stress (Smith, 2003). If this stress rises to a certain level, it would cause root cracks which can propagate very quickly and lead to the loss of a large piece of the tooth or even the whole tooth. The causes of tooth breakage may lie in a tooth design that is overloaded, bad stress raisers in the root or in unsuspected transient overload due to vibration.

All these faults occur due to different reasons and on different gear tooth positions. For example, the pitting normally occurs on the gear pitch line while the gear crack normally starts from the gear tooth root. Other information that should be paid attention to is how distributed the gear fault is. For example, tooth wear and scuffing are normally distributed faults, which mean that almost every tooth surface in the gear system would have the fault and the fault would affect the operating during the whole shaft rotation. However, the gear tooth crack is normally a local defect, which means only one tooth or several teeth instead of every tooth would have the crack on the root and the fault would only affect the operating during a very short period of the shaft rotation. As a result, when the gear fault is simulated, the characteristic behaviour of the fault should be known in advance.

It should be noted that all these types of failures are not separate events and there is often a combination of different gear faults in the gear degradation process, which means the gear condition changes from the good condition to the bad condition. As a result, Bartelmus suggested treating the gear system as a whole unit (Bartelmus, 2011, 2014). The consideration of the gear degradation process is most close to the real situation that happens in the gear system condition monitoring, however the problem is this process normally

happens over a long period and it is hard to simulate this process by computer techniques. Multiple factors can contribute to the gear degradation process (Bartelmus, 2008, 2011). Bartelmus discussed these factors and analysed the gear damage process (Bartelmus, 2011, 2014). It was indicated by these publications that the first cause for a gear system break-down was the inner gearbox shafts and gear misalignment, which will cause the scuffing and tooth fatigue crack and further development until tooth brittle breakage or gear crack. In this research, the gear crack will be focused on because this type of fault is most dangerous and can directly lead to catastrophe or the breakdown of the whole gear system.

2.3 The review of gear crack propagation paths

The finite element modelling methods are the most common and reasonable approaches to simulate the gear crack propagation. Extensive previous studies have focused on the fixed-axis gears, especially the spur gear with either plane stress or plane strain assumptions for 2D models. Recently, with the availability of super-computing capabilities, 3D gear finite element models and extended finite element method (XFEM) have been used to study the gear crack propagation with more practical assumptions.

FRANC is a 2D FE program developed in the late 1980's at Cornell University and it was first used by Lewicki to study the gear tooth crack propagation (Lewicki & Ballarini, 1997). Linear elastic fracture mechanics was used in this program and the crack propagation path was used to automate numerical re-meshing in the software (Lewicki & Ballarini, 1997). Later on, the crack propagation path predictions were also studied under the effect of moving gear tooth loads by the same author and this time, the criteria of Erdogan and Sih was used for predicting gear crack propagation paths (Lewicki et al., 2001). Glodez developed a computational model for determining the gear service life and the Paris equation was used for the gear crack propagation prediction (Glodez et al., 2002). The effect of gear parameters (like the backup ratio, pressure angle and the gear root fillet shape) on the gear tooth crack propagation was studied by Pandya and the simulation results suggested that the crack would follow a combination of tooth and rim fracture for different gear parameters (Pandya & Parey, 2013a, 2013b, 2013c). However, the aforementioned publications were limited by the

assumption that the loading was constant and the loading variations due to stiffness reduction of the cracked tooth have been neglected. This limitation drove the further development of the crack propagation prediction study in the dynamic situation. Based on the modified Paris equation, Yin utilized a non-linear dynamic model to study the gear tooth crack growth pattern while considering the varying load conditions (Yin et al., 2013). Guilbault integrated a LEFM analysis of the tooth fillet crack propagation problem into a nonlinear dynamic modelling of spur gear sets (Guilbault et al., 2015).

In order to simulate the crack propagation in all possible directions, three dimensional gear models were preferable options, especially for the bevel and helical gears (Lewicki et al., 1998). Spievak investigated fatigue crack growth in spiral bevel gears and arbitrarily created the curved crack fronts and the modelled crack trajectories were then included in the analysis (Ural et al., 2003; Ural et al., 2005). Ghaffari developed a 3D FE model to investigate the crack initiation and the crack propagation under partial contact loading conditions based on the width of the contact load acting along the thickness (Ghaffari et al., 2015). Recent studies on the XFEM have shown it to be an effective numerical tool for the analysis of crack problems and this method gets rid of the LEFM assumptions when modelling the crack growth (Giner et al., 2009). Rad has used XFEM to simulate 3D fatigue crack growth in a helical gear tooth root and obtained the growth path. It was found that XFEM could decrease the modelling time considerably by re-meshing only the crack front and the obtained path suggested that the crack tends to grow towards the top of the tooth (Amiri Rad et al., 2014).

The purpose of this research is to improve the gear fault detection using the vibration measurement and it is known that the gear mesh stiffness is closely related to its vibration response. As a result, it would be desirable to know the gear crack path before the gear mesh stiffness evaluation. The most preferable way is firstly using the finite element model to determine the crack propagation path and then evaluating the mesh stiffness based on the obtained crack path. The problem is that it takes a long time to run the finite element simulation and it needs super-computer access. To simplify the analysis, the gear crack propagation paths can be classified as the following based on the previous research literature,

(1) The crack path is a straight line and it crosses the whole gear tooth width (Chen & Shao, 2011, 2013a, 2013b; Howard et al., 2001; Ma et al., 2015; Smith, 2003). The maximum stress position is assumed to occur where a tangent at 30° to a radial line meets the tooth, as for the example shown in Fig. 2.1.

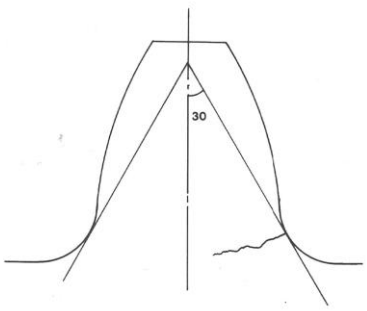

Figure 2.1 Example of straight line crack path (Smith, 2003)

(2) The crack path is a straight line but its propagation along the tooth width follows a curved path (Mohammed et al., 2012; Mohammed et al., 2013). This situation is suitable for a 3D modelling strategy, as for the example shown in Fig. 2.2.

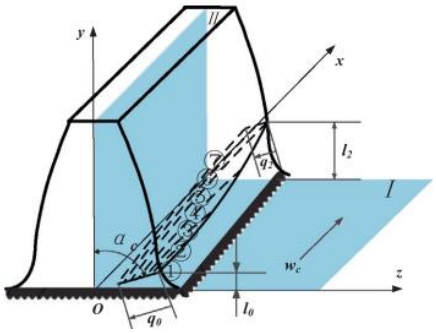

Figure 2.2 Example of straight line crack path with cured path along the tooth width (Mohammed et al., 2013)

(3) The crack path is a curved line while the path along the tooth width can cross the whole tooth or can follow a different path like in type (2) (Liang et al., 2014; Ma et al., 2015; Ma et al., 2014; Pandya & Parey, 2013d; Wu et al., 2008; Zhao et al., 2013). This path type is more practical and close to the real situation, but it needs an accurate curve equation, such as the example shown in Fig. 2.3.

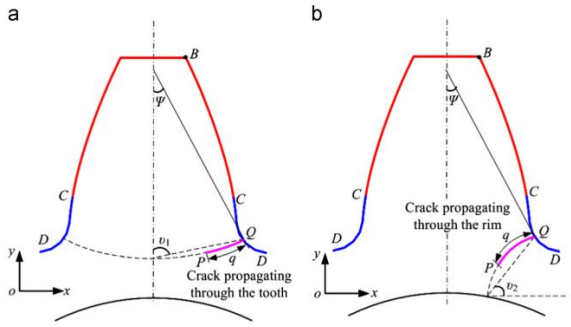

Figure 2.3 Example of straight line crack path with cured path along the tooth width (Wu et al., 2008)

(4) The gear fault is spalling and it normally occurs on the tooth surface (Chaari et al., 2008; Del Rincon et al., 2010; Del Rincon et al., 2012; Jia & Howard, 2006; Ma & Chen, 2012), as for the example shown in Fig. 2.4.

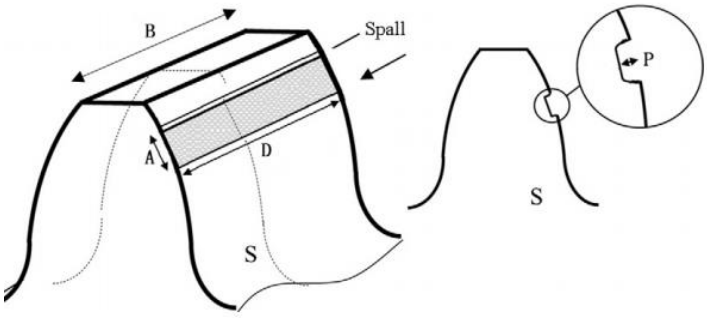

Figure 2.4 Example of spalling fault (Chaari et al, 2008)

2.4 The review of gear mesh stiffness calculation

2.4.1 Analytical method

After evaluating gear crack propagation paths, the shaft-variant gear mesh stiffness with cracks can be calculated using either the analytical method or the finite element (FE) method.

Analytical methods are simpler and have a higher computational efficiency and therefore they have been widely used to calculate the mesh stiffness in both fixed axis gear systems and planetary gear systems. According to R.W. Cornell (Cornell, 1981), a pair of teeth in contact would deflect elastically and this deflection is due to a combination of the gear tooth as a cantilever beam, local contact compression, and tooth foundation flexibility (Lin & Liou,

1998). Based on the potential energy method (Yang et al., 1987), Wu calculated the gear mesh stiffness with different crack increments by including the Hertzian stiffness, bending stiffness and axial compressive stiffness (Wu et al., 2008). However, Wu's model ignored the effect of tooth fillet foundation and Chaari further developed Wu's model by considering the bending stiffness of the fillet-foundation. Further, the effect of a tooth root crack was analysed (Chaari et al., 2009). Wan adjusted the potential energy method to consider the gear root circle size and presented models based on whether the root circle was greater or smaller than the base circle (Chen & Shao, 2011; Mohammed et al., 2012; Wan et al., 2014).

The gear mesh stiffness calculation method used for fixed axis gears could also be used to calculate the mesh stiffness of the planetary gear after some modification. Chen and Shao modified their mesh stiffness for a fixed gear pair (Chen & Shao, 2011) for the planetary gear model with a tooth crack. The tooth cracks with different sizes and inclination angles on the sun and planet gear were investigated respectively (Chen & Shao, 2013a, 2013b). On the basis of the same potential energy method, Chen and Shao evaluated the gear mesh stiffness of the internal gear pair and then further evaluated the reduction of its mesh stiffness due to a gear tooth crack (Chen & Shao, 2013c). As the ring gear rim is flexible, Chen improved the mesh stiffness calculation model for the ring gear with pin supports as well as the tooth root crack by considering the ring gear rim flexibility (Chen et al., 2015). The potential energy method was also used by Liang to evaluate the time-varying mesh stiffness of a planetary gear set (Liang et al., 2014). It was found that the sun-planet and ring-planet mesh stiffness value in a planetary gear system could be evaluated by the corresponding fixed axis gear cases by considering the mesh period difference. In a planetary gear system, there were multiple sun–planet pairs and ring–planet pairs meshing at the same time. Even though each of the sun-planet or ring-planet meshes could have the same mesh stiffness variation shape, they are not necessarily in phase with each other. The phasing relationships of the planetary gears were calculated in Ref. (Parker & Lin, 2004).

2.4.2 FE method

Some difficult issues have been found when using the analytical method for calculating the gear mesh stiffness with the damaged tooth fault. Owing to the gear body flexibility, the extended tooth contact can occur outside the theoretical contact line (Ma et al., 2015). The use of FE modelling was found to be most suitable for capturing the extended tooth contact phenomenon, especially when there was a crack at the gear tooth root, which can aggravate this effect. Another issue was that the deviation between the gear mesh stiffness obtained from the analytical method and the FEA method which was found to become larger with the increase in the crack size. The FE model was found to be more suitable for modelling the gear tooth mesh stiffness with larger gear tooth crack size (Ma et al., 2014; Mohammed et al., 2013). In fact, the FE method has been a reliable and effective tool to study the gear mesh stiffness with or without a gear tooth fault. With the principle of linear elastic fracture mechanics, the crack propagation path for gear pairs with different contact ratio was investigated (Pandya & Parey, 2013a, 2013b). Shuting used 3−D FEM to study a pair of spur gears with machining errors, assembly errors and tooth modifications (Li, 2007). Vijaya used 2-D FEA to calculate the sun-planet and ring-planet mesh stiffness for a planetary gear system (Ambarisha & Parker, 2007). Jiande compared a large number of 2−D and 3−D gear models using parameters such as the torsional stiffness, tooth stresses and the stress intensity factors (Wang & Howard, 2006) and it was found that the results from the plane stress assumption were close to those from 3−D gear models when the gear tooth width was less than 100mm. With the plane stress assumption, Jiande studied the torsional stiffness of a spur gear and the effect of the tip modification on the torsional stiffness (Wang, 2003; Wang & Howard, 2004).

The analytical method and FE method both have their own advantages and disadvantages. For the analytical method, less computing resources are required and it is more suitable for the parametric study of the gear system (Cornell, 1981; Lin & Liou, 1998; Yang & Lin, 1987) even though some researchers used this method to study the crack effect of the gear system (Chaari & Haddar, 2009; Chen & Shao, 2013c; Chen et al., 2015; Mohammed et al., 2013; Parker & Lin, 2004; Wan et al., 2014). For the FE method, much more computing resources

are required but it can accurately capture the stiffness change when a crack occurs on the gear tooth (Ambarisha & Parker, 2007; Li, 2007; Ma et al., 2014; Mohammed et al., 2013; Pandya & Parey, 2013a, 2013b; Wang, 2003; Wang & Howard, 2004; Wang & Howard, 2006). As a result, this research will employ the FE method to calculate the gear mesh stiffness with the crack on the gear tooth.

2.5 The review of gear dynamic models

This section reviews the gear dynamic models that have been developed for studying the gear tooth crack effect. The models include fixed-axis gear dynamic models and the planetary gear dynamic models. All these models were developed to study different aspects of the gear system based on different assumptions. The calculated resultant gear mesh stiffness could be further incorporated into these dynamic models to study the crack effect.

2.5.1 Fixed-axis gear dynamic model

A single degree-of-freedom (DOF) gear model was used by Litak and Friswell to examine the effect of tooth shape imperfections and defects in mesh stiffness (Litak & Friswell, 2005). A four DOF gear model excluding the friction effect was created by Ma to explore the failure mechanism due to the local defects on the mesh stiffness and results obtained from the model were shown to have good agreement with the experimental work (Ma & Chen, 2012). A six DOF gear model including a spur gear pair, two shafts, the load, the mover and the bearings was developed by Parey. The excitations in the model were assumed to be the mesh stiffness and damping, backlash and the gear local defects (Parey et al., 2006). A similar six DOF gear model where the action line of the gear pair is parallel to one of the axes was used by Chen to predict the dynamic responses due to a gear tooth fault (Chen & Shao, 2013c). Mohammed also utilized this six degree of freedom model to investigate the gear response due to different crack propagation scenarios in the tooth root (Mohammed et al., 2012). This six degree of freedom gear model also showed good capability to capture the dynamic behaviour of the perforated gear system (Ma et al., 2015). An 8DOF model was presented by Bartelmus and in the model, two lateral degrees of freedom from the bearing were considered into the previous 6DOF models to simulate and aid the gear box diagnostics

(Bartelmus, 2001). However, in the model, the gyroscopic effects were ignored and this was further developed by Mohammed into a 12DOF gear dynamic model to compare the response with those vibration results from the 6DOF model and the 8DOF model (Mohammed et al., 2015). Zhou adopted a 16DOF mathematic model to study the response from the gear system considering the shaft-varying mesh stiffness and different levels of crack in the pinion (Zhou et al., 2012). A 16 DOF gear test rig mathematical model was produced by Endo to reproduce the gear fault signals (Endo et al., 2009). Jia and Howard presented a 26DOF mathematic model of three shafts and two pairs of spur gears in mesh for comparison of localised tooth spalling and crack damage (Jia & Howard, 2006). Wan developed a coupled lateral and torsional vibration dynamic model to calculate the vibration responses of a cracked gear-rotor system. In his model, the shaft was modelled using the FEA beam element (Wan et al., 2014).

2.5.2 Planetary gear dynamic model

August and Kasuba developed a mathematical model to study the planetary gear load sharing. The model was comprised of a power source, load, and planetary gear set and it was set to be equivalent to a conventional gear train by assuming a rotating coordinate (August, 1984). The natural frequencies of a single planetary gear were analysed using a similar planetary gear model (Botman, 1976). Kahraman presented a single-stage planetary gear train including the rigid body motions of the gears and the carrier arm to study the load sharing characteristic, the manufacturing error and the wear effect on the planetary gear dynamic response (Kahraman, 1994a, 1994b, 1994c). Lin and Parker proposed a new planetary gear dynamic model with two distinctions from the Kahraman's model: (1) the planet deflections were described by radial and tangential coordinates, and (2) gyroscopic effects induced by carrier rotation were modelled (Lin & Parker, 1999a, 199b). They used this model to investigate a series of factors influencing the planetary gear natural frequency. An extended three-dimensional model was developed by Velex to calculate the dynamic tooth loads on a planetary gear (Velex & Flamand, 1996). A planetary gear lumped parameter model considering the eccentricity error and planet position error was developed by Gu and the instantaneous gear geometry was used in the model (Gu & Velex, 2012; Gu & Velex, 2013).

Chen incorporated the mesh stiffness of the internal gear pair with a crack into a 21DOF planetary gear model to investigate the dynamic response (Chen & Shao, 2013a, 2013c). Based on a lump-parameter model, Liang investigated the vibration signal features of each component in the planetary gear system in the perfect and cracked situations (Liang et al., 2015).

All these gear mathematical models were utilizing the lump-parameter method to study the dynamic responses. Numerous DOFs were considered in these models and the model including the torsional and transversal motions was the most practice approach. Some other methods have also been developed recently. Parker et al. (Parker et al., 2000) used a combined finite element/contact mechanics formulation to study the dynamic response of gear pairs (Parker et al., 2000; Tanmminana et al., 2007), the quasi-static loads in planetary gears (Ligata et al., 2008), and the root stresses in planetary gears (Prueter et al., 2011). Abousleiman used a hybrid model to include deformable ring gears using beam elements (Abousleiman & Velex, 2006). These methods require great knowledge in software programming and the availability of significant computing resources. Most importantly, it has not been easy to analyse the crack effect on the dynamic responses. As a result, this research will use the lump-parameter methods incorporating the gear mesh stiffness to study the gear dynamic responses.

2.6 The review of signal processing methods for the gear fault diagnosis

The basic vibration waveforms generated by the gear system can be described as deterministic signals, which include both vibration in normal condition and vibration due to various faults (Randall, 2011). In this section, a review is made about some current vibration analysis techniques used for gear fault diagnosis. These techniques include the signal processing methods in the time domain, frequency domain and the time-frequency domain.

2.6.1 Time synchronous average technique

The time synchronous average (TSA) was developed in 1970s to enhance the gear vibration signal measured from helicopter gearboxes (Stewart, 1977). The idea behind TSA was that the gear rotation will keep the same rotation phase as that with its associated shaft. In this

way, the gear dynamic movements can be divided into numerous segments, each of which was exactly one shaft rotation in length. After obtaining sufficiently large number of segments, these signals could be added up so that the vibration movement which was consistent with the shaft rotation will be reinforced while vibration which is not periodic with the shaft rotation will be weakened (Braun, 1975; Braun et al., 1979; Forrester, 1996; McFadden, 1986; McFadden, 1987a, 1987b; McFadden et al., 1985; Wang & Wong, 2002). Fig. 2.5 illustrates how the TSA works. However, it is suggested that order tracking should be used as precursor to TSA if the speed of the gear system is fluctuating (Forrester, 1996). As TSA is based on the rotation of the shaft rather than time, it is more proper to refer to it as an angle domain signal. In the spectrum, the frequency is expressed in shaft orders, where

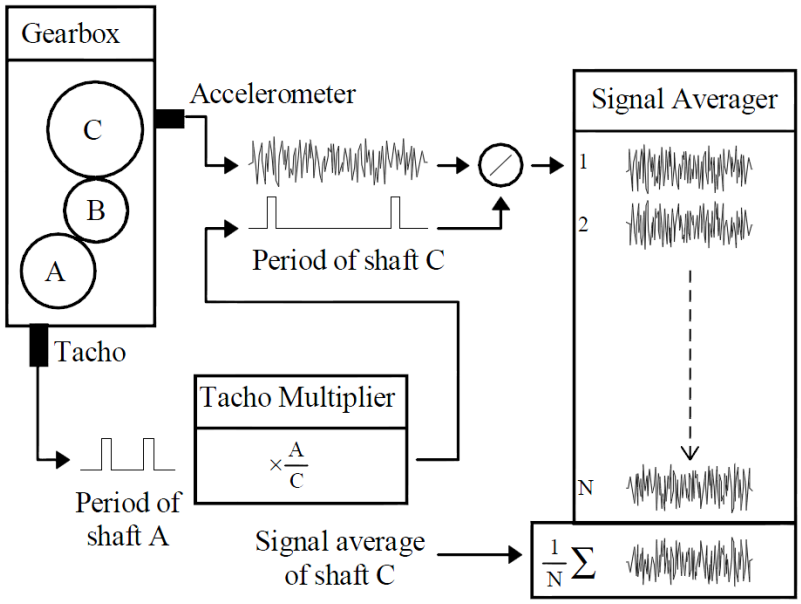

Figure 2.5 Time synchronous average (Forrester, 1996)

1shaft order equals to 1 cycle per revolution of the shaft.

2.6.2 Residual signal analysis

The residual signal can be obtained by removing the regular gearmesh component and its harmonics while keeping the local variations. Initially, the residual signal was operated in the frequency domain by removing the known gear mesh harnomics and then used inverse

Fourier transform to transform the rest back to the time domain (Braun, 1975). Some drawbacks were found using this method, which would create some false signals that were not related to the faults, and as a result, one or two pairs of sidebands around each tooth mesh harmonic might also be removed to improve the signal (Randall, 2011).

Linear prediction is another way to obtain the residual signal. Originally, the linear prediction is a basic way of obtaining the deterministic part of a signal based on a certain number of samples in the immediate past (Wang & Wong, 2002). The residual part of the signal can then be obtained by the subtraction from the actual signal value..

2.6.3 Narrowband envelope analysis

Narrowband envelope analysis was one of the prominent vibration signal processing techniques initially developed for the rolling bearing failure detection (McFadden & Smith, 1984). The idea behind this is that each time a localised defect in the gear makes contact under load with another surface it generated an extremely short duration impulse and its energy will be distributed across a very wide frequency range (McFadden & Smith, 1984). The centre frequency should be selected to coincide with the resonance to be studied and here, it was the tooth mesh harmonics. McFadden proposed that by narrow bandpass filtering about the selected tooth meshing harmonic, removing the other tooth meshing harmonic, and calculating the angle domain envelope, a signal could be obtained which contains contributions from both the amplitude and phase modulations (Forrester, 1996; Howard, 1994; McFadden & Smith, 1984; Wang, 2001).

2.6.4 Amplitude and phase demodulation analysis

An analytical signal can be written in a complex format, in which the imaginary part is the Hilbert transform of the real part. The amplitude modulation of the signal can be calculated by taking the absolute value of the signal's analytical signal and the phase modulation can be calculated by taking the phase of the analytical signal (McFadden, 1986; McFadden, 1987b; McFadden & Smith, 1985a). McFadden analysed the amplitude modulation of the residual signal and it was found it was much more effective than using the TSA method alone (McFadden & Smith, 1985a). Later on, McFadden also used the phase modulation of the

residual TSA signal to detect fatigue cracks in the helicopter's main rotor gearbox (McFadden, 1986; McFadden, 1987b). Brie proposed an adaptive demodulation with an abrupt change detector. It was shown to have some superiority over the traditional demodulation process in some aspects (Brie et al., 1997).

2.6.5 Frequency domain analysis technique

Frequency domain or spectrum analysis entails the conversion of the TSA signals into a frequency domain representation through the Fast Fourier Transform (FFT). In the frequency domain, the frequency is expressed in shaft orders, where 1shaft order equals exactly 1 cycle per revolution of the shaft. The advantage in using the frequency analysis is that the amplitude at each discrete frequency can be monitored instead of monitoring the overall amplitude of the TSA signal (De Silva, 2007). Log scale in the y-axis can be used to improve the dynamic range of the shaft order components. A defect on a particular component will cause the change of the amplitude of the corresponding frequency component and this characteristic can be used to monitor the condition of this component by measuring the amplitude change (Davies, 2012; Goldman, 1999).

Mark predicted additional sidebands in the frequency spectra produced by planet-carrier torque modulations, which might potentially mask the sidebands caused by damage in planetary gearboxes (Mark, 2009; Mark & Hine, 2009). To implement early fault detection of a planetary ring gear, Mark also suggested a simple frequency-domain method, which was able to eliminate the effects of transducers and structural-path-caused amplitude changes (Mark et al., 2010). Liu developed a mathematical vibration signal model to explore the diagnosis of equi-spaced planetary gear sets using the frequency features containing the gear faults information (Hong et al., 2014). McFadden and Smith pointed out that this effect was caused by the fact that each planet gear had varying phase angles (McFadden & Smith, 1985b). McNames applied Fourier series analysis to explain the source of the asymmetry observed in the spectrum and identified the location of the dominant frequency components near all harmonics of the meshing frequency (McNames, 2002). Kahraman classified the planetary gear into five distinct groups based on their sideband behaviour in terms of their

frequencies and amplitudes (Inalpolat & Kahraman, 2009; Inalpolat & Kahraman, 2010). Zhipeng considered both the amplitude and frequency modulations due to gear damage, the variant working condition and the effect of the transfer path. He deduced explicit equations for the characteristic frequency of local and distributed gear faults (Feng & Zuo, 2012). Zhipeng further gave explicit equations for the torsional signal model as torsional vibrations are theoretically free from the amplitude modulation effect caused by the transfer path and it was believed to be more effective in detecting the planetary gear fault (Feng & Zuo, 2013).

2.6.6 Time-frequency domain analysis technique

In some applications, the gear system is subject to a non-stationary loading environment and the traditional spectrum analysis or demodulation methods can have some difficulties in identifying the characteristic frequency from the non-stationary signals. Time-frequency analysis techniques were found to be very effective for conducting non-stationary signal analysis on vibration measurements to detect faults (Meltzer & Ivanov, 2003).

Forrester investigated the joint time-frequency energy patterns produced by different types and extent of gear faults using the in-flight vibration data from Royal Australian Navy helicopters (Forrester, 1990). Some limitations were found when using the traditional time-frequency analysis technique, like the cross-terms (Forrester, 1996). Forrester proposed a new approach to improve the detection based on time-frequency analysis and it was shown to have significant improvement in eliminating the cross-terms, which provided an enhanced visual representation of the instantaneous frequency (Forrester, 1996). W.J. Wang discussed the window function for the spectrogram and it was shown that the Gaussian function is well suited to the calculation of the energy distribution (Wang & McFadden, 1993a). Image processing techniques were further used to assist in the automatic interpretation of the gear vibration signatures based on the spectrogram (Wang & McFadden, 1993b). Pattern recognition procedures based on statistical and neural pattern recognition were reported to be applied to the detection of faults in the gear system (Staszewski et al., 1997). Chaari simulated tooth pitting and crack fault modes in a planetary gearbox and then used Wigner-Ville distributions to analyse the simulated signals (Chaari et al., 2006). Some

efforts were also made on reducing the cross-terms and enhancing the frequency resolution recently. Zhipeng explored the condition monitoring of the planetary gear in a wind turbine using the adaptive optimal kernel method because of its fine resolution and cross-term free nature (Feng & Liang, 2014). Synchrosqueezing transform and reassignment could improve the readability of the time-frequency plot, but it could still introduce some pseudo interferences. The iterative generalized method was used to reduce the interferences and resulted in much clearer time-frequency plots that could be utilized to diagnose the gear fault (Feng et al., 2015; Chen & Feng, 2016).

2.6.7 Condition monitoring in non-stationary operations

Most signal processing techniques mentioned above are effective for the gear condition monitoring under constant operation. Another fast growing research area is gear condition monitoring under non-stationary operation as the gear systems used in wind turbines, helicopters, and mining machinery work under condition of varying operation. The majority of the difficulties in vibration-based condition monitoring come from the variation of diagnostic features caused by load changes. A series of conferences on the condition monitoring of machines in non-stationary topic was begun in Wroclaw Poland in 2011. This topic has continued in Hammamet Tunisia 2012 (Fakhfakh, et al., 2012), Ferrara Italy 2013 (Dalpiaz, et al., 2013), Lyon France 2014 (Chaari, et al., 2014), until the recent one in Gliwice Poland 2016. Additionally, the Journal of Mechanical Systems and Signal Processing has published one special issue in 2013 about the non-stationary condition monitoring topic. Since then, various new techniques and condition indicators have been proposed aiming to meet the requirement of solving the problem of condition monitoring of machinery under varying operation (Antoniadou, et al., 2015; Urbanek, et al., 2013; Maheswari, et al., 2017). Among all these researches, a new diagnostic feature has been developed and discussed by Bartelmus (Bartelmus, 2009). This diagnostic feature has been presented as a function of transmitted power or load (Zimroz, et al., 2014; Bartelmus, et al., 2010), which was called load susceptibility characteristics (LSCh). In order to provide diagnostic decisions, two kinds of information (measurements) have been acquired: namely vibration based features (peak-to-peak, RMS, etc) and generator power that is related to the

operating conditions. A regression analysis can be performed and in a certain range of load, the relation could be linear (Bartelmus, 2009). The parameters ‘a’ and ‘b’ will change once the gear condition is changing, but the pattern depends on the damage type. It was concluded that a machine in good condition is less sensitive to load changes than a machine in bad condition.

2.7 Conclusion

This chapter has presented an overview of gear fault diagnostics using the gear dynamic modelling method, from the gear failure modes to the signal processing technique. First, the gear crack failure modes were reviewed and it was found that the gear crack was the most dangerous failure mode. Then, the crack propagation path was reviewed and it was found that the gear tooth root was the most common position for the crack as the stress on this position was the highest. As the crack could affect the mesh stiffness variation, the next section reviewed methods that have been developed for calculating the gear mesh stiffness with the effect of the tooth crack. It was found that the FE method was the most suitable approach to calculate the gear mesh stiffness as it could capture the motion outside the action line as well as large tooth motion. After this, as the mesh stiffness could be further incorporated into the dynamic model to evaluate the dynamic response of the cracked gear, the gear dynamic model was reviewed. It was found that the dynamic models, especially the lump-parameter modelling approaches, were able to effectively reveal the dynamic response. Finally, some common signal processing methods were reviewed to assist the detection of the gear fault. The following chapters will use the knowledge and techniques reviewed here to improve the gear fault diagnostic understanding.

Chapter 3 The overall spur planetary gear torsional stiffness

3.1 Introduction

Planetary gears have substantial advantages over parallel shaft drives, including compactness and large torque-to-weight ratio and because of these characteristics, planetary gear sets are used to transmit power in a wide range of industrial applications including automotive, aerospace, wind turbines and so on.

Typically, a planetary gear train consists of sun gear, ring gear, planet gear, carrier arm, bearings and other accessories. The sun gear, ring gear and carrier arm are often referred to as central members and they can kinematically rotate about the same axis, while, the planet gears are connected by bearings to the carrier arm and simultaneously in mesh with the sun and ring gears. The planet can not only rotate about the central members' axis but can also rotate about its own axis. A schematic of a planetary gear is shown in Fig. 3.1.

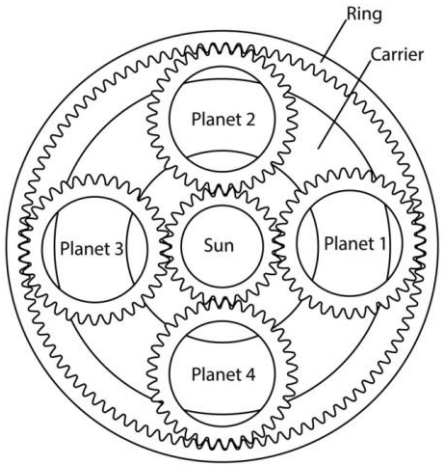

Figure 3.1 Schematic of a planetary gear (Cooley & Parker, 2014)

In practical applications, one of the central members has to be held stationary and there are six basic arrangements of planetary gear trains (Radzevich, 2012). When the carrier arm is held at rest, the gear train will become a fixed axis train with one external-external gear pair and one internal-external gear pair. When the sun gear is held at rest, the carrier or the ring gear can be the input driving component. More often, the ring gear will be held fixed and if

the driving component is the sun gear, the planetary gear train operates as a speed reducer. If the driving component is the carrier arm, the planetary train operates as a speed multiplier.

Despite their advantages, noise and vibration, reliability and early detection of damage remain major concerns in their applications. In automotive applications, vibration from the transmission, which contains several planetary gears, leads to noise that, is perceived negatively as a measure of vehicle quality (Sheng, 2012). In most helicopters, planetary gears are used in the last stage of gear reduction and are mounted directly to the helicopter cabin. As a result, the planetary gears are the main noise source in helicopter cabins and the measured sound levels can exceed 100dB (Krantz, 1992). This causes communication problems and a hazardous noise environment in the helicopter. Noise is also an issue in wind turbines, which contain one or more planetary gears. Dynamic tooth and bearing loads affect the lifetimes of planetary gear components. Planet bearings fail in wind turbines as a result of dynamic loads and vibration from the gear mesh excitation. Such vibration, along with excitation from wind loading on the blades, is a dominant vibration source (Cooley & Parker, 2014; Struggl et al., 2015).

Planetary gear trains were the subject of intensive research, focussing on the determination of planetary gear mathematical models (Botman, 1976; Cunliffe et al., 1974; Kahraman, 1994a, 1994b, 1994c; Lin & Parker, 1999), planet load sharing (Bodas & Kahraman, 2004; Boguski et al., 2012; Kahraman, 1994c; Kahraman, 1999; Ligata et al., 2009; Ma & Botman, 1985; Singh, 2004, 2010; Singh et al., 2008), vibration mode properties (Ericson & Parker, 2009, 2013; Kahraman, 1994a; Lin & Parker, 1999a, 1999b; Parker & Wu, 2010; Wu & Parker, 2008), and dynamic response (Chen & Shao, 2011, 2013a, 2013c; Chen et al., 2015; Gu & Velex, 2013; Kim et al., 2012; Sun & Hu, 2003; Velex & Flamand, 1996). As experiments are very expensive and hard to control, PHM (Prognostics and Health Management) researchers tend to employ different lumped-parameter models to analysis the dynamic response of the planetary gear system. Each of the sun, ring, carrier and N planets can be treated as rigid bodies where the gear mesh interactions can be represented by springs and damping acting along the line of action (Kahraman, 1994b). The variations in tooth mesh stiffness are the main internal vibration generation mechanism in the system and shaft

phase-variant mesh stiffness considerations are the most appropriate model for the internal excitation. The incorporation of more realistic gear mesh stiffness functions improves the accuracy of modelling the response from a damaged gear train and can be used to generate more efficient diagnostic tools.

This chapter mainly covers three parts: first, the method for calculating subsystem and overall planetary gear systems torsional stiffness using FEM (Finite Element Method) was presented; second, predictive models using subsystem stiffness to predict the overall stiffness were discussed; finally, crack sensitivity analysis based on the predictive models has also been developed in this chapter.

3.2 Planetary gear FEA models

The planetary gear train used in this thesis was initially based on a 750kW wind turbine drivetrain at the National Renewable Energy Laboratory (NREL), USA. In order to reveal the causes and loading conditions in wind turbine gearboxes, NREL established the Gearbox Reliability Collaborative (GRC) by exploring the drivetrain numerical analysis, full-scale dynamometer testing and field testing (Sheng et al., 2011). The drivetrain includes the hub, main bearing, main shaft, gearbox, brake, high speed shaft, and generator, as shown in Fig. 3.2.

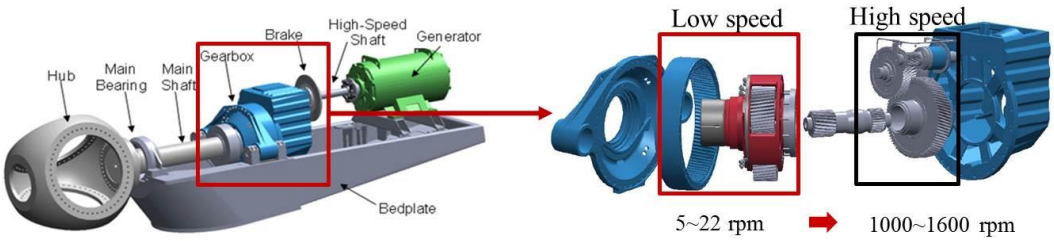

Figure 3.2 Wind turbine drivetrain from GRC (Sheng et al., 2011)

In the drivetrain, the gearbox has an overall ratio of 1:81.491. It is composed of one low speed planetary gear stage (ratio 5.71) and two high speed parallel shaft stages (ratio 14.27). The input speed is normally 5−22 rpm and after the planetary gear box stage, the speed can increase to 1000−1600 rpm. The planetary gear stage accommodates three planet gears, an

annulus gear, and a sun gear. The planetary gear parameters used in this chapter are listed in table 3.1.

Table 3.1 Planetary gear parameters

	Sun gear	Planet gear	Ring gear
Number of teeth, Z_i	Z_s=21	Z_p=39	Z_r=99
Module, m_n	10 mm	10 mm	10 mm
Pressure angle, α_i	α_s=20º	α_p=20º	α_r=20º
Pitch diameter, d_i=m Z_i	d_s=210 mm	d_p=390 mm	d_r=990 mm
Addendum, $h_{ai}=h^*_a$ m, h^*_a=1, 0.89	h_{as} =10 mm	h_{ap} =10 mm	h_{ar} =8.9 mm
Dedendum, $h_{fi}=h^*_f$m, h^*_f=1.25	h_{fs} =12.5 mm	h_{fp} =12.5 mm	h_{fr} =12.5 mm
Basic diameter, $d_{bi}= d_i \cos\alpha_i$	d_{bs}=197 mm	d_{bp}=366 mm	d_{br}=930 mm
Elastic Modulus, E	210MPa	210MPa	210MPa
Paisson's Ratio, ν	0.3	0.3	0.3
Friction coefficient	0.2	0.2	

3.2.1 Mesh phase of planetary gear trains

The concept of mesh phase is used to represent the number of teeth in contact and it includes the phase between the various sun-planet meshes, the phase between the various ring-planet meshes, and the relative phase between the ring-planet and sun-planet meshes (Parker & Lin, 2004). The mesh phasing relationships differ slightly depending on the direction of planet rotation, which is decided by which element (sun, carrier, or ring) is fixed, which element is the input, and what the input element rotation direction is. There are twelve possible combinations as listed in reference (Parker & Lin, 2004). For the clockwise rotation, the mesh phasing relations between the various sun-planet meshes and the mesh phasing relations between the various ring-planet meshes are,

$$\gamma_{sn} = \frac{Z_s \Psi_n}{2\pi}, \quad \gamma_{rn} = -\frac{Z_r \Psi_n}{2\pi} \ . \tag{3.1}$$

Ψ_n is the circumferential orientation of each planet and it is an integer multiple of the least mesh angle,

$$\Psi_n = P_n \frac{2\pi}{Z_r + Z_s} \ , \tag{3.2}$$

where P_n is an integer number. However, it is found that $\gamma_{sn}=\gamma_{rn}$, which means the phase of the sun-planet and the phase of the ring-planet meshes on the same branches of the planetary gear are always identical (Parker & Lin, 2004). The calculation of relative phasing between the ring-planet and sun-planet meshes at a given planet was also given in reference, as shown in Fig. 3.3 (Parker & Lin, 2004).

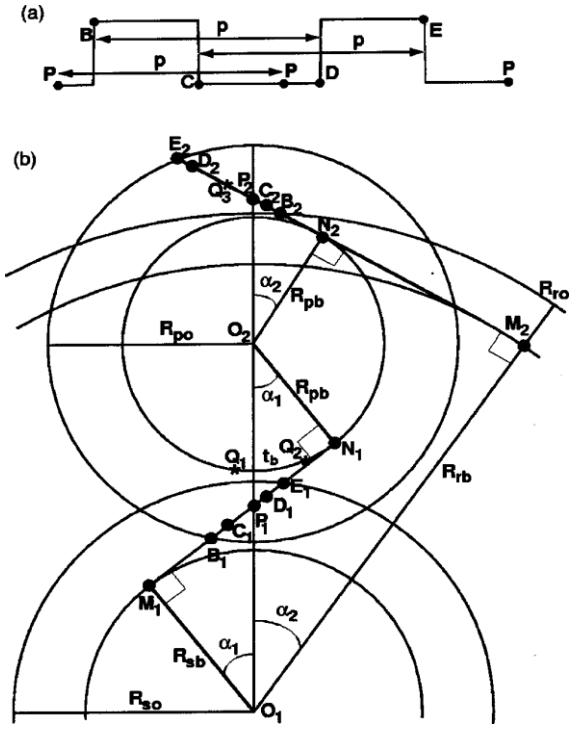

Figure 3.3 (a) Example mesh tooth variation. (b) sun-planet and ring-planet mesh details (Parker & Lin, 2004).

The following nomenclature is helpful in understanding the meshing process:

B, point where second tooth enters contact;

C, point where first tooth exits contact;

P, second tooth at pitch point;

D, point where third tooth enters contact;

E, point where second tooth exits contact;

1, sun-planet mesh subscript;

2, ring-planet mesh subscript;

R_{sb}, R_{pb}, R_{rb} are sun, planet, ring base radii separately;

R_{so}, R_{po} are sun and planet outer radii;

R_{ro} is the inner radius of the ring gear teeth;

$\alpha_{1,2}$ are pressure angles;

t_b is the planet tooth thickness at the base circle;

Q_1 is the image of P_1;

Q_2 is the point which is an arc-length t_b away from Q_1;

Q_3 is the point which is an integer number of base pitches away from Q_2.

For the sun-planet mesh, we have

$$B_1E_1 = M_1E_1 + B_1N_1 - M_1N_1 = \sqrt{R_{so}^2 - R_{sb}^2} + \sqrt{R_{po}^2 - R_{pb}^2} - (R_{sb} + R_{pb})\tan\alpha_1, \tag{3.3}$$

$$B_1P_1 = M_1P_1 - M_1B_1 = R_{sb}\tan\alpha_1 - \left(\sqrt{R_{so}^2 - R_{sb}^2} - B_1E_1\right), \tag{3.4}$$

$$B_1C_1 = B_1E_1 - p, \tag{3.5}$$

$$B_1D_1 = p = \frac{2\pi R_{sb}}{Z_s} = \frac{2\pi R_{pb}}{Z_p}, \tag{3.6}$$

For the ring-planet mesh, we have

$$B_2E_2 = M_2N_2 + N_2E_2 - M_2B_2 = O_1O_2\sin\alpha_2 + \sqrt{R_{po}^2 - R_{pb}^2} - \sqrt{R_{ro}^2 - R_{rb}^2}\ , \tag{3.7}$$

$$B_2P_2 = M_2N_2 - M_2B_2 = R_{rb}\tan\alpha_2 - \sqrt{R_{ro}^2 - R_{rb}^2}\ , \tag{3.8}$$

$$B_2C_2 = B_2E_2 - p, \tag{3.9}$$

$$B_2D_2 = p, \tag{3.10}$$

$$O_1O_2 = \frac{(R_{sb}+R_{pb})}{\cos\alpha_1}, \tag{3.11}$$

And then,

$$Q_2B_2 = P_1P_2 - B_2P_2 - t_b = \left[R_{pb}\tan\alpha_1 + R_{pb}(\pi - \alpha_1 - \alpha_2) + R_{pb}\tan\alpha_2\right] - B_2P_2 - t_b, \tag{3.12}$$

The position of Q_3 within the contact region B_2E_2 is

$$B_2Q_3 = p - p[dec(\frac{Q_2B_2}{p})], \tag{3.13}$$

$dec(\frac{Q_2B_2}{p})$ is the decimal portion of $\frac{Q_2B_2}{p}$. Then,

$$P_2Q_3 = |B_2Q_3 - B_2P_2|, \tag{3.14}$$

Consequently, the magnitude of the relative phase between the pitch points is,

$$|\gamma_{rs}| = \frac{P_2Q_3}{p}. \tag{3.15}$$

The sign of γ_{rs} depends on: 1) whether Q_3 falls within B_2P_2 or P_2E_2, and 2) whether contact along the line of action progresses from B→E or E→B. The direction of contact along the line of action is indicated in reference (Parker & Lin, 2004) for all configurations.

For the planetary gear parameters described in table 3.1, the mesh phases γ_{sn} and γ_{rn} for counter-clockwise planet rotation can be calculated using equation (3.1),

$$\begin{Bmatrix}\gamma_{s1}\\ \gamma_{s2}\\ \gamma_{s3}\end{Bmatrix} = \frac{21}{2\pi}\begin{Bmatrix}0\\ \frac{2\pi}{3}\\ \frac{4\pi}{3}\end{Bmatrix} = \begin{Bmatrix}0\\ 7\\ 14\end{Bmatrix} \rightarrow \begin{Bmatrix}0\\ 0\\ 0\end{Bmatrix},$$

$$\begin{Bmatrix}\gamma_{r1}\\ \gamma_{r2}\\ \gamma_{r3}\end{Bmatrix} = -\frac{99}{2\pi}\begin{Bmatrix}0\\ \frac{2\pi}{3}\\ \frac{4\pi}{3}\end{Bmatrix} = \begin{Bmatrix}0\\ -33\\ -66\end{Bmatrix} \rightarrow \begin{Bmatrix}0\\ 0\\ 0\end{Bmatrix}. \tag{3.16}$$

For this system, the result indicates that each sun-planet mesh has identical tooth mesh phase engagement conditions as does each ring-planet mesh, which is a special case. The relative mesh phase γ_{rs} required between the nth ring-planet pair and nth sun-planet can be calculated using equation (3.15). For planetary gear system in table 3.1, B2P2=26.72mm, Q2B2=563.8956mm, B2Q3=26.1mm, P2Q3=0.62mm and it will give a result of $|\gamma_{rs}|$=0.02 and γ_{rs} has a positive sign.

However, in a more general situation, γ_{sn} will not be identical to each other and neither will γ_{rn}. For example, in the planetary gear type–2, in which the sun gear teeth number is 19, the planet gear teeth number is 32 and the ring gear teeth number is 83. The mesh phase can be calculated as,

$$\begin{Bmatrix}\gamma_{s1}\\ \gamma_{s2}\\ \gamma_{s3}\end{Bmatrix} = \frac{19}{2\pi}\begin{Bmatrix}0\\ \frac{2\pi}{3}\\ \frac{4\pi}{3}\end{Bmatrix} = \begin{Bmatrix}0\\ \frac{19}{3}\\ \frac{38}{3}\end{Bmatrix} \rightarrow \begin{Bmatrix}0\\ \frac{1}{3}\\ \frac{2}{3}\end{Bmatrix},$$

$$\begin{Bmatrix}\gamma_{r1}\\ \gamma_{r2}\\ \gamma_{r3}\end{Bmatrix} = -\frac{83}{2\pi}\begin{Bmatrix}0\\ \frac{2\pi}{3}\\ \frac{4\pi}{3}\end{Bmatrix} = \begin{Bmatrix}0\\ -\frac{83}{3}\\ -\frac{166}{3}\end{Bmatrix} \rightarrow \begin{Bmatrix}0\\ -\frac{2}{3}\\ -\frac{1}{3}\end{Bmatrix} \rightarrow \begin{Bmatrix}0\\ \frac{1}{3}\\ \frac{2}{3}\end{Bmatrix} . \quad (3.17)$$

For this system, it was found γ_{s2} is 1/3 mesh cycle behind γ_{s1} and γ_{s3} is 2/3 mesh cycle behind γ_{s1}. Same results were found in the ring-planet mesh phases. $|\gamma_{rs}|$ is found to be 0.4994 in this planetary gear system and the sign is positive.

3.2.2 Planetary gear geometry profile generation

3.2.2.1 Planetary gear geometry profile equation

Transmission of motion and power between gears is accomplished by means of the teeth of the driven gear pushing the teeth of the driving gear. Theoretically, there is an infinite number of conjugate profiles that can be used as gear teeth profiles. Nevertheless, involute profiles are the most widely used conjugate profiles in practice. There are various methods for manufacturing tooth profiles, such as planing, shaping, hobbing, broaching, rolling, grinding and honing (Simth, 2003). Because of the cutting tool tooth tip trajectory, it will also generate a gear tooth fillet section besides the involute profile. As a result, the major teeth profile can be divided into two parts: involute profile and the fillet. The planetary gear includes both external and internal gears and the basic equations for calculating the involute profiles are the same for both of them. Meanwhile, the equations for calculating the fillet depends on the manufacturing tool. The involute profile equations can be found in references (Dooner, 2012; Hwang, 1986; Litvin, 1989; Savage, 1995; Nair, 2005; Wang, 2003; Ye, 2001) and the detailed fillet equations can be found in references (Dooner, 2012; Hwang, 1986; Litvin, 1989; Savage, 1995; Nair, 2005; Wang; 2003). Some researchers also used a section of arc to represent the fillet shape (Hwang, 1986). The external and internal gear tooth profiles are shown in Fig. 3.4.

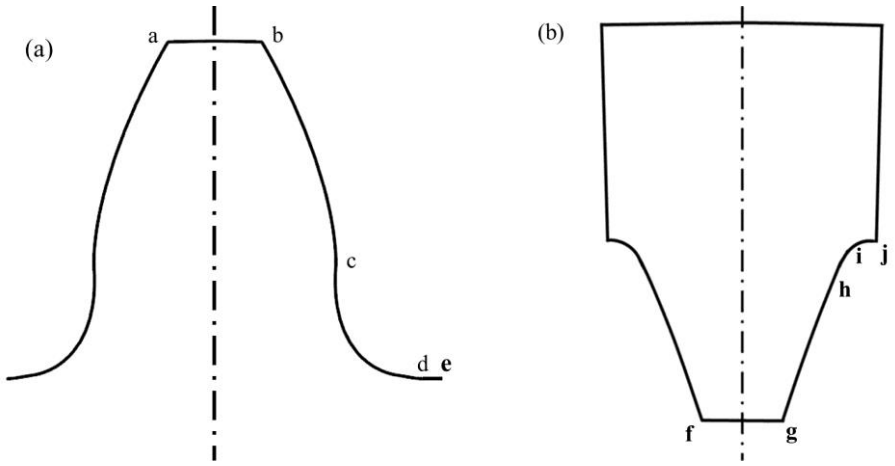

Figure 3.4 Gear tooth profile, (a) external gear tooth profile, (b) internal gear tooth profile

Section a−b and section f−g are the addendum curve, which are generated by the semifinished gear product and their equations under Cartesian coordinate system are,

$$x = r_a \cos\varphi,$$

$$y = r_a \sin\varphi, \tag{3.18}$$

where r_a is the radius of tooth addendum and φ is the angle from point a(f) to point b(g). Section b−c and section g−h are the pure involute curves and their equations under the Cartesian coordinate system are,

$$x = r_i \cos\gamma,$$

$$y = r_i \sin\gamma,$$

$$\gamma = inv\phi_p - inv\phi_i,$$

$$inv\phi_p = t_b/2r_b,$$

$$inv\phi_i = tan(\phi_i) - \phi_i,$$

$$\phi_i = \arccos(r_b/r_i), \tag{3.19}$$

where ϕ_i is the pressure angle at any point along the involute curve, t_b is the base tooth thickness, and r_i is the radius of any point on the involute curve. The equations for the fillet curve under the Cartesian coordinate system are,

$$x = r\sin\mu - (\frac{a_1}{\sin\alpha'} + r_p)\cos(\alpha' - \mu),$$

$$y = r\cos\mu - (\frac{a_1}{\sin\alpha'} + r_p)\sin(\alpha' - \mu),$$

$$\mu = r(\frac{a_1}{\tan\alpha'} + b_1),$$

$$a_1 = h_f - r_p,$$

$$\alpha' = \alpha + (90^\circ - \alpha)\cdot i,$$

$$b_1 = \frac{\pi m}{4} + h_a\tan\alpha + r_p\cos\alpha, \qquad (3.20)$$

where r is the radius of the pitch point, h_f is the dedendum height, i is the number of the points on the fillet, h_a is the addendeum height and, r_p is the radius of the cutting tool tip. Section d–e and i–j represent the gear root curve and they are the arc extension from point d(i).

To generate external and internal tooth involute and fillet tooth profile in ANSYS (FEA software), there are three methods that could be used:

1. CAD/FEA method. The profle can be generated using CAD software first and then transformed into the FEA software. The available CAD softwares include AutoCad, Solidworks and Pro/ENGINEER Wildfire. Sirichai (Sirichai, 1999) developed a customised AutoCad programming language to generate the profiles of external teeth. Recent Solidworks (2014) and Pro/ENGINEER (4.0) have their own design toolbox, in which the modules of standard gears can be found.

2. 'Discrete points' method. To use this method, the equation of the tooth profile needs to be known in advance and then numerious discrete points can be generated using Matlab or Excel software. These discrete data points contain the information of the coordinates of the tooth profile and they can be introduced into the FEA software. After that, these points can be connected to form a smooth tooth profile. Hao used this method to study the gear profile modification (Hao, 2012).

3. APDL method. APDL is an acronym for ANSYS Parametric Design Language and it allows the researcher to build their model in terms of parameters. With this method, the equation of tooth profiles can be incorporated in FEA software directly. Jiande Wang used this method to generate the involute and fillet tooth profiles (Wang, 2003).

Any of the three methods can be used to generate the gear tooth profile and this research adapted the APDL method for its high accuracy. The APDL program for generating the overall planetary gear profiles can be found in *Appendix A*. This program can be used to generate the whole planetary gear geometry with parameters. The number of the teeth and the modulus can be modified in order to generate the other types of planetary gears with different design parameters.

3.2.2.2 Planetary gear FEA modelling guidelines and consideration

By employing the equations (3.18), (3.19) and (3.20), the profiles of the gear teeth can be generated. However, the requirement for producing high quality elements with no excess distortion and well-shaped-aligned boundary elements has to be met. Additionally, by using the mapped mesh, a monotonic convergence curve could be obtained to improve the result accuracy (Wang, 2003). In order to achieve the mapped mesh goal, the whole gear tooth can be divided into a tooth involute region, a transition region and the gear body, as shown in Fig. 3.5. Eight-node solid element PLANE183 was chosen to produce a primary mapped mesh. PLANE183 has quadratic displacement behaviour and is well suited to modelling irregular meshes. The whole gear tooth mapped mesh is shown in Fig. 3.6.

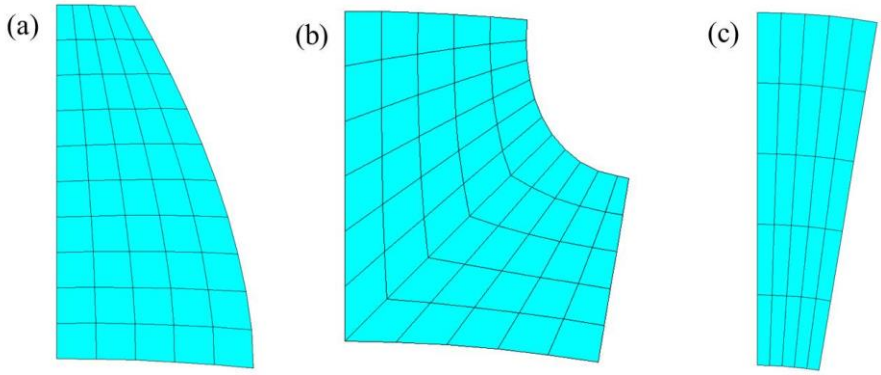

Figure 3.5 External gear tooth division, (a) tooth involute region, (b) transition region, (c) gear body region

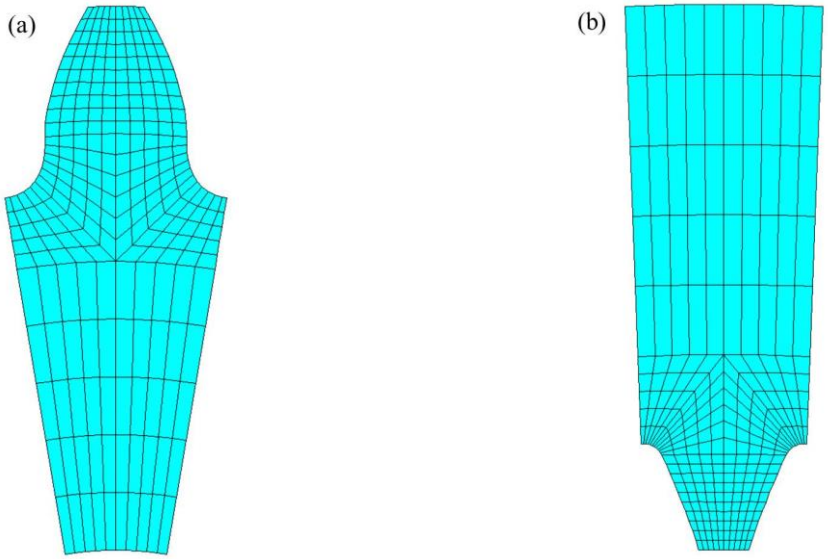

Figure 3.6 Gear tooth mapped mesh, (a) external gear, (b)internal gear

However, the gear tooth contact zone will experience high stress and the distortion field in the meshing gears varies with meshing position. Free meshing and adaptive re-mesh has been compared by Jiande. A solution error of 0.07% was found at the pitch point compared with the adaptive mesh (Wang, 2003). After applying the adaptive re-mesh with the meshing position, the whole tooth will be mapped with mapped mesh (transition region and gear body region) and adaptive mesh (contact side of tooth involute region), as shown in Fig. 3.7. The adaptive meshing will make the elements near the contact have relatively small dimension that enable the analysis to cope with the chaotic non-linear nature of the contact region. Within a looping program, adaptive re-mesh with contact was used at each mesh position.

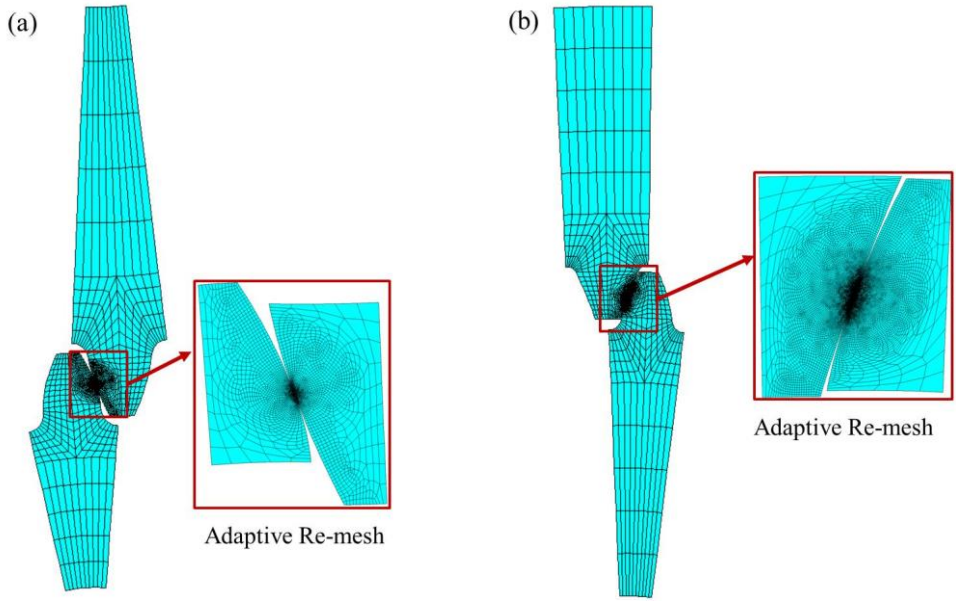

Figure 3.7 Gear adaptive re-mesh near contact zone, (a) external gear, (b) internal gear

Three-dimensional modelling with adaptive re-mesh within the contact zone is closer to the practical situation and will give the best torsional results. However, two-dimensional modelling with plane stress or plane strain assumptions can reduce the problem and greatly enhance the computation efficiency. Jiande created three different models to study the effect of changing thickness on the variations of the stiffness: the first model was a simple disk, the second model was based on a pair of meshing gears with one tooth and the third model was similar to the second model except that there is a 4mm crack located in the root area. In each model, the results of torsional stiffness were calculated under assumptions of plane stress, plane strain and 3D respectively. 3D model has been set as a benchmark and the relative error between plane stress and 3D and the relative error between plane strain and 3D have been compared (Wang, 2003). The plane stress assumption can achieve a smaller relative error (smaller than 3%) when the tooth thickness is less than 50mm. If the thickness becomes the major dimension in the model, the plane strain should be considered (Wang, 2003). However, both plane stress and plane strain assumptions will include errors compared to the 3D models.

The major limitation on gear stiffness study using FEA methods is the ‘rigid body motion’. For a precision gear set, there is no gap between the two contact teeth surfaces and the elastic

deformation is the main component for the transmission error. However, when generating the gear tooth profile, it is hard to create the surface of the gears in the just-touching position, especially when the gear surface is curved, as shown in Fig. 3.8. Additionally, if the meshing gear pair is modelled with tip-relieved teeth, the 'gap' between the surfaces of the gears is even larger and the 'rigid body motion' will be the main component of the total transmission error.

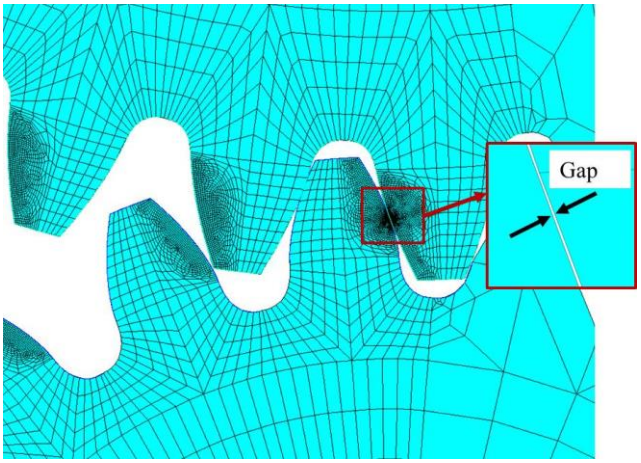

Figure 3.8 Gap between gear teeth in FEA model

In ANSYS, with this case, the program will give error massages, like *a DOF limit exceeded* message. ANSYS offers several options to overcome this difficulty in convergence,

1. *Build the model in the just-touching position*. This method requires the user to know where the position is and as the gear surfaces are curved, it becomes very hard to know the precise position.

2. *Use imposed displacements to move the model into position*. Similar with method 1, one needs to know a specified displacement value in order to move the model into its starting position.

3. *Solve the problem dynamically*. In a mesh cycle of a meshing gear pair, if part of the solution is obtained by static analysis and the other part by dynamic analysis, then the overall solution wouldn't be so good for the study of gear stiffness.

4. *Use weak springs to connect the bodies*. With this method, all the elements are connected together along with sufficient displacement constraint to prevent rigid-body motion. The suggested spring stiffness would typically be 6 to 8 orders of magnitude weaker than the contact stiffness and care must be taken when very flexible elements are connected to very

rigid elements. Additionally, care must also be taken with the position of the weak spring. Jiande suggested that the weak spring element can be connected to the master node of the input gear hub, which means the nodes of the input gear hub have to be coupled in rotation about the global coordinate system. During the rotation of the gear into each position of the mesh cycle, the length and the orientation of the link element have to remain constant and tangent to the input gear hub. One example can be found in Fig. 3.9.

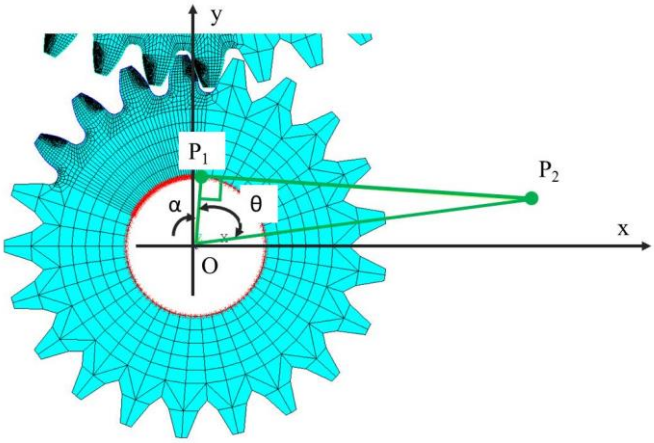

Figure 3.9 Weak spring attached on the input gear hub 'master node'

$P_1(x_1, y_1)$ is the master node located on the input gear hub and $P_2(x_2, y_2)$ is the node on the other end of the weak spring. O is the centre of the gear hub. The coordinate of P_1 can be found once the gear model was created and to create the weak spring, the coordinate of P_2 has to be known. OP_1 is the radius of the input gear hub and the length of P_1P_2 is user-defined. So the length of OP_2 is,

$$OP_2 = \sqrt{{OP_1}^2 + {P_1P_2}^2},$$

$$\alpha = \tan^{-1}\frac{|x_1|}{|y_1|},$$

$$\theta = \tan^{-1}\frac{|P_1P_2|}{|OP_1|},$$

$$x_2 = |OP_2| \cdot \cos[90° - \theta - (\alpha + ANG)],$$

$$y_2 = |OP_2| \cdot \sin[90° - \theta - (\alpha + ANG)]. \quad (3.21)$$

The weak spring was only used for the initial step with a very small torque until the teeth were just in contact. When the actual load torque was applied, the spring was disabled using the *birth&death* command (Wang, 2003).

3.2.3 Carrier arm and bearing simplification

As an important component in planetary gears, the planet carrier bears the support load of the planetary gears, which makes it the maximal torque bearing part in the planetary gearbox (Radzevich, 2012). The structural design and manufacturing quality of the planet carrier arm have tremendous influence on the load distribution among planetary gears, the load bearing capacity of the transmission device and noise and vibration levels. Kahraman (Bodas & Kahraman, 2004) studied the influence of carrier planet pinhole position error on the static load sharing behaviour of planetary gear sets. Abousleiman evaluated the contribution of the deflection of the carrier via substructures derived from 3D finite element models (Abousleiman & Velex, 2006). It showed that the carrier flexibility can modify the dynamic tooth loads on the sun-planet and ring-planet meshes. Jan Helsen (Helsen et al., 2011) used flexible multibody models to study the complexity for modal behaviour analysis of wind turbine gearboxes. Two new mode categories (the planet carrier modes and planetary ring modes) were found beside the traditional rotational-axial modes, translational-tilting modes and planet modes. To measure the carrier arm motion, four different sensors were placed around the carrier to capture the axial motion and two sensors were placed on the outer circumference of the carrier rim to capture the radial motion (Sheng et al., 2011). All the displacements are measured relative to the housing of the gearbox. Haastrup (Haastrup et al., 2011) developed an Adams model to model the planet carrier and the results showed good accordance with the carrier motion data mention above.

However, there are no specified requirements for the planetary carrier in the current gearbox standard (ISO, 2012). Most engineers and researchers still use trial and error methods and material mechanics methods to design and confirm the parameters of the planet carrier (Radzevich, 2012). Fig. 3.10 gives out one design from GRC and it can be found that the whole carrier arm is a hollow structure with end B connecting with the main shaft as the input. Bearings can be assembled in holes O_1, O_2, O_3 and then the planet gears can be connected with the bearings to rotate with the carrier arm.

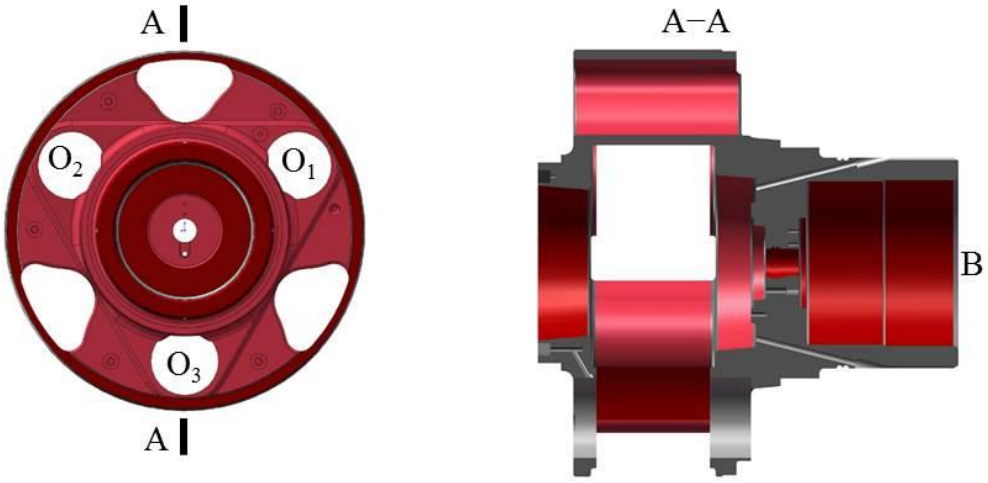

Figure 3.10 Planet carrier arm from GRC (Sheng et al., 2011)

From Fig. 3.10, it can be found that the structure of the carrier arm can be very complex and including all the details into the FEA software can cause great difficulty in the computation efficiency. In order to consider the carrier arm in a general situation, the carrier arm will be considered as a flexible beam with a square cross-section. As the FEA model is a 2−D model, one end of the beam was chosen to be the carrier arm input end B and the other end was chosen to be the planet gear hub A. The torque was applied to end B, which was connected by the pin support. The flexibility of the carrier arm is equivalent to the beam section, as shown in Fig. 3.11. By this way, the whole carrier arm can be modelled as three beams connecting the carrier arm hub and the planet gear hub. The dimension of the section can choose any value as long as the stiffness of the beam is equivalent to the carrier arm that is to be studied. However, further detailed analysis of the carrier arm will be given in chapter 6.

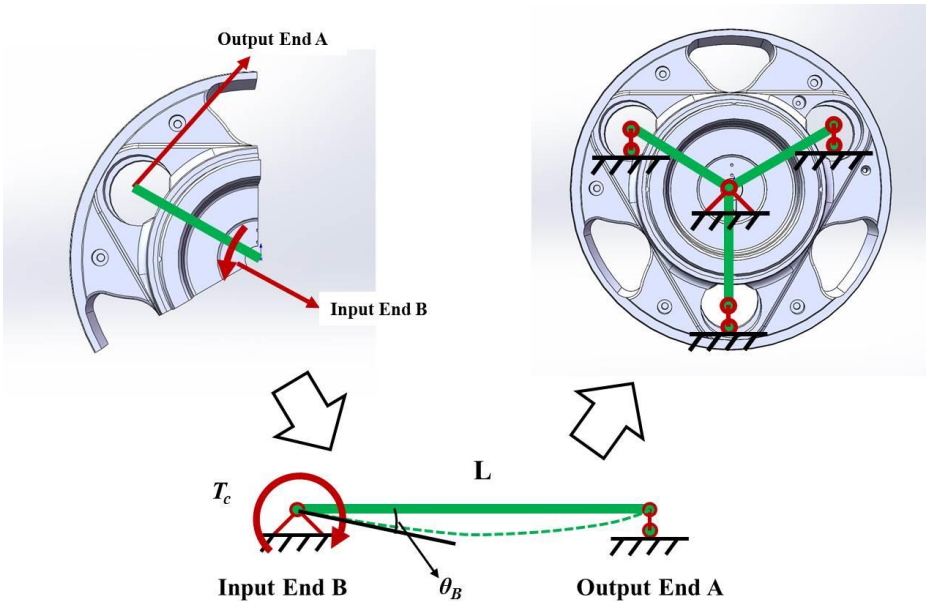

Figure 3.11 Beam model to represent carrier arm flexibility

The bearing configuration in the planetary gear from GRC can be seen in Fig. 3.12. The planet carrier is supported upwind (upwind is the entrance side of the planetary gear before power has passed through the gear and it can also be termed rotor side) and downwind (downwind is the side located on the aft end of the shaft and it can also be termed generator side) by full complement cylindrical roller and taper roller bearings. PLC−A is the roller bearing for supporting the planet carrier at the upwind side and PLC−B is the roller bearing for supporting the planet carrier at the downwind side. The planet gears are supported by two single row cylindrical roller bearings (PL−A and PL−B). PL−A is the roller bearing for supporting each planet gear at the upwind side and PL-B is the roller bearing for supporting each planet gear at the downwind side (Sheng et al., 2011). Bearings in FEA software can be modelled as contact elements or as stiffness matrices. To enhance the FEA computation efficiency, the bearing between the carrier and planet was modelled as a rigid revolute joint, (ANSYS MPC 184 element). The revolute joint is a two-node element that has only one primary degree of freedom, the relative rotation about the revolute axis. However, further detailed analysis of the bearing will be given in chapter 6.

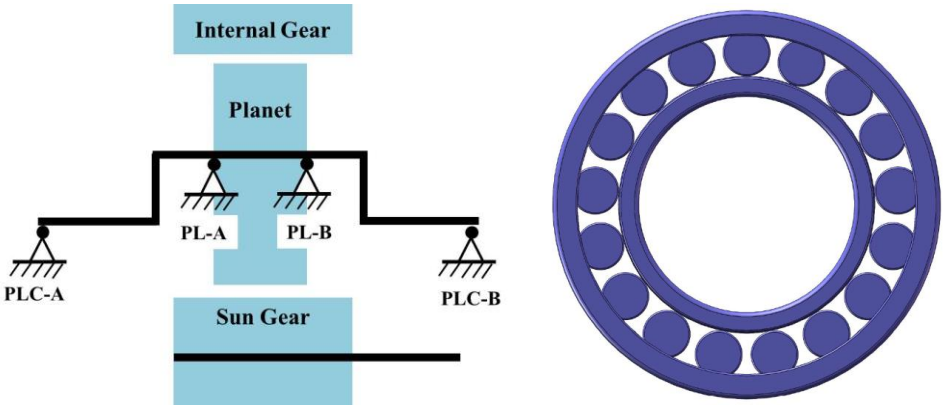

Figure 3.12 Planetary gear bearing arrangement and roller bearing example (Sheng et al., 2011)

3.3 FEA torsional stiffness results

Transmission error is the difference between the position that the output shaft of a drive would occupy if the drive were perfect and the actual position of the output shaft. Transmission error exists in three forms: 1) Manufacturing transmission error, 2) Static transmission error and 3) Dynamic transmission error. Manufacturing T.E. (M.T.E.) is measured at low speeds and in the unloaded state. Normally, it includes profile inaccuracies, spacing errors and gear tooth run out. Static T.E. (S.T.E.) is also measured under low speed conditions, but in a loaded state. S.T.E. includes the effect of elastic deflection of the gears. Dynamic T.E. includes the effects of inertia on top of all the effects of the errors considered in M.T.E. and in S.T.E.. The transmission error mentioned in this research is the S.T.E..

Torsional stiffness can be defined as the ratio between the torque acting on the input pinion and the resulting relative elastic angular rotation between the input pinion and the output gear hubs (Wang, 2003),

$$K = \frac{T}{\Delta\theta}, \tag{3.22}$$

where T is the input torque load and, $\Delta\theta$ is the relative elastic angular rotation between the two gears. At each particular meshing position, the angular rotation of the loaded drive gear is calculated in the gear reference frame by restraining the output gear from rotating. In relation to the input gear reference frame, it is restrained from further rotating, while the torque input load and the resulting angular rotation of the gear is computed. The angular rotation is the static transmission error of gears under load at low speed as mentioned above.

It includes the elastic deformation of the local tooth contact, tooth bending, shearing and the deflection of the gear body (Wang, 2003). To find the value of $\Delta\theta$, Jiande used a specified cylindrical coordinate system and then all the nodal coordinate system around the input gear hub was rotated into the specified coordinate. All the nodes also coupled with a master node (also on the input gear hub), which would give the same value on UY (linear tangential arc length). If r is the radius of the input gear hub, the value of $\Delta\theta$ is,

$$\Delta\theta = \frac{UY}{r}. \tag{3.23}$$

The input torque was also be expressed as the sum of the applied nodal forces at radius r,

$$T = \sum_{i=1}^{n} f_i \cdot r, \tag{3.24}$$

where n is the total number of nodes around the input gear hub and f_i are the corresponding tangential nodal forces. This strategy will create a rigid area around the input gear hub and the elastic deformation effect from the shaft will be excluded. Alternatively, instead of rotating all the nodal coordinates, a pilot node can be created in the centre of the hub and all the DOF (degrees of freedom) of the nodes on the edge of the hub can be coupled with the pilot node. Contact methods can be used to generate a similar rigid area in the hub area. After applying the input torque to the pilot node in the *Mz* direction, the value of *ROTZ* in the FEA model will be the value of $\Delta\theta$. Both methods can be used and experience has shown there to be hardly any difference between them.

However, when the stiffness was represented along the line of action, another term will also be mentioned in some publications (Howard et al., 2001), which is the linear mesh stiffness. A simple relationship between linear and torsional mesh stiffness can be derived as follows (Howard et al., 2001),

$$K_{mb} = \frac{K_m}{r_b^2}, \tag{3.25}$$

where r_b is the base radius of the gear, K_{mb} is the linear mesh stiffness and K_m is the torsional mesh stiffness.

The load sharing ratio between different teeth can also be calculated from the FEA model. Consider one pair of spur gears in mesh, as shown in Fig. 3.13, where two gears are in mesh at the start of the double tooth pair contact zone. For involute gears, the line of action is in the common tangent line to the base circles, where the total contact force acts along. F_p^A is the total contact force of the 1st pinion tooth at position A and F_p^D is the total contact force of the 2nd pinion tooth at position D. F_g^A is the total contact force of the 1st pinion tooth at position A and F_g^D is the total contact force of the 2nd pinion tooth at position D. There is no contact force between the 3rd tooth pair, however, as the gear rotates, the point of contact will move along the line of action and the gear pair will experience both single contact zones and double contact zones. In the single contact zone, the load sharing will always be 1 while in the double contact zone, the load sharing can be calculated as follows.

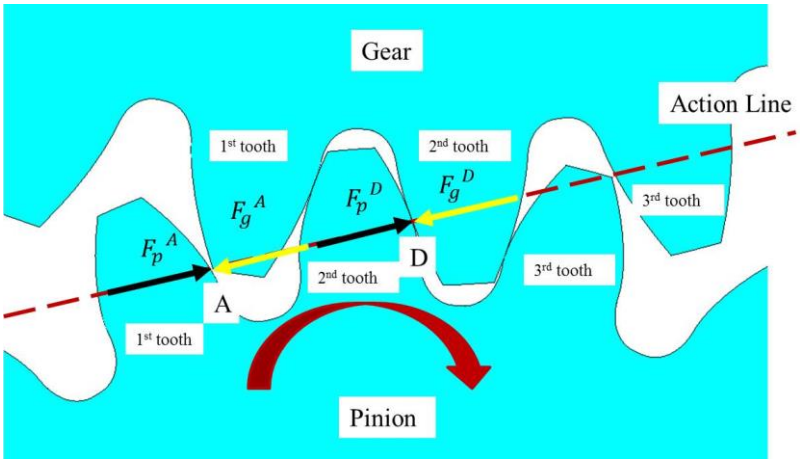

Figure 3.13 Gear meshing force diagram

For the pinion,

$$F_{total,p}^{A,D} = F_p^A + F_p^D,$$

for the gear,

$$F_{total,g}^{A,D} = F_g^A + F_g^D,$$

the resultant load sharing ratio for the gear pair at A and pair D is then given by,

$$L_p^A = \frac{F_p^A}{F_{total,p}^{A,D}}, \quad L_p^D = \frac{F_p^D}{F_{total,p}^{A,D}},$$

and,

$$L_{np}^{A} + L_{np}^{D} = \frac{F_{np}^{A}}{F_{total,np}^{A,D}} + \frac{F_{np}^{D}}{F_{total,np}^{A,D}} = 1. \quad (3.26)$$

The major assumptions in this research are the following:

(1) Plane stress assumptions were used in the 2–D FEA planetary gear model;

(2) Quasi-static conditions exist and no inertia effects influence the mesh stiffness curve;

(3) The manufacturing and assembly errors are not included and the transmission error is only due to the elastic deformation;

(4) The stiffness of the bearings is not included;

(5) The sun gear can move only in the torsional direction.

3.3.1 Isolated sun-planet subsystem torsional stiffness

The tooth mesh stiffness variation of a sun-planet gear pair was modelled from the isolated sun-planet FE model, shown in Fig. 3.14. The sun gear hub was constrained to be fixed in the radial direction while the planet hub was fully constrained in both tangential and radial directions. However, with the sun gear rotation, the planet gear will still move around the sun gear, acting as though there were a rigid carrier arm carrying the planet gear. This will give the same movement of the planet in the overall planetary gear model. However, when the planet moves to each simulated position, its inner hub was again constrained not to rotate and the torque T_{sp1} was applied to the sun gear. If $\Delta\theta_{sp1}$ denotes the elastic angular rotation of the sun gear hub, the torsional stiffness K_{sp1} can be obtained using equation (3.22). The starting mesh point was calculated at the mesh position of the sun-planet gear pitch point (defined as 0º) and then the sun gear was rotated clockwise with an angular increment for the next solution. In this research with the fixed ring gear, one tooth mesh cycle covers the carrier arm rotation angle of $360º/Z_r=3.64º$ and calculations were carried out covering two mesh periods. An APDL program has been developed to control the gears to be rotated to the corresponding positions before the model was solved.

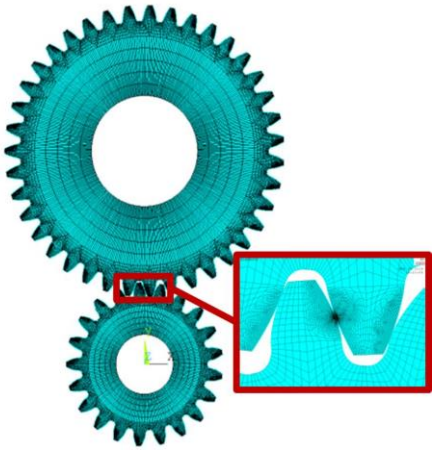

Figure 3.14 Isolated sun-planet external pair

Initially, no tip-relief was used in this research, apart from a round-off with a 0.1 mm radius at the tooth tip, to keep the original form of the involute curve. The tooth tip round off was used to assist the FE solution convergence where corner contact occurred. Different torque magnitudes can be applied to the sun gear hub and the corresponding static transmission error ($\Delta\theta_{sp1}$), gear tooth mesh stiffness variation and the gear tooth load sharing ratio are shown in Fig. 3.15, Fig. 3.16 and Fig. 3.17 separately.

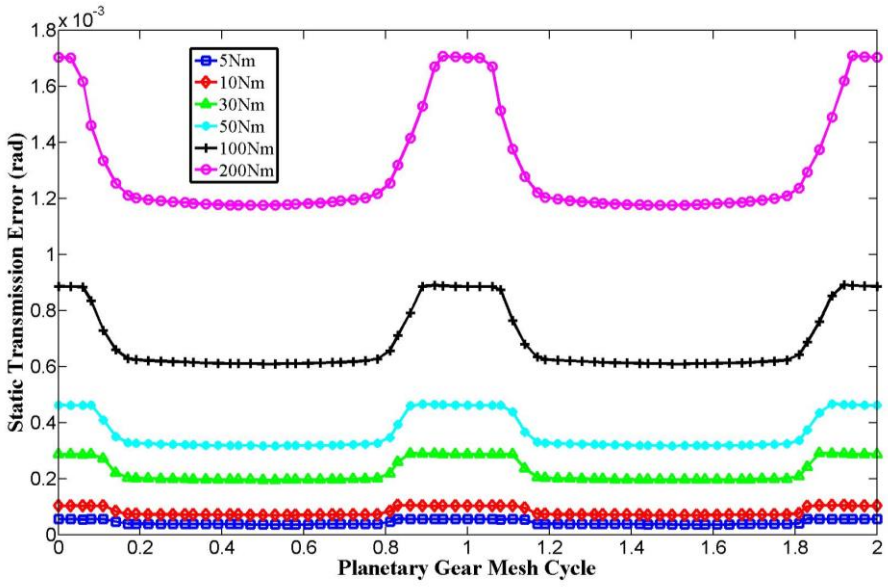

Figure 3.15 Sun-planet transmission error under different torque levels

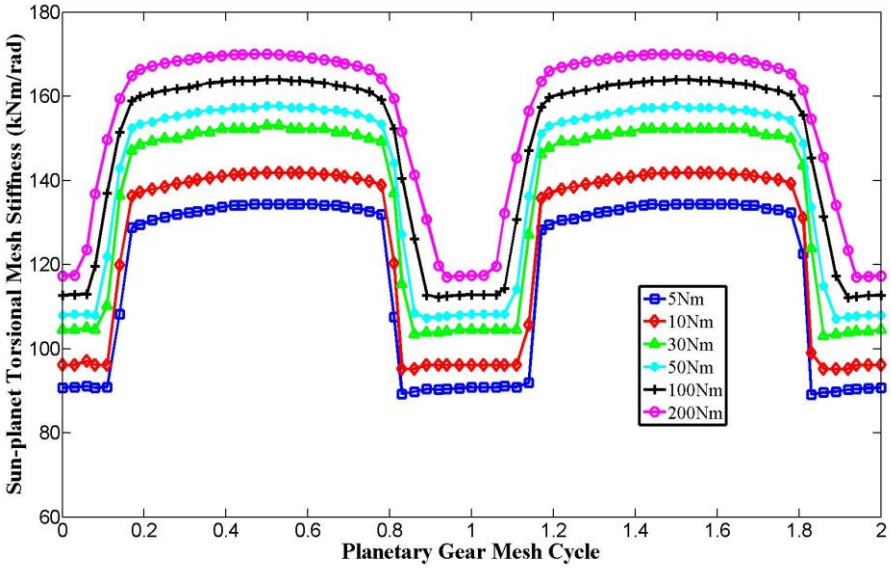

Figure 3.16 Sun-planet torsional mesh stiffness under different torque levels

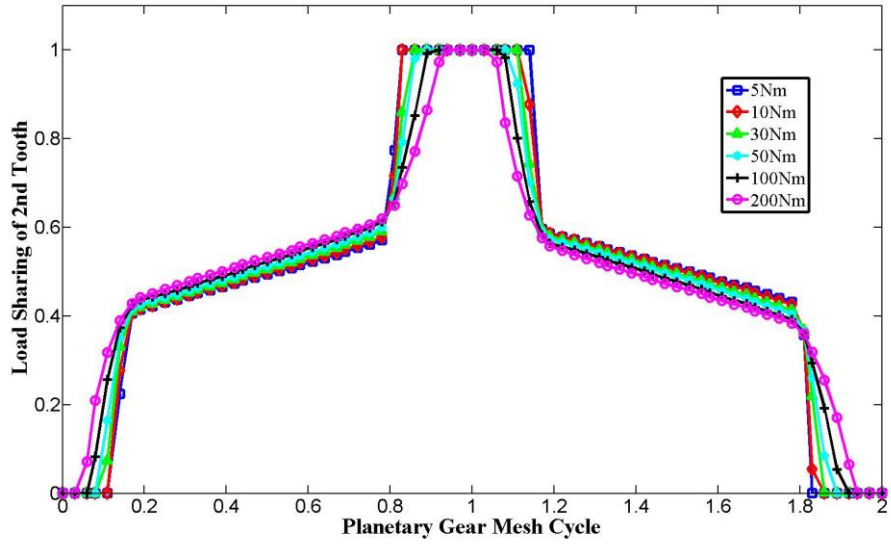

Figure 3.17 2nd tooth in sun-planet mesh load sharing ratio under different torque levels

The major components of the sun-planet mesh stiffness are: (i) the gear body stiffness, (ii) the teeth bending stiffness and (iii) the nonlinear Hertzian contact stiffness. From the results, it was found that as the input loads increased, the sun-planet mesh stiffness varied slightly, which was mostly due to the Hertzian contact stiffness. The relative different between the torsional mesh stiffness under 5Nm and the torsional mesh stiffness under 200Nm is around 23.5%. Based on the FEA models, a common formula was developed for calculation of the

combined torsional mesh stiffness (Kiekbusch et al., 2011). In the formula, the stiffness of body, teeth and contact zone can be considered to act like three springs in a row. The stiffness of the gear body is assumed to only depend on the following parameters: shaft radius r_s, dedendum radius r_d, face width w and Young's modulus E. The following equation was used to combine all the parameters together,

$$K_B = c_B \cdot E \cdot w \cdot \ln(r_d - r_s)^{1.6} \cdot r_s^{1.6}, \tag{3.27}$$

where c_B is the coefficient and is equal to 9.555e^{-4}. The bending stiffness of the teeth is assumed to depend on the height and width w of the teeth and Young's modulus E. The following equation was used to combine all the parameters together,

$$K_T = c_T \cdot E \cdot w \cdot m^2 \cdot z^{2.2}, \tag{3.28}$$

where c_T is the coefficient and is equal to 3.2e^{-5}. m is the gear modulus and z is the number of teeth. The stiffness of the contact is assumed to depend on the load torque T, gear modulus, number of teeth, Young's modulus and face width. The following equation was used to combine all the parameters together,

$$K_C = c_C \cdot E \cdot w \cdot m^{1.85} \cdot z^2 \cdot T^{0.105}, \tag{3.29}$$

where c_C is the coefficient and is equal to 7.937e^{-5}. Also, the angle of the handover region from two teeth in mesh to a single tooth in mesh varied with the increased load, which is very similar to previously published stiffness curves of a fixed axis gear pair (Wang & Howard, 2004).

In the sun-planet subsystem model, the planet gear can rotate not only around the co-axis but also around its own axis, just like a carrier arm carries it. However, if the carrier is fixed, the planet gear will only rotate around its own axis, which will result in the planetary gear system equivalent to a pair of fixed shaft external-external gear mesh and a pair of fixed shaft external-internal gear mesh. The torsional mesh stiffness will be the same shape and the major components will still include gear body, teeth bending and Hertzian contact. The only difference between the case of fixed carrier and the case of rotating carrier is the mesh period, as shown in Fig. 3.18 and it can be expressed as follows (Liang et al., 2013),

$$K_{sp1rotating} = K_{sp1fixed}(\lambda\theta_c), \tag{3.30}$$

where θ_c is the carrier arm rotation angle and λ is the mesh frequency ratio and in the case of fixed ring gear,

$$\lambda = \frac{Z_r}{Z_s + Z_r}, \tag{3.31}$$

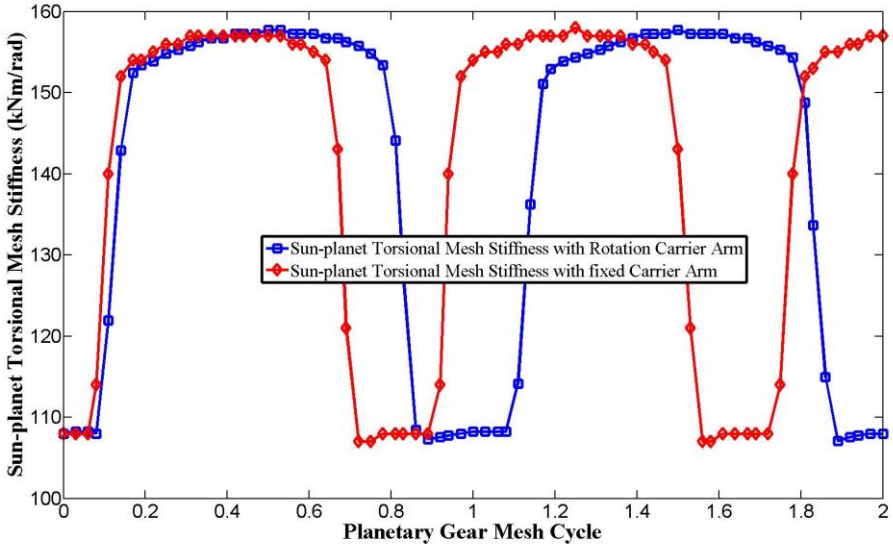

Figure 3.18 Comparison between sun-planet stiffness with rotation carrier arm and sun-planet stiffness with fixed carrier arm

3.3.2 Isolated ring-planet subsystem torsional stiffness

The mesh stiffness variation of the ring-planet mesh was obtained from the isolated ring–planet pair model, as shown in Fig. 3.19. The ring-planet pair shared the same planet gear with the sun-planet mesh, but with different meshing faces. The outer rim of the ring gear was fully constrained, with no rotation and the planet was allowed the same movement as in the overall model, with the rigid carrier arm constraining the planet movement inside the ring gear. However, when the planet moves to each simulated position, its inner hub was again constrained not to move in the radial direction and the torque $T_{rp1}= (Z_p/Z_s)\times T_{sp1}$ was applied to the planet gear hub and $\Delta\theta_{rp1}$ denotes the resulting elastic angular rotation of the planet gear hub. The torsional stiffness K_{rp1} was also obtained using equation (3.22). The starting mesh point was selected according to the sun-planet pitch point (starting point for

sun-planet mesh) and it can be decided by the relative phase between the sun-planet mesh and ring-planet mesh. Detailed calculation can be found in equation (3.15). Similarly, two meshing cycles were covered, which will give the carrier rotation angle of $360^o/Z_r=3.64^o$. An APDL program has been developed to control the gears to be rotated to the corresponding positions before the model was solved. Initially, there was no tip-relief applied to both planet gear and ring gear to keep the original form of the involute curve. The input torque T_{sp1} from the sun gear will result an input torque of $T_{rp1}= (Z_p/Z_s)\times T_{sp1}$. Corresponding to the sun-planet mesh torque levels, the same torque levels were applied to the planet gear hub. The resulting ring-planet mesh static transmission error ($\Delta\theta_{rp1}$), gear mesh stiffness variation and gear tooth load sharing ratio are shown in Fig. 3.20, Fig. 3.21 and Fig. 3.22 separately.

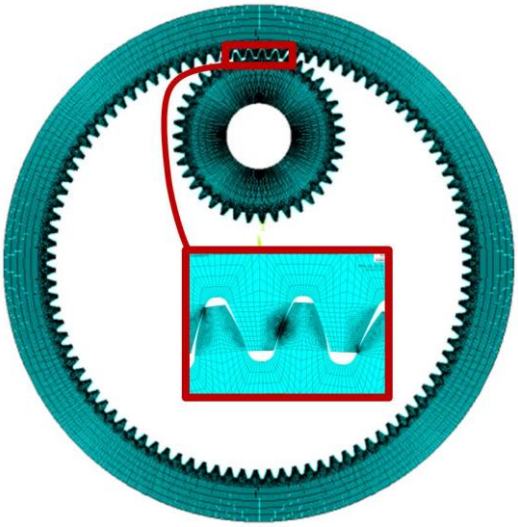

Figure 3.19 Isolated ring-planet internal pair

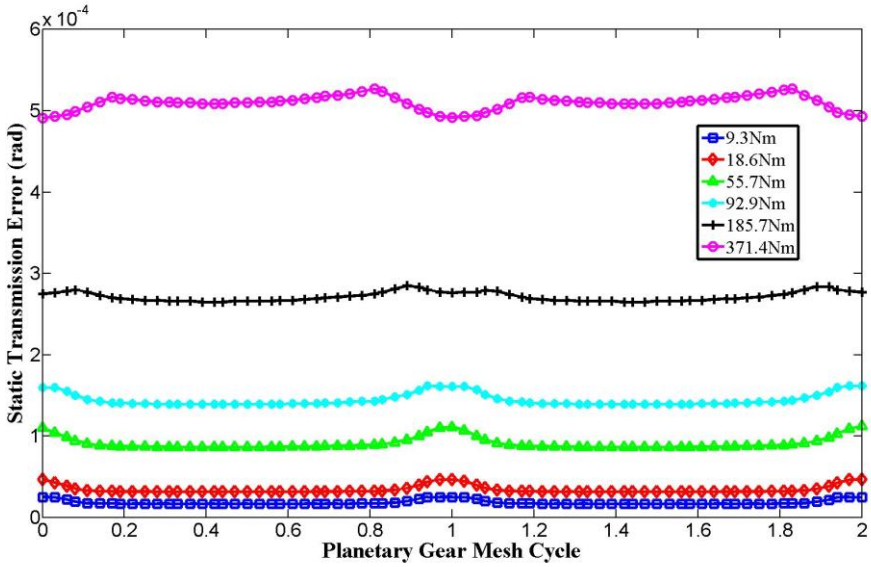

Figure 3.20 Ring-planet transmission error under different torque levels

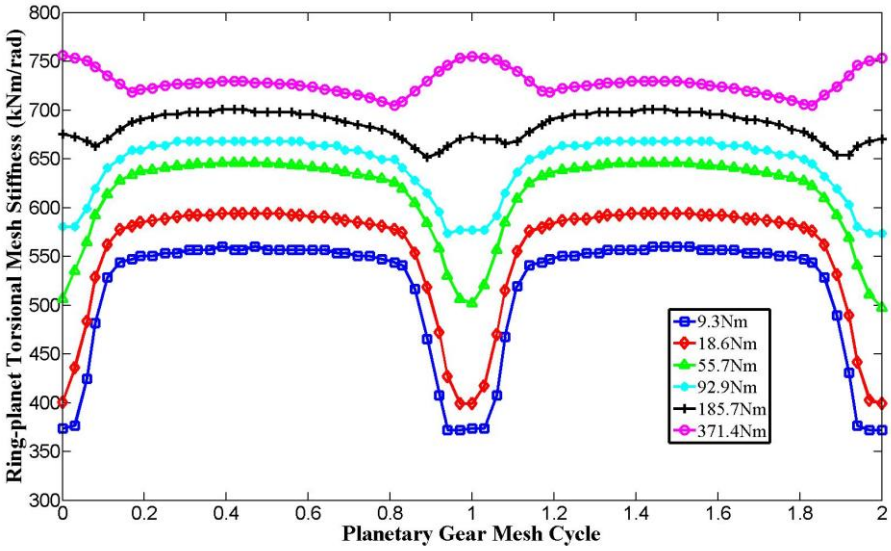

Figure 3.21 Ring-planet torsional mesh stiffness under different torque levels

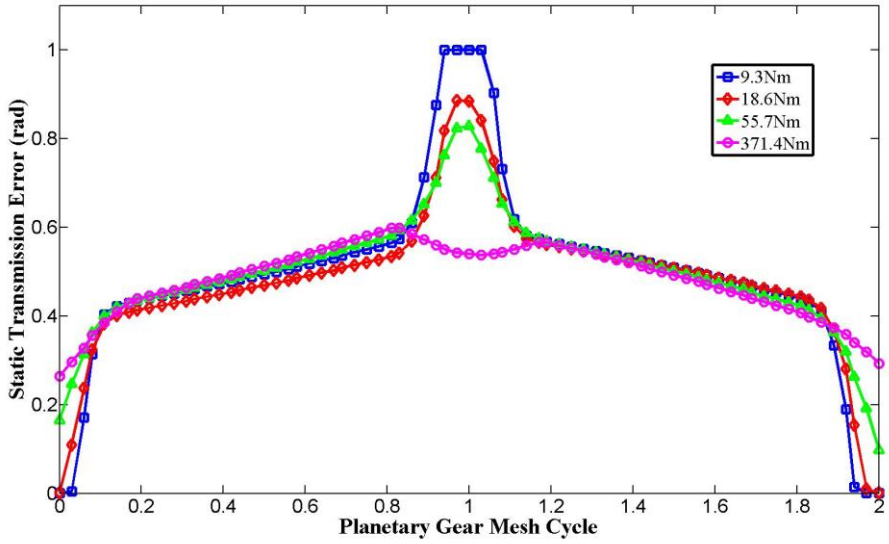

Figure 3.22 2nd tooth in sun-planet mesh load sharing ratio under different torque levels

Similar to the sun-planet mesh, the major components of the ring-planet mesh stiffness are: (i) the gear body stiffness, (ii) the teeth bending stiffness and (iii) the Hertzian contact stiffness. The ring-planet subsystem includes one external gear and one internal gear. The stiffness of the external gear can still be estimated using equations (3.27) − (3.29). The stiffness of the internal gear also includes body stiffness, teeth bending stiffness and Hertzian contact stiffness. However, the stiffness of the internal gear can be influenced by the boundary conditions, which will be discussed in detail in chapter 5. In this chapter, only one ring gear boundary condition was used, that is the outer rim was fully fixed and the rim thickness was 99 mm. With the increase of the load, it is interesting to note there is large variation in the single tooth zone mesh stiffness where this single tooth contact becomes triple teeth contact as the higher mesh forces are applied, as shown in Fig. 3.23.

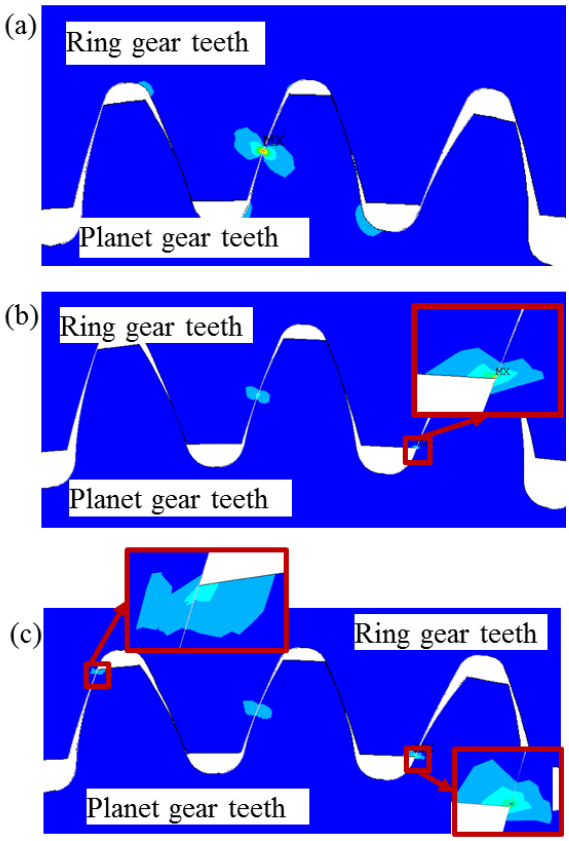

Figure 3.23 Ring-planet Von Misses stress distribution under different loads, (a) 9.3Nm with single tooth contact, (b) 55.7Nm with double tooth contact, (c) 371.4Nm with triple tooth contact

In the ring-planet subsystem model, similar to the sun-planet subsystem, the planet gears have both the movement of self-rotation and the movement of rotation about the co-aixs. If $K_{rp1fixed}$ is the ring-planet mesh stiffness when the carrier is fixed and $K_{rp1rotating}$ is the ring-planet mesh stiffness when the carrier is rotating, a relationship between the two can be expressed and compared as shown in Fig. 3.24 (Liang et al., 2014),

$$K_{rp1rotating} = K_{rp1fixed}(\lambda\theta_p), \tag{3.32}$$

where θ_P is the planet gear rotation angle and λ is the mesh frequency ratio which in the case of the fixed ring gear becomes,

$$\lambda = \frac{Z_r}{Z_s+Z_r}. \tag{3.33}$$

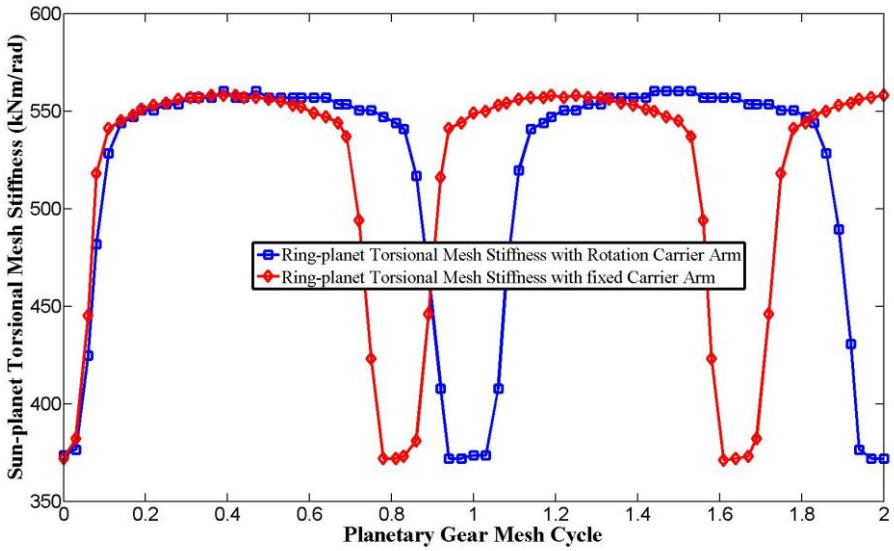

Figure 3.24 Comparison between ring-planet stiffness with rotating carrier arm and ring-planet stiffness with fixed carrier arm

3.3.3 Influence of carrier arm stiffness and bearing stiffness

One branch of the planetary gear set with the sun-planet-ring-carrier was chosen to study the influence of carrier arm stiffness, as shown in Fig. 3.25. Instead of detailed 3D carrier arm and bearing stiffness, a simplified carrier arm and rigid bearing was modelled using a beam element and the MPC 184 revolute element. The combined sun-planet-ring mesh can be modelled either with a flexible carrier arm or with a rigid carrier arm. The outer rim of the ring gear was fully fixed and the planet gear was connected with the carrier arm with rigid bearing (MPC 184 revolute). The sun gear hub and the carrier arm end were constrained to be fixed in the radial direction. An APDL program was written to control the gear movements, to give all gears the same movement in a complete planetary gear system but in a quasi-static condition. The input torque load T_{spr1} was applied to the sun gear hub. If $\Delta\theta_{spr1}$ denotes the elastic angular rotation of the sun gear hub, the torsional stiffness K_{spr1} can be obtained using equation (3.22). The corresponding mesh stiffness curves under different loads are shown in Fig. 3.41.

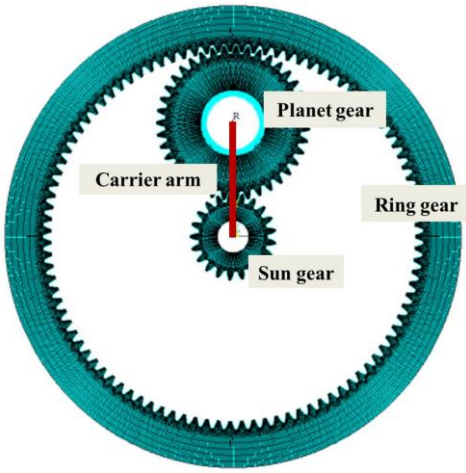

Figure 3.25 Isolated sun-planet-ring pair with carrier arm

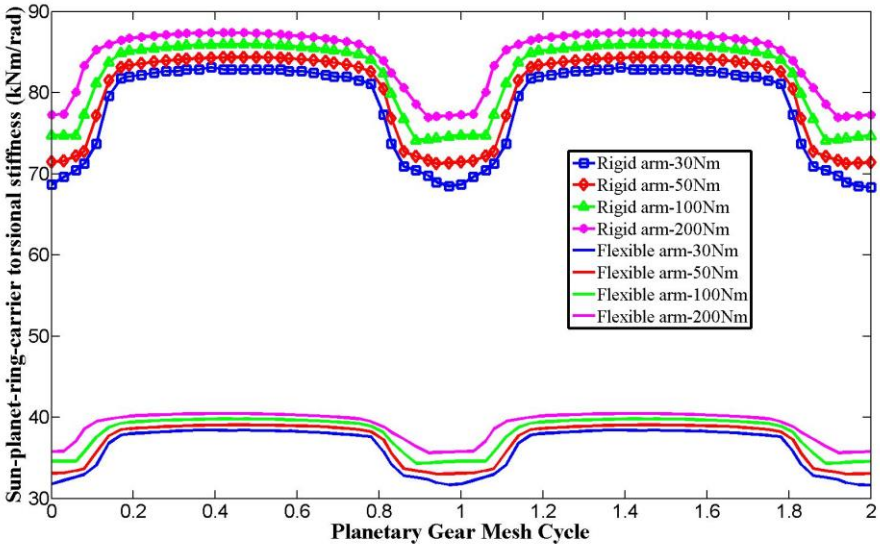

Figure 3.26 Comparison of sun-planet-ring mesh stiffness
with flexible carrier arm and with rigid carrier arm

The sun-planet-ring torsional mesh stiffness with the flexible arm includes the sun-planet mesh stiffness, ring-planet mesh stiffness and the carrier arm stiffness while the sun-planet-ring mesh with rigid arm only includes the sun-planet mesh stiffness and the ring-planet mesh stiffness. As shown in Fig. 3.26, the torsional stiffness of the flexible arm can also be determined from beam bending theory,

$$K_{carrier} = T_c/\theta_B = 3EI/l, \tag{3.34}$$

where E is the Elastic modulus which is 210 kN/mm^2 for steel, I is the second moment of area and l is the length of the carrier arm, chosen to be 300 mm in this research. From equation (3.34), the carrier arm stiffness is a function of the square cross section dimension, chosen to be 60mm, in this analysis, which results in a carrier arm torsional stiffness of 2.16×10^3 kNm/rad.

3.3.4 Overall planetary gear torsional stiffness

The overall planetary gear mesh stiffness variation can also be obtained from the planetary gear sets with the three planet model, as shown in Fig. 3.27. The outer rim of the ring gear was again constrained not to rotate and the torque T_s=3T_{sp1} was applied on the sun gear hub. If $\Delta\theta_s$ denotes the resulting elastic angular rotation of the sun gear hub, the overall torsional stiffness K_s can be obtained using equation (3.22), as shown in Fig. 3.28. The overall planetary gear mesh stiffness includes the sun-planet-ring mesh stiffness from the 3 planet branches and also the carrier arm stiffness. An APDL program in *appendix B* has been developed to control all the gears to be rotated to the corresponding positions and then the overall planetary gear mesh stiffness can be calculated accordingly.

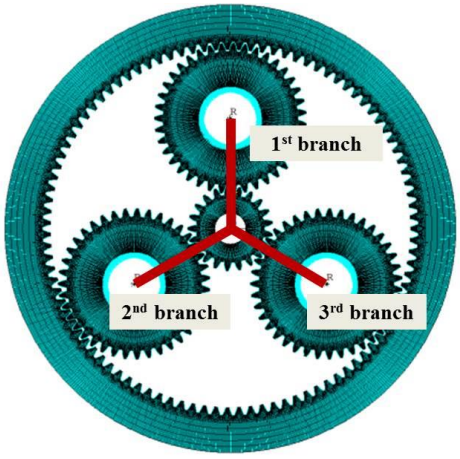

Figure 3.27 Planetary gear model with 3 planets and a flexible carrier arm

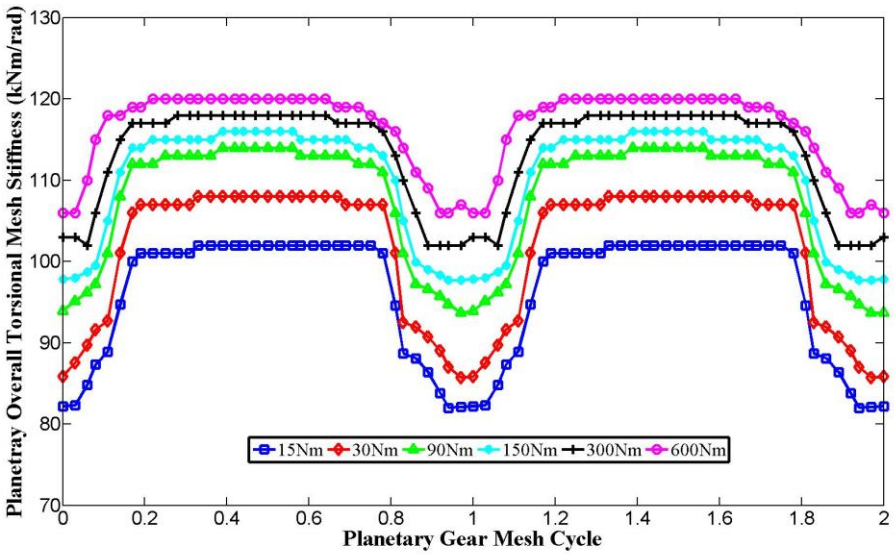

Figure 3.28 Overall planetary gear torsional stiffness with 3 planets and flexible carrier arm

3.4 Predictive model for planetary gear torsional stiffness

3.4.1 Relationships of 1st and *n*th sun-planet and ring-planet pair in planetary gear systems

In a planetary gear set, there are several pairs of sun-planet gear pairs and several ring-planet gear pairs meshing simultaneously. While each of the sun-planet meshes has the same shape of mesh stiffness variation, they are not necessarily in phase with each other. Similar situation exists in the ring-planet meshes. The stiffness of the *n*th sun-planet pair (K_{spn}) with respect to the 1st sun-planet pair (K_{sp1}) and the stiffness of the nth ring-planet pair (K_{rpn}) with respect to the 1st ring-planet pair (K_{rp1}) are given as (Parker & Lin, 2004),

$$K_{spn} = K_{sp1}(t - \gamma_{sn}T_m),$$
$$K_{rpn} = K_{rp1}(t - \gamma_{rn}T_m - \gamma_{rs}T_m). \quad (3.35)$$

where γ_{sn} is the relative phase between the *n*th sun-planet pair with respect to the 1st sun-planet pair, γ_{rn} is the relative phase between the *n*th ring-planet pair with respect to the 1st ring-planet pair and γ_{rs} is the relative phase between the *n*th sun-planet and ring-planet. K_{sp1} is the mesh stiffness of the 1st sun-planet pair with t=0 meshing at the pitch point and T_m is the mesh period which is the same for both the sun-planet meshing and the ring-planet meshing.

The mesh stiffness can also be expressed as a function of rolling angle. If the phase difference of the sun-planet gear pairs is $\gamma_{sn}T_m$ in time, the corresponding phase difference in terms of the carrier arm rotation angle is $\theta_{sn}= \gamma_{sn}T_m\omega_c=\gamma_{sn}\theta_m$. The symbol ω_c represents the angular velocity of the carrier arm and the symbol θ_m is the rotation angle of the carrier in one mesh period, $\theta_m=2\pi/Z_r$. Similarly, the phase difference of the ring-planet gear pair in terms of the carrier arm rotation angle is $\theta_{rn}= \gamma_{rn}T_m\omega_c=\gamma_{rn}\theta_m$. The relative phase of the nth sun-planet and ring-planet in terms of the carrier arm rotation angle is $\theta_{rs}= \gamma_{rs}T_m\omega_c=\gamma_{rs}\theta_m$. By this way, K_{spn} and K_{rpn} can be expressed as,

$$K_{spn} = K_{sp1}(\theta - \gamma_{sn}\theta_m),$$
$$K_{rpn} = K_{rp1}(\theta - \gamma_{rn}\theta_m - \gamma_{rs}\theta_m), \quad (3.36)$$

K_{sp1} is the mesh stiffness of the 1st sun-planet pair with θ=0 meshing at the pitch point.

3.4.2 Gear mesh stiffness determined from a pinion hub and a gear hub perspective

The combined torsional mesh stiffness measured from a gear hub will be different from that measured from the pinion hub, as shown in Fig. 3.29.

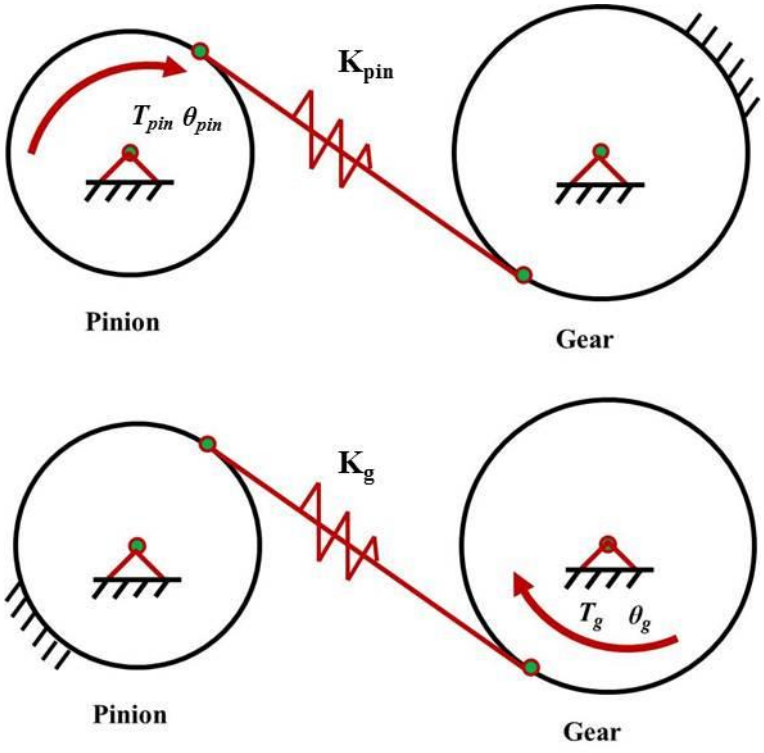

Figure 3.29 Example of a gear pair

As shown in the figure, when there is torque T_{pin} applied on the pinion hub, the gear was constrained not to rotate. θ_{Pin} is the total rotation angle measured from the pinion hub at this condition. As a result, $K_{pin}=T_{pin}/\theta_{pin}$ is the combined torsional mesh stiffness calculated from the pinion hub. When there is torque T_g applied on the gear hub, the pinion was constrained not to rotate. θ_g is the total rotation angle measured from the pinion hub at this condition. As a result, $K_g=T_g/\theta_g$ is the combined torsional mesh stiffness calculated from the gear hub. From the gear characteristics, there are relationships, which are $T_{pin}=u\cdot T_g$ and $\theta_{pin}=\theta_g/u$. Finally, the relationship between the two stiffnesses is,

$$K_{pin} = T_{pin}/\theta_{pin} = (u \cdot T_g)/(\theta_g/u) = u^2 \cdot T_g/\theta_g = u^2 \cdot K_g, \tag{3.37}$$

where u is the gear speed ratio. From the theoretical analysis, it was found that when the gear mesh stiffness value is calculated from the pinion hub, it has to be scaled with the gear speed ratio squared. This indicates that the gear stiffness calculated from the sun gear hub also has to be scaled with the speed ratio squared for comparison with the gear stiffness calculated from the carrier arm hub.

3.4.3 Planetary gear torsional stiffness when acting as a speed reducer and as a speed multiplier

When the ring gear is held fixed and the driving component is the sun gear, the planetary gear train operates as a speed reducer. When the driving component is the carrier arm, the planetary gear train operates as a speed multiplier. The torsional stiffness calculated from the sun and the carrier arm perspective will be different for both cases in both magnitude and phase. The magnitude stiffness relationship can be written from equation (3.37),

$$K_c = u_{sc}^2 K_s\,,$$

$$K_s = u_{cs}^2 K_c, \tag{3.38-1}$$

where K_s represents the torsional stiffness measured from the sun gear hub and K_c denotes the torsional stiffness measured from the carrier arm hub. For example, K_s is the 1st sun-planet mesh stiffness measured from sun gear hub, which is equal to K_{sp1}. When K_{sp1} is measured from carrier hub, the stiffness value will become $u_{sc}^2 K_{sp1}$. $u_{sc}=1+Z_r/Z_s$ represents

the multiplier speed ratio for the planetary gear system with the fixed ring gear and $u_{cs}=1/u_{sc}$ represents the corresponding reducer speed ratio.

The phase difference exists because there will be different tooth face in mesh when planetary gear operates as a speed reducer and as a speed multiplier. When the planetary gear operates as a speed reducer, the driving component is the sun gear and the driven component is the carrier arm. If the sun gear rotates clockwise, the carrier arm should also rotate clockwise according to the planetary characteristics. When the planetary gear operates as a speed multiplier, the driving component is the carrier arm and the driven component is the sun gear. If the sun gear is still kept rotating clockwise, the carrier arm needs to rotate clockwise. This situation is shown in Fig. 3.30.

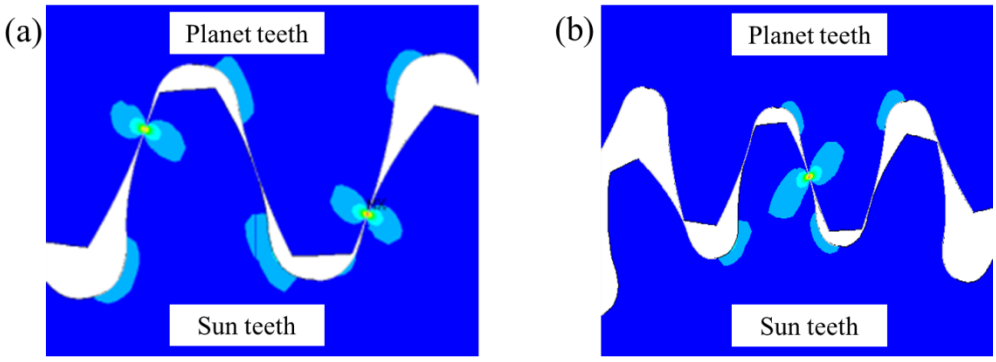

Figure 3.30 First sun-planet mesh von Mises stress distribution with different driving components; a. carrier arm as the driving component rotating clockwise, b. sun gear as the driving component rotating clockwise

To account this effect, a parameter δ=1/2 can be assigned to equation (3.38−1), which will become,

$$K_c = u_{sc}^2 K_s\,(\theta - \delta\theta_m),$$

$$K_s = u_{cs}^2 K_c(\theta - \delta\theta_m)\,, \qquad (3.38-2)$$

θ_m is the rotation angle of the carrier arm in one mesh cycle and it is equal to $\theta_m=2\pi/Z_r=3.64^o$. δ=1/2 stands for the two mesh stiffness will always have 1/2 cycle difference. An example is shown in Fig. 3.31.

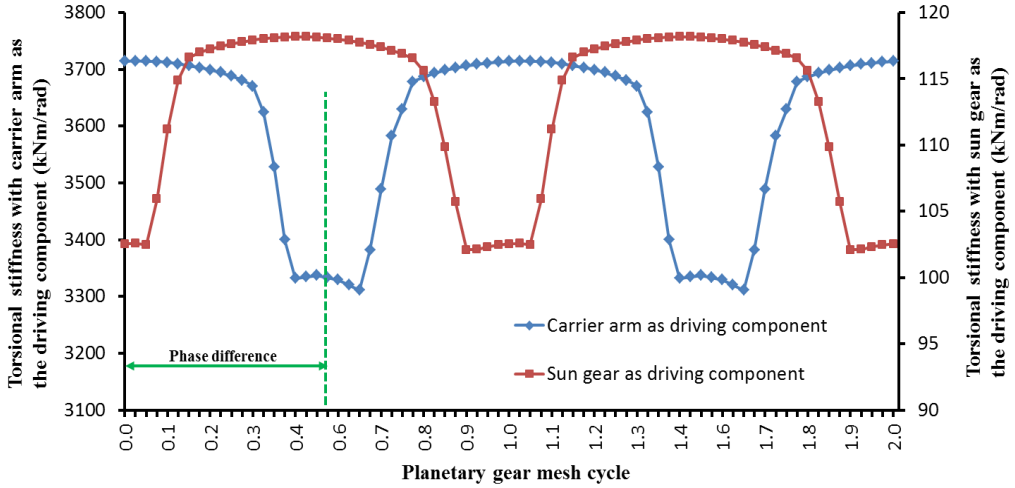

Figure 3.31 Example of FEA torsional stiffness of different driving components

3.4.4 Predictive model for planetary gear torsional stiffness

In the previous analysis, the sun-planet mesh stiffness, ring-planet mesh stiffness and the carrier arm stiffnesses were found to be the fundamental components of the overall planetary gear torsional mesh stiffness. There are two situations that have been considered, which are planetary gear speed reducer and planetary gear speed multiplier.

3.4.4.1 Predictive model for planetary gear reducer

First of all, only the 1st sun-planet-ring branch has been considered and the other branches have a phase relationship with the 1st branch as shown in section 3.1. A model having torsional springs connected in series can be used, as shown in Fig. 3.32.

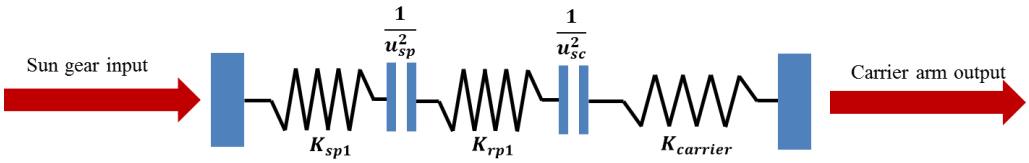

Figure 3.32 Predictive model for a single branch of the sun-planet-ring mesh stiffness

As all the stiffness values are measured from the sun gear hub, the values of the planet-ring mesh and the arm stiffnesses have to be scaled with the corresponding gear ratios. The single branch sun-planet-ring torsional stiffness can then be calculated as,

$$\frac{1}{K'_{spr1}} = \frac{1}{K_{sp1}(\theta)} + \frac{u_{sp}^2}{K_{rp1}(\theta - \gamma_{rs}\theta_m)} + \frac{u_{sc}^2}{K_{carrier}}, \tag{3.39–1}$$

where K'_{spr1} is the 1st sun-planet-ring torsional mesh stiffness calculated using the prediction model and $u_{sp}=Z_p/Z_s$ is the sun-planet gear ratio. The stiffness of the nth sun-planet-ring mesh stiffness can be calculated as,

$$\frac{1}{K'_{sprn}} = \frac{1}{K_{spn}} + \frac{u_{sp}^2}{K_{rpn}} + \frac{u_{sc}^2}{K_{carrier}} = \frac{1}{K_{sp1}(\theta - \gamma_{sn}\theta_m)} + \frac{u_{sp}^2}{K_{rp1}(\theta - \gamma_{rs}\theta_m - \gamma_{sn}\theta_m)} + \frac{u_{sc}^2}{K_{carrier}}, \tag{3.39–2}$$

For the example in table 3.1, the analytical results from equation (3.39-1) for input loads of 50Nm and 100Nm for the 1st sun-planet-ring branch case are shown in Fig. 3.33, along with the comparison of the FEA results modelled with the flexible carrier, originally shown in Fig. 3.26.

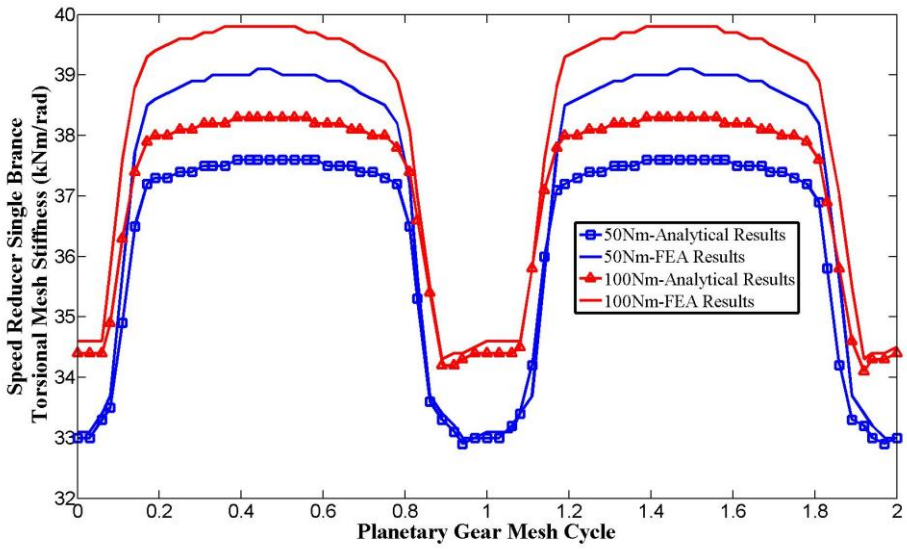

Figure 3.33 Comparison between the single branch analytical and FEA torsional stiffness

The overall predictive model of torsional stiffness for the n branches of the sun-planet-ring mesh and the carrier arm stiffnesses can also be established. In the predictive model, the torsional stiffness of every sun-planet-ring branch can be treated as torsional springs connected in series as shown in Fig. 3.32 and equation (3.39). All the branches can then be connected in parallel, as shown in Fig. 3.34.

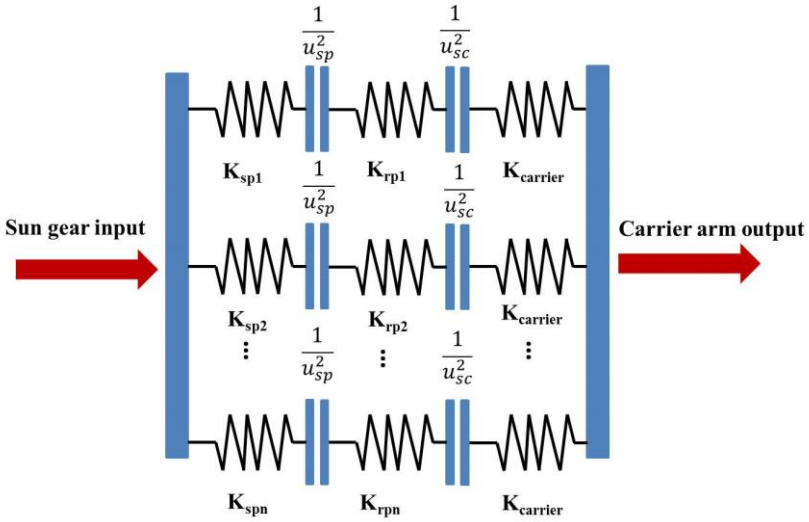

Figure 3.34 Prediction model for the overall planetary gear

The overall planetary gear torsional stiffness can be calculated as,

$$
\begin{aligned}
K_{so}^{'} &= K_{spr1}^{'} + K_{spr2}^{'} + \ldots + K_{sprn}^{'} \\
&= \frac{1}{\frac{1}{K_{sp1}(\theta)} + \frac{u_{sp}^2}{K_{rp1}(\theta - \gamma_{rs}\theta_m)} + \frac{u_{sc}^2}{K_{carrier}}} \\
&+ \frac{1}{\frac{1}{K_{sp1}(\theta - \gamma_{s2}\theta_m)} + \frac{u_{sp}^2}{K_{rp1}(\theta - \gamma_{rs}\theta_m - \gamma_{r2}\theta_m)} + \frac{u_{sc}^2}{K_{carrier}}} \\
&+ \ldots + \frac{1}{\frac{1}{K_{sp1}(\theta - \gamma_{sn}\theta_m)} + \frac{u_{sp}^2}{K_{rp1}(\theta - \gamma_{rs}\theta_m - \gamma_{rn}\theta_m)} + \frac{u_{sc}^2}{K_{carrier}}}
\end{aligned}
\quad , \qquad (3.40)
$$

where K'_{so} is the overall planetary gear torsional stiffness calculated from sun gear hub; K'_{spr1} can be calculated using equation (3.39) and the other stiffness can be calculated similarly. For the example shown in table 3.1, there are three sun-planet-ring branches and the analytical results for the overall planetary gear torsional stiffness are shown in Fig. 3.35, along with the FEA comparison.

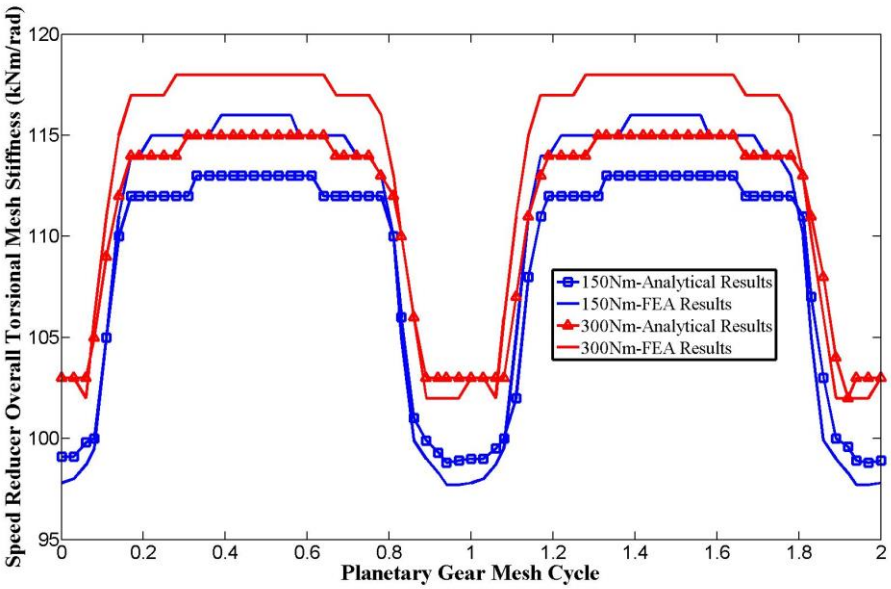

Figure 3.35 Comparison between the overall planetary analytical and FEA torsional stiffness

3.4.4.2 Predictive model for planetary gear multiplier

Similarly, a model having torsional springs connected in series can be used as a predictive model for the case of a single sun-planet-ring operating as a multiplier, as shown in Fig. 3.36.

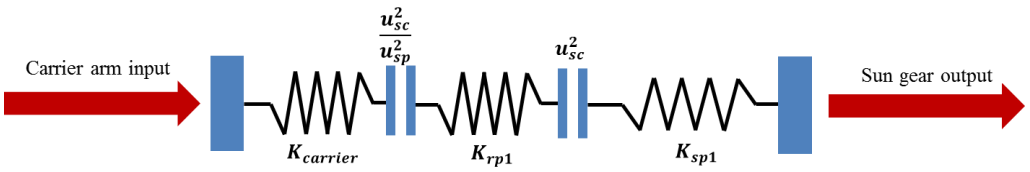

Figure 3.36 Prediction model for single branch of the sun-planet-ring mesh stiffness as a multiplier

As all the stiffness values were measured from the carrier arm hub, the values of the planet-ring mesh and the sun-planet mesh stiffnesses have to be scaled with the corresponding gear ratios. One way to calculate the planet-ring mesh stiffness from the carrier arm hub is firstly to calculate the stiffness value from the sun gear hub scaled with sun-planet ratio squared as was done for the speed reducer case and then scale this value with the sun-carrier speed ratio squared. The magnitude for the single branch sun-planet-ring torsional stiffness as a multiplier can be calculated as,

$$\frac{1}{K'_{rps1}} = \frac{1}{K_{carrier}} + \frac{u_{sp}^2}{K_{rp1}(\theta - \gamma_{rs}\theta_m - \delta\theta_m)\cdot u_{sc}^2} + \frac{1}{K_{sp1}(\theta - \delta\theta_m)\cdot u_{sc}^2} = \frac{1}{K'_{spr1}(\theta - \delta\theta_m)\cdot u_{sc}^2} \quad (3.41\text{–}1)$$

where K'_{rps1} is the torsional stiffness magnitude for the single branch sun-planet-ring as a multiplier. The theoretical angle difference δ =1/2 mesh cycle was analysed in section 3.4.3. It was found that K'_{rps1} could also be predicted using K'_{spr1} with the speed ratio squared. The stiffness of the *n*th sun-planet-ring mesh stiffness can be calculated as,

$$\frac{1}{K'_{rpsn}} = \frac{1}{K_{carrier}} + \frac{u_{sp}^2}{K_{rpn}(\theta - \gamma_{rn}\theta_m - \gamma_{rs}\theta_m - \delta\theta_m)\cdot u_{sc}^2} + \frac{1}{K_{spn}(\theta - \gamma_{rn}\theta_m - \delta\theta_m)\cdot u_{sc}^2} = \frac{1}{K'_{sprn}(\theta - \delta\theta_m)\cdot u_{sc}^2} \quad (3.41\text{–}2)$$

The results from the predictive model have been compared with the FEA result, as shown in Fig. 3.37.

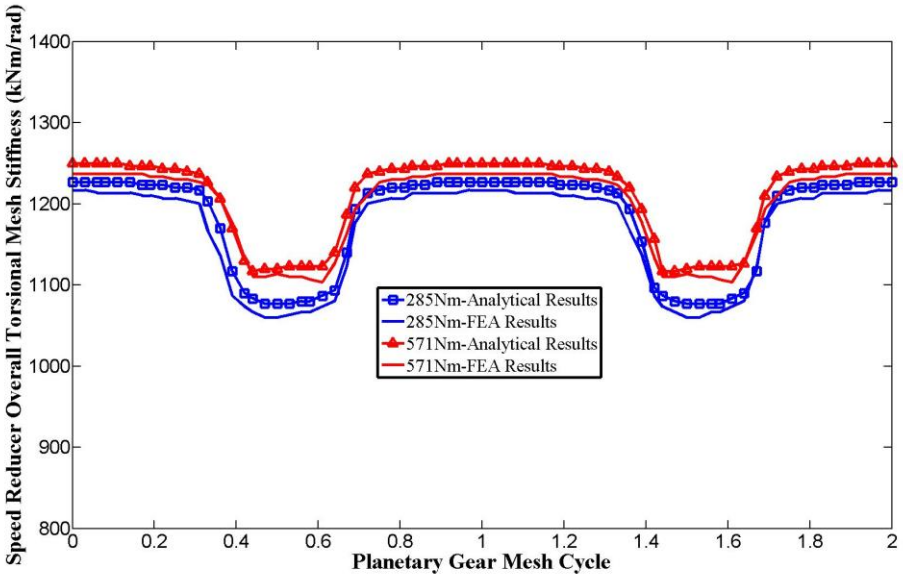

Figure 3.37 Comparison between the single branch analytical and FEA torsional stiffness

The corresponding torsional stiffness predictive model for the overall three branch planetary gear system operating as a multiplier is shown in Fig. 3.38.

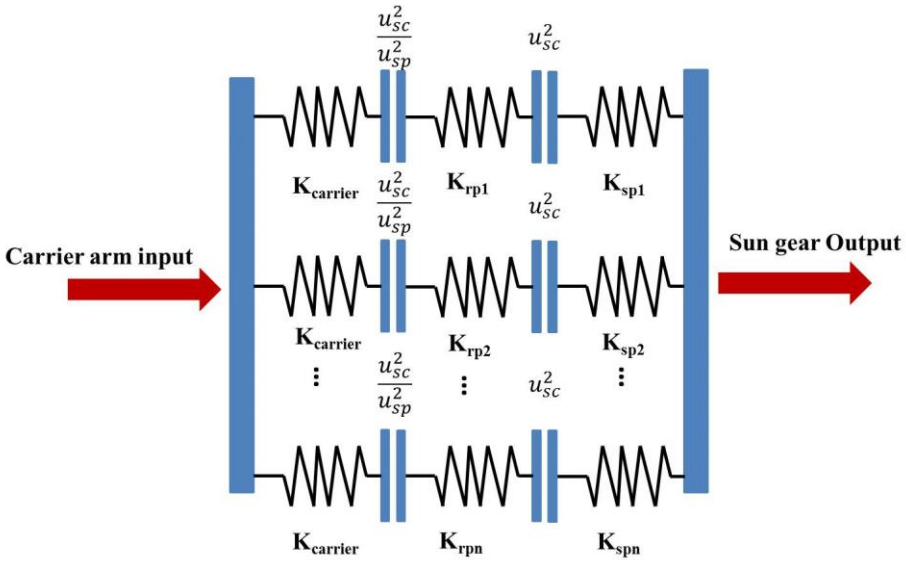

Figure 3.38 Predictive model for overall planetary gear multiplier

The magnitude of the overall planetary gear torsional stiffness as a multiplier can be calculated as,

$$
\begin{aligned}
K_{co}^{'} &= K_{rps1}^{'} + K_{rps2}^{'} + \ldots + K_{rpsn}^{'} \\
&= \frac{1}{\frac{1}{K_{carrier}} + \frac{u_{sp}^2}{K_{rp1}(\theta - \gamma_{rs}\theta_m - \delta\theta_m)u_{sc}^2} + \frac{1}{K_{sp1}(\theta - \delta\theta_m)u_{sc}^2}} \\
&+ \frac{1}{\frac{1}{K_{carrier}} + \frac{u_{sp}^2}{K_{rp1}(\theta - \gamma_{rs}\theta_m - \gamma_{r2}\theta_m - \delta\theta_m)u_{sc}^2} + \frac{1}{K_{sp1}(\theta - \gamma_{s2}\theta_m - \delta\theta_m)u_{sc}^2}} \\
&+ \ldots + \frac{1}{\frac{1}{K_{carrier}} + \frac{u_{sp}^2}{K_{rp1}(\theta - \gamma_{rs}\theta_m - \gamma_{rn}\theta_m - \delta\theta_m)u_{sc}^2} + \frac{1}{K_{sp1}(\theta - \gamma_{sn}\theta_m - \delta\theta_m)u_{sc}^2}} \\
&= u_{sc}^2 \cdot K_{spr1}^{'}(\theta - \delta\theta_m) + u_{sc}^2 \cdot K_{spr2}^{'}(\theta - \delta\theta_m) + \ldots + u_{sc}^2 \cdot K_{sprn}^{'}(\theta - \delta\theta_m) \\
&= u_{sc}^2 \cdot K_{so}^{'}(\theta - \delta\theta_m)
\end{aligned}
\quad , (3.42)
$$

where K'_{co} is the overall planetary gear torsional stiffness as a multiplier. For the example mentioned in table 3.1, the theoretical phase difference $\delta\cdot\theta_m$ is π/Z_r=1.8º. As shown in equation (3.41), the mesh stiffness of single branch K'_{rpsn} can be predicted using K'_{sprn} with speed ratio squared and as a result, the overall mesh stiffness K'_{co} can also be predicted using K'_{so} with speed ratio squared. For the example shown in table 3.1, the analytical results for the overall planetary gear torsional stiffness with the system operating as a multiplier is shown in Fig. 3.39, along with the FEA comparison.

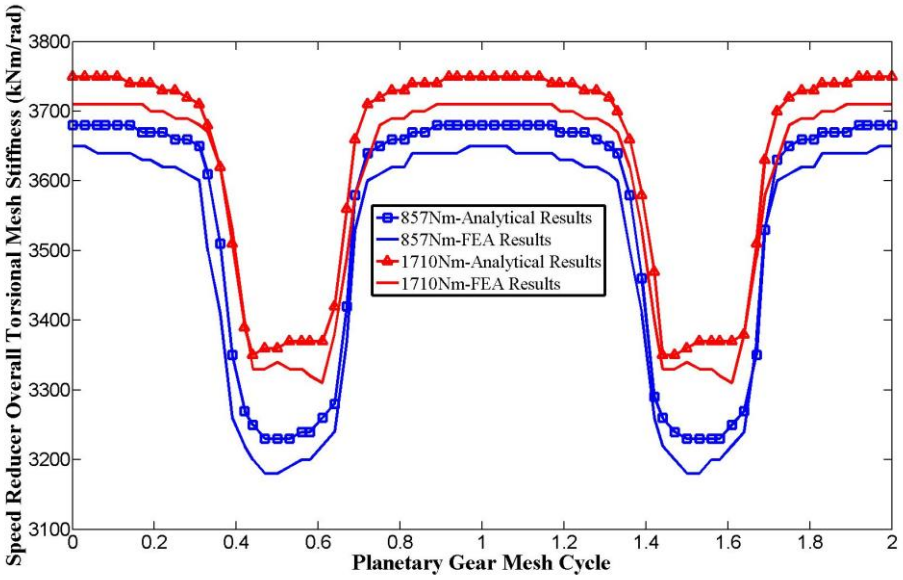

Figure 3.39 Comparison between the analytical torsional stiffness and FEA torsional stiffness

A summary of relative errors between the analytical and FEA torsional stiffness models with flexible carrier arm is presented in table 3.2. The pitch points and the points in the middle of the double contact zone have been selected to calculate the relative errors. It was found that the relative error at the pitch point was small and the relative error in the middle of the double contact zone was larger. However, all relative errors between the analytical and FEA results were found to be less than 4%.

Normally, in order to get the overall planetary gear mesh stiffness, a complicated overall model has to be established, as shown in Fig. 3.27. To solve this model, huge computation resources and computation time are needed. Instead, the predictive model discussed here provides a method to calculate the overall planetary gear mesh stiffness efficiently and it can also give a reasonable results compared with the overall model.

However, this predictive model could also be modified to predict the overall torsional mesh stiffness of any design of gearbox, no matter if it is a simple gear train or a compound gear train. As the mesh stiffness is the inherent characteristics between two gears, this method could evaluate the inherent mesh characteristics of any gear train combination. To do this, the mesh stiffness of each gear pair has to be known before the calculation. Once the input

end is chosen, the overall mesh stiffness for the whole gear train can be evaluated. For example, one gear train is shown in Fig. 3.40.

Table 3.2 Comparison of analytical and FEA results

	Location	FEA Results (kNm)	Analytical Results (kNm)	Relative Error (%)
Single branch as a reducer with flexible arm (100 Nm)	Pitch point (0º)	3.46×10^{1}	3.44×10^{1}	0.6
	Double contact point (1.8º)	3.98×10^{1}	3.83×10^{1}	3.8
Multiple planets with sun gear input (300Nm)	Pitch point (0º)	1.032×10^{2}	1.026×10^{2}	0.6
	Double contact point (1.8º)	1.15×10^{2}	1.18×10^{2}	2.6
Single branch as a multiplier with flexible arm (571Nm)	Pitch point (1.8º)	1.13×10^{3}	1.12×10^{3}	0.8
	Double contact point (0º)	1.30×10^{3}	1.25×10^{3}	3.8
Multiple planets with carrier input (1713Nm)	Pitch point (1.8º)	3.33×10^{3}	3.37×10^{3}	1.2
	Double contact point (0º)	3.71×10^{3}	3.75×10^{3}	1.1

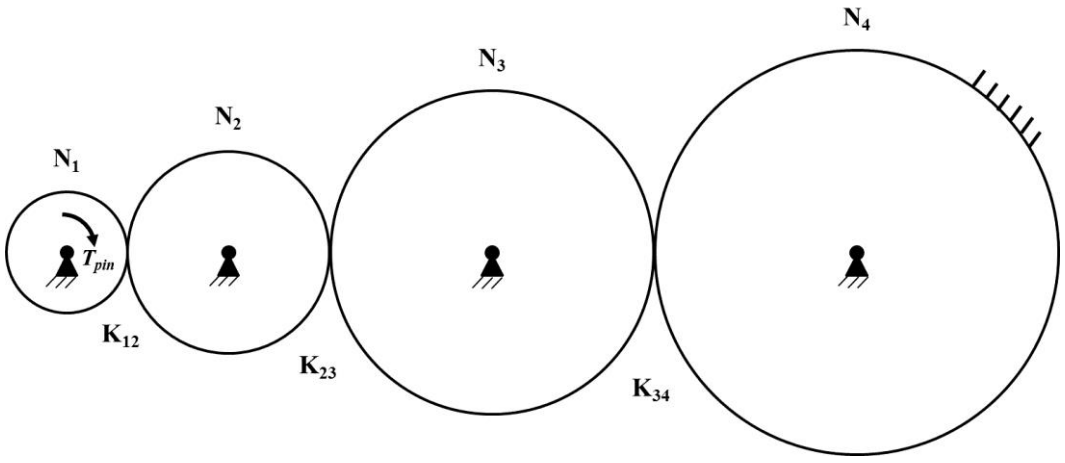

Figure 3.40 Gear train example

There are four gears in this train and the gear teeth number are N_1, N_2, N_3, and N_4 separately. The input torque is applied on gear 1 and the output torque is applied on gear 4. K_{12} is the mesh stiffness between gear 1 and gear 2 and it is calculated from gear 1 hub. K_{23} is the

mesh stiffness between gear 2 and gear3 and it is calculated from gear 2 hub. K_{34} is the mesh stiffness between gear 3 and gear 4 and it is calculated from gear 3 hub. The overall mesh stiffness for this gear train is,

$$\frac{1}{K_{overall}} = \frac{1}{K_{12}} + \frac{(\frac{N_2}{N_1})^2 \cdot (\frac{N_3}{N_2})^2}{K_{23}} + \frac{(\frac{N_2}{N_1})^2 \cdot (\frac{N_3}{N_2})^2 \cdot (\frac{N_4}{N_3})^2}{K_{34}} = \frac{1}{K_{12}} + \frac{(\frac{N_3}{N_1})^2}{K_{23}} + \frac{(\frac{N_4}{N_1})^2}{K_{34}}, \quad (3.43)$$

3.5 Planetary gear crack sensitivity based on predictive models

The common gear failures include pitting, scuffing, wear, and root cracking (Smith, 2003). Tooth root cracking is very uncommon but once it happens, it can result in catastrophic destruction of the gearbox. Cracks in the tooth often start from small stress concentrations at the root of the tooth. Stress concentrations can result in crack propagation from any stress raisers at the early stage, such as machining marks or surface defects and can eventually break off the complete tooth (Smith, 2003). Lewicki used a finite element program (FRANC) to simulate gear tooth crack propagation and to study the effect of rim thickness on the gear crack propagation path (Lewicki & Ballarini, 1997; Radzevich, 2012). The German practice in calculating tooth strength has developed by taking the tangency point of a 30º angle as the critical stress point on the root fillet. In this research, the German practice will be used to simulate the gear crack, as shown in Fig. 3.41.

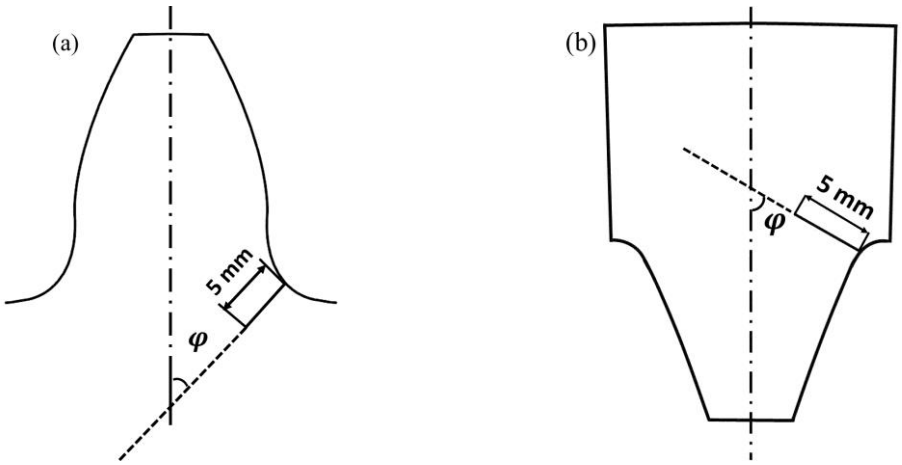

Figure 3.41 Gear crack example with crack angle φ=60º and crack length *l*=5mm, (a) external gear, (b) internal gear

To use finite element methods to ascertain the changes in the teeth stiffness or transmission error with the existence of root cracks, the all-quad element meshing strategy is no longer possible due to the singularity near the crack front. Instead, triangular elements with their mid-side nodes located at ¼ of their adjacent edges from the crack tip will be used (Wang, 2003), as shown in Fig. 3.42. The LEFM (linear elastic fracture mechanics) assumption was used in this research.

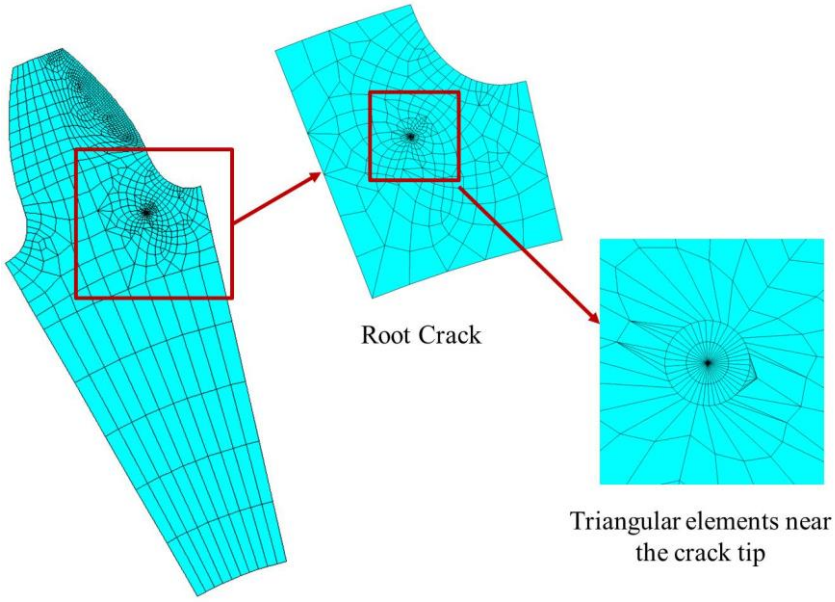

Figure 3.42 Gear tooth with root crack meshed with triangular elements near the crack tip

The mesh stiffnesses with cracks in the sun-planet mesh subsystem were shown in Fig. 3.43 and the mesh stiffnesses with cracks in the ring-planet mesh subsystem were shown in Fig. 3.44. To be more realistic with the application in industry, models with tip-relieved gears were used. In the sun-planet mesh subsystem, a tip relief (length 6mm and relief angle 0.5 rad) was applied to both sun gear and planet gears simultaneously. In the ring-planet mesh subsystem, a tip relief (length 3mm and relief angle 0.39 rad) was applied to both ring gear and planet gear simultaneously.

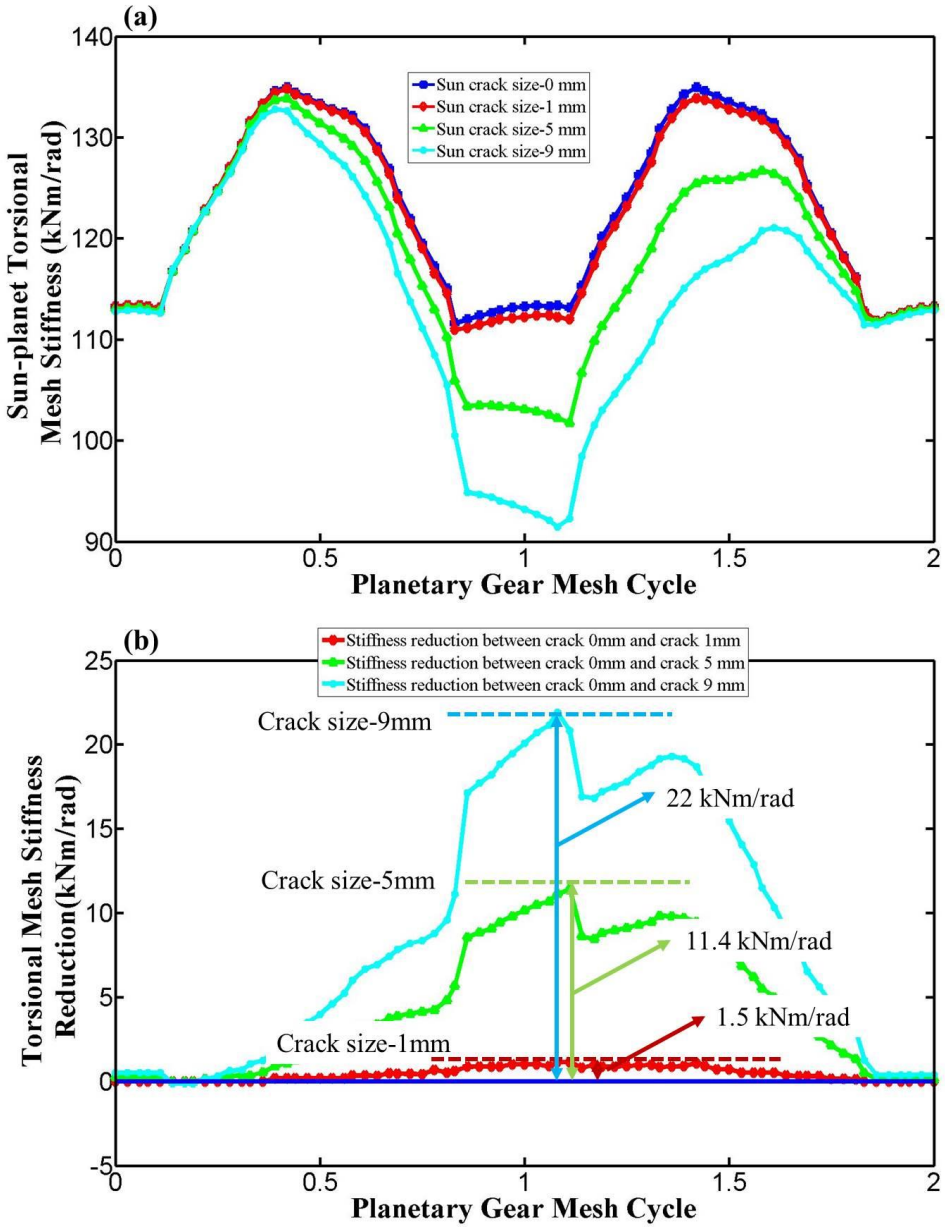

Figure 3.43 Sun-planet torsional mesh stiffness with different crack size on sun gear, (a) sun-planet mesh stiffness with different crack size, (b) torsional mesh stiffness reduction

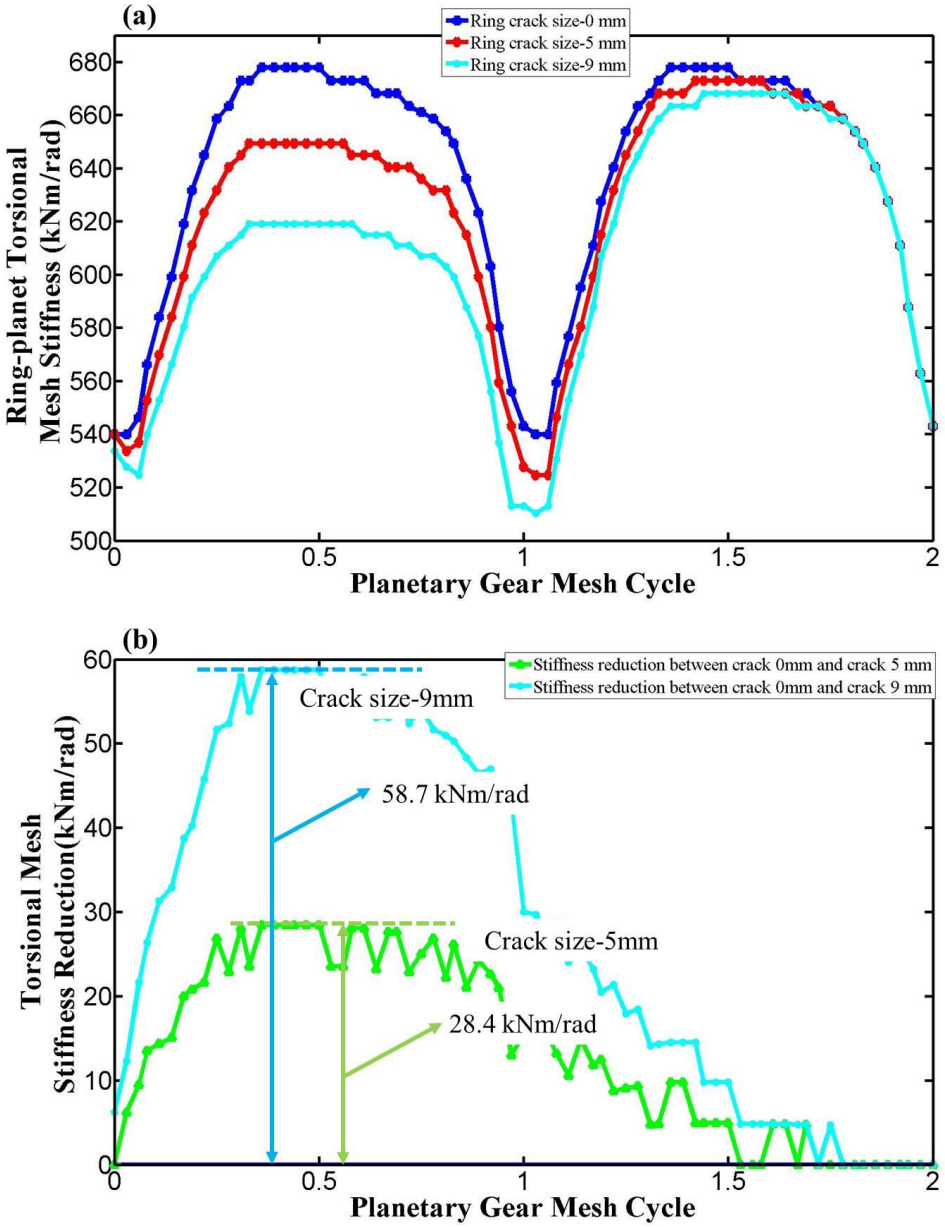

Figure 3.44 Ring-planet torsional mesh stiffness with different crack size on ring gear, (a) ring-planet mesh stiffness with different crack size, (b) torsional mesh stiffness reduction

From Fig. 3.43 and 3.44, it was found that once a crack occurs, the subsystem gear mesh stiffness will change dramatically and larger crack size would result a larger mesh stiffness reduction compared with the healthy mesh stiffness curve. When the crack size is 5mm, only 89.8% sun-planet mesh stiffness will be left and 95.8% ring-planet mesh stiffness will be left. When the crack size increases to 9mm, 80% sun-planet mesh stiffness will be left while 91.4% ring-planet mesh stiffness will be left.

A crack coefficient C_i ***(i=sp, rp)*** ($0<C_i\leq 1$) can be introduced to assist the analysis the crack sensitivity on different components. The coefficient stands for the change ratio of the stiffness. For example, ***Ci=0.1*** means the corresponding stiffness will only have 10% left compared with the perfect meshing stiffness and could be considered a worst case. Correspondingly, ***Ci=1*** means the resulting damage has caused no change of component stiffness.

3.5.1 Crack sensitivity analysis for planetary gear reducer

If a crack occurs on the sun gear or in the planet gear on the sun gear side, the sun-planet mesh stiffness will be affected and the crack coefficient C_{sp} can be assigned in the predictive model for a single branch of the sun-planet-ring mesh as a speed reducer (Fig. 3.32). Equation (3.39−1) would then become,

$$\frac{1}{K'_{spr1\_csp}} = \frac{1}{K_{sp1}(\theta)\cdot C_{sp}} + \frac{u_{sp}^2}{K_{rp1}(\theta-\gamma_{rs}\theta_m)} + \frac{u_{sc}^2}{K_{carrier}}, \tag{3.44}$$

The overall mesh stiffness as a speed reducer would become,

$$\begin{aligned} K'_{so\_csp} &= K'_{spr1\_csp} + K'_{spr2} + \ldots + K'_{sprn} \\ &= \frac{1}{\frac{1}{K_{sp1}(\theta)\cdot C_{sp}} + \frac{u_{sp}^2}{K_{rp1}(\theta-\gamma_{rs}\theta_m)} + \frac{u_{sc}^2}{K_{carrier}}} \\ &+ \frac{1}{\frac{1}{K_{sp1}(\theta-\gamma_{s2}\theta_m)} + \frac{u_{sp}^2}{K_{rp1}(\theta-\gamma_{rs}\theta_m-\gamma_{r2}\theta_m)} + \frac{u_{sc}^2}{K_{carrier}}} \\ &+ \ldots + \frac{1}{\frac{1}{K_{sp1}(\theta-\gamma_{sn}\theta_m)} + \frac{u_{sp}^2}{K_{rp1}(\theta-\gamma_{rs}\theta_m-\gamma_{rn}\theta_m)} + \frac{u_{sc}^2}{K_{carrier}}} \end{aligned}, \tag{3.45}$$

The sun-planet crack sensitivity ζ_{sp} measured from the sun gear hub can then be calculated as,

$$\zeta_{sp} = \frac{K'_{so} - K'_{so\_csp}}{K'_{so}} = 1 - \frac{K'_{so\_csp}}{K'_{so}}, \tag{3.46}$$

If a crack occurs on the ring gear or in the planet gear on the ring gear side, the ring-planet mesh stiffness would be affected and the crack coefficient C_{rp} can be assigned in the

predictive model for a single branch of the sun-planet-ring mesh as a speed reducer (Fig. 3.47). Equation (3.39) would become,

$$\frac{1}{K'_{spr1\_csp}} = \frac{1}{K_{sp1}(\theta)} + \frac{u_{sp}^2}{K_{rp1}(\theta - \gamma_{rs}\theta_m)\cdot C_{rp}} + \frac{u_{sc}^2}{K_{carrier}}, \tag{3.47}$$

The overall mesh stiffness as a speed reducer would become,

$$\begin{aligned} K'_{so\_crp} &= K'_{spr1\_crp} + K'_{spr2} + K'_{spr3} \\ &= \frac{1}{\frac{1}{K_{sp1}(\theta)} + \frac{u_{sp}^2}{K_{rp1}(\theta - \gamma_{rs}\theta_m)\cdot C_{rp}} + \frac{u_{sc}^2}{K_{carrier}}} \\ &+ \frac{1}{\frac{1}{K_{sp1}(\theta - \gamma_{s2}\theta_m)} + \frac{u_{sp}^2}{K_{rp1}(\theta - \gamma_{rs}\theta_m - \gamma_{r2}\theta_m)} + \frac{u_{sc}^2}{K_{carrier}}} \\ &+ \ldots + \frac{1}{\frac{1}{K_{sp1}(\theta - \gamma_{sn}\theta_m)} + \frac{u_{sp}^2}{K_{rp1}(\theta - \gamma_{rs}\theta_m - \gamma_{rn}\theta_m)} + \frac{u_{sc}^2}{K_{carrier}}} \end{aligned}, \tag{3.48}$$

The ring-planet crack sensitivity ζ_{rp} measured from the sun gear hub can be calculated as,

$$\zeta_{rp} = \frac{K'_{so} - K'_{so\_crp}}{K'_{so}} = 1 - \frac{K'_{so\_crp}}{K'_{so}}, \tag{3.49}$$

3.5.2 Crack sensitivity analysis for planetary gear multiplier

Similarly, the crack coefficient C_{sp} can be assigned in the predictive model for a single branch of the sun-planet-ring mesh as a speed multiplier (Fig. 49). However, as discussed in section 3.4.3, a different tooth face will be in mesh when having different driving components, (Fig.3.45). This indicates that the calculation from the carrier arm perspective will detect cracks either on the other side of the sun gear tooth root (compared with that calculated from the sun gear hub) or on the planet gear (ring gear side). Equation (3.43) would then become,

$$\frac{1}{K'_{rps1-csp}} = \frac{1}{K_{carrier}} + \frac{u_{sp}^2}{K_{rp1}(\theta - \gamma_{rs}\theta_m - \delta\theta_m)\cdot u_{sc}^2} + \frac{1}{K_{sp1}(\theta - \delta\theta_m)\cdot C_{sp}\cdot u_{sc}^2} = \frac{1}{K'_{spr1-csp}(\theta - \delta\theta_m)\cdot u_{sc}^2}, \tag{3.50}$$

The overall mesh stiffness as a speed multiplier would become,

$$
\begin{aligned}
K'_{co\_csp} &= K'_{rps1\_csp} + K'_{rps2} + \ldots + K'_{rpsn} \\
&= \frac{1}{\frac{1}{K_{carrier}} + \frac{u_{sp}^2}{K_{rp1}(\theta - \gamma_{rs}\theta_m - \delta\theta_m)\cdot u_{sc}^2} + \frac{1}{K_{sp1}(\theta - \delta\theta_m)\cdot C_{sp}\cdot u_{sc}^2}} \\
&+ \frac{1}{\frac{1}{K_{carrier}} + \frac{u_{sp}^2}{K_{rp1}(\theta - \gamma_{rs}\theta_m - \gamma_{r2}\theta_m - \delta\theta_m)u_{sc}^2} + \frac{1}{K_{sp1}(\theta - \gamma_{s2}\theta_m - \delta\theta_m)u_{sc}^2}} \\
&+ \ldots + \frac{1}{\frac{1}{K_{carrier}} + \frac{u_{sp}^2}{K_{rp1}(\theta - \gamma_{rs}\theta_m - \gamma_{rn}\theta_m - \delta\theta_m)u_{sc}^2} + \frac{1}{K_{sp1}(\theta - \gamma_{sn}\theta_m - \delta\theta_m)u_{sc}^2}} \\
&= u_{sc}^2 \cdot K'_{spr1\_csp}(\theta - \delta\theta_m) + u_{sc}^2 \cdot K'_{spr2}(\theta - \delta\theta_m) + \ldots + u_{sc}^2 \cdot K'_{sprn}(\theta - \delta\theta_m) \\
&= u_{sc}^2 \cdot K'_{so\_csp}(\theta - \delta\theta_m)
\end{aligned}
\quad , \qquad (3.51)
$$

The sun-planet crack sensitivity η_{sp} measured from the carrier arm hub can then be calculated as,

$$
\eta_{sp} = \frac{K'_{co} - K'_{co\_csp}}{K'_{co}} = 1 - \frac{K'_{co\_csp}}{K'_{co}} = 1 - \frac{u_{sc}^2 \cdot K'_{so\_csp}(\theta - \delta\theta_m)}{u_{sc}^2 \cdot K'_{so}(\theta - \delta\theta_m)} = 1 - \frac{K'_{so\_csp}(\theta - \delta\theta_m)}{K'_{so}(\theta - \delta\theta_m)} \text{ , (3.52)}
$$

As shown in equation (3.52), η_{sp} can also be calculated using the stiffness measured from the sun gear hub with different mesh phase.

The crack coefficient $\boldsymbol{C_{rp}}$ can be assigned in the predictive model for a single branch of sun-planet-ring mesh as a speed multiplier (Fig. 3.51). Equation (3.41) would then become,

$$
\frac{1}{K'_{rps1\_crp}} = \frac{1}{K_{carrier}} + \frac{u_{sp}^2}{K_{rp1}(\theta - \gamma_{rs}\theta_m - \delta\theta_m)\cdot u_{sc}^2 \cdot C_{rp}} + \frac{1}{K_{sp1}(\theta - \delta\theta_m)\cdot u_{sc}^2} = \frac{1}{K'_{spr1\_crp}(\theta - \delta\theta_m)\cdot u_{sc}^2}
$$

, (3.53)

The overall mesh stiffness as a speed multiplier would become,

$$
\begin{aligned}
K'_{co\_crp} &= K'_{rps1\_crp} + K'_{rps2} + \ldots + K'_{rpsn} \\
&= \frac{1}{\frac{1}{K_{carrier}} + \frac{u_{sp}^2}{K_{rp1}(\theta - \gamma_{rs}\theta_m - \delta\theta_m)\cdot u_{sc}^2 \cdot C_{rp}} + \frac{1}{K_{sp1}(\theta - \delta\theta_m)\cdot u_{sc}^2}} \\
&+ \frac{1}{\frac{1}{K_{carrier}} + \frac{u_{sp}^2}{K_{rp1}(\theta - \gamma_{rs}\theta_m - \gamma_{r2}\theta_m - \delta\theta_m)u_{sc}^2} + \frac{1}{K_{sp1}(\theta - \gamma_{s2}\theta_m - \delta\theta_m)u_{sc}^2}} \\
&+ \ldots + \frac{1}{\frac{1}{K_{carrier}} + \frac{u_{sp}^2}{K_{rp1}(\theta - \gamma_{rs}\theta_m - \gamma_{rn}\theta_m - \delta\theta_m)u_{sc}^2} + \frac{1}{K_{sp1}(\theta - \gamma_{sn}\theta_m - \delta\theta_m)u_{sc}^2}} \\
&= u_{sc}^2 \cdot K'_{spr1\_crp}(\theta - \delta\theta_m) + u_{sc}^2 \cdot K'_{spr2}(\theta - \delta\theta_m) + \ldots + u_{sc}^2 \cdot K'_{sprn}(\theta - \delta\theta_m) \\
&= u_{sc}^2 \cdot K'_{so\_crp}(\theta - \delta\theta_m)
\end{aligned}
\quad , \qquad (3.54)
$$

The sun-planet crack sensitivity η_{rp} measured from the carrier arm hub can then be calculated as,

$$
\eta_{rp} = \frac{K'_{co} - K'_{co\_crp}}{K'_{co}} = 1 - \frac{K'_{co\_crp}}{K'_{co}} = 1 - \frac{u_{sc}^2 \cdot K'_{so\_crp}(\theta - \delta\theta_m)}{u_{sc}^2 \cdot K'_{so}(\theta - \delta\theta_m)} = 1 - \frac{K'_{so\_crp}(\theta - \delta\theta_m)}{K'_{so}(\theta - \delta\theta_m)} , \qquad (3.55)
$$

As shown in equation (3.55), η_{rp} can also be calculated using the stiffness measured from the sun gear hub with different mesh phase.

3.5.3 Crack sensitivity analysis results

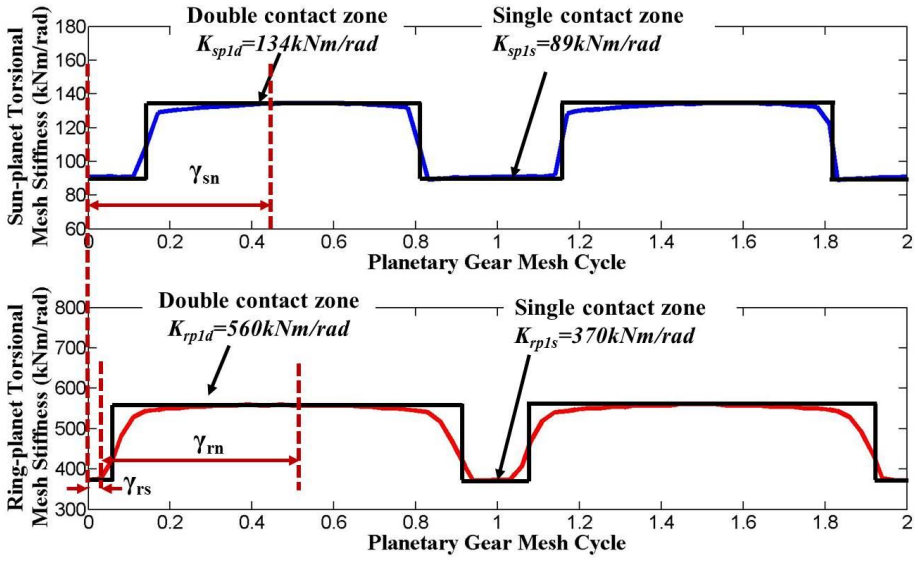

Figure 3.45 Sun-planet mesh stiffness and ring-planet mesh stiffness

The sun-planet mesh and ring-planet mesh can be divided into double contact zone and single contact zone, if a square wave curve was used to represent the mesh stiffness, two constant values will be used in the double contact zone and in the single contact zone separately, as shown in Fig. 3.45. As the mesh stiffness in the *n*th pair can be related to that of the 1st pair, the stiffness (K_{sp} or K_{rp}) will choose either the value in the double contact zone or the value in the single contact zone. If the planetary gear has *n* branches, the number of possible K_{so} values will be 4^n with different phase combination. However, the maximum value will happen when all the sun-planet and ring-planet meshes are in their double contact zone and the minimum value will happen when all the meshes are in their single contact zone. In other words, as long as all the meshes are in the same contact zone, the maximum and minimum value will happen no matter what the mesh phases combination are. As a result, when all the meshes are in the single contact zone or all the meshes are in the double contact zone, the value of ζ_{sp} is,

$$\zeta_{sp} = 1 - \frac{K_{so\_csp}}{\min(K_{so})}, \text{ or } \zeta_{sp} = 1 - \frac{K_{so\_csp}}{\max(K_{so})}, \tag{3.56–1}$$

and the value of ζ_{rp} is,

$$\zeta_{rp} = 1 - \frac{K_{so\_crp}}{\min(K_{so})}, \text{ or } \zeta_{rp} = 1 - \frac{K_{so\_crp}}{\max(K_{so})}, \tag{3.56–2}$$

Similarly, the values of η_{sp} and η_{rp} can also be calculated using K_{so_csp}, K_{so_crp}, and K_{so}. The value of η_{sp} is,

$$\eta_{sp} = 1 - \frac{K_{so\_csp}}{\min(K_{so})}, \text{ or } \eta_{sp} = 1 - \frac{K_{so\_csp}}{\max(K_{so})}, \tag{3.57–1}$$

and the value of η_{rp} is,

$$\eta_{rp} = 1 - \frac{K_{so\_crp}}{\min(K_{so})}, \text{ or } \eta_{rp} = 1 - \frac{K_{so\_crp}}{\max(K_{so})}, \tag{3.57–2}$$

For the example shown in table 3.1, there are three branches of sun-planet-ring. The sun-planet mesh stiffnesses in the single contact zone and double contact zone are 89kNm/rad and 134kNm/rad. The ring-planet mesh stiffnesses in the single contact zone and double contact zone are 370kN/rad and 560kNm/rad. Initially, the carrier arm stiffness was

chosen to be 2.16×10^3 kNm/rad. Each crack coefficient was changed from 0.1 to 1, indicating that the corresponding stiffness changed from the worst case to perfect meshing.

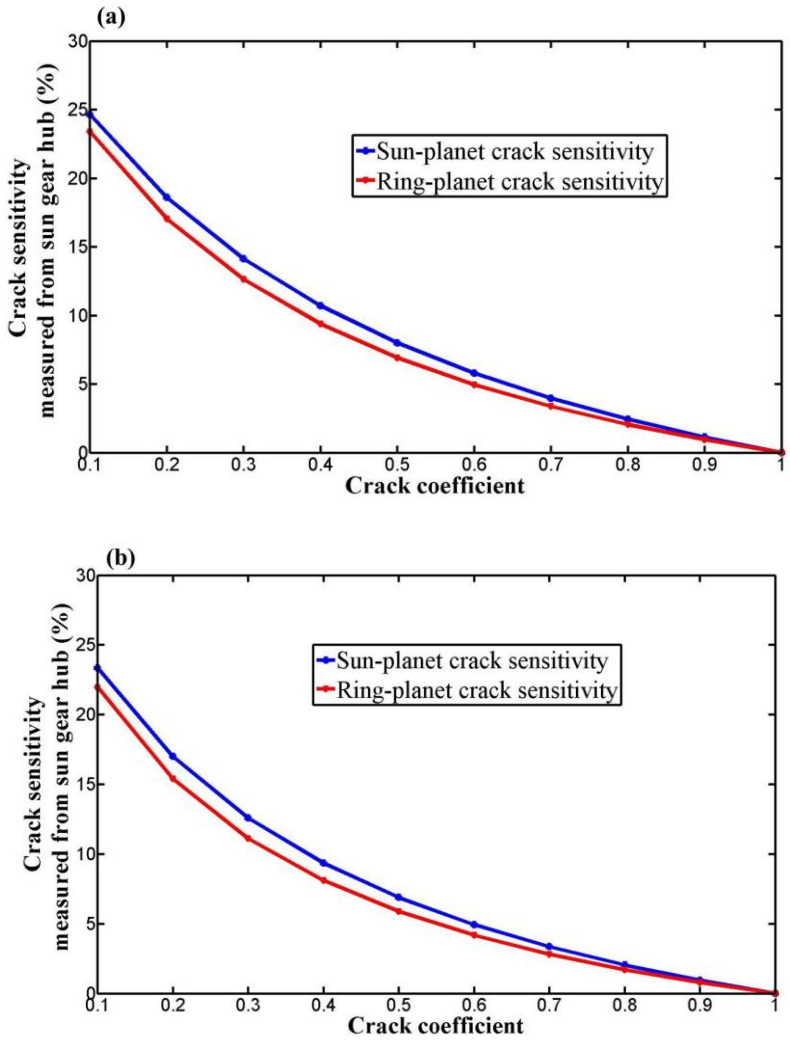

Figure 3.46 Crack sensitivity measured from sun gear hub, (a) when all the meshes are in the single contact zone, (b) when all the meshes are in the double contact zone

Fig. 3.46 shows the resulting crack sensitivity results measured from the sun gear hub, in which Fig. 3.46(a) shows the results when all the meshes are in the single contact zone and Fig. 3.46(b) indicates the results when all the meshes are in the double contact zone. It was found that the cracks in the sun-planet mesh tended to be more sensitive than the cracks in the ring-planet mesh no matter if all the meshes were in the single contact zone or if they were in the double contact zone. Also, there was only slight difference between the crack sensitivity measured from the single contact zone and the crack sensitivity measured from

the double contact zone. For example, when the crack coefficient C_{sp}=0.1, the sun-planet crack sensitivity in the single contact zone was 24.64% while the sun-planet crack sensitivity in the double contact zone was 23.34%. As the maximum value will happen when all the sun-planet and ring-planet meshes are in their double contact zone and the minimum value will happen when all the meshes are in their single contact zone, the crack sensitivity for the other kinds of mesh phase combination are expected to vary between the results shown in Fig. 3.46(a) and Fig. 3.46(b).

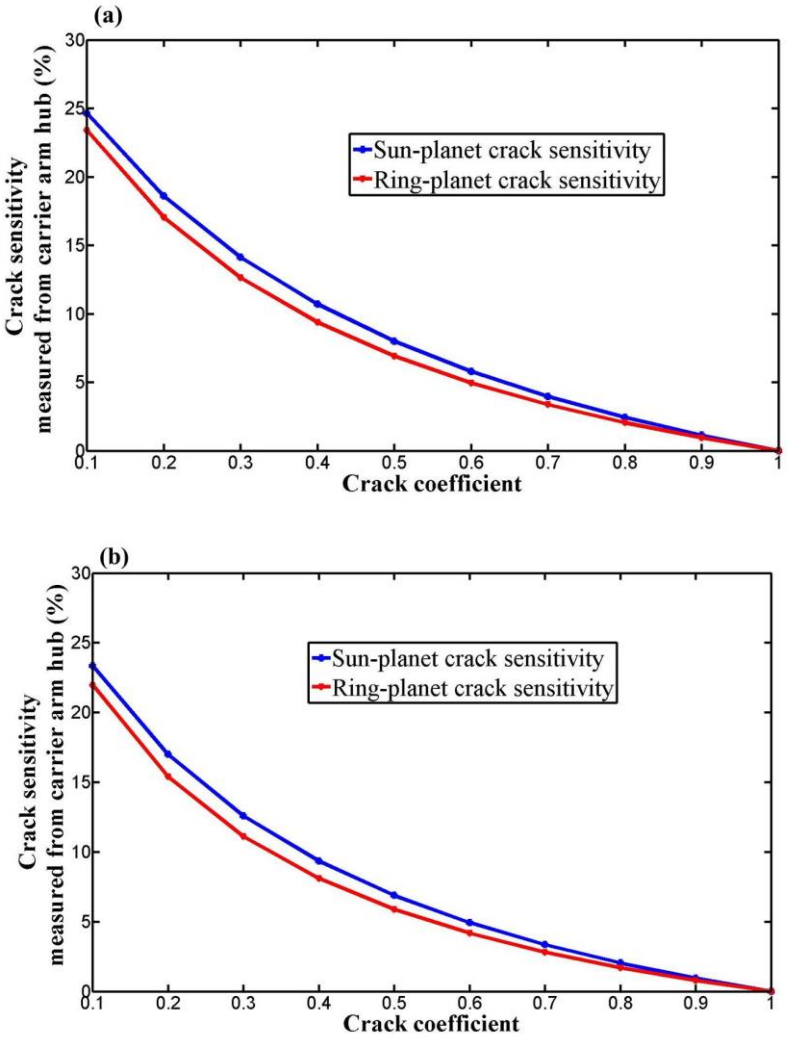

Figure 3.47 Crack sensitivity measured from carrier arm hub, (a) when all the meshes are in the single contact zone, (b) when all the meshes are in the double contact zone

Fig. 3.47 described the resulting crack sensitivity results measured from the carrier arm hub, in which Fig. 3.46(a) is the results when all the meshes are in the single contact zone and Fig.

3.46(b) is the results when all the meshes are in the double contact zone. It was found that the crack sensitivity measured from the carrier arm hub and those from the sun gear hub was identical as expected. This phenomenon can also be found in equation (3.56) and equation (3.57).

In this chapter, the carrier arm was calculated using beam bending theory, as shown in equation (3.34). When the carrier arm stiffness was equal to 2.16e3 kNm/rad, the crack sensitivity results were analysed in Fig. 3.46 and Fig. 3.47. However, when the carrier arm stiffness increases or decreases, the crack sensitivity will be different. The crack sensitivity under six different carrier arm stiffnesses were analysed, as shown in Fig. 3.48.

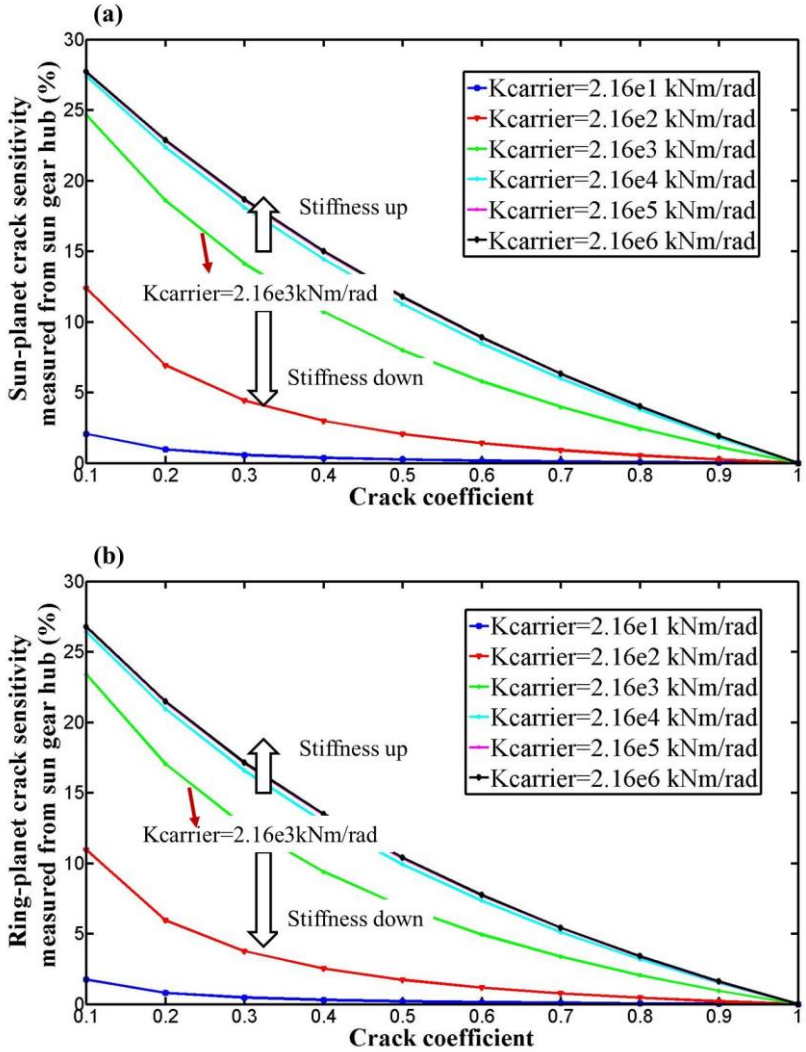

Figure 3.48 Influence of carrier arm stiffness on crack sensitivity, (a) sun-planet crack sensitivity, (b) ring-planet crack sensitivity

Fig. 3.48 showed the influence of carrier arm stiffness on sun-planet and ring-planet crack sensitivities. Only the crack sensitivity measured from the sun gear hub when all the meshes are in the single contact zone was analysed. It was found that both the sun-planet and ring-planet cracks become more sensitive when the carrier arm stiffness increases and cracks tend to be harder to be detected when the carrier arm stiffness becomes minimal. For example, when the crack coefficient C_{sp} was assigned in the model, the sun-planet crack sensitivity was only 2% when carrier arm stiffness is 2.16e1 kNm/rad and the sun-planet crack sensitivity increases to 24.6% when the carrier arm stiffness increases to 2.16e3 kNm/rad. However, when the carrier arm stiffness increases to 2.16e5 kNm/rad, it was found it is difficult to enhance the sensitivity any more. Similarly results were found in the ring-planet crack sensitivity.

3.6 Conclusion

A detailed calculation procedure for estimating the overall torsional mesh stiffness of a planetary gearbox has been developed in this chapter. It included the FEA modelling of the individual sun-planet, ring-planet and carrier arm components and illustrated how they can be combined together via the gear speed ratios.

The predictive models for the overall torsional stiffness based on the subsystem models agreed well with the results from the FEA calculation and the relative error was found to be less than 4%. It was found that the relationship between the overall model and subsystem models was directly related to the square of the speed ratios between the various components.

The crack sensitivity analysis based on the predictive models has been performed. The effect of a crack on the sun-planet mesh and ring-planet mesh stiffness has been introduced into the predictive models via a crack coefficient. It was found that the overall stiffness was most sensitive to the crack on the sun-planet mesh. Finally, the influence of the carrier arm stiffness on the crack sensitivity was discussed and it was found that both the sun-planet and ring-planet crack become more sensitive when the carrier arm becomes stiffer.

Chapter 4 Dynamic modelling of flexibly supported gears using iterative convergence of tooth mesh stiffness

4.1 Introduction

Most gear designs are based on standard tooth proportions and such gears are intended to mesh on standard centre distances. However, the actual centre distance at which a gear will operate will be different from the standard design value. The actual operating centre distance is influenced by the combined effects of manufacturing tolerances, mounting inaccuracies, bearing backlash, different expansion between the gears and their mountings due to temperature, deflections in the mountings due to service load, the gear system (gear, bearing or shaft) faults and so on (Townsend, 1991). Additionally, gears may be designed to operate at non-standard centre distance to introduce backlash, to accommodate space constraints, and to adjust for anticipated deflections under load as well as geometry changes due to thermal effects (Lin et al., 1996). The actual operating centre distance will have a large influence on the way that the gear will perform. For example, the gear pitch diameters, gear pressure angle and contact ratio are all influenced by the variation in gear centre distance and consequently, the gear mesh stiffness will also be affected. As a result, the gear dynamic performance will also be influenced by this operating centre distance variation.

Dynamic modelling of gear vibration can be used to further the understanding of the vibration generation mechanisms in gear transmissions as well as the dynamic behaviour of the transmission in the presence of various types of gear faults. A comprehensive review of gear dynamic models can be found in (Özgüven & Houser, 1988). Among the various models, the coupled torsional and transverse model is one of the common modelling approaches that have been used recently. The advantage of this model is that it includes the flexibility of the shaft and bearings as well as the tooth mesh deformation and therefore the dynamic response from this type of model is more realistic and closer to the measured vibration data (Bartelmus, 2001; Chaari et al., 2008; Du, 1997; Howard et al., 2001; Jia & Howard, 2006; Özgüven & Houser, 1988). Mathematical gear simulation, where both torsional and lateral vibrations have been considered, has been used as an aid to gearbox

diagnostics (Bartelmus, 2001). It suggests that a one-stage gearbox model which consists of a motor, couplings, and a driven machine is the best approach for investigation of the gear dynamic behaviour. Based on the model developed by Du (Du, 1997), Howard et al. developed a 16-degree-of-freedom gear dynamic model which included the effect of friction and the effect of a tooth crack (Howard et al., 2001). Some diagnostic techniques were used to deal with the resultant vibration signal and it showed that the result obtained from the simulation was very similar to that observed from a helicopter gearbox, but in most cases, friction gave a negligible change in the resulting diagnostic value. Later on, a 26-degree-of-freedom gear dynamic model which included three shafts and two pairs of gears in mesh was developed for the purpose of comparing localised tooth spalling and crack damage (Jia & Howard, 2006). The effect of spalling and tooth breakage on the gear mesh stiffness was analytical formulated and then the resultant gear mesh stiffness curves was incorporated into a one-stage spur gear model where the flexibility of the shaft and bearing was considered (Chaari et al., 2008).

One of the major assumptions in these models mentioned above is that gear pairs are intended to mesh on standard centre distance and its contribution to the change of the gear design parameters, such as pressure angle, contact ratio and even the gear mesh stiffness, is limited. In fact, the actual operating gear centre distance is influenced by the combined effects of manufacturing tolerances, bearing backlash and deflections in the support structure (Townsend, 1991). Especially for a flexible supported gear system, the change of the operating gear centre distance from its nominal value cannot be neglected and therefore, the dynamic performance induced by the change of the gear centre distance is expected to be different.

However, few studies have been found that were focused on the influence of gear centre distance on the gear dynamic performance. Hsiang His Lin presented an analytical study on using hob offset to balance the dynamic tooth strength of spur gears operating at a centre distance greater than the standard value (Lin & Liou, 1996). A new dynamic model considering the time-varying gear centre distance was proposed in (Kim et al., 2010). They found that the bearing stiffness had a significant effect upon the gear vibration. Later, they

extended the time-varying factor to planetary gear systems, finding that the dynamic response of planetary gears with time-varying pressure angles and contact ratios had more frequency components than the dynamic responses with constant pressure angles and contact ratios (Kim et al., 2012). Despite these publications, there remains a paucity of research on the effect of the gear centre distance variation on the gear dynamic performance, and the gear centre distance variation on the resulting gear fault diagnosis methods.

In this chapter, a new gear dynamic model is proposed that considers the gear centre distance variation, which has been selected as the iteration criteria to ascertain the accuracy of the dynamic response. Based on the dynamic response, some common diagnostic techniques are used to examine the gear system vibration behaviour results compared with the results from the model without considering the gear centre distance variation. The first section of this chapter derives the differential equations used for the gear system. The finite element analysis (FEA) method was then used to analyse the gear mesh stiffness with different gear centre distance changes. The effect of a 5 mm root crack on the gear mesh stiffness curve has also been modelled with different gear centre distances. As the change of the gear mesh stiffness largely relies on the variation of the gear centre distance, a subsequent iteration strategy was developed by comparing the gear centre distance at two nearby time steps. This was then used in the gear dynamic model to ensure the gear dynamic solution convergence at each time step as outlined in the third section. The fourth section compares the findings of the diagnostic results, which have been examined by coherent time synchronous averaging, followed by root mean squared (RMS) spectrum analysis, residual signal, Pseudo Wigner-Ville distribution (PWVD), narrow band envelope, amplitude modulation, phase modulation and analytic signal plots.

4.2 Modelling of a pair of spur gear

4.2.1 Equation of gear motion

A simplified transverse-torsional gear dynamic model was used in this research and as the focus of this chapter is to investigate the gear centre distance impact on gear dynamic motion instead of the whole system effect, only a single one-stage gear system was modelled with

the motor and load. The input load T_{in} was provided by the motor and it is assumed constant. The motor shaft and the shaft that the pinion mounts on are coupled with a flexible coupling. The output load T_{out} was applied on to the gear and it was assumed to depend on the gear angular velocity. A flexible coupling was also attached to the output load shaft and gear shaft. In Fig. 4.1, O_p is the designed pinion centre position and O_g is the designed gear centre position. A bearing was used to connect the gear centre and the ground and the bearing model includes the radial stiffness k_{ij} (i=x, y; j=p,g) and damping q_{ij} (i=x, y; j=p,g) and damping q_{stj} (i=x, y; j=p,g). Linear gear meshing stiffness k_{mb} and damping q_{mb} are used to connect the two gears and by this way, the torsional and transverse motions of the gears are coupled. A coordinate x_p-O_p-y_p was attached to the pinion centre and the pinion can move in x_p, y_p and θ_p directions. A coordinate x_g–O_g–y_g was attached to the gear centre and the gear can move in x_g, y_p and θ_g directions.

The following nomenclatures were used in the gear system,

I_m: mass moment of inertia of the motor;

I_p: mass moment of inertia of the pinion;

I_g: mass moment of inertia of the gear;

I_{out}: mass moment of inertia of the output load;

m_p: mass of the pinion;

m_g: mass of the gear;

θ_m: angular displacement of the motor;

θ_p: angular displacement of the pinion;

θ_g: angular displacement of the gear;

θ_{out}: angular displacement of the output load;

x_p: linear displacement of pinion in the horizontal direction (the x direction);

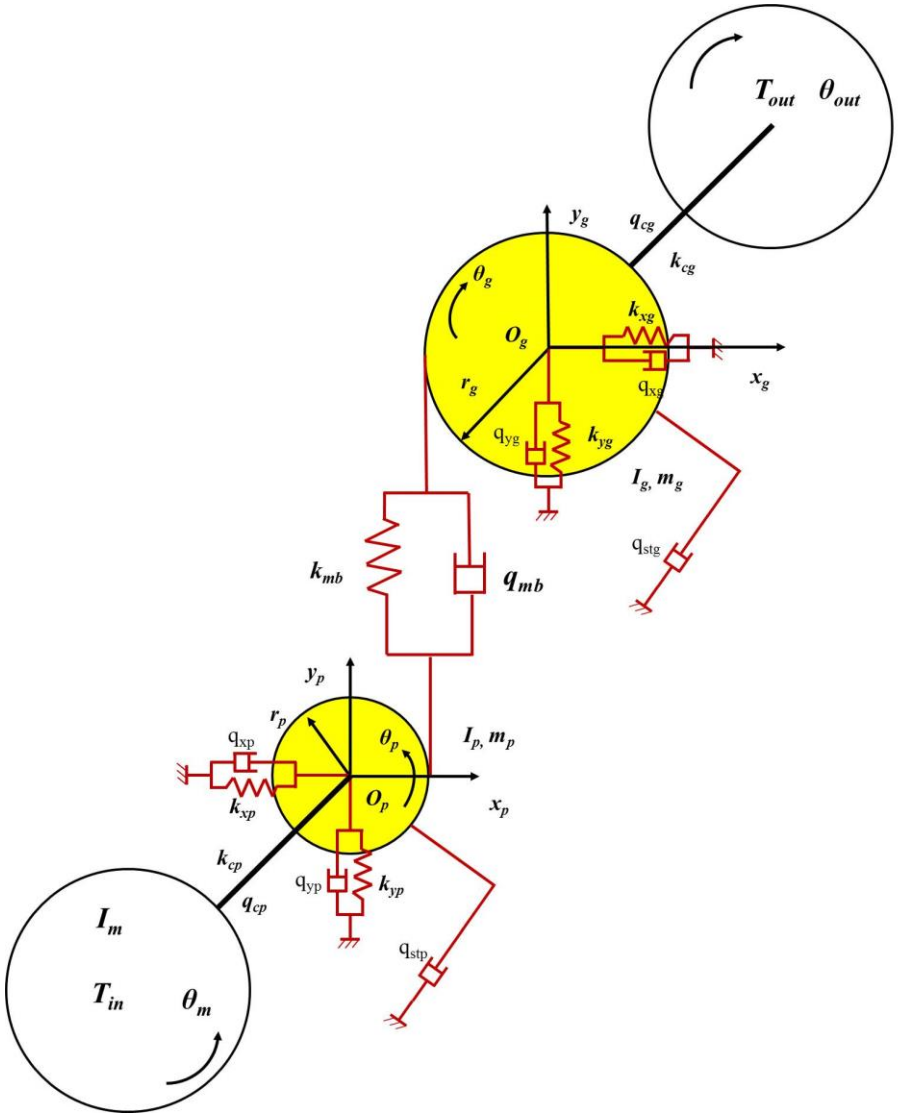

Figure 4.1 Spur gear dynamic model with constant gear centre distance

x_g: linear displacement of gear in the horizontal direction (the x direction);

y_p: linear displacement of pinion in the vertical direction (the x direction);

y_g: linear displacement of gear in the vertical direction (the x direction);

k_{cp}: stiffness of the input coupling and shaft;

k_{cg}: stiffness of the output coupling and shaft;

q_{cp}: damping of the input coupling and shaft;

q_{cg}: damping of the output coupling and shaft;

k_{xp}, k_{yp}: radial stiffness of the pinion;

k_{xg}, k_{yg}: radial stiffness of the gear;

q_{xp}, q_{yp}: radial damping of the pinion;

q_{xg}, q_{yg}: radial damping of the gear;

q_{stp}: torsional damping of the pinion;

q_{stg}: torsional damping of the gear;

k_{mb}: linear translation tooth stiffness along line of contact between pinion and gear;

q_{mb}: linear translation tooth damping along line of contact between pinion and gear;

T_{in}: input motor torque;

T_{out}: output load torque;

N: normal tooth contact force along the line of contact between pinion and gear;

p: relative mesh displacement.

The assumptions in this model were that,

1). the pinion and gear only have in-plane motion;

2). the bearing stiffness in x and y directions are identical;

3). Proportional damping is used in the gear mesh;

4). the input load T_{in} is constant;

5). the output load T_{out} depends on the gear output velocity.

The resulting equations of motion for this gear system are shown as follows.

For the rotary motion of the motor, the motion equation is,

$$I_m\ddot{\theta}_m = T_{in} - k_{cp}(\theta_m - \theta_p) - q_{cp}(\dot{\theta}_m - \dot{\theta}_p). \quad (4.1)$$

For the motion of the pinion, the motion equation is,

$$m_p\ddot{y}_p = -h \cdot N - k_{yp} \cdot y_p - q_{yp} \cdot \dot{y}_p, \tag{4.2}$$

$$I_p\ddot{\theta}_p = k_{cp}(\theta_m - \theta_p) + q_{cp}(\dot{\theta}_m - \dot{\theta}_p) - N \cdot r_p - q_{stp} \cdot \dot{\theta}_p. \tag{4.3}$$

For the motion of the gear, the motion equation is,

$$m_g\ddot{y}_g = h \cdot N - k_{yg} \cdot y_g - q_{yg} \cdot \dot{y}_g, \tag{4.4}$$

$$I_g\ddot{\theta}_g = h \cdot N \cdot r_g - k_{cg}(\theta_g - \theta_{out}) - q_{cg}(\dot{\theta}_g - \dot{\theta}_{out}) - q_{stp} \cdot \dot{\theta}_g, \tag{4.5}$$

where *N* is the normal contact force between pinion and gear and it is,

$$N = k_{mb} \cdot (y_p + r_p \cdot \theta_p - y_g - r_g \cdot \theta_g) + q_{mb} \cdot (\dot{y}_p + r_p \cdot \dot{\theta}_p - \dot{y}_g - r_g \cdot \dot{\theta}_g). \tag{4.6}$$

h is a unit step function to represent the tooth separation phenomenon,

$$h = \begin{cases} 1, p \geq 0 \\ 0, p < 0 \end{cases},$$

where *p* is the relative gear mesh displacement defined as,

$$p = y_p + r_p \cdot \theta_p - y_g - r_g \cdot \theta_g. \tag{4.7}$$

This way, if *p* is at a given position, the teeth will lose contact and the resulting spring force will be equal to zero.

For the rotary motion of the load, the motion equation is,

$$I_{out}\ddot{\theta}_{out} = -T_{out} + k_{cg}(\theta_g - \theta_{out}) + q_{cg}(\dot{\theta}_g - \dot{\theta}_{out}), \tag{4.8}$$

The derived gear equations of motion can be represented in a matrix-vector form. This matrix-vector form is useful in computing dynamic responses when applying a numerical time integration algorithm. The matrix-vector form of the nonlinear equations can be written as,

$$M\ddot{x} + C\dot{x} + Kx = F, \tag{4.9}$$

where x is the displacement vector, M is the mass matrix, K is the stiffness matrix, C is the damping matrix and F is the external loading force.

$$M = \begin{bmatrix} I_m & 0 & 0 & 0 & 0 & 0 \\ 0 & m_p & 0 & 0 & 0 & 0 \\ 0 & 0 & I_p & 0 & 0 & 0 \\ 0 & 0 & 0 & m_g & 0 & 0 \\ 0 & 0 & 0 & 0 & I_g & 0 \\ 0 & 0 & 0 & 0 & 0 & I_{out} \end{bmatrix},$$

$$x = [\theta_m, y_p, \theta_p, y_g, \theta_g, \theta_{out}]^T,$$

$$C = \begin{bmatrix} q_{cp} & 0 & -q_{cp} & 0 & 0 & 0 \\ 0 & q_{yp} + hq_{mb} & hq_{mb}r_p & -hq_{mb} & -hq_{mb}r_g & 0 \\ -q_{cp} & hq_{mb}r_p & hq_{mb}r_p^2 + q_{cp} + q_{stp} & -hq_{mb}r_p & -hq_{mb}r_p r_g & 0 \\ 0 & -hq_{mb} & -hq_{mb}r_p & q_{yg} + hq_{mb} & hq_{mb}r_g & 0 \\ 0 & -hq_{mb}r_g & -hq_{mb}r_p r_g & hq_{mb}r_g & hq_{mb}r_g^2 + q_{cg} + q_{stg} & -q_{cg} \\ 0 & 0 & 0 & 0 & -q_{cg} & q_{cg} \end{bmatrix}$$

,

$$K = \begin{bmatrix} k_{cp} & 0 & -k_{cp} & 0 & 0 & 0 \\ 0 & k_{yp} + hk_{mb} & hk_{mb}r_p & -hk_{mb} & -hk_{mb}r_g & 0 \\ -k_{cp} & hk_{mb}r_p & hk_{mb}r_p^2 + k_{cp} & -hk_{mb}r_p & -hk_{mb}r_p r_g & 0 \\ 0 & -hk_{mb} & -hk_{mb}r_p & k_{yg} + hk_{mb} & hk_{mb}r_g & 0 \\ 0 & -hk_{mb}r_g & -hk_{mb}r_p r_g & hk_{mb}r_g & hk_{mb}r_g^2 + k_{cg} & -k_{cg} \\ 0 & 0 & 0 & 0 & -k_{cg} & k_{cg} \end{bmatrix},$$

$$F = [T_{in}, 0,0,0,0, -T_{out}]^T.$$

4.2.2 Gear centre distance analysis

The gear centre distance is determined by the pinion centre and gear centre, as shown in Fig. 4.2.

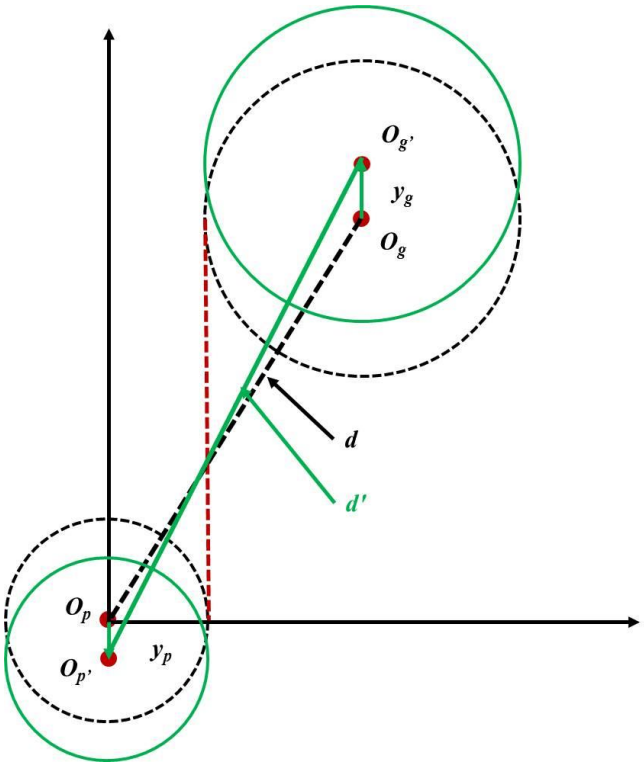

Figure 4.2 Spur gear centre distance variation

In the reference coordinate, the designed position for pinion centre O_p is,

$$\overrightarrow{d_p} = (0)\vec{x} + (0)\vec{y}, \tag{4.10}$$

and the designed position for gear centre O_g is,

$$\overrightarrow{d_g} = (r_p + r_g)\vec{x} + \left((r_p + r_g)\tan\alpha\right)\vec{y}, \tag{4.11}$$

where r_p is the base radius of the pinion and r_g is the base radius of the gear. The designed gear centre distance is (Townsend, 1991),

$$d = \frac{r_p + r_g}{\cos\alpha}. \tag{4.12}$$

The designed position angle is chosen to be equal to the designed pressure angle α (Townsend, 1991),

$$\alpha = \cos^{-1}\frac{r_p + r_g}{d}. \tag{4.13}$$

The designed gear contact ratio is (Townsend, 1991) ,

$$m_p = \frac{\sqrt{r_{ap}^2 - r_p^2} + \sqrt{r_{ag}^2 - r_g^2} - d\sin\alpha}{p_b} = \frac{\sqrt{r_{ap}^2 - r_p^2} + \sqrt{r_{ag}^2 - r_g^2} - d\sin\alpha}{\pi \cdot m \cdot \cos\alpha}. \tag{4.14}$$

where r_{ap} is the pinion addendum radius and r_{ag} is the gear addendum radius. p_b is the base pitch. The gear contact ratio is closely related to the variation in gear mesh stiffness as the proportions of the single and double contact zones are determined by the contact ratio m_p, as shown in Fig. 4.3. T_m is the gear mesh period. The gear mesh stiffness is said to be shaft phase variant mesh stiffness as it is a function of the shaft rolling angle.

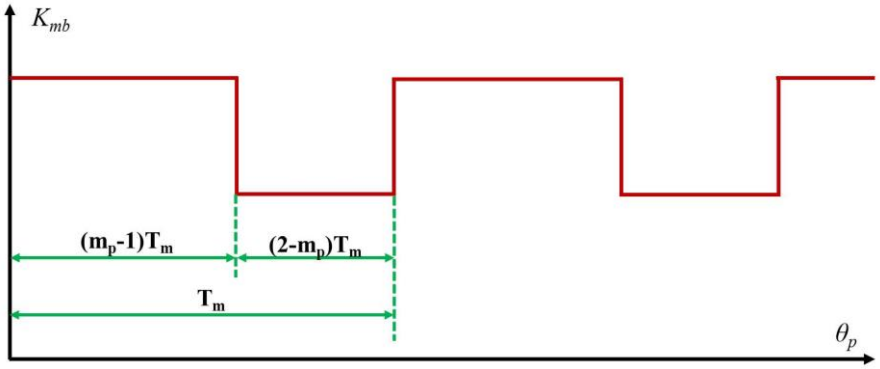

Figure 4.3 Gear mesh stiffness with single and double contact zones

Once there is input load, the load will introduce displacements in all the directions. The pinion centre will change from position O_p to position O_p' and the gear centre will change from position O_g to position O_g', as shown in Fig. 4.2. In the reference coordinate, the operating position for pinion centre O_p' is,

$$\overrightarrow{d_p} = (0)\vec{x} + (y_p)\vec{y}, \tag{4.15}$$

and the operating position for gear centre O_g' is,

$$\overrightarrow{d_g} = (r_p + r_g)\vec{x} + \left((r_p + r_g)\tan\alpha + y_g\right)\vec{y}. \tag{4.16}$$

The operating gear centre distance will become,

$$d' = \sqrt{\left[(r_p + r_g)\right]^2 + \left[(r_p + r_g)\tan\alpha + y_g - y_p\right]^2}\ . \tag{4.17}$$

The operating gear pressure angle will become,

$$\alpha' = \cos^{-1}\frac{r_p + r_g}{d'} \quad . \tag{4.18}$$

The operating gear contact ratio will become,

$$m_p' = \frac{\sqrt{r_{ap}^2 - r_p^2} + \sqrt{r_{ag}^2 - r_g^2} - d'\sin\alpha'}{\pi \cdot m \cdot \cos\alpha'} . \tag{4.19}$$

From equation (4.18) and (4.19), it was found that the gear centre distance variation has great impact on gear pressure angle and gear contact ratio. Also, as the property of the gear mesh stiffness was also dependent on the gear contact ratio, it could be concluded that the gear centre distance variation could also have great impact on the gear mesh stiffness. Because the gear mesh stiffness is important in analysing the dynamic responses of the spur gear set, the gear centre distance variation should also be considered when analysing the gear dynamic responses. The following section studies the gear mesh stiffness with different gear centre distances using the FEA method.

4.3 Effect of gear centre distance variation on gear mesh stiffness using FEA methods

As mentioned in the last section, the gear mesh stiffness will be affected by the gear centre distance in both magnitude and phase. In this section, FEA models were developed to study the effect of gear centre distance variation on gear mesh stiffness. The gear parameters used in this chapter was shown in table 4.1. There are two types of gear sets.

Table 4.1 Gear parameters

	Gear type-1	Gear type-2
Number of teeth, pinion, Z_p	23	21
Number of teeth, gear, Z_g	23	39
Module, m_n	6 mm	10 mm
Designed pressure angle, α	20º	20º
Base radius, pinion, r_p	129.7 mm	197 mm
Base radius, gear, r_g	129.7 mm	366 mm
Designed gear centre distance, d	138 mm	300 mm
Designed gear contact ratio, ctr	1.59	1.6388
Base pitch, p_b	17.7 mm	29.5 mm
Young's modulus, E	69 GPa	210 GPa
Mass, pinion, m_p	0.7 kg	3.4 kg
Mass, gear, m_g	0.7 kg	11.7 kg
Moment of inertia, I_p	0.0025 kgm^2	0.0247 kgm^2
Moment of inertia, I_g	0.0025 kgm^2	0.2935 kgm^2

The equations used for generating the profiles of the gear teeth can be found in chapter 3 (equations (3.5), (3.6), (3.7)). Using the strategy mentioned in Fig. 3.10, one FEA spur gear model with one pinion and one gear can be obtained. Then, the whole gear model can be moved intentionally in the vertical direction with a distance increment of Δd, as shown in Fig. 4.4. This resulted in a new gear centre distance $d+\Delta d$. However, the distance increment Δd will also introduce a backlash between pinion involute profile and gear involute profile (Townsend, 1991),

$$\Delta B=2\cdot\Delta d\cdot\tan\alpha, \tag{4.20}$$

where ΔB is the total backlash introduced by the distance increment and each side will have a backlash of $\Delta d\cdot\tan\alpha$. As a result, an imposed displacements of $\Delta d\cdot\tan\alpha/r_{pp}$ can be implied on the pinion gear hub to rotate to eliminate the backlash caused by the distance increment. r_{pp} is the pinion pitch radius. After rotating, the adaptive re-mesh as mentioned in Fig. 3.12 can be used at each contact position. The weak spring connected with the pinion hub node method as mentioned in Fig. 3.14 is also needed followed by the element *birth&death* command to disable the weak spring after the pinion moves just in contact with the gear profile.

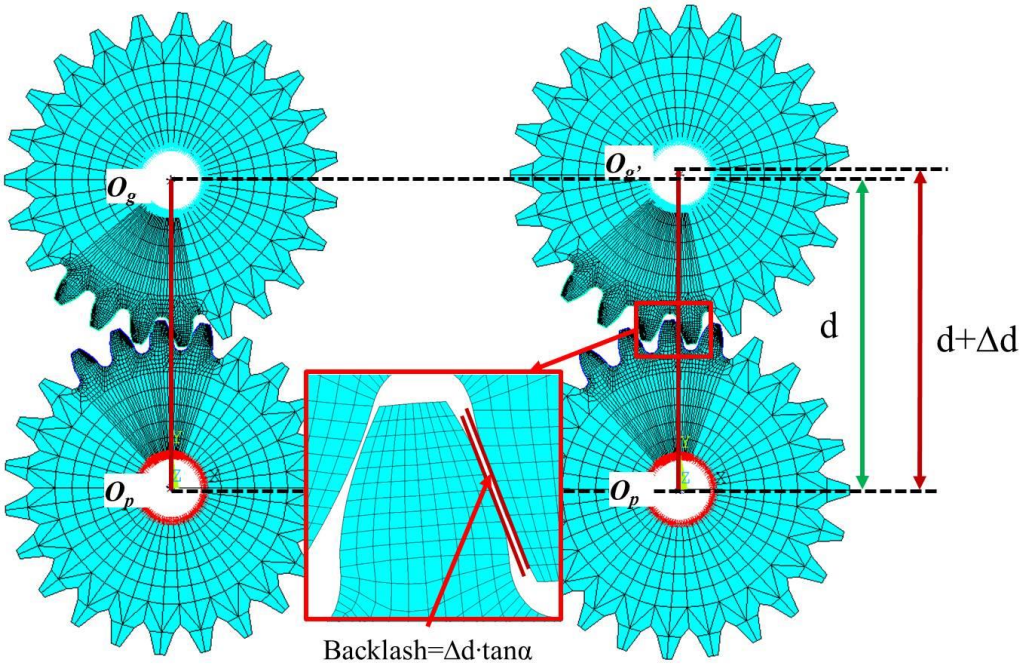

Figure 4.4 FEA gear model with distance increment

There are two kinds of backlash mentioned in the above model. The first one is the backlash caused by the distance increase and it is equal to $\Delta d \cdot tan\alpha / r_{pp}$. For example, if a $\Delta d = 0.5mm$ was moved, this will need a gear rotation of 1.7e−3 rad to eliminate this backlash. However, the rotation to eliminate the backlash caused by the weak spring to prevent rigid-body motion is around 9e−7 rad, which is 5.3e−4 times smaller than the first one.

For gear type 1, the initial contact point was selected at the pitch mesh position and the pinion gear hub was constrained in the radial direction while the gear hub was constrained in both tangential and radial directions at each mesh point. An input load T_p=100Nm was applied to the pinion hub and different distance increments can be applied to the gear. In this research, several different distance increments were considered, Δd=0mm, Δd=0.1mm, Δd=0.5mm and Δd=1mm. The corresponding shaft phase-variant gear mesh stiffness is shown in Fig. 4.5.

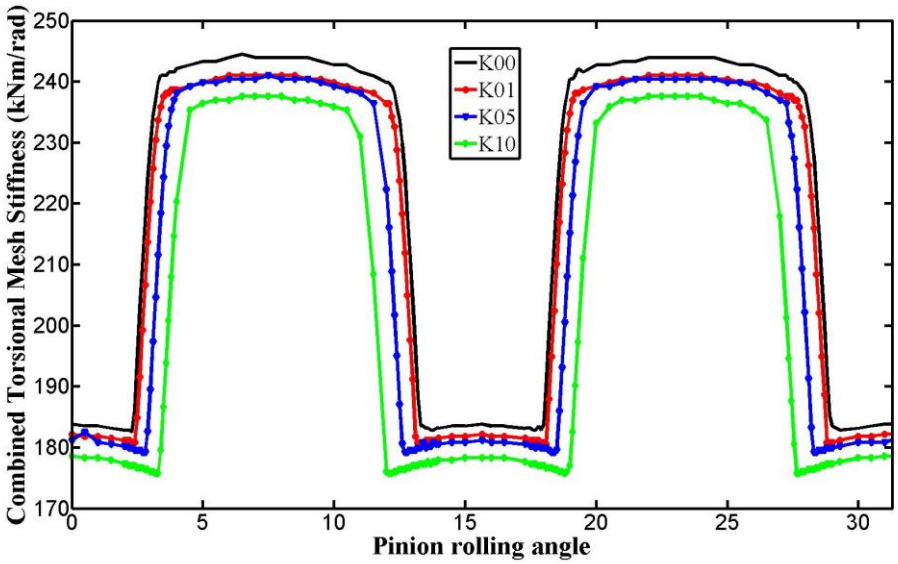

Figure 4.5 Combined torsional mesh stiffness for gear type 1

Fig. 4.5 describes the combined shaft phase-variant gear mesh stiffness at each meshing position. *K00* stands for the gear mesh stiffness when the gear centre distance increment Δd is 0mm, which is the standard design value. *K01* stands for the gear mesh stiffness when the gear centre distance increment Δd is 0.1mm. *K05* is the gear mesh stiffness when the gear centre distance increment Δd is 0.5mm. *K10* stands for the gear mesh stiffness when the gear centre distance increment Δd is 1mm. It was found that the overall gear mesh stiffness amplitude decreases due to the increase of the gear centre distance for both single contact zone and double contact zones. Traditionally, only the *K00* curve will be interpolated into the gear dynamic equation when the gear dynamic response was studied, no matter what the gear centre distance variation was. In the other word, the gear mesh stiffness $k_m(\theta_p)$ was assumed to be only the function of the pinion rolling angle. However, if the gear centre distance increment varies from 0mm to 1mm during the operation, the mesh stiffness will have to vary between *K00* and *K10* accordingly, which will result in a dramatically different dynamic performance. Fig. 4.6 showed the comparison of the mesh stiffness under different gear centre distances and the relative mesh stiffness.

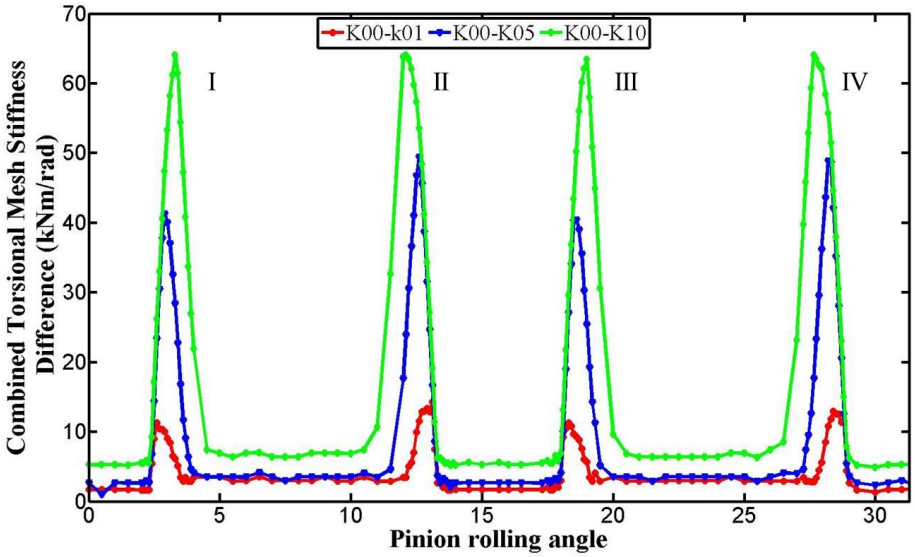

Figure 4.6 Gear mesh stiffness comparison for gear type 1

In Fig. 4.6, a much clearer view of how the gear mesh stiffness changes between the different centre distances can be observed, especially in the handover region. The red line shows the gear mesh stiffness difference between *K00* and *K01*. The blue line shows the gear mesh stiffness difference between *K00* and *K05*. The green line shows the gear mesh stiffness difference between *K00* and *K10*. During the two gear mesh periods, there are four cone shaped areas observed in the picture. This is because the gear mesh stiffness can be divided into single and double contact zones, the proportions of the two zones being determined by the gear contact ratio. When the gear centre distance changed, the gear contact ratio will also change accordingly. That is, while *K00* keeps the designed proportions of the two zones, the proportions of *K01*, *K05* and *K10* will be changed. In the other words, with the rolling of the shaft, when *K00* enters the double contact zone, *K10* still stays in the single contact zone. This delay causes the cone shaped difference in Fig. 4.6. There are four cone shaped areas, designated domain I, domain II, domain III and domain IV. These areas are referred to as the gear recess and gear approach areas separately. Theoretically, domain I and domain III are the same in their shape and occur in the tooth approach region. Domains II and IV are also the same in shape and occur in the tooth recess area.

Beside the cone shaped area in the handover region observed from Fig. 4.6, several straight line sections with almost constant value exist in the mesh stiffness change curves. For instance, the constant different value for K00-K05 is around 5kNm/rad and the constant different value for K00-K10 is 7kNm/rad. This constant change was caused by the change of the force position on the gear teeth. Analytically, the gear tooth can be modelled as a beam (Chen & Shao, 2011) and it is assumed that one end is fully fixed and a concentrated force was applied at a position with a distance *a* away from the end. The deflection of the beam can be calculated as,

$$\delta_{max} = \frac{Fa^2}{6EI}(3l - a), \tag{4.21}$$

and the stiffness of the beam can be calculated as,

$$K = \frac{F}{\delta_{max}} = \frac{6EI}{a^2(3l - a)}. \tag{4.22}$$

If there is a distance increment, the concentrated force will deviate a distance of Δa from its initial position and the new position will be $a+\Delta a$. Mathematically, the differential equation was commonly used to determine how the function will change with respect to a variable in the equation. As a result, if the equation can be differentiated with respect to position *a*, it becomes,

$$\frac{dK}{da} = -\frac{18EI(2l - a)}{a^3(3l - a)^2}. \tag{4.23}$$

As *a* changes from 0 to *l*, *dK/da* will always be positive, which means the stiffness *K* will always decrease with the increment of *a* and this change will always be a constant value. However, this constant different value is relatively small compared to the stiffness change due to the gear contact ratio, which means the dominate change due to the gear centre distance variation is still the cone shaped areas. The change of gear contact ratio can also be observed from the gear load sharing ratio, as shown in Fig. 4.7.

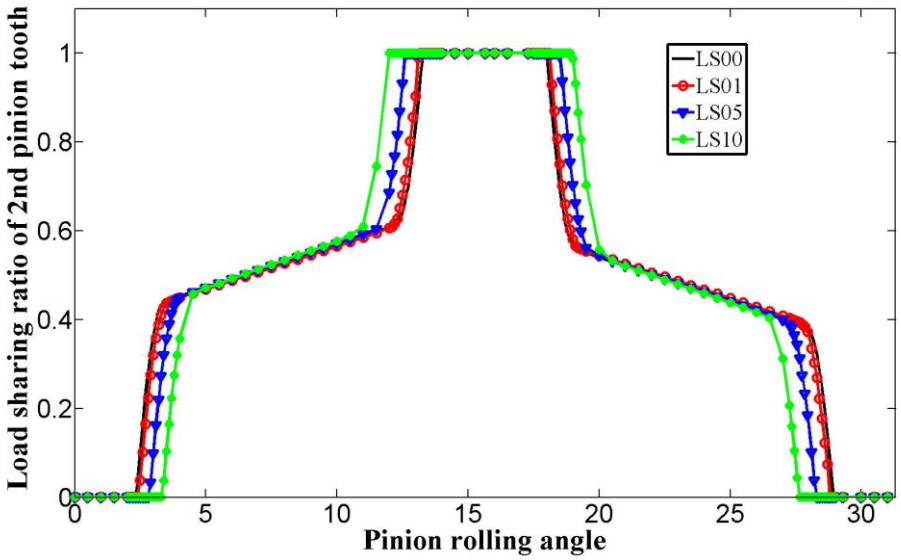

Figure 4.7 Load share ratio of 2nd pinion tooth comparison between different distance increments

Fig.4.7 illustrates the load share ratio comparison of 2nd pinion tooth for different distance increments. *LS00* stands for the gear load sharing when the gear centre distance increment is 0mm. *LS01* stands for the gear load sharing when the gear centre distance increment is 0.1mm, *LS05* stands for the gear centre distance increment of 0.5mm and *LS10* stands for the gear centre distance increment of 1mm. The figure provides further evidence for the change of the gear contact ratio. When the load sharing ratio is equal to 1, that means the gear is in the single contact zone. The length of the single contact zone is $(2-m_p)T_m$, as shown in Fig. 4.3. It was found that with the increment of the gear centre distance, the length of gear single contact ratio increases correspondingly. As a result, the gear contact ratio will decrease with the increment of the gear centre distance. The critical points located at the edge of the single contact zone for various gear centre distances can also be obtained from Fig 4.7. These points include both the approach points and the recess points, which are counted as the rolling angle moves away from the pitch point (defined as 0º). The results were shown in table 4.2.

Table 4.2 Single zone edge point under different distance increment, gear type 1

	Recess Position	Approach Position	Duration
Δd=0mm	13.2º	18.1º	4.9º
Δd=0.1mm	13.1º	18.2º	5.1º
Δd=0.5mm	12.5º	18.6º	6.1º
Δd=1mm	12º	19.1º	7.1º

The German practice in calculating tooth strength has developed into taking the tangency point of a 30º angle as the critical stress point on the root fillet (Smith, 2003). To use finite element methods to ascertain the changes in the teeth stiffness or transmission error with the existence of a tooth root crack, the all-quad element meshing strategy is no longer possible due to the singularity near the crack front. Instead, triangular elements with their mid-side nodes located at ¼ of their adjacent edges from the crack tip will be used (Wang, 2003), as shown in Fig. 3.15. The LEFM (linear elastic fracture mechanics) assumption was used in this research. With the presence of the crack, the centre distance of the FEA gear model can also be changed with various distance values as shown in Fig. 4.8. Three different gear centre distance increment values were chosen and they were $\Delta d=0mm$, $\Delta d=0.5mm$ and $\Delta d=1mm$.

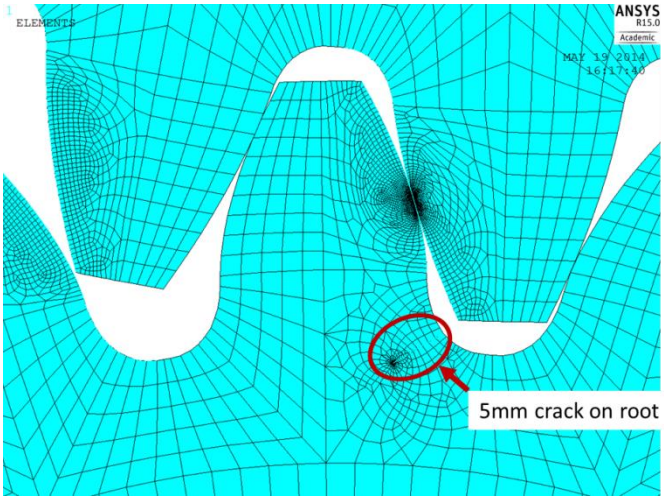

Figure 4.8 Gear crack in the FEA model

The corresponding gear mesh stiffness variation can be found in Fig. 4.9.

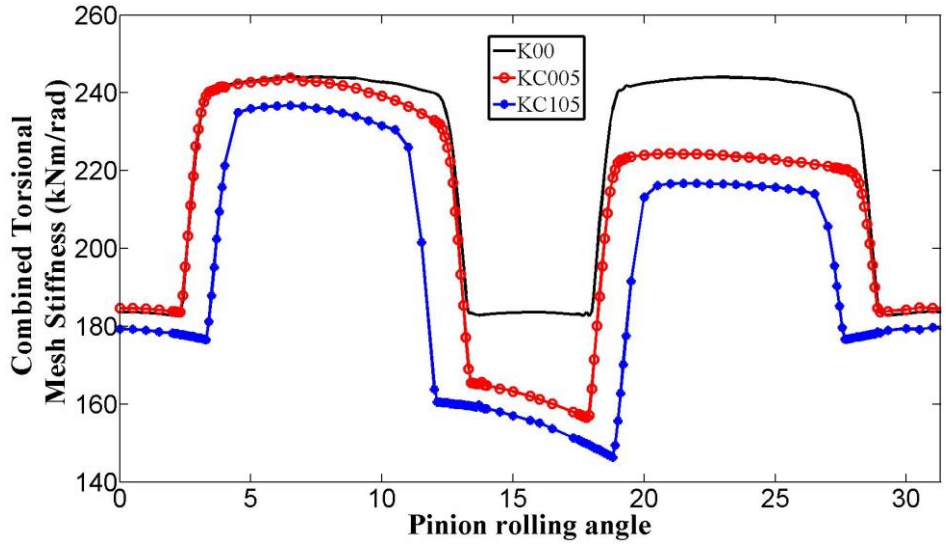

Figure 4.9 Combined torsional mesh stiffness comparison with different centre distance increment and a 5mm tooth root crack

K00 is the gear mesh stiffness when the gear centre distance increment is 0mm and there is no crack on the gear tooth. *KC005* is the gear mesh stiffness when the gear centre distance increment is 0mm and there is a 5mm crack on the gear tooth. *KC105* is the gear mesh stiffness when the gear centre distance increment is 1mm and there is a 5mm crack on the gear tooth. Compared to the healthy gear (*K00*), the gear mesh stiffness decreased considerably due to the crack fault on the tooth. However, due to the increment of the gear centre distance, the changes of the amplitude of the mesh stiffness with gear crack are significantly different. As shown in Fig. 4.9, the amplitude of *KC105* reduced the most due to the Δd=1mm centre distance increment.

The FEA mesh stiffness curve discussed here is just one case from gear type−1, as shown in table 4.1. However, this study used the APDL method to generate the gear profiles and different gear design parameters can be used to analyse the effect of gear centre distance change on the gear mesh stiffness for a range of different gear design parameters. For example, the gear type−2 shown in table 4.1 was also studied. The gear centre distance increments Δd=0mm, Δd=0.5mm and Δd=1mm were used. The torsional mesh stiffnesses under different gear centre distance increments are shown in Fig. 4.10. The load sharing ratios under different gear centre distance increments are shown in Fig.4.11.

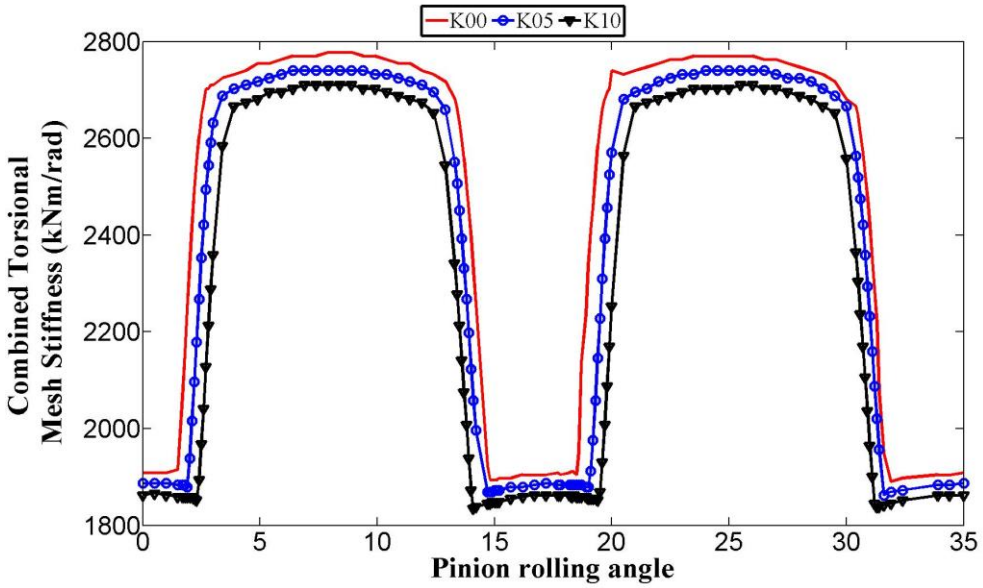

Figure 4.10 Combined torsional mesh stiffness for gear type 2

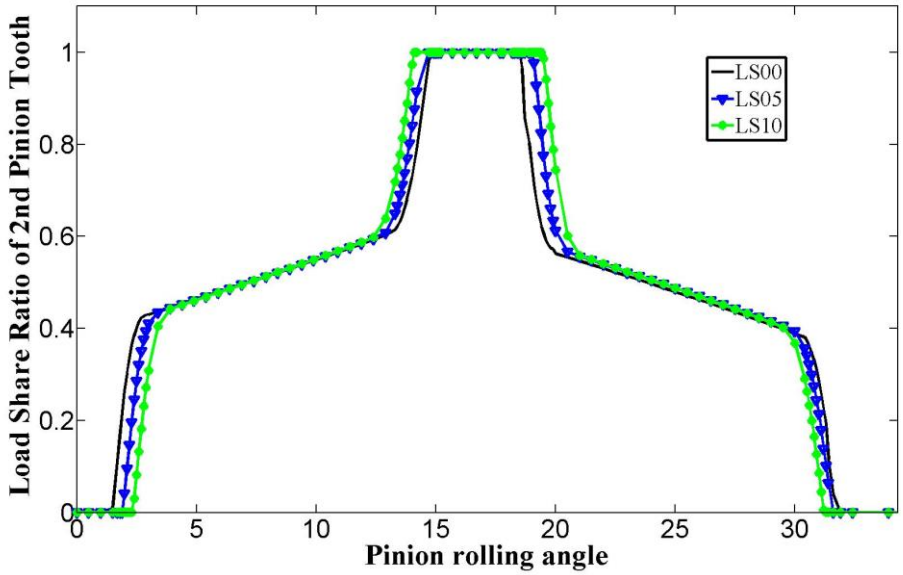

Figure 4.11 Load share ratio of 2nd pinion tooth comparison between different distance increments for gear type 2

The critical points located at the edge of the single contact zone for various gear centre distances can be summarized in table 4.3, where all points were counted as the rolling angle moves away from the pitch point.

Table 4.3 Single zone edge point under different distance increment, gear type 2

	Recess Position	Approach Position	Duration
Δd=0mm	14.7º	18.6º	3.9º
Δd=0.5mm	14.5º	19.1º	4.6º
Δd=1mm	14º	19.5º	5.5º

The resulting gear mesh stiffnesses with 5mm tooth crack under different gear centre distance increments are shown in Fig. 4.12.

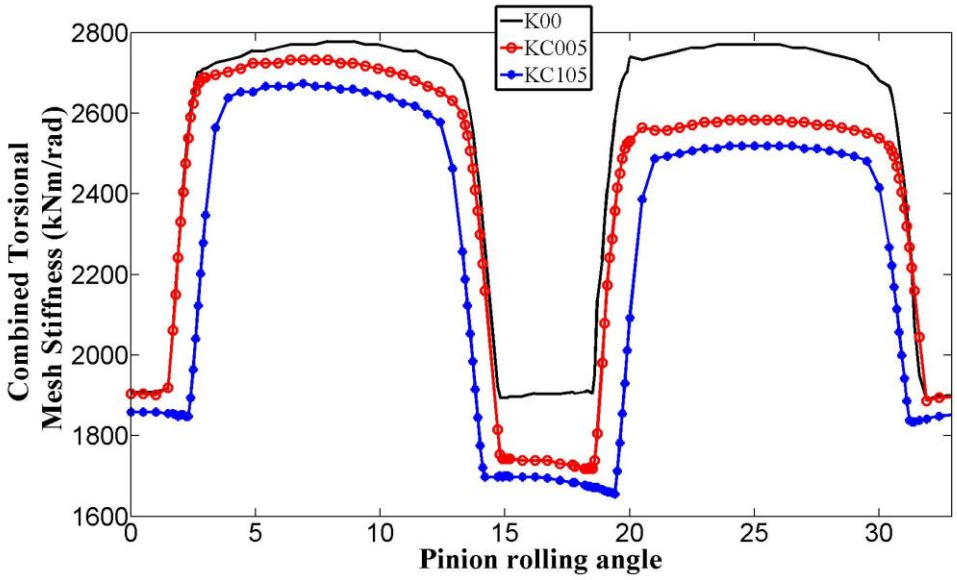

Figure 4.12 Combined torsional mesh stiffness comparison with different distance increments and a 5mm tooth root crack for gear type 2

Two types of gear have been analysed and it was found that the increase of gear centre distance could reduce the gear contact ratio and further change the gear mesh stiffness. During this process, the length of single contact zone will increase while the length of double contact zone will decrease. By comparing the mesh stiffness under different gear centre distances, unique cone shaped areas can be observed in the tooth recess region and approach region. The effect of the gear tooth crack under different gear centre distances could also be studied in the model. The reduction of mesh stiffness due to the increase of gear centre distance can still be observed and in addition, the gear tooth crack can further reduce the gear mesh stiffness. In a words, the gear centre distance change has a great impact on gear mesh

stiffness and subsequently, the gear dynamic response will be affected by this distance variation.

4.4 Analysis of the gear system dynamic response

To solve the matrix dynamic equations of the gear pair, a procedure based on the direct time-integration Newmark method was developed in this study and the flow chart of the gear dynamic simulation scheme can be found in Fig. 4.13. As shown in the flow chart, the parameters for the Newmark method were initialized at the beginning, and the gear centre distance **d(t)** was set to be equal to the designed gear centre distance as there is no input load applied to the system. Based on the initial values of pinion rotation angle and gear centre distance, the stiffness **K(θ, d(t))** can be evaluated accordingly and then the stiffness matrix for the Newmark method can be assembled. The gear system responses can be calculated for the time step **t**+Δ**t** and subsequently, the new gear centre distance **d(t**+Δ**t)** can be calculated using equation (4). However, as the gear centre distance can have great impact on the gear dynamic response, an inspection at each time step should be made to examine whether the gear centre distance has converged or not. Initially, the iteration step **m** is set to be 0 and b1(**m**) is set to be the gear centre distance at time step **t** and b2(**m**) is set to be the gear centre distance at time step **t**+Δ**t**. The |b1(**m**) −b2(**m**)| convergence criterion was used in this study and the value of ***eps*** was chosen to be 0.1μm. If the convergence criterion result is smaller than ***eps***, the procedure will then continue for the next time step. If not, the procedure will pass the value of b2(m) to b1(m) and then re-evaluate the gear mesh stiffness based on b1(m). As a result, the gear system responses need to be re-calculated for time step **t**+Δ**t** and the gear centre distance for time step **t**+Δ**t** will be re-calculated as well. If the result satisfies the convergence condition, that is, it is less than ***eps***, the procedure will keep the gear responses and if not, the calculation will be forced into the iteration again until it satisfies the convergence criteria. A Matlab program in *appendix C* has been developed to obtain the dynamic responses from the flexibly support gear using the above procedure.

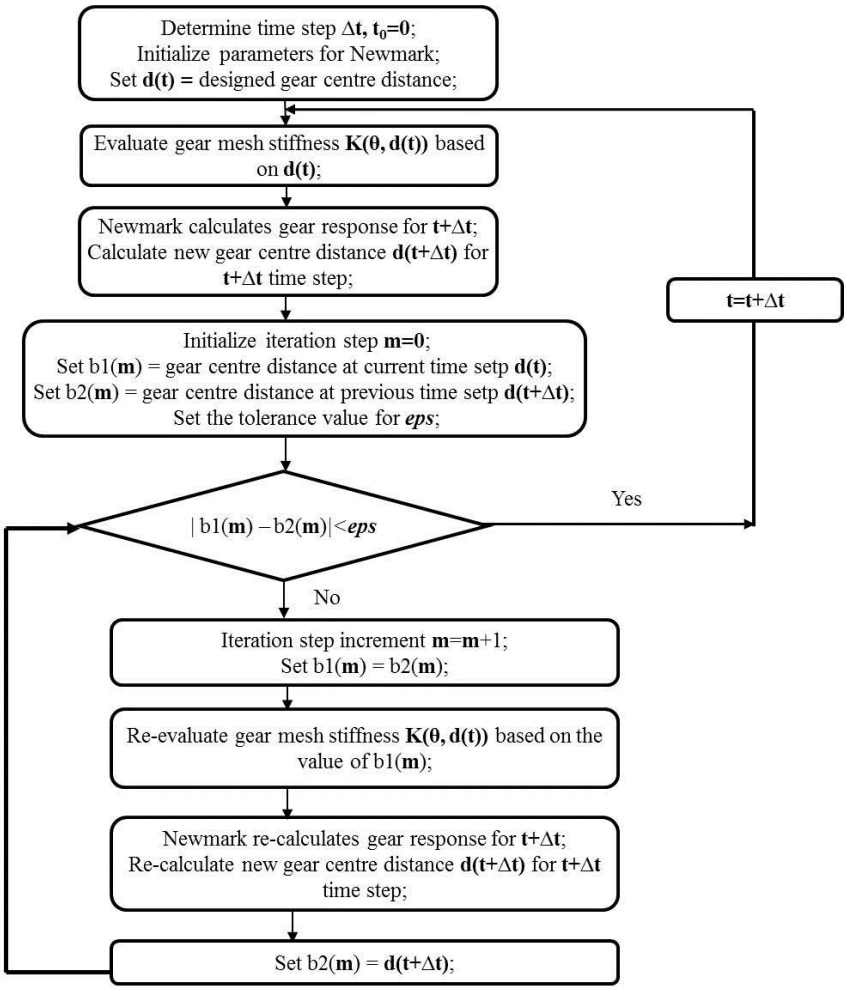

Figure 4.13 Flowchart of iterative numerical gear dynamic time integration

There are two models used in this study. The spur gear dynamic model with constant gear centre distance is called model I and this model has been widely used by previous studies (Jia & Howard, 2006; Özgüven & Houser, 1988). The spur gear dynamic model with varying gear centre distance is called model II and this model is newly proposed in this study. Initially, there is no mounting error or manufacturing error considered and only model I and model II have been compared. The gear set was assembled at the designed gear centre distance. The input pinion angular velocity, output gear vertical motion velocity and gear transmission error have been selected to compare the dynamic response from the two models. Two bearing situations have been studied, which are rigid bearing and flexible bearing. When the gear system is subject to a rigid support, the gear centre distance is supposed to be stable at the designed value. The dynamic responses of the two models are supposed to be

identical. When the gear system is subject to a flexible support, the gear centre distance can vary in a large span and correspondingly, the dynamic responses of model I and model II are supposed to be significantly different from each other. The effects of a gear root crack and fluctuating external load on gear centre distance variation have also been investigated.

4.4.1 Rigid bearing influence on gear dynamic response

For a rigid bearing support, the value of 1×10^{10} N/m has been used. The comparison of the gear centre distance, gear pressure angle and gear contact ratio between model I and model II is shown in Fig. 4.14.

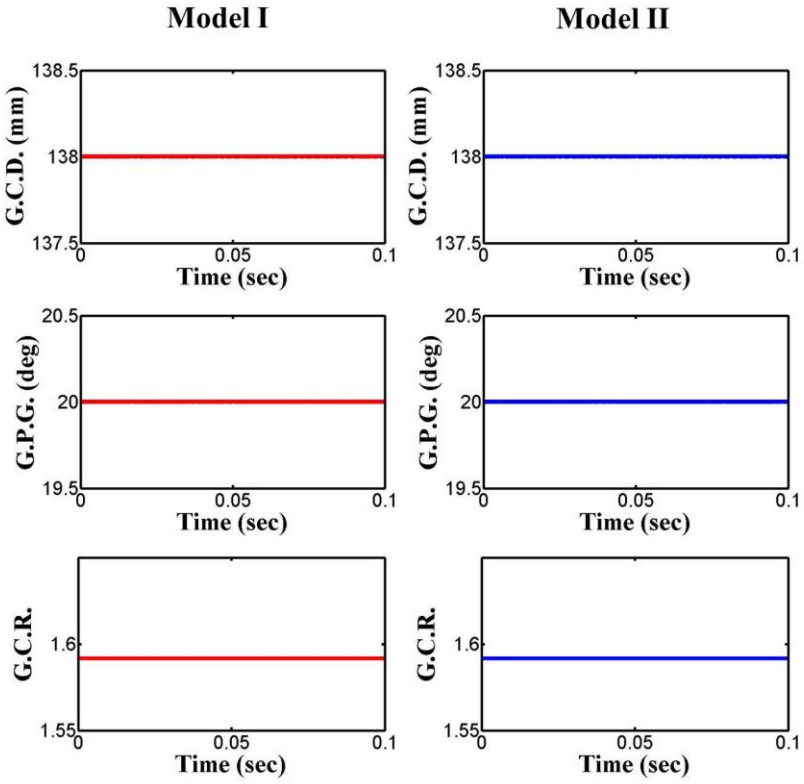

Figure 4.14 Gear centre distance (G.C.D.), gear pressure angle (G.P.G), and gear contact ratio (G.C.R.) comparison between the model I and model II when the bearing stiffness is 1×10^{10}N/m, gear type 1

Traditionally, the gear centre distance, gear pressure angle and gear contact ratio were considered as constant values during the operation, which were the designed value. When the gear system is subject to the rigid support (1×10^{10}N/m), the operating gear centre distance

will be constant and kept the same value with the designed value. As the variation of the pressure angle and contact ratio were induced by the gear centre distance, their values will also keep the same value with the designed values, as shown in Fig. 4.14.

As analysed before, the gear mesh stiffness was found to not only depend on the shaft rolling angle, but also on the gear centre distance. As shown in Fig. 4.15, curve (a) stands for the gear mesh stiffness variation from model I and curve (b) stands for the gear mesh stiffness variation from model II. As the support is rigid, the gear centre distance will keep the same value with the designed value, which means there is little impact from the variation of the gear centre distance during the operation. This will result in two identical stiffness curves from the two models, which can verify the result from the new model.

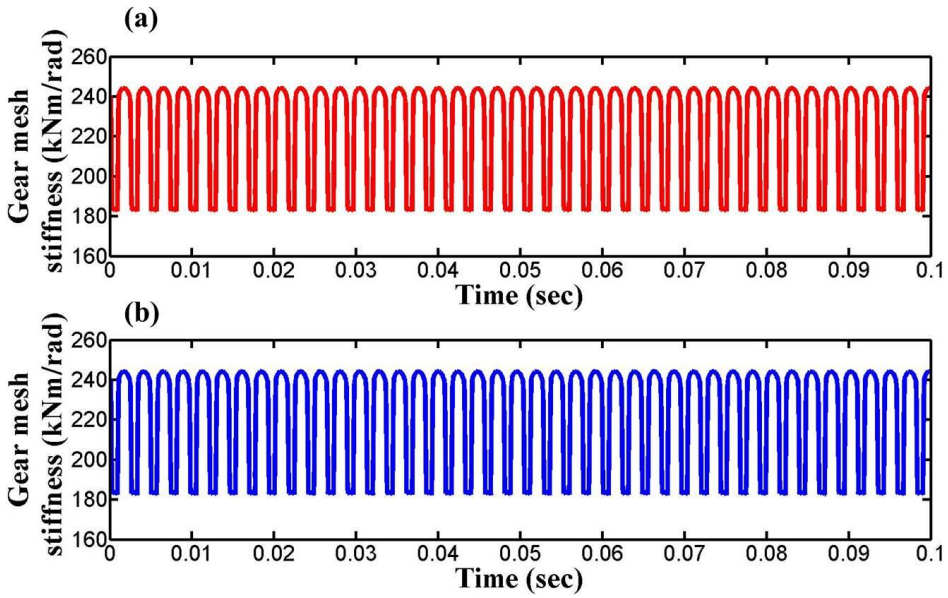

Figure 4.15 Gear mesh stiffness with rigid support (gear type 1),
(a) model I, (b) model II

Fig. 4.16 illustrates the input pinion angular velocity ($\dot{\theta}_p$) response with the rigid bearing support from both the previous model and the new model. After the initial transient start-up phase, the gear system reached steady-state conditions and the pinion angular velocities stabilized at around 114 rad/s. The results of the original time step data have been resampling into equi-spaced phase form. Exactly one revolution of resampled data was used

to compare between the two models. As shown in the figure, two identical velocity responses were found in this situation.

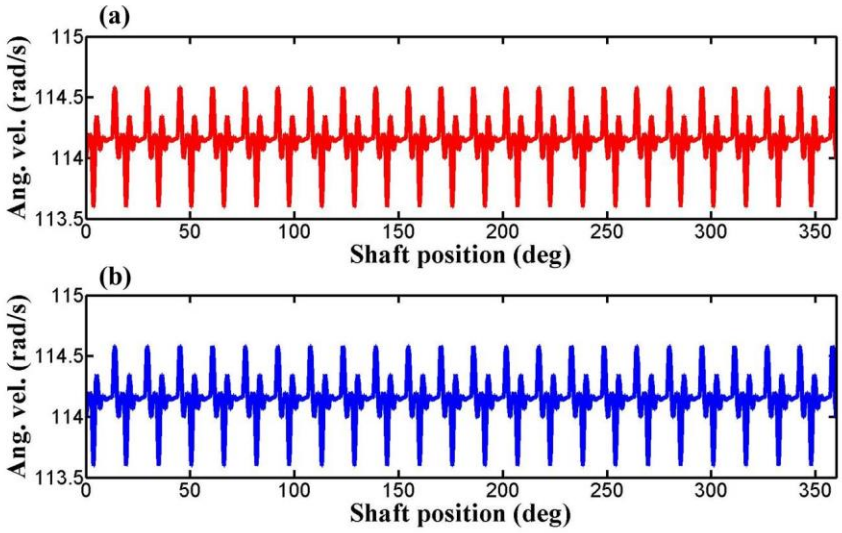

Figure 4.16 Input Pinion angular velocity with rigid bearing support (gear type 1), (a) model I, (b) model II

Fig. 4.17 illustrates the transmission error (T.E.) response ($\theta_p - \theta_g$) with a rigid bearing support from both the previous model and the new model. The results have also been resampled into equi-space phase form and the same transmission responses were observed in the two figures from the two models with the rigid bearing support.

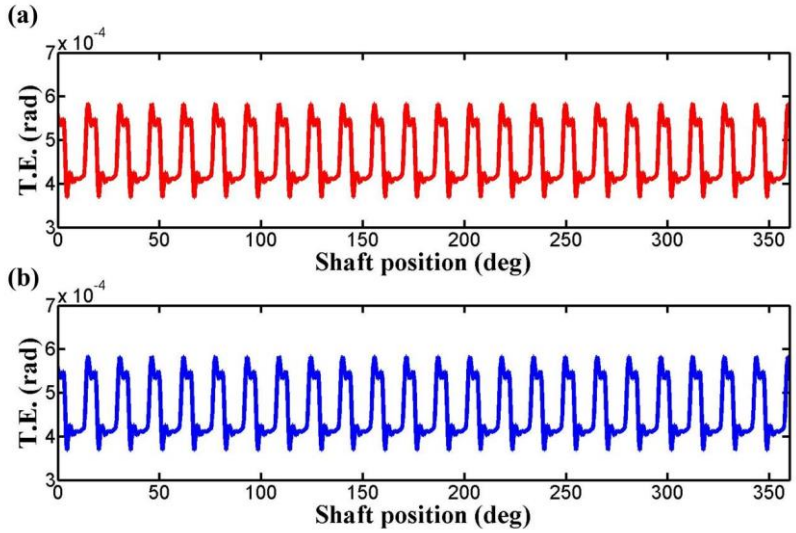

Figure 4.17 Transmission error (T.E.) with rigid support (gear type 1), (a) model I, (b) model II,

From Fig. 4.14 to Fig. 4.17, it was found that when the support is rigid, the same responses were observed between the two models. This is because the gear centre distance keeps the same value with the designed value and it has limited impact on the pressure angle, contact ratio and gear mesh stiffness in this situation. All these results from the previous model can verify the results from the new model.

4.4.2 Flexible bearing influence on gear dynamic response

However, when the bearing stiffness was reduced to be 1×10^6 N/m, the gear centre distance will vary off its designed value due to the decrease of the elasticity of the bearing. From the MATLAB program, the gearbox system was simulated over several seconds, after which the initial transient start-up phase has decayed away and the steady-state conditions were obtained. The gear mesh stiffness curve due to a 5 mm crack was then incorporated into the differential equations of motions. The presence of the crack can introduce some transient disturbance into the gear system affecting the gear centre distance, even though the gear system is still in the steady-state vibration stage. Fig. 4.18 illustrates the variation of gear centre distance change, gear pressure angle and gear contact ratio with the presence of the gear tooth root crack during the steady-state stage.

From Fig. 4.18, it is apparent that all the gear design parameters vary during the simulation. The gear centre distance change was calculated as the instantaneous gear centre distance minus the designed gear centre distance ($d\,(t) - d$). During this stage, the gear centre distance stabilized at the new value, which was around 1.07mm away from its designed value. The gear pressure angle stabilized at around 21.18º, which was 1.18º away from its designed value. The gear contact ratio stabilized at around 1.43, which was 0.17 away from its designed value. The presence of the crack can be seen in all the results at approximately t=0.049s. It was noted that the gear crack could change the gear centre distance from its newly stable value (139.07mm), but after the crack event, the gear centre distance again went back to its stable value. The gear pressure angle and gear contact ratio were also affected by the presence of the crack, but similarly, they both went back to their stable response values after the crack event.

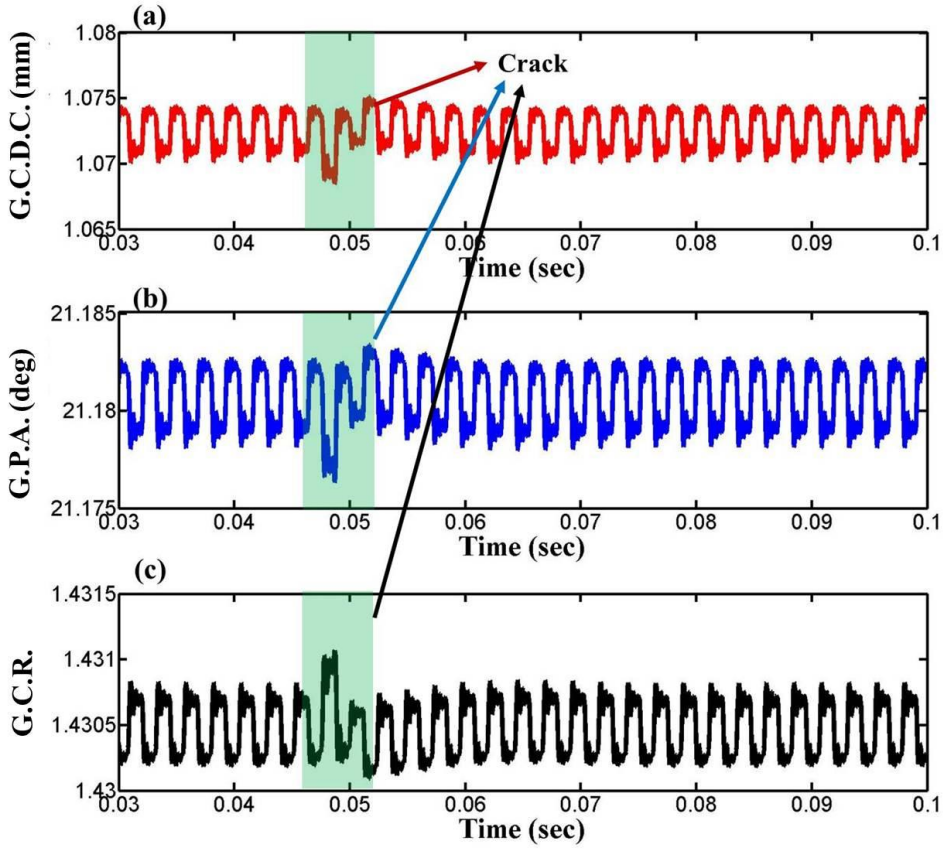

Figure 4.18 The effect of the gear crack on gear design parameters, (a) gear centre distance change (G.C.D.C.), (b) gear pressure angle (G.P.A.), (c) gear contact ratio (G.C.R.).

The iteration process due to the crack can also be obtained and the resultant gear mesh stiffness behaviour is shown in Fig. 4.19. In Fig. 4.19(a), the red line shows the value of $|b1(m) - b2(m)|$ before the iteration and the black line illustrates the value of $|b1(m) - b2(m)|$ after the iteration.

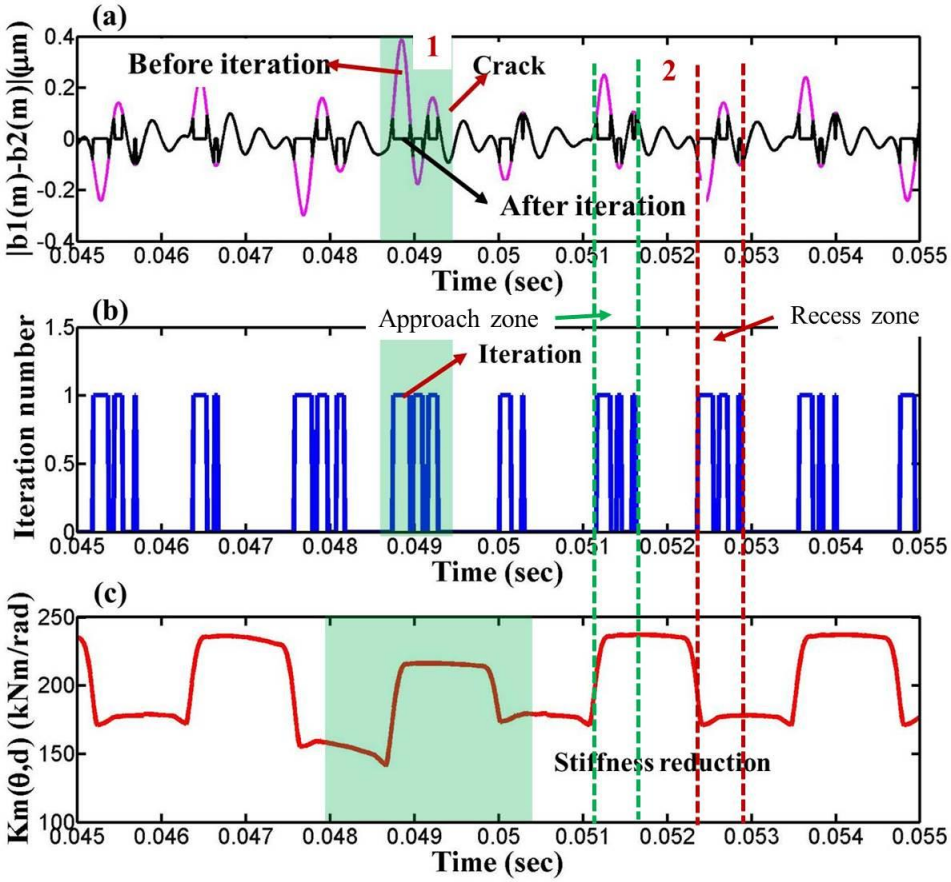

Figure 4.19 The effect of gear crack on iteration, (a) | *b1(m) −b2(m)*| before and after the iteration, (b) iteration number, (c) the resultant gear mesh stiffness $K_m(\theta, d)$.

As shown in Fig. 4.19, the iteration process happened in the gear handover regions (approach zone and recess zone) where the value of |b1*(m)* −b2*(m)*| in this region was 0.2μm and it was marked as 2 in the figure. When *t*=0.049s, the crack was in the mesh zone and it can be seen that the presence of the crack caused a larger |b1*(m)* −b2*(m)*| value, which was 0.4μm. This value was marked as 1 in the figure. The iteration occurrence during the simulation for the crack can be observed in Fig. 4.19. The resultant gear mesh stiffness $K_m(\theta, d)$ was shown in Fig.4.19(c) and a comparison between $K_m(\theta, d)$ and $K_m(\theta)$ can be found in Fig. 4.20.

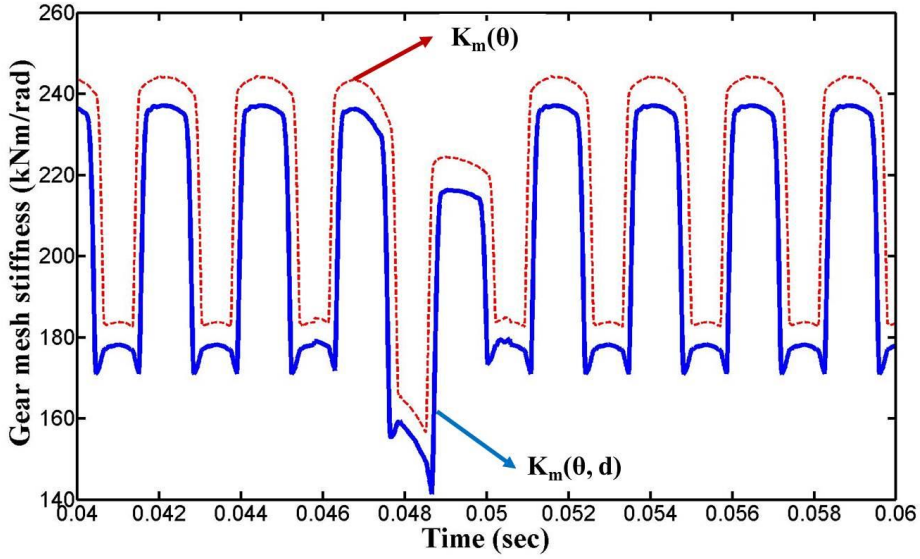

Figure 4.20 Comparison of faulted gear mesh stiffness variation with or without the effect of gear centre distance variation. $K_m(\theta)$ is the mesh stiffness without considering centre distance variation, $K_m(\theta, d)$ is the mesh stiffness with centre distance variation.

Compared with the variation of $K_m(\theta)$ obtained from neglecting centre distance changes, it was found that the reduction of the gear mesh stiffness caused by the crack, $K_m(\theta, d)$, was larger when the centre distance changes were used. This different decrease of the mesh stiffness would result in a different gear dynamic response due to the presence of the gear tooth crack.

4.5 Gear fault diagnostic result analysis

Two models have been used in this study. Model I is the gear system incorporating the stiffness curve $K_m(\theta)$ and Model II is the gear system incorporating the stiffness curve $K_m(\theta, d)$. After the initial transient start-up was observed to have decayed away, the input pinion angular velocity $\dot{\theta}_p$, gear vertical velocity $\dot{y}_g$ as well as the transmission error $\theta_p - \theta_g$ have been obtained to compare the difference of the diagnostic results. The diagnostic algorithms which are commonly used for gearbox vibration analysis were used on the simulation results from the two models. These diagnostic techniques include coherent time synchronous averaging, RMS spectrum, residual signal, narrow band envelope, amplitude modulation, phase modulation and analytic signal plots.

Fig. 4.21 shows the results of the coherent time synchronous averaged signal, where the gear vertical velocity, pinion angular velocity and transmission error are resampled into equispaced phase data and then averaged over several rotations of the shaft. The dynamic motions from model I (without considering the effect of gear centre distance) are shown in the left column and those from model II (including the effect of gear centre distance) are shown in the right column.

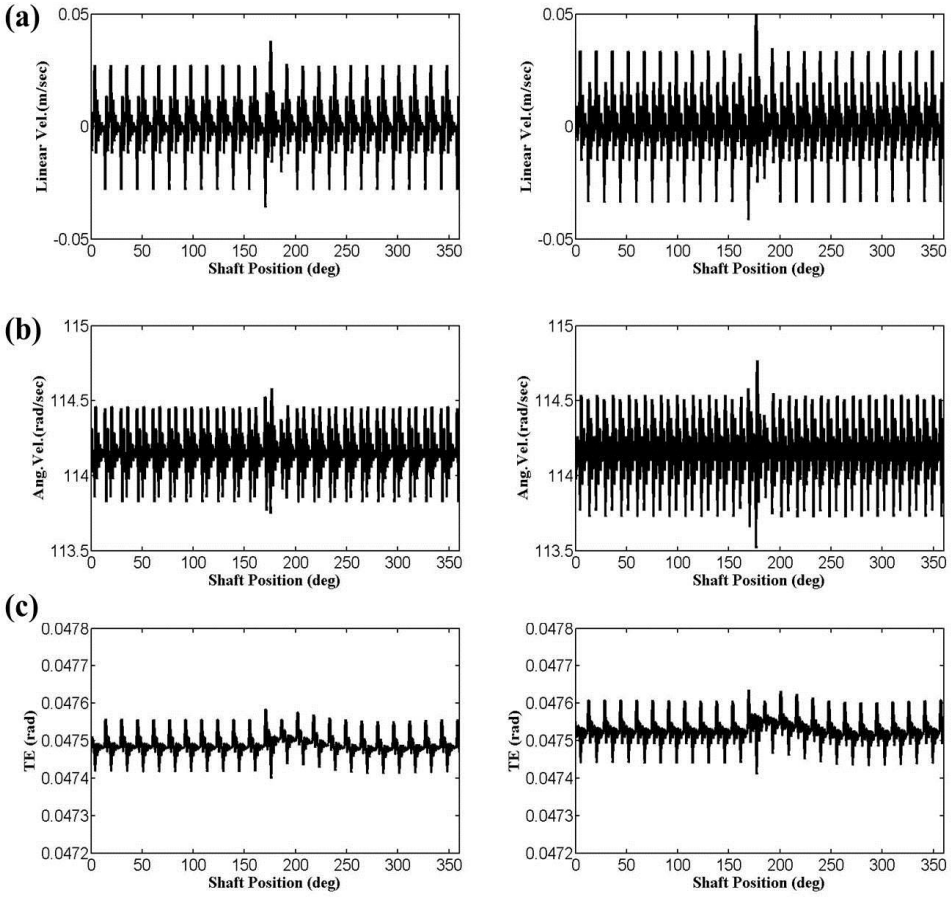

Figure 4.21 Dynamic motion over one complete revolution from model I (left column) and from model II (right column). (a) output gear vertical velocity $\dot{y}_g$; (b) input pinion angular velocity $\dot{\theta}_p$; (c) transmission error $\theta_p - \theta_g$.

As shown in Fig. 4.21, the presence of the crack can be seen in all the results at approximately 170° rotation of the shaft and the inclusion of the gear centre distance effect can be seen to slightly change the simulation results as the crack goes through the mesh. It can be oberved that the inclusion of the centre distance iteration effect increases the magnitude of the dynamic motions, especially in the gear vertical velocity and in the pinion

torsional velocity. A closer look at the simulation results can be found in table 4.4, which provides the mean, standard deviation (STD), skewness, kurtosis and crest factor of the signals.

Table 4.4 Comparison of diagnostic results for models I and II

	Output gear vertical velocity $\dot{y}_g$		Input pinion angular velocity $\dot{\theta}_p$		Transmission error θ_p-θ_g	
	Model I	Model II	Model I	Model II	Model I	Model II
Mean	0	0	114.14	114.14	0.05	0.05
STD	0.0100	0.0127	0.1389	0.1815	2.6e-5	3.2e-05
Skewness	-0.07	0.11	0.04	-0.13	0.31	0.15
Kurtosis	4.56	4.22	3.21	3.11	4.83	4.51
Crest factor	7.39	7.51	5.99	6.88	7.02	7.04

Fig. 4.22 shows the results of the RMS spectra, which are based on the time averaged signals obtained in Fig. 4.21. As the time signal covers exactly one shaft revolution, the RMS spectral results are presented in terms of shaft orders. The dynamic motions from model I (without considering the effect of gear centre distance) are shown in the left column and those from model II (including the effect of gear centre distance) are shown in the right column.

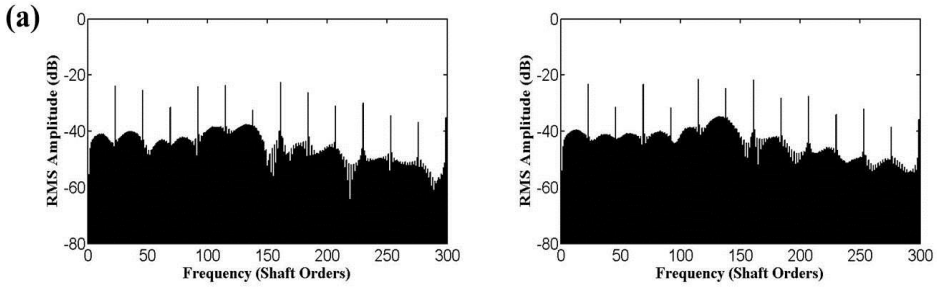

Figure 4.22 RMS spectrum amplitude results from model I (left column) and from model II (right column). (a) output gear vertical velocity $\dot{y}_g$; (b) input pinion angular velocity $\dot{\theta}_p$; (c) transmission error $\theta_p - \theta_g$.

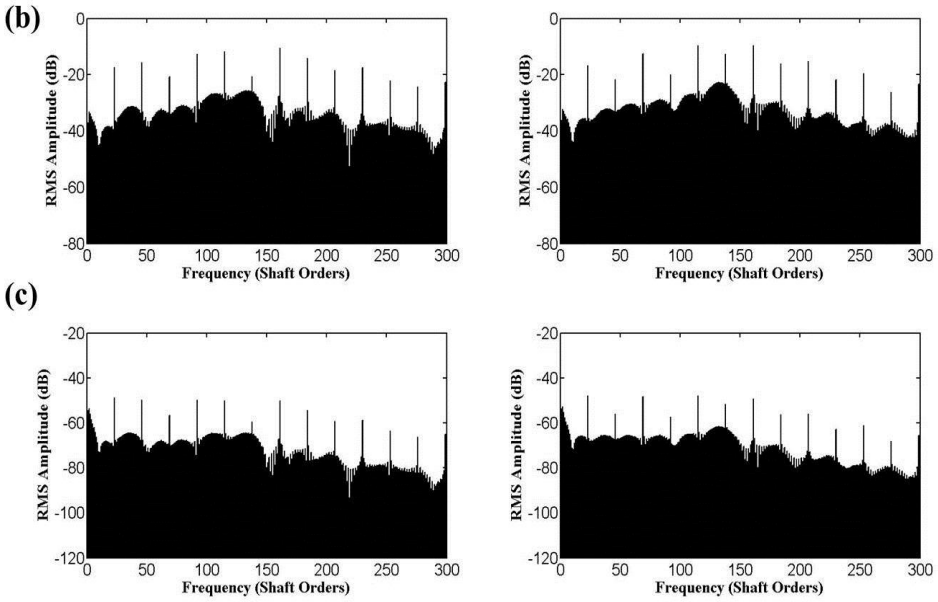

Figure 4.22 (Continued) RMS spectrum amplitude results from model I (left column) and from model II (right column). (a) output gear vertical velocity $\dot{y}_g$; (b) input pinion angular velocity $\dot{\theta}_p$; (c) transmission error $\theta_p - \theta_g$.

As shown in Fig. 4.22, both RMS spectrum plots are dominated by strong gear mesh sidebands and the inclusion of the gear distance effect started to change the frequency content from the second gear mesh frequency, which is 46 shaft orders. It can be oberved that inclusion of this effect reduces the amplitude of the second and fourth mesh harmonic in all three spectrum plots, while increasing the third. For example, in the RMS spectrum of the output gear vertical velocity, the amplitude at the second harmonic from model I was around −25.28 dB and the result from model II was around −31.36 dB. A close look at the gear mesh sideband can be achieved by examining the residual signal, which removes all the gear mesh harmonics and only includes the sideband in the RMS spectra and then uses the inverse Fourier transform to obtain the signal in the time domain, as shown in Fig. 4.23.

Fig. 4.23 shows the results of the residual signal and it can be noted that the presence of the crack can be observed in all three results and the inclusion of the gear centre distance effect changes the residual signal waveform shape significantly. However, it should be noted that the inclusion of this gear centre effect gives a smaller kurtosis value in the output gear residual signal (62.29 *vs* 52.47) and the input pinion residual signal (47.60 *vs* 41.43).

Moreover, the overall magnitude of the transmission error increases slightly and the inclusion of this gear centre effect gives a higher kurtosis value here (5.71 *vs* 6.04).

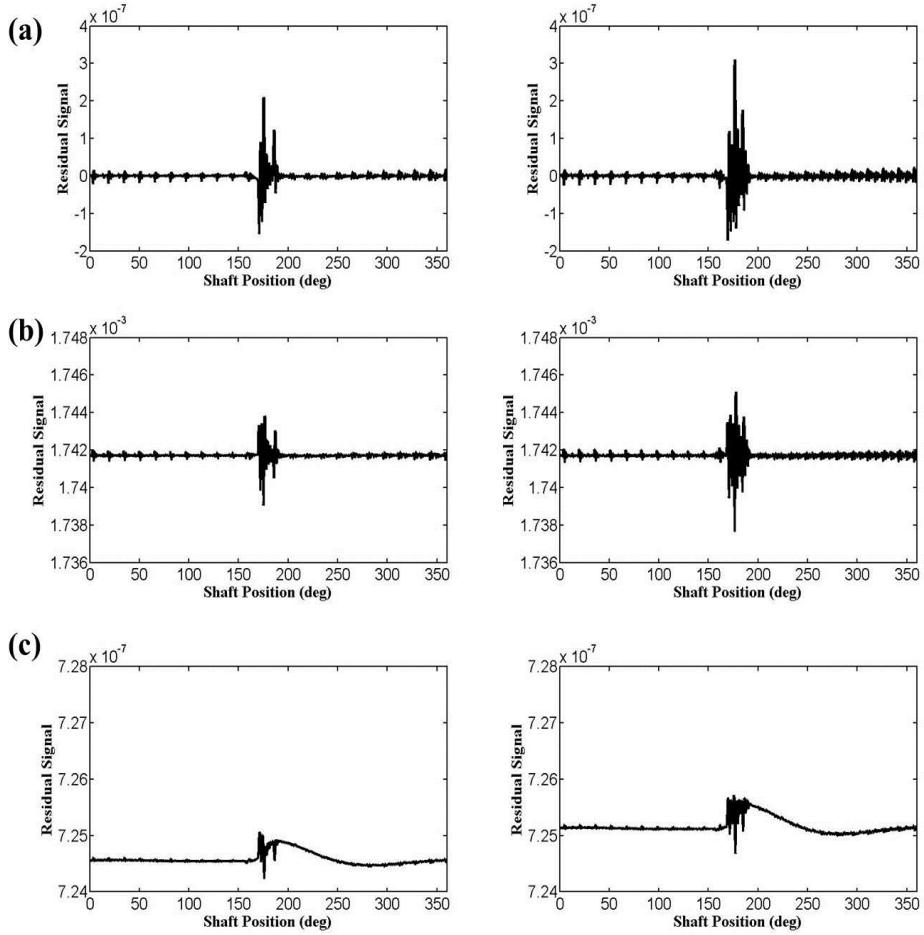

Figure 4.23 Residual signal for model I (left column) and from model II (right column). (a) output gear vertical velocity $\dot{y}_g$; (b) input pinion angular velocity $\dot{\theta}_p$; (c) transmission error $\theta_p - \theta_g$.

The simultaneous representation in both time and frequency domains offers important advantages for the analysis of non-stationary signals (Cohen, 1995). The Wigner−Ville distribution (WVD) is one of the well known time−frequency methods and its application to the detection of the gear damage has been widely described in publications (Forrester, 1996). By applying a suitable window function in the time domain, the cross-terms in the WVD can be attenuated and the windowed version of the WVD is often called the pseudo Wigner−Ville distribution (PWVD) (Forrester, 1996). In this research, the PWVD technique was employed to further compare the signals from model I and model II. Note that the 'shaft

domain' synchronous signal averages with the rotation 'angle' being analogous to 'time' and the frequency was therefore in terms of shaft order (Forrester, 1996).

Fig. 2.24 shows the PWVD of the output gear velocity signal. The synchronous signal averages generated in Fig. 11(a) were used as input for the PWVD and Fig. 14 (a) shows the PWVD for the gear signal in model I and Fig. 4.24 (b) shows the PWVD for the gear signal in model II. The pinion has 23 teeth, and as expected, the PWVD gave a vibration signal with major components at the tooth mesh frequency (23 orders) and its harmonics (n×23) as shown in the figure. If no fault existed in the gear system, a uniform distribution would be expected in the PWVD, whilst once a fault happens, the energy distribution would be expected to change correspondingly and these energy redistributions are largely because of the amplitude modulation and phase modulation induced by the gear fault (Forrester, 1996). Even though the cross-terms can still be observed in both figures, compared with the result in Fig. 4.24(a), Fig. 4.24 (b) was observed to have wider energy distributed through the shaft rotation angle when the crack occured between 150° and 200°.

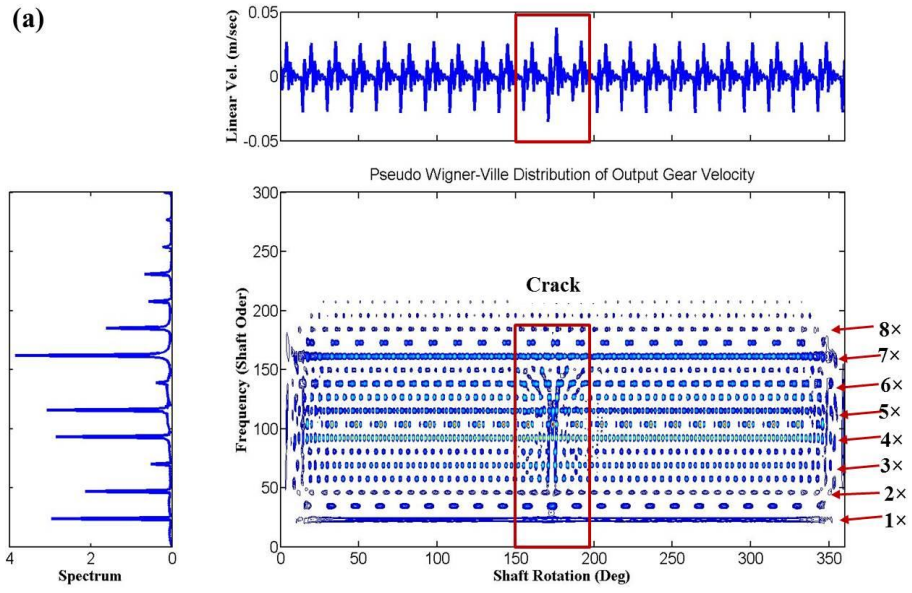

Figure 4.24 The Pseudo Wigner-Ville distribution (PWVD) of the output gear vertical velocity $\dot{y}_g$, (a) PWVD of the signal from model I; (b) PWVD of the signal from model II.

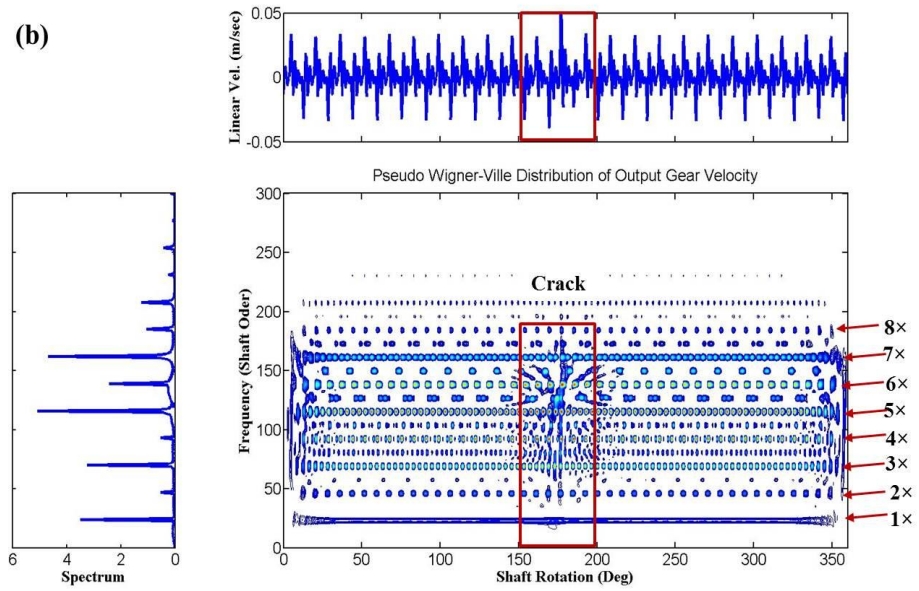

Figure 4.24 (Continued) The Pseudo Wigner-Ville distribution (PWVD) of the output gear vertical velocity $\dot{y}_g$, (a) PWVD of the signal from model I; (b) PWVD of the signal from model II.

The limitation of using the synchronous averaged signal for PWVD analysis was that the gear mesh harmonics were found to dominate the distribution and removing the components at the meshing harmonics can increase the sensitivity to energy changes related to the damage (Wang & McFadden, 1993a). Further analysis can be found in Fig. 4.25, which presents the PWVD analysis of the residual signal of the output gear vertical velocity $\dot{y}_g$. A much clearer difference in the energy distribution pattern can be observed and these results further indicated that the highest energy occurred around the fifth mesh harmonic.

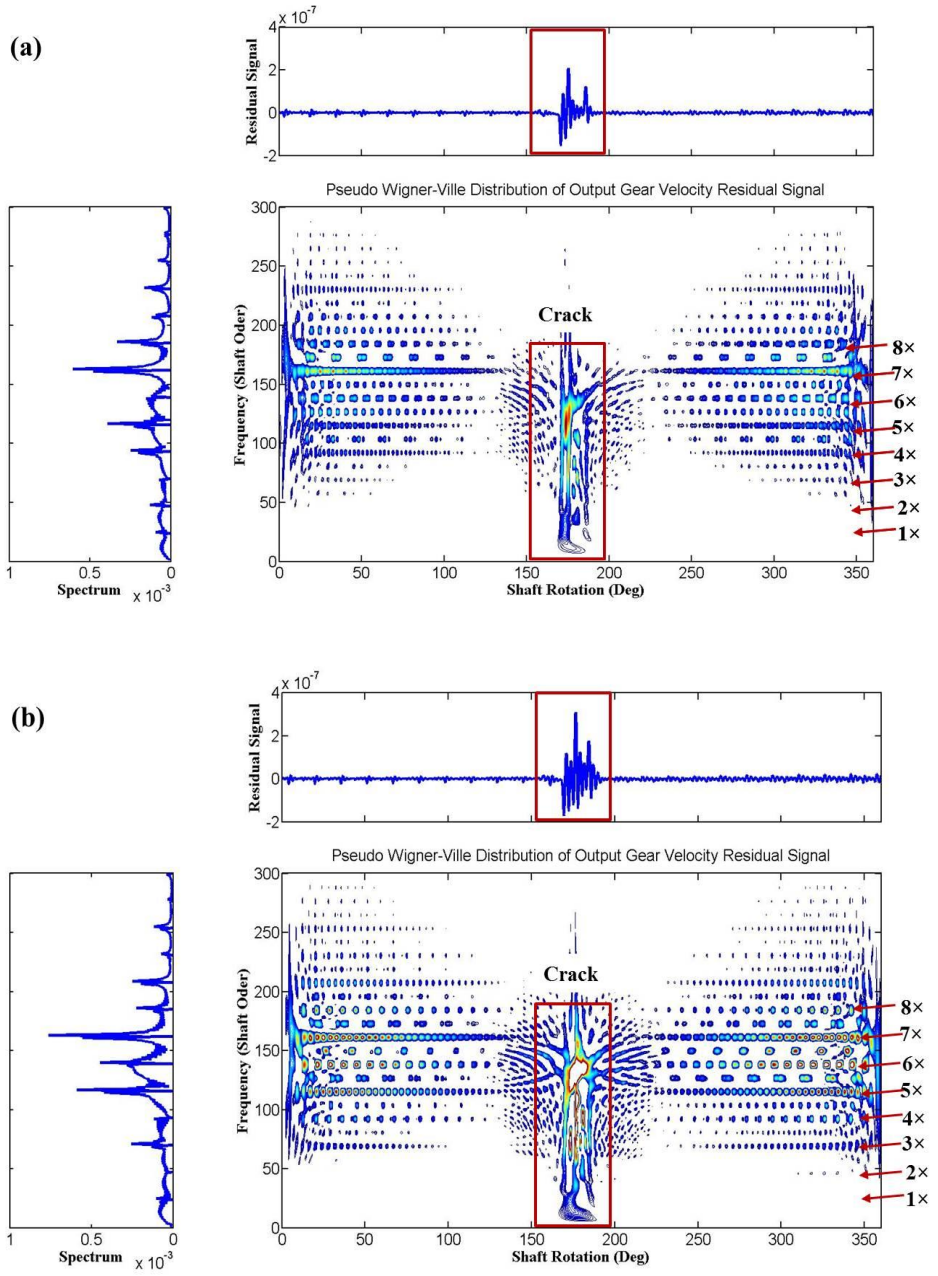

Figure 4.25 The Pseudo Wigner−Ville distribution (PWVD) of the residual output gear vertical velocity $\dot{y}_g$, (a) PWVD of the signal from model I; (b) PWVD of the signal from model II.

The non-uniformly distributed energy is closely related to the amplitude modulation and phase modulation, so the narrowband envelope, amplitude modulation and phase modulation techniques were further used for subsequent analysis. As the highest energy in Fig. 4.25

occurred around the fifth mesh harmonic, it was chosen for the demodulation process and a bandwidth of 22 shaft orders (±11) was used for the analysis.

Fig. 4.26 shows the results of the narrow band envelope, amplitude modulation and phase modulation from the output gear vertical velocity $\dot{y}_g$, including the crack. The left column shows the results from model I and the right column shows the results from model II. The presence of the crack can be clearly observed in both models at around 170° rotation of the shaft whilst the diagnostic results from model II are found to be different with those from model I in several ways even though the kurtosis value in the narrow band envelope is almost identical (14.65 *vs* 14.28). First, the overall value in the amplitude modulation of model I is less than half of the value of model II. Second, although the presence of the crack can be observed in both phase modulation results, a striking observation can be found in the overall value of the phase modulation. The phase modulation result from model I stays around 40° whilst the phase modulation result from model II stays around −130°.

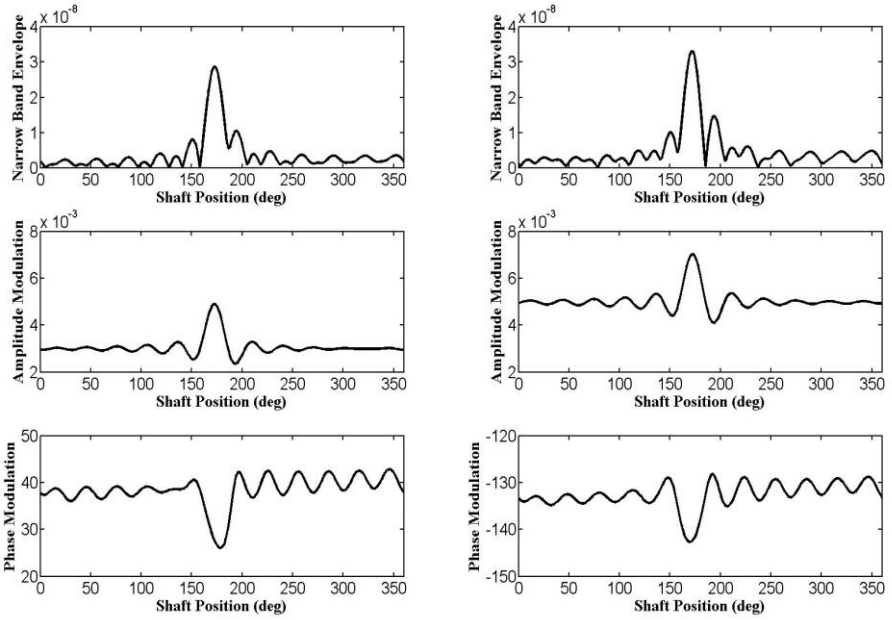

Figure 4.26 Narrowband envelope, amplitude modulation and phase modulation of the output gear vertical velocity $\dot{y}_g$ from model I (left column) and from model II (right column).

The amplitude and phase modulation can be further observed in the analytical signal obtained from the fifth mesh harmonic, as shown in Fig. 4.27. It can be found in the figure

that the inclusion of the gear centre distance effect provides a significant influence on the amplitude and phase modulation, especially the phase. The kurtosis values for the amplitude modulation of model I and model II were 14.25 and 12.79 respectively. The kurtosis values for the phase modulation of the model I and model II were 7.98 and 6.3 respectively.

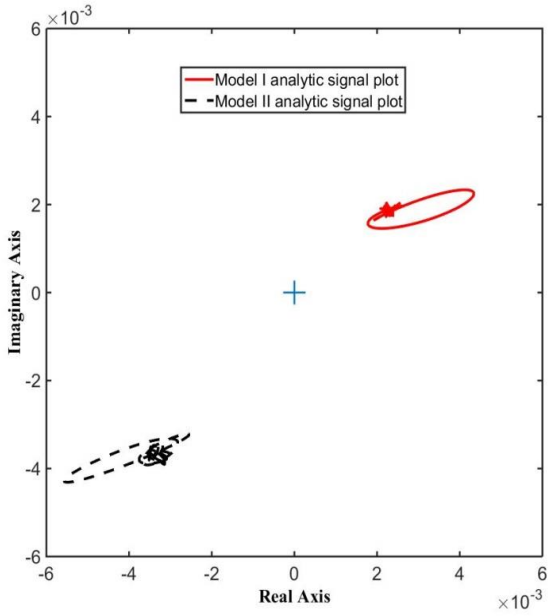

Figure 4.27 The analytic signal from the fifth mesh harmonic of the output gear vertical velocity $\dot{y}_g$.

Fig. 4.28 shows the PWVD of the input pinion angular velocity residual signal. Fig. 4.28 (a) shows the PWVD for the pinion residual signal in model I and Fig. 4.28 (b) shows the PWVD for the pinion residual signal in model II. Similar with the pattern in Fig. 4.25, the highest energy can be observed at the fifth mesh harmonic between 150° and 200°. A wider energy distribution due to the localised tooth root crack on the pinion can be found in the PWVD of model II, which indicated that the results from model II has different amplitude and phase modulation.

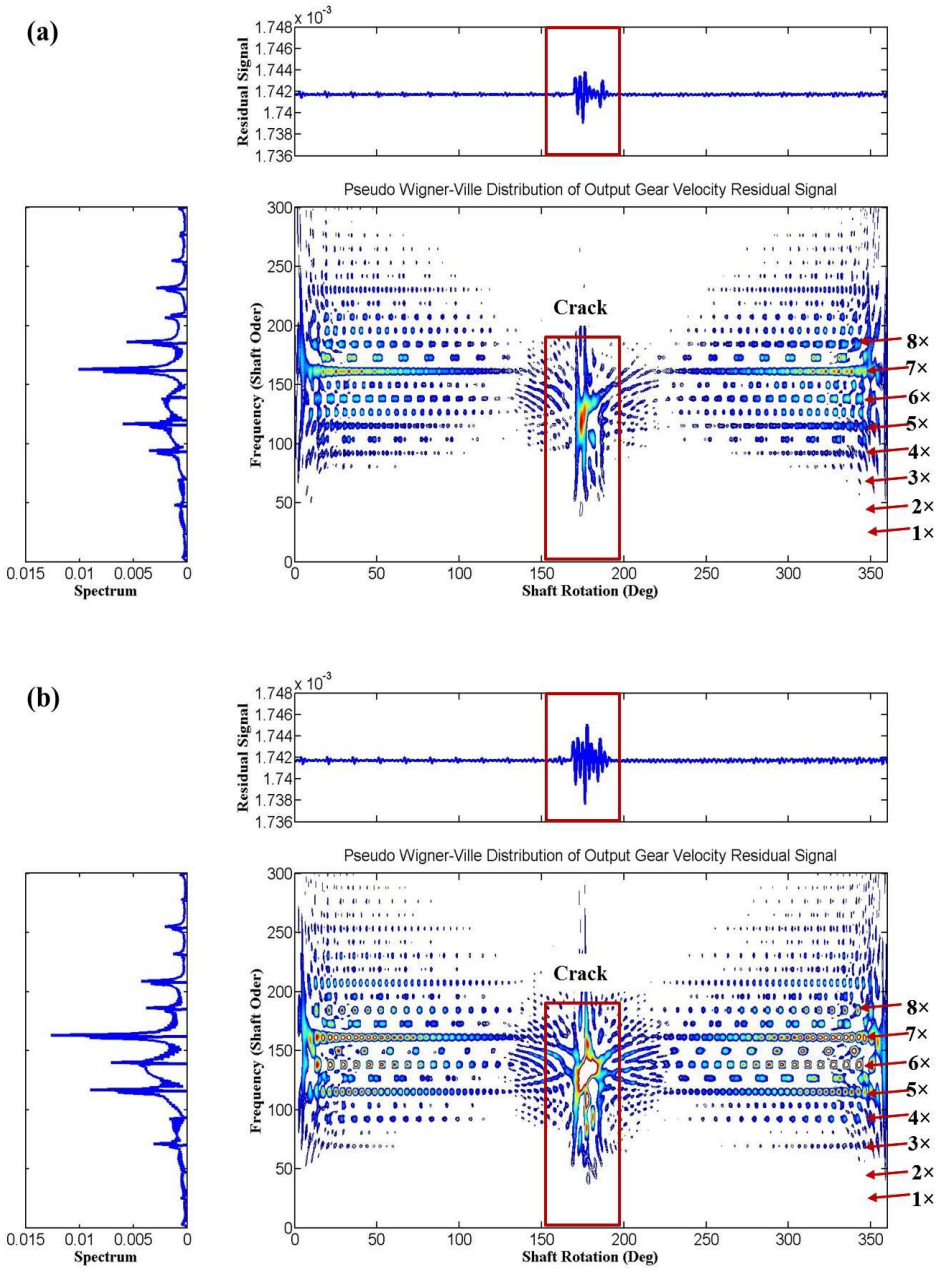

Figure 4.28 The Pseudo Wigner-Ville distribution (PWVD) of the input pinion angular velocity $\dot{\theta}_p$ residual signal (a) PWVD of the residual signal from model I; (b) PWVD of the residual signal from model II.

Fig. 4.29 shows the results of the narrow band envelope, amplitude modulation and phase modulation obtained from the demodulation of the input pinion torsional velocity $\dot{\theta}_p$, about the fifth mesh harmonic. The left column shows the results from model I and the right column shows the results from model II. Similar trends as observed in Fig. 4.26 can be found in these results. The overall magnitude of the amplitude modulation of model II is slightly

higher than that from model I. The most striking results can still be found in the phase modulation as the phase modulation result from model I stays around −110° while the result from model II stays around 80°.

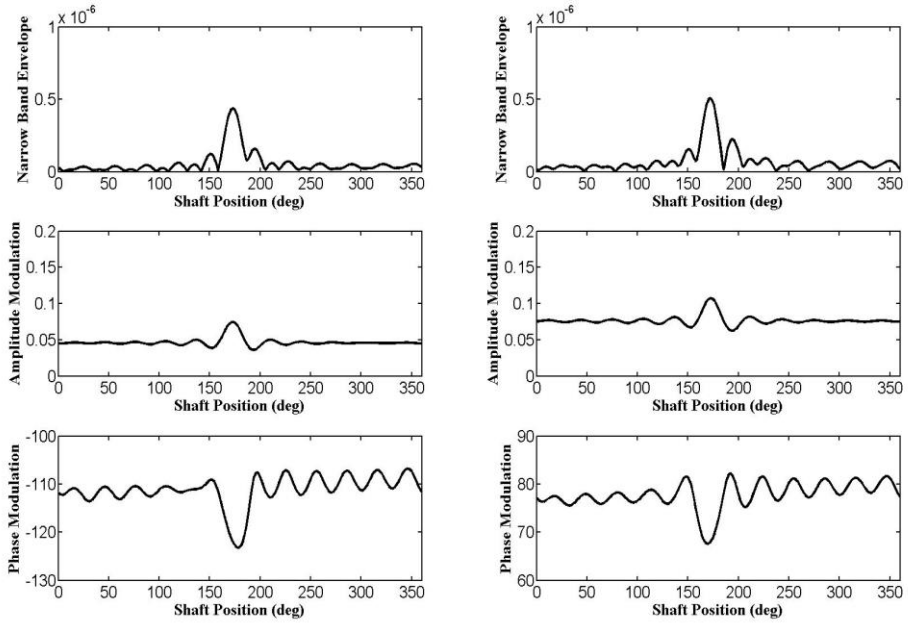

Figure 4.29 Narrowband envelope, amplitude modulation and phase modulation of the input pinion torsional velocity $\dot{\theta}_p$ from model I (left column) and from model II (right column).

The amplitude and phase modulation can be further observed in the analytical signal obtained from the fifth mesh harmonic, as shown in Fig. 4.30. It can be seen in the figure that the inclusion of the gear centre distance effect provides a significant influence on the amplitude and phase modulation. The kurtosis values for the amplitude modulation from model I and model II are 14.25 and 12.71 respectively. The kurtosis values for the phase modulation from model I and model II are 7.74 and 6.27 respectively.

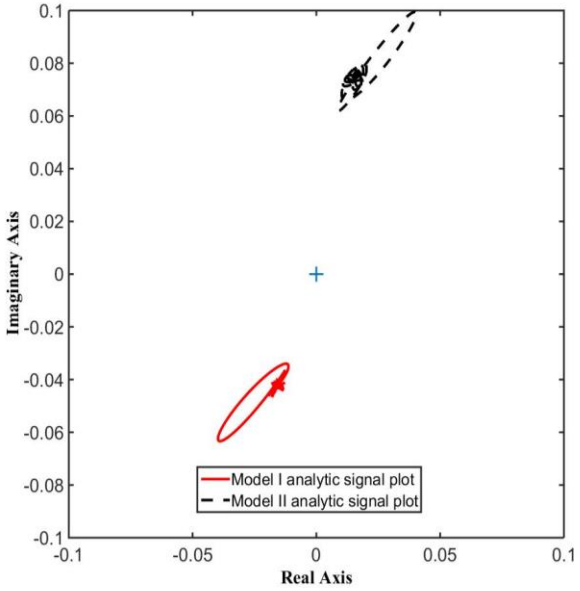

Figure 4.30 The analytic signal from the fifth mesh harmonic of the input pinion torsional velocity $\dot{\theta}_p$.

Fig. 4.31 shows the PWVD of the transmission error residual signal. Fig. 4.31 (a) shows the PWVD for the transmission error residual signal in model I and Fig. 4.31 (b) shows the PWVD for the transmission error residual signal in model II. A strong DC component can be found when initially ploting the spectrum and as a result, this DC component needs to be eliminated. Unlike the energy distribution pattern shown in Fig. 4.25 and Fig. 4.28, the range of the energy distribution covers from the first mesh harmonic to the sixth mesh harmonic in both pictures. The second frequency component seems to dominate the PWVD distribution as the highest energy can be found there.

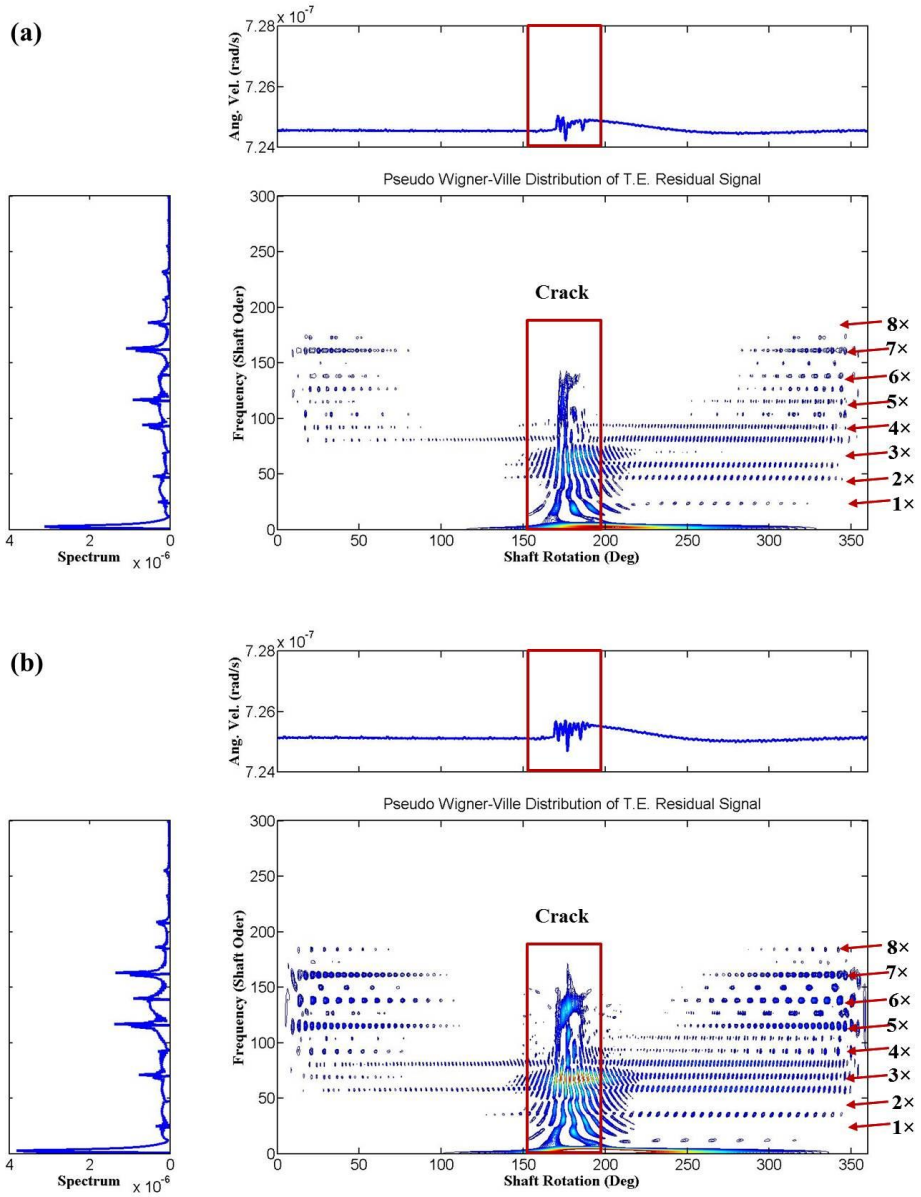

Figure 4.31 The Pseudo Wigner-Ville distribution (PWVD) of the transmission error residual signal, (a) PWVD of the signal from model I; (b) PWVD of the signal from model II.

As the range of the energy distribution due to the gear fault covers from the first mesh harmonic to the sixth mesh harmonic, the fifth mesh harmonic was still chosen to demodulate the signal in order to keep consistent with the previous results from the output gear and input pinion. Fig. 4.32 shows the results of the narrow band envelope, amplitude modulation and phase modulation from the transmission error $\theta_p - \theta_g$, including the crack. This would be expected to help further compare the modulation difference of the two models. The left column shows the results from model I and the right column shows the results from

model II. It can be found in the figure that the kurtosis value for the narrow band envelope from the two models were 14.84 and 13.07 respectively. The overall magnitude of the amplitude modulation of model II can be observed slightly higher than that from model I. The most striking results can still be found in the phase modulation as the phase modulation result from model I stays around 160° while the result from model II stays around −10°. The amplitude modulation and phase modulation can be further observed in Fig. 4.33.

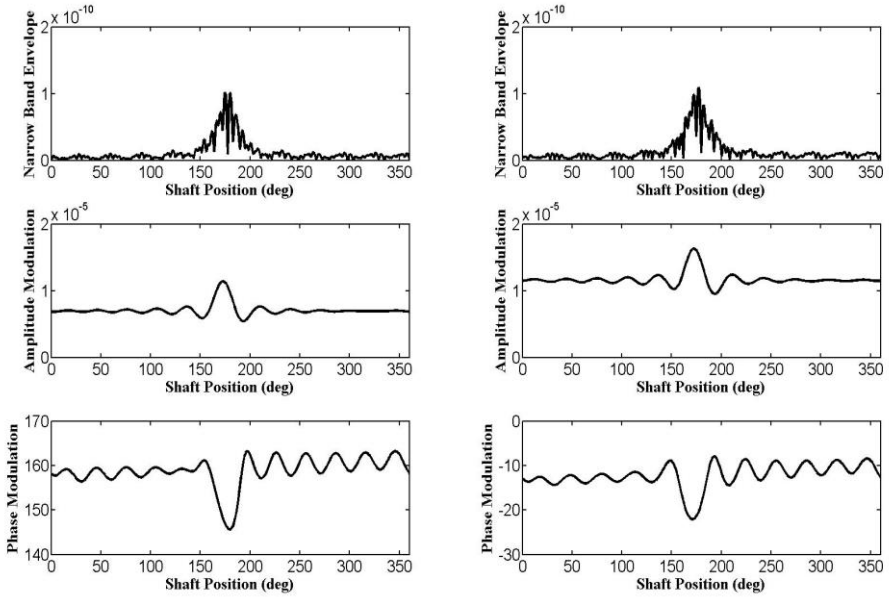

Figure 4.32 Narrowband envelope, amplitude modulation and phase modulation of the transmission error $\theta_p - \theta_g$ from model I (left column) and from model II (right column).

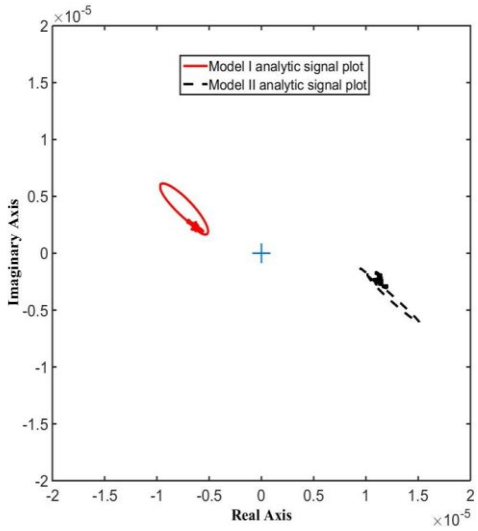

Figure 4.33 The analytic signal from the fifth mesh harmonic of the transmission error $\theta_p - \theta_g$.

The results shown in Figs 4.21−4.33 compare the outcomes from the simulation with or without the gear centre distance changes in the time and frequency domains, as well as in the joint time-frequency domain. In most cases, the diagnostic results from the two models were very close to each other except for some magnitude differences, for example, the synchronous averaged signal, the narrow band envelope and so on. The major difference can be found in the PWVD energy distribution pattern and the phase modulation. A summary of the residual signal, narrow band envelope, amplitude modulation and phase modulation can be found in table 4.5, in which the common diagnostic parameter kurtosis was presented.

Table 4.5 Summary of the diagnostic kurtosis results for the two models

	Output gear vertical velocity $\dot{y}_g$		Input pinion angular velocity $\dot{\theta}_p$		transmission error $\theta_p - \theta_g$	
	Model I	Model II	Model I	Model II	Model I	Model II
Envelope kurtosis	14.65	14.28	14.73	14.21	14.84	13.07
Amplitude modulation kurtosis	14.25	12.79	14.25	12.71	14.23	12.95
Phase modulation kurtosis	7.98	6.30	7.74	6.27	8.50	6.37

As shown in table 4.5, the inclusion of the gear centre distance variation seems to have a significant effect on the kurtosis values compared with the results from model I, especially the amplitude modulation and phase modulation kurtosis values while this inclusion appears to have negligible effect on the kurtosis values of the narrow band envelope. The largest change with the inclusion of the gear centre distance in the presence of the tooth crack occurred for the transmission error phase modulation kurtosis, where the kurtosis value decreased from 8.50 to 6.37. In all cases, the introduction of the tooth crack gave a substantial decrease in the kurtosis value with the inclusion of the gear centre distance.

4.6 Conclusion

This chapter has demonstrated the major effect of the gear centre distance variation on the diagnostic response of a gear tooth crack using a simplifed one stage gear dynamic model, where the geometrical error and eccentricity effects have been neglected. The inclusion of

the gear centre distance variation has been shown to change the behaviour of the gear mesh stiffness curve, which has been incorporated into the gear dynamic model. The iteration process proposed in the new gear dynamic model can reduce the errors caused by the gear centre distance variation during the simulation and the resultant vibration behaviour can still clearly show the effect of the presence of the crack. When comparing the diagnostic results from the previous model that neglected the gear centre distance variation, it was seen that a notable difference can be observed, especially in the phase modulation. All these data indicated that the effect of the gear centre distance variation has a significant effect on the detection of the gear fault for the flexible supported gear. The iteration method used in this study provides a possible way to improve the accuracy of gear dynamic modelling and hence further improve the accuracy of gear fault diagnostic methods.

Chapter 5 Ring-planet mesh stiffness study with different boundary conditions and crack locations

5.1 Introduction

Sun-planet and ring-planet tooth mesh stiffness variations are found to be the main internal vibration sources for planetary gear systems (Kahraman, 1994b, 1994c,). The methods of using a floating sun gear or flexible ring gear were often employed by gear designers to help reduce the gear vibration (Radzevich, 2012), which means the gear boundary conditions can have great influence on gear dynamic behavior. The purpose of this chapter is to develop a method to study the effect of the ring gear boundary conditions on the ring-planet mesh stiffness curve, which is one of the main vibration generation mechanisms for planetary gear systems.

The ring-planet gear mesh can be regarded as an internal gear pair and the mesh stiffness of the gear pair can be calculated using beam theory as well as the FEA method (Chen & Shao, 2013a, 2013b, 2013c, 2013d; Kahraman & Vijayakar, 2001; Kahraman et al., 2003; Kahraman et al., 2010; Ma et al., 2015; Mohammed et al., 2013; Savage, 1995). Based on the Lewis constant strength parabolic beam, M. Savage presented a model for the bending strength of an internal gear tooth as a function of the applied load pressure angle and evaluated the deflection of the internal spur gear tooth due to bending, shearing and Hertzian contact deformation (Savage, 1995). Based on the uniformly distributed Timoshenko beam theory, Zaigang Chen and Yimin Shao studied the effect of the ring deformation on the internal gear mesh stiffness (Chen & Shao, 2013b, 2013d). The effect of the support type, ring thickness and number of supports on the mesh stiffness has also been investigated and it was found that the mesh stiffness appeared to be modulated due to the presence of the supports (Chen & Shao, 2013d, Chen et al., 2013; Chen et al., 2015). Several crack cases were also created to evaluate the internal gear mesh stiffness with or without a crack in the ring gear tooth. When dealing with extended tooth contact phenomenon as well as the large gear crack size, the FEA method was found to be more suitable compared with the beam theory method (Ma et al., 2015; Mohammed et al., 2013). However, limited publications

using the FEA method to study the internal gear pair mesh stiffness were found. Kahraman used the FEA method to study the influence of rim thickness on gear deflections, bending stresses and load sharing of a planetary gear set. All the gears in the planetary gear system were treated as deformable bodies and it was found that the rim thickness influenced the quasi-static behavior significantly (Kahraman & Vijavakar, 2001; Kahraman et al., 2003). A following experimental study on the influence of rim thickness of the ring gear on the quasi-static behavior was presented to verify the results from previous studies (Kahraman et al., 2010).

The main objective of this chapter is to evaluate the ring-planet mesh stiffness under different boundary conditions with or without a tooth crack on the ring gear teeth using FEA methods. Based on this method, multiple cracks on ring gear teeth placed on different locations will be created to study the effect of crack locations on the ring-planet mesh stiffness. This study is expected to provide additional information for identifying the ring gear crack location for condition monitoring and fault diagnosis of planetary gear systems.

5.2 Ring-planet FEA models

The relationship between the overall planetary gear mesh stiffness and the subsystem mesh stiffness has been discussed in chapter 3, which provides a way to combine the subsystem mesh stiffness together via the speed ratio. The planetary gear tooth parameters used in chapter 3 will be adopted again in this chapter, as shown in Table 5.1.

Table 5.1 Ring-planet mesh pair parameters

	Planet gear	Ring gear
Number of teeth	Z_p=39	Z_r=99
Module, m_n	10 mm	10 mm
Pressure angle	20º	20º
Addendum	10 mm	8.9 mm
Face width	17 mm	17 mm
Material	Steel	Steel

The ring gear supports at the outside surface can prevent the ring gear from rotating and special care was given to the modelling of the actual constraint situation. Kahraman used straight splines blocks to model the contact between the ring gear and the fixed point, as shown in Fig. 5.1(a). The advantage of this model is that it incorporated any potential loss of contact between the spline and the housing surface due to excessive internal gear deformations (Kahraman & Vijayakar, 2001; Kahraman et al., 2003). In cases when the ring gears have external spline teeth, like in the wheel motor of larger electrically driven mining trucks, the support geometry is more complicated. Kirov and Wang (Kirov & Wang, 2013) used the FEA method to carefully model the geometry of the external spline teeth, as shown in Fig. 5.1(b). In their model, the ring gear was able to float in all directions and the radial and circular movements of the gear were limited by the backlash in the assembly. Another common situation is that the ring gear can be supported by a pin support, which connects the ring gear to the gearbox housing (Link et al., 2013), as shown in Fig. 5.1(c).

In this chapter, the pin support type was investigated and a large portion of this chapter will be focused on the effect of the pin support number and the pin's flexibility. To model the pin support, an area with a diameter ϕ was created around the ring gear rim and the position of this pin hole was in the middle of the rim, as schematically illustrated in Fig. 5.2(a). The choice of the pin support number can be in a large range, but generally, there were two scenarios, namely the ratio between the ring gear teeth number and the pin support number is an integer, or else the ratio between the ring gear teeth number and the pin support number is a non-integer. For the former case, the choice of the support number is limited once the ring gear teeth number is known. For example, in this study, the ring gear teeth number is 99 and therefore the number of pins when the ratio is an integer can be 3, 9, 11, 33, and 99. While, for the cases when the ratio is a non-integer, the choice is much larger. Fig. 5.2(b) showed an example for the case when the support number is 11 and they were uniformly distributed around the ring gear, with an angle of 32.7°. An APDL program in *appendix D* has been developed to create the pin support in the ring gear rim.

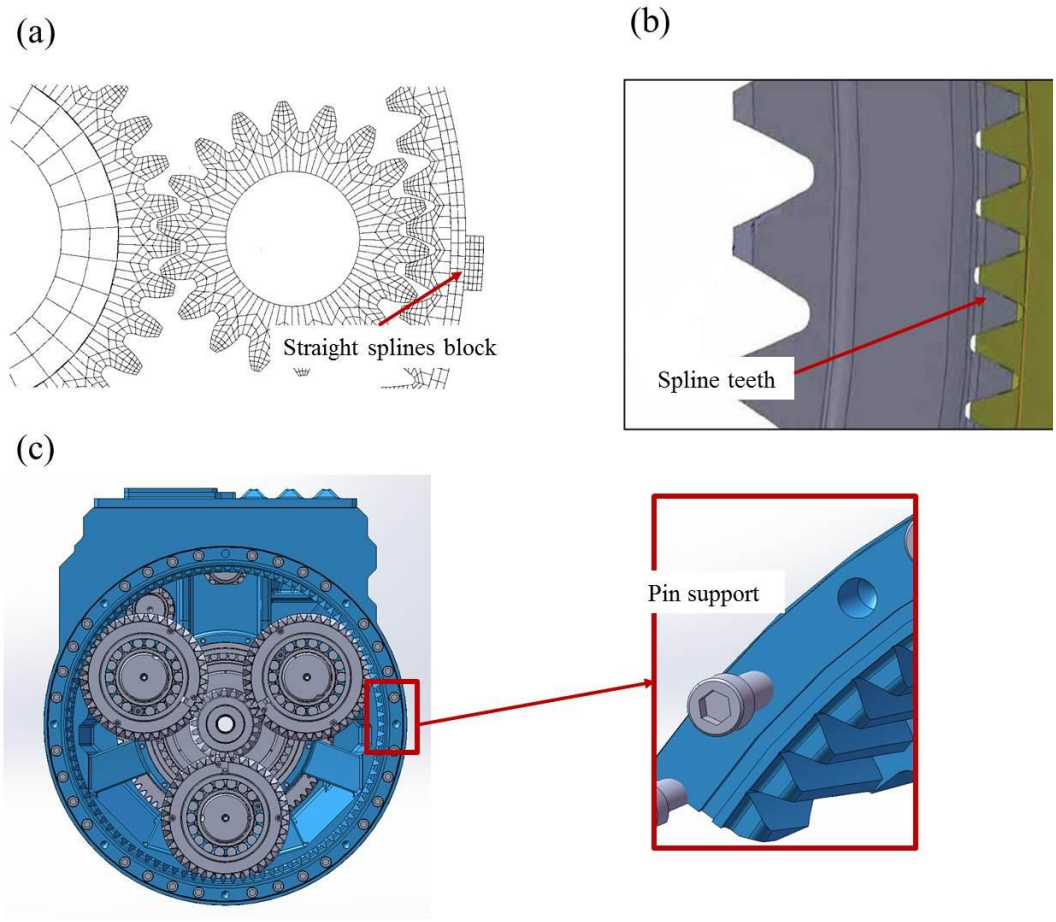

Figure 5.1 Ring gear support at the outside surface, (a) straight spline block model, (b) external spline teeth model, (c) pin support model

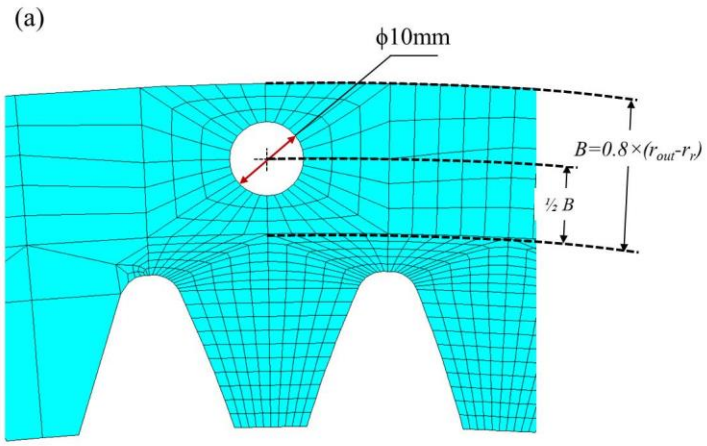

$r_{out}=a\times r_r$: the radius of the ring gear outside surface;

$r_r=(Z_r\times M_n)/2+1.25\times M_n$: the radius of ring gear dedendum;

Figure 5.2 Ring gear pin support, (a) pin support dimensions, (b) uniformly distributed pin support

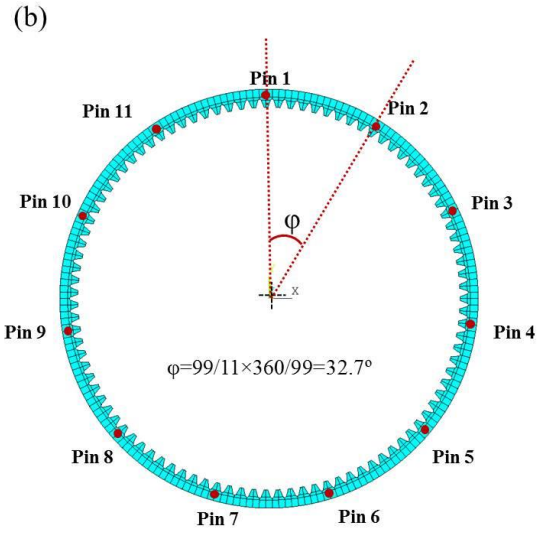

Figure 5.2 (Continued) Ring gear pin support, (a) pin support dimensions, (b) uniformly distributed pin support

In practice, the pin support is not rigid, which can further enable the movement of the ring gear. To consider the effect of pin support flexibility, a bearing element provided by ANSYS (Kohnme, 2003) was used in the analysis. ANSYS provides several bearing element options, which are COMBIN14, COMBI214, MPC184, and MATRIX27. In this research, element MATRIX27 was used, whose kinematic response can be specified by stiffness, damping, or mass coefficients in matrix form (Kohnme, 2003). The matrix was assumed to be related by two nodes, each with six degrees of freedom per node, as shown in Fig. 5.3. As shown in the figure, the matrix is symmetrical. If the pin support stiffness in the x−direction is 10^7 N/m, then the values of k_1 and k_{58} are set to be 10^7 N/m while the value of k_7 has to be set to be -10^7 N/m. Similarly, we can define the pin support stiffness in the other directions.

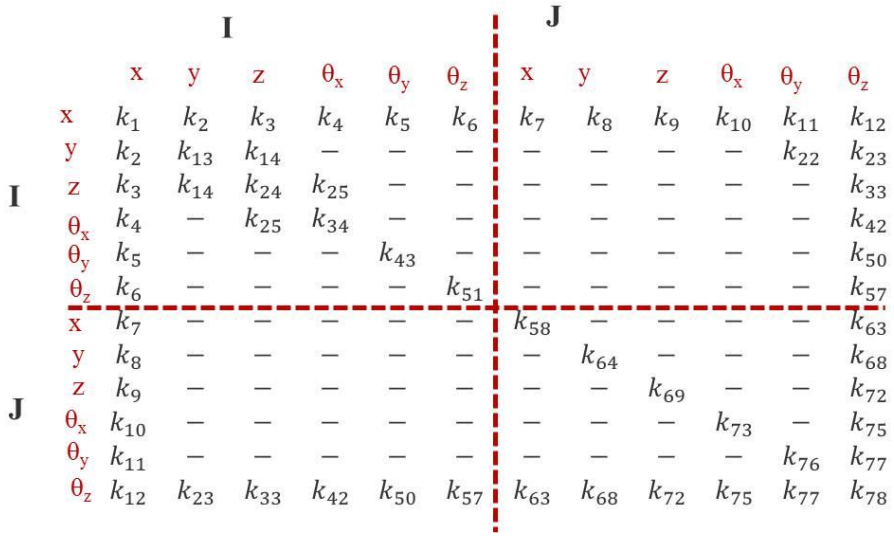

Figure 5.3 MATRIX27 element input matrix (Kohnme, 2003)

5.3 The effect of different boundary condtions and their results

This section presented the results for the influence of different ring gear boundary conditions on the ring-planet gear mesh stiffness and there are four cases in this research, the influence of the ring gear rim thickness, influence of the number of supports, influence of the flexibility of the support and the influence of the ring gear crack locations.

5.3.1 The effect of ring gear rim thickness and its results

The rim thickness effect was investigated in the full constraint situation initially, where the nodes on the outside surface of the ring gear were fully constrained (x, y and θ_z directions). The rim thickness effect has been extensively studied by Kahraman and a so-called back-up ratio has been used to evaluate the influence of the ring gear rim thickness on gear deflections, stresses and load sharing (Kahraman & Vijayakar, 2001; Kahraman et al., 2010). The back-up ratio was also used in this research and it can be defined as,

$$\Lambda_{int} = \frac{R_{oD} - R_{root}}{R_{root} - R_{minor}}, \tag{5.1}$$

where R_{OD}, R_{root}, and R_{minor} are the ring gear outer, root and minor radius respectively. In this research, two cases have been compared, as defined in table 5.2.

Table 5.2 Ring gear dimension parameters and corresponding backup ratio

	Outer radius	Root radius	Minor radius	Λ_{int}
Case 1	609 mm	507.5 mm	486.51 mm	4.8
Case 2	533 mm	507.5 mm	486.51 mm	1.2

As shown in table 5.2, the ring gear root radius and minor radius are the same for the two cases and the only difference exists in the ring gear outer radius which resulted in the different back-up ratios. Case 1 has a back-up ratio of 4.8, which indicates the ring gear has a thick rim. Case 2 has a back-up ratio of 1.2, which indicates the ring gear has a thin rim.

The 2D plane stress assumption was used in the FEA models and to obtain quality solutions, adaptive meshing should be applied near the contact, as discussed in chapter 3. The planet was controlled by an APDL program to move around the center of the ring gear and the center of the planet itself, acting as though there were a rigid carrier arm carrying the planet gear. This will give the same movement of the planet in a complete planetary gear set as shown in chapter 3. Calculations were carried out covering nine mesh periods, which gave a total carrier rotation angle of 360º/11=32.7º. With the rotation increment angle of 0.1º, a total of 330 points were calculated in this calculation. This carrier rotation angle covered all the teeth between two adjacent pins. When the planet moves to each simulated position, a torque T_{rp} was applied to its hub and the resultant gear mesh stiffness can be obtained.

Only one torque magnitude was considered here and the corresponding ring-planet tooth mesh stiffness variations under the two conditions are shown in Fig. 5.4. As shown in the figure, the planet-ring mesh stiffness includes the planet and ring gear teeth bending stiffness, the Hertzian contact stiffness and the gear body stiffness (Wang, 2003). The bending and Hertzian stiffnesses are identical in both thick and thin cases as the gear teeth number and gear module are the same in the two cases. However, the thick ring gear has extra gear body rim compared with the thin case, which induced a different peak-to-peak magnitude. The peak-to-peak magnitude of the thick rim case is 3240 kNm/rad while the peak-to-peak magnitude of the thin rim case is 3640 kNm/rad. It is interesting to notice that the mesh stiffness with the thin rim has a higher value compared with that with the thick rim, which

was largely due to the outside of the rim being fully constrained where it acts like a rigid boundary increasing the stiffness of the rim while the extra gear body in the thicker rim case adds additional flexibility to the total mesh stiffness. Another interesting finding was that the relative stiffness increase in the double contact zone (830 kNm/rad) which was a little bit higher than the relative stiffness increase in the single contact zone (430 kNm/rad). However, in order to conveniently estimate the influence of the rim thickness on the mesh stiffness, a rough constant value can be used to account for the extra gear body stiffness and in this case, a constant factor of 1.1 can be assigned.

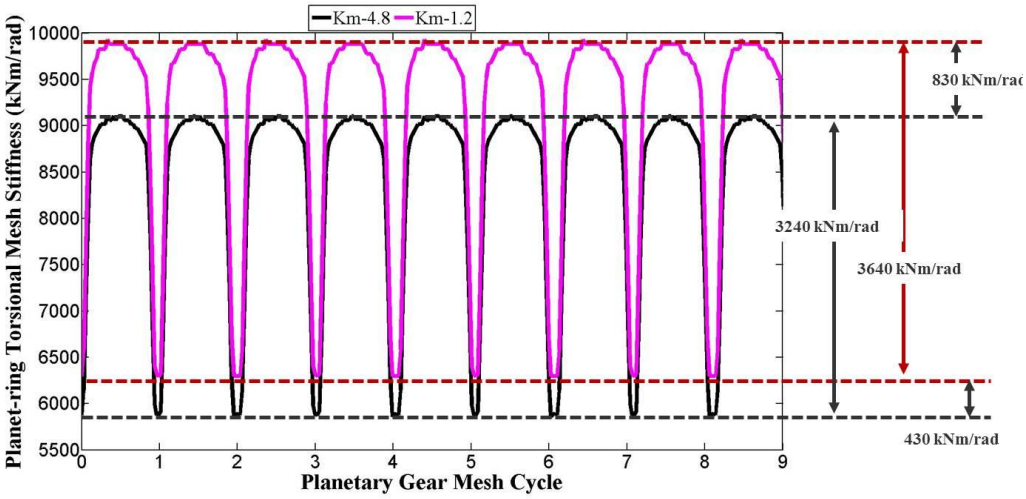

Figure 5.4 Effect of ring rim thickness on ring-planet mesh stiffness under full constraint conditions

One of the issues with using this FEA model was that there are three planet gears in the planetary gear system while when calculating the ring-planet mesh stiffness, there was only one planet gear considered and it was assumed that the effect of the other two planet gears was negligible. However, the ring gear will experience greater deformation due to the other planet gears that can also apply forces to the ring gear. Here, the effect of the other planet gears on the ring-planet mesh stiffness was investigated under the full constraint condition. Another two planet gears were subsequently added into the planetary FEA model, as shown in Fig. 5.5. Along with the torque applied on the hub of planet gear 1, two identical torques were also applied on the hubs of planet gear 2 and planet gear 3, based on the assumption that each planet gear shared the same load from the sun gear. The same procedure of calculating the torsional stiffness was performed and the results of the torsional stiffness of

the planet gear 1 pair were obtained from the FEA model. A comparison between the results of the single planet gear FEA model and the results of the three planet gears FEA model is shown in Fig. 5.6. As indicated, the torsional stiffness calculated from the FEA model with one planet was identical with the torsional stiffness calculated from the FEA model with three planets. Even though these results were only for the thick ring gear rim case, it still can be concluded that the ring gear deformation due to the other planet gears was minimum under the full constraint condition and this local deformation will not affect the calculation of the torsional stiffness.

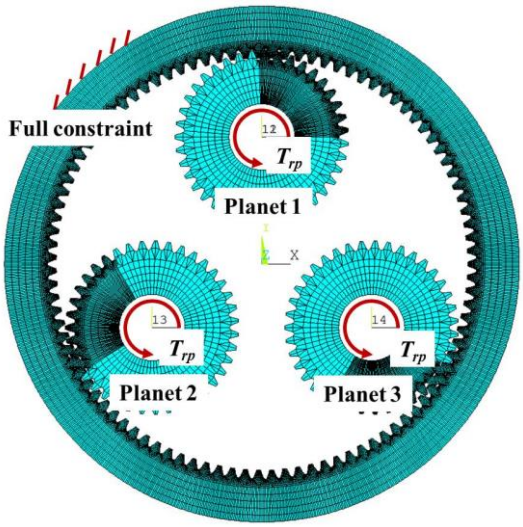

Figure 5.5 FEA Model with three planet gears

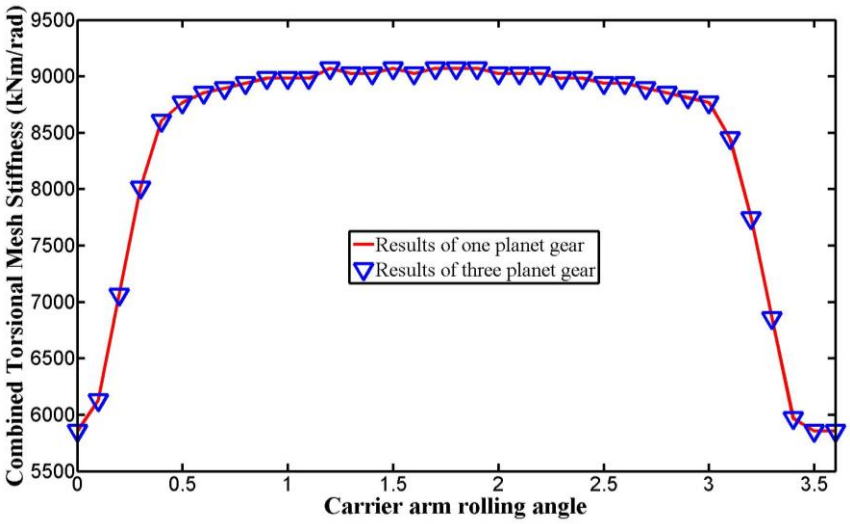

Figure 5.6 Comparison between FEA results of one planet gear and FEA results of three planet gear under full constraint condition

5.3.2 The effect of ring gear pin support number and its results

The effect of the pin support number was investigated in this section. 11 pins and 22 pins (ring gear teeth number is 99) were chosen in this study and they represent the scenarios when the ratios are integer and non-integer separately. Besides, the full constraint situation mentioned in section 5.3.1 can also be considered as one of the non-integer situations as there are a total of 556 nodes outside of the ring gear rim, which can be considered as 556 pin supports in total.

Fig. 5.7 shows the FEA models for the ring gear with 11 pin supports and 22 pin supports. There are 10 gear teeth between two adjacent pins in the case of 11 pin supports, which are uniformly distributed around the ring gear, as shown in Fig. 5.2. The method of creating 22 pin supports involves inserting another pin support between two adjacent supports in the 11 support scenario while still keeping all the pins uniformly distributed, as shown in the example in Fig. 5.7(b).

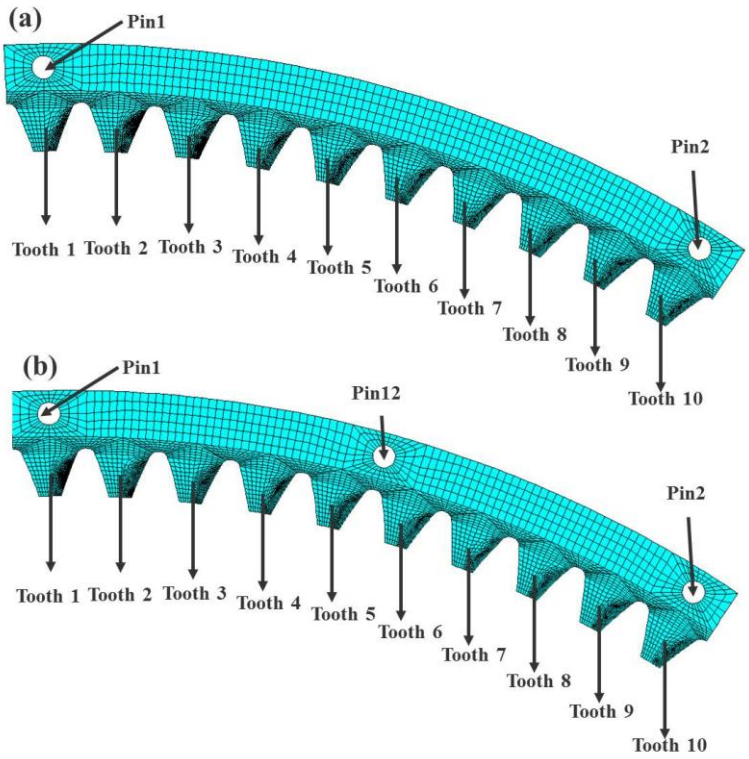

Figure 5.7 The FEA models with (a) integer ratio of pin supports and (b) non-integer ratio of pin

Fig. 5.8 describes the variation of the gear mesh stiffness with different pin support numbers. Pin-556 is the resultant gear mesh stiffness when the pin support number was 556. Pin−22 is the resultant gear mesh stiffness when the pin support number was 22. Pin−11 is the resultant gear mesh stiffness when the pin support number was 11. As shown in the figure, there was hardly any modulation effect observed in the Pin−556 curve during this rotation and the only variation was caused by the change from the single contact zone to the double contact zone. The starting point of Pin−22 curve was directly on one of the pin supports and during this rotation, it passed one adjacent pin support and ended at the next pin support. As shown in the figure, the Pin−22 curve clearly showed an additional variation besides the variation due to the change from the single contact zone to the double contact zone. It reached its highest point at around 5° and 20° where the pin support was located. This additional variation caused a modulation effect to the original mesh stiffness curve (Pin−556). Similar modulation effects were observed in curve Pin−11. Because the Pin−11 passed no support during the rotation, it reaches its lowest point at around 22°.

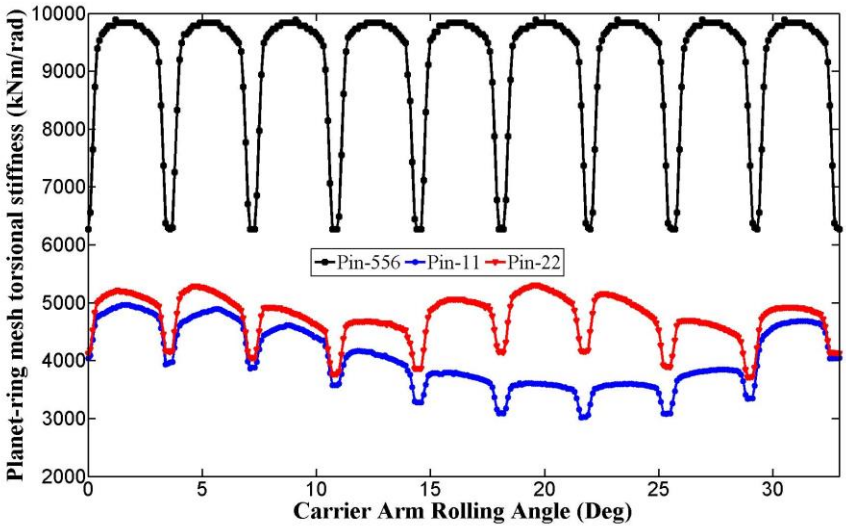

Figure 5.8 Comparison of ring-planet mesh stiffness from support pin number changes

Fig. 5.9 extended the Pin−11 and Pin−22 mesh stiffness curves over one carrier arm revolution to show a clear view of the modulation effect. The Fourier transform was applied to the mesh stiffness curves separately to demonstrate the spectral frequency content, as

shown in Fig. 5.9 (c) and (d). In Fig. 5.9 (a) and (b), it is apparent that the trend of the mesh stiffness was dominated by the modulation effect and what is interesting in the two figures is that there are 11 peaks in curve Pin−11 and 12 peaks in curve Pin−22, which is exactly the same as the pin support number. This further indicated that the modulation effect is caused by the number of pin supports. The frequency spectra further confirmed this finding as there were strong components appearing at 11 and 22, as shown in Fig. 5.9 (c) and (d). One can still identify the components on the ring gear tooth number, but compared to that on the pin support number, they showed much smaller frequency magnitude. A reasonable conclusion is that the modulation effect can dominate the mesh stiffness curve and the number of the periodicities is equal to the number of the supports.

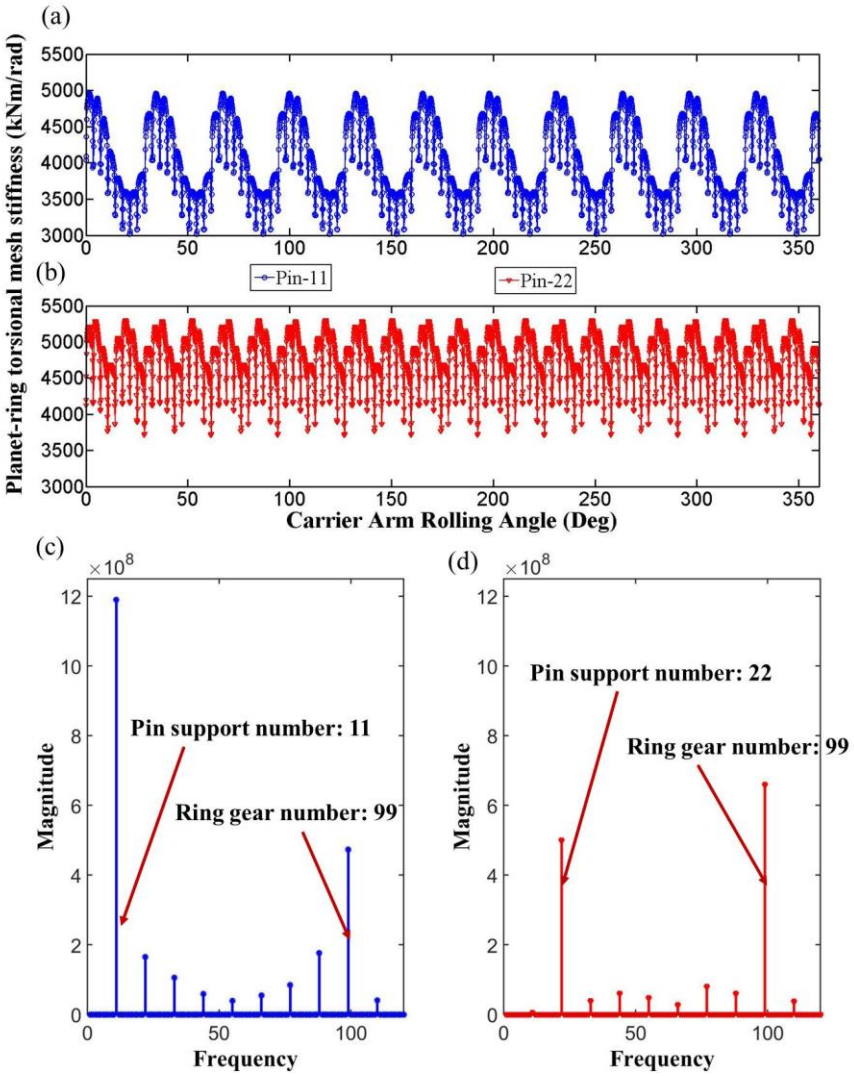

Figure 5.9 Effect of pin support number on ring-planet mesh stiffness

The influence of the ring gear rim thickness can be further investigated in the pin support situations. Fig. 5.10 describes the gear mesh stiffness results with pin support, but with different ring gear rim thickness. Km−11−4.8 curve illustrates the gear mesh stiffness results with 11 pin supports and the thick ring gear rim. Km−11−1.2 curve, which is the same with curve Pin−11 in Fig. 5.8, shows the gear mesh stiffness results with 11 pin supports and the thin ring gear rim. It can be observed that there is a weaker modulation effect in the case of Km−11−4.8 compared with that in Km−11−1.2 as the variation of Km−11−4.8 showed much smaller magnitude variation and the modulation has obviously been weakened.

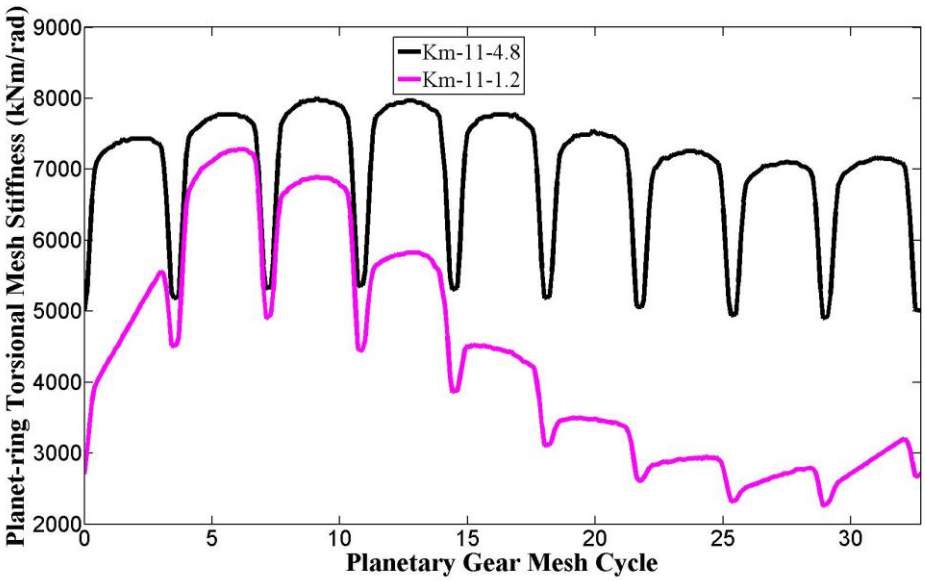

Figure 5.10 Comparison between the ring-planet mesh stiffness with thin rim and the ring-planet mesh stiffness with thick rim

The effect of the other planet gears on the resultant gear mesh stiffness was studied using the model shown in Fig. 5.11. Instead of using full constraint, the pin support was applied and the pin support number 11 was used to study this effect. To simplify the calculation, 20 positions in the middle of the single contact zone and double contact zones were selected and the mesh stiffness values in these positions were compared, as shown in Fig. 5.12, which suggested that the effect of the other planet gears on the mesh stiffness calculation was limited in this situation even though slight variation can be found when the position was close to the pin support.

Figure 5.11 FEA Model of three planet gears

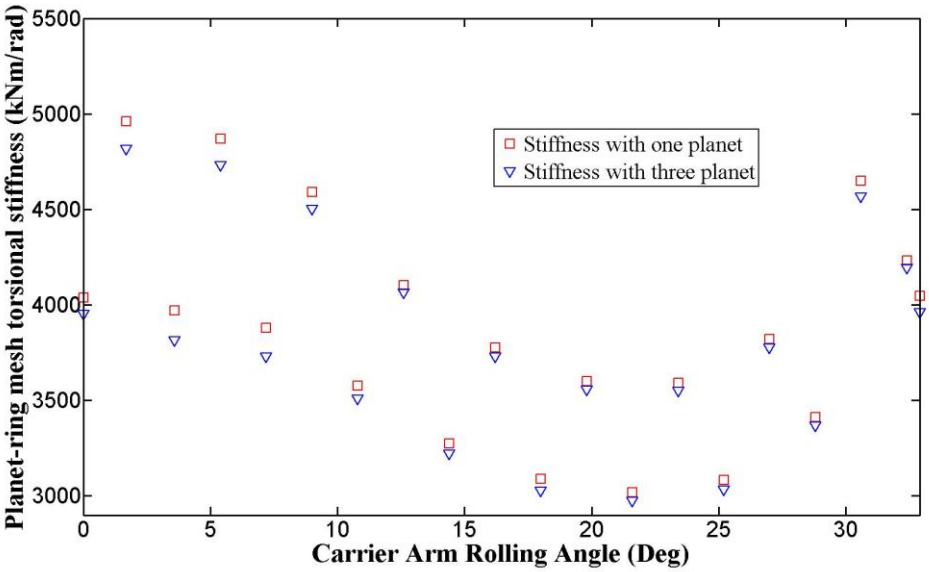

Figure 5.12 Comparison between FEA results of one planet gear and FEA results of three planet gears under fixed pin-supported conditions

5.3.3 The effect of ring gear pin support flexibility and its results

In all the previous sections, the pin has been considered as rigid and the pin flexibility has been excluded from the ring-planet mesh stiffness. However, it is almost impossible to ignore this effect in reality, especially as the floating ring method has been used to reduce the

planetary gear vibration (Valco, 1992). The MATRIX27 element with user-defined values in its stiffness matrix in ANSYS has made the incorporation of the pin flexibility into the FEA model possible. It was assumed here that the pin stiffness in the x and y directions had the same value. Three cases listed in table 3 were chosen to study the effect of pin flexibility on ring-planet mesh stiffness. 1×10^7 N/m stands for the case of a flexible pin while 1×10^9 N/m stands for the case of a rigid pin.

Table 5.3 The flexibility of the pin support

	Case 1	Case 2	Case 3
Kxx (N/m)	1×10^7	1×10^8	1×10^9
Kyy (N/m)	1×10^7	1×10^8	1×10^9

Fig. 5.13 shows the resultant mesh stiffness with the inclusion of the pin support flexibility. As the gear design parameters are the same in all three cases, the difference between the curves were due to the value of the pin stiffness. It can be observed that the ring-planet mesh stiffness is almost a straight line when the pin is flexible, which was expected to reduce the noise of the planetary gear. With the increase of pin stiffness, the modulation effect becomes obvious and the total stiffness amplitude increases. When the pin stiffness is 1×10^9 N/m, the mesh stiffness value is almost the same with that when the pin was considered as rigid. The figure suggested that the pin support stiffness dominated the gear mesh stiffness when there is a flexible pin support.

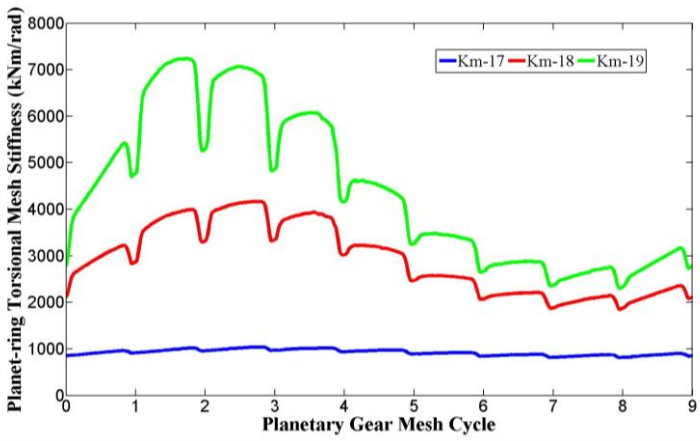

Figure 5.13 Ring-planet stiffness with flexible pin supports

Normally, the gear stiffness includes the teeth bending stiffness, gear body stiffness and Hertzian contact stiffness (Wang, 2003). By using the method mentions above, the gear mesh stiffness can be extended to include the flexibility of the pin support and the ring-planet mesh stiffness composition can then be represented as illustrated in Fig. 5.14.

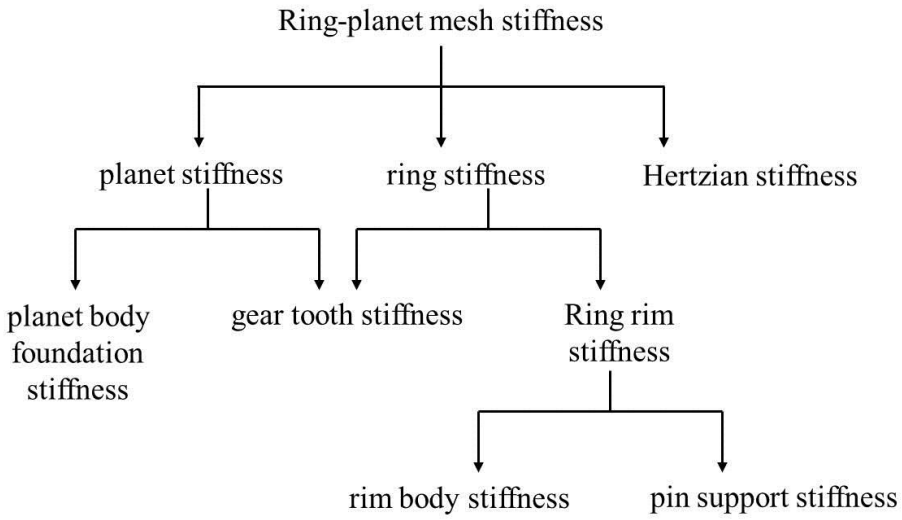

Figure 5.14 Composition of the ring-planet mesh stiffness

Fig. 5.15 describes the load sharing ratio between the tooth pairs in mesh and only the load sharing ratio in the range between pin support No.1 and No.2 are shown. It can be observed that the load sharing is symmetrical when the mesh was on tooth 2, but as the mesh continued, the load sharing ratio lost its symmetrical characteristics and some variation can be observed in the double-tooth engagement region, as shown in Fig. 5.15(a). It can be noted that when the teeth enter the mesh, the load sharing ratio appears to decrease while it increases when the teeth exit the mesh. If only the fifth tooth was considered, the load sharing ratio can be studied with different pin support flexibility, as shown in Fig. 5.15(b). It can be observed that the bearing flexibility has some notable influence on the load sharing ratio, mainly in the double contact zone when the mesh exists. It shows that the load sharing ratio decreases slightly when the bearing flexibility increases. Even though this figure only shows the case of tooth 5, it is expected this bearing flexibility influence can affect every teeth that is in mesh.

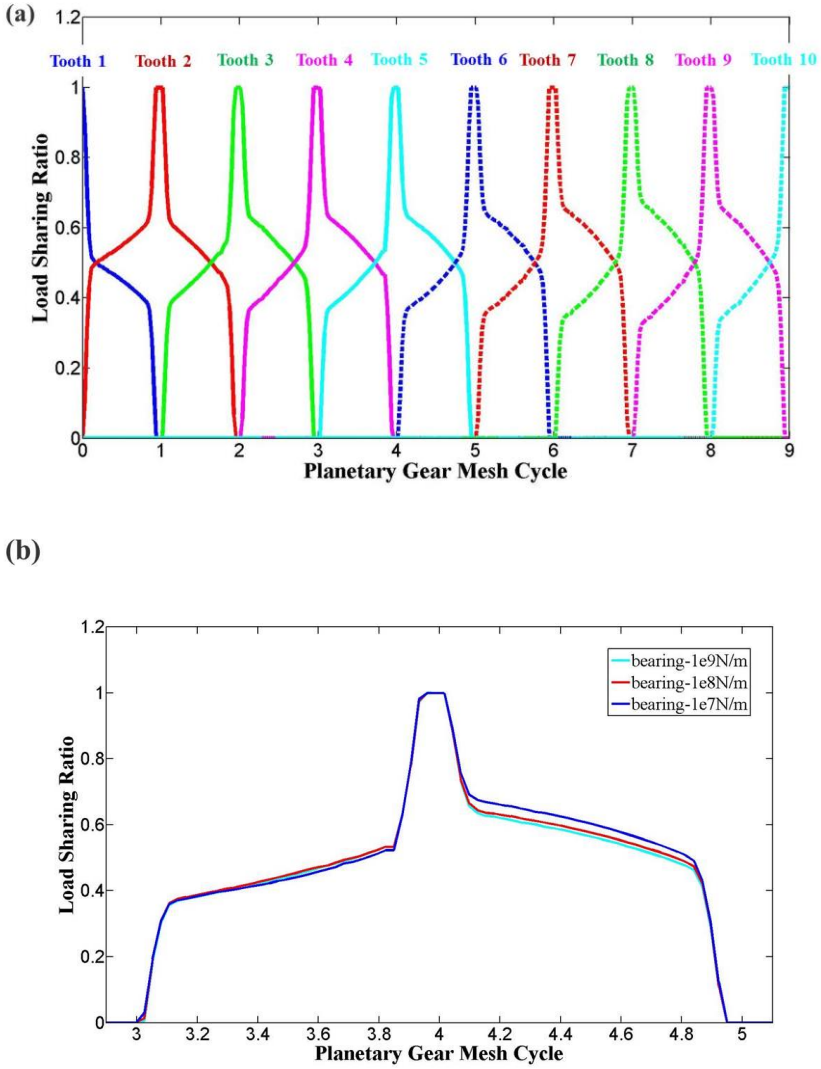

Figure 5.15 Ring gear tooth load sharing ratio, (a) load sharing ratio for all teeth during the rotation, (b) load sharing ratio for the 5th tooth

The effect of the other planet gears on the resultant gear mesh stiffness can also be studied using the model shown in Fig. 5.11. Instead of using the rigid pin support, the flexible pin support 1×10^7 N/m was considered in the model. To simplify the calculation, the mesh stiffnesses at 20 uniformly distributed positions were compared, as shown in Fig. 5.16. Comparing the two results, it can be seen that the mesh stiffness with one planet gear is shown to have higher value compared with that with three planet gears. Another observation about the two results is that adding the other planet gears will not change the mesh stiffness shape variation significantly and the value of mesh stiffness with three planet gears was

found to be around 0.89 times smaller than that with one planet gear through the whole carrier arm rotation range.

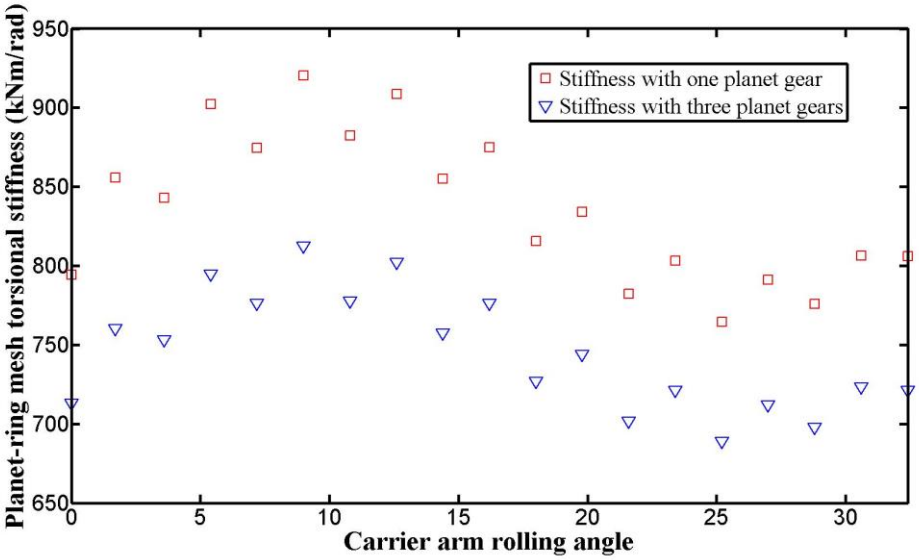

Figure 5.16 Comparison between FEA results of one planet gear and FEA results of three planet gears under flexible pin-supported conditions

5.3.4 The effect of ring gear crack locations and its results

Stress concentrations can assist crack propagation from any stress raisers at the early stage, such as machining marks or surface defects and can eventually break off the complete tooth (Smith, 2003). Once a crack happens, the corresponding gear mesh stiffness will change correspondingly. In this section, the effect of the ring gear crack location will be investigated and the LEFM (linear elastic fracture mechanics) assumption was used in this analysis. A constant crack length (5mm) and a constant crack inclination angle (φ=60º) was used to study the effect of crack locations on the ring-planet gear mesh stiffness, as shown in Fig. 5.17.

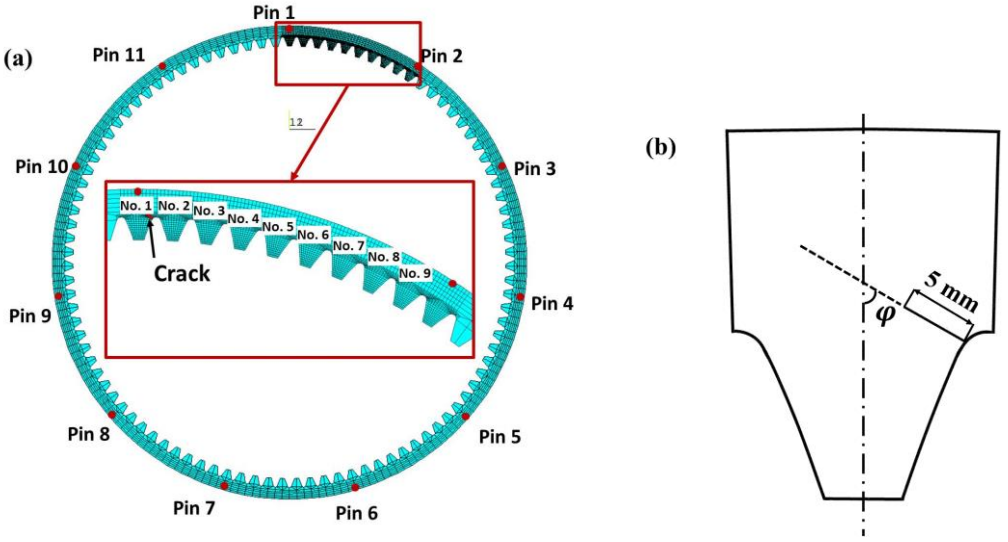

Figure 5.17 Composition of the ring-planet mesh and the ring tooth crack

As shown in Fig. 5.17, there are 9 teeth, whose boundary conditions are different, between two adjacent pins. As shown in Fig. 5.8, the pins exert a modulation effect on the shape of the planet-ring stiffness curve and therefore the mesh stiffness curve will be expected to show a different variation once the crack occurs on different ring gear teeth. Fig. 5.18 describes the resultant planet-ring mesh stiffness with 9 cracks in 9 separate FEA models to study the effect of the crack location on the ring-planet mesh stiffness.

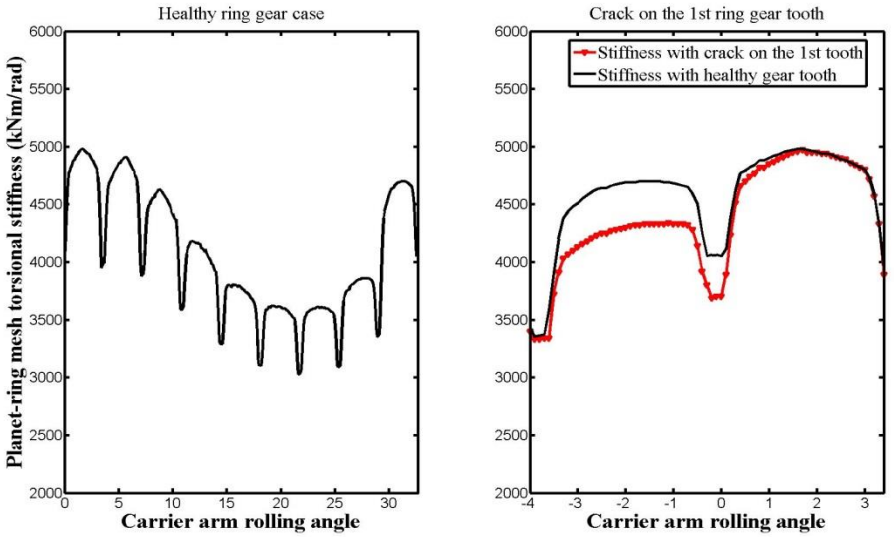

Figure 5.18 Ring-planet stiffness with healthy gear tooth and crack on the 1st gear tooth

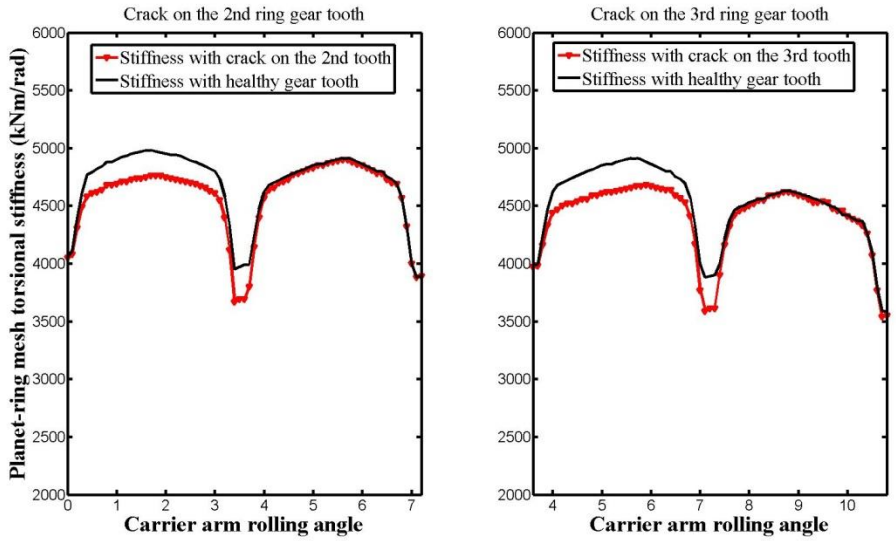

Figure 5.19 Ring-planet stiffness with crack on the 2nd gear tooth and crack on the 3rd gear tooth

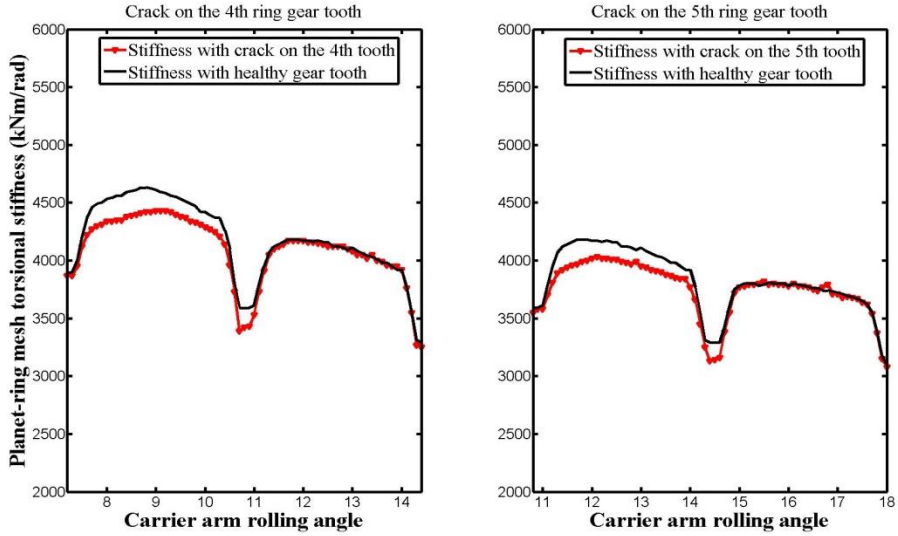

Figure 5.20 Ring-planet stiffness with crack on the 4th gear tooth and crack on the 5th gear tooth

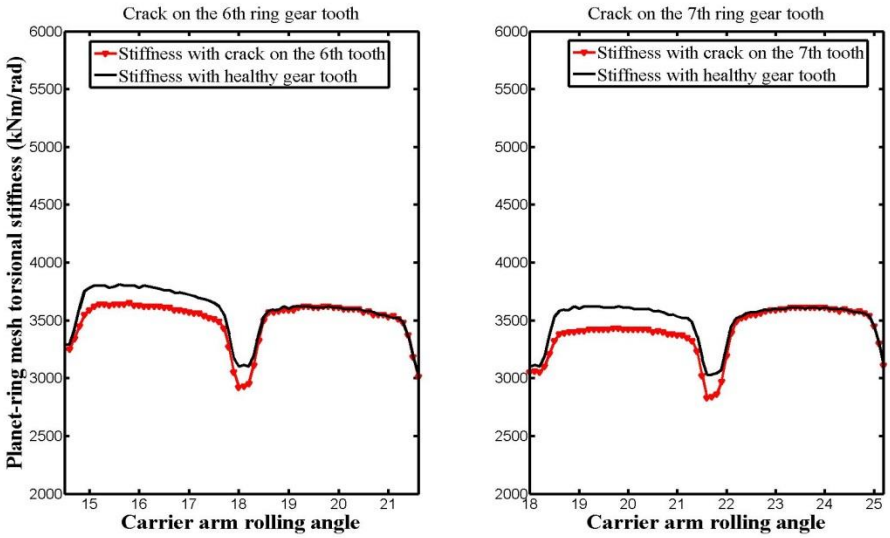

Figure 5.21 Ring-planet stiffness with crack on the 6th gear tooth and crack on the 7th gear tooth

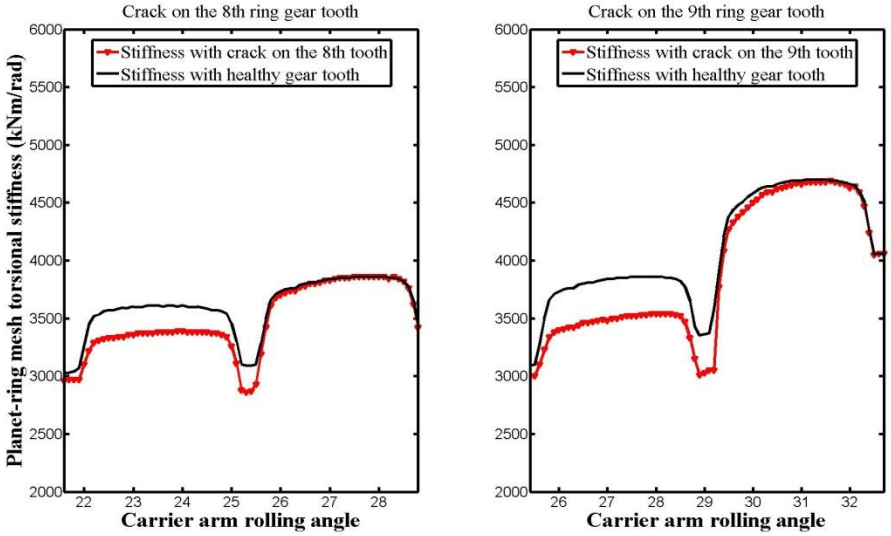

Figure 5.22 Ring-planet stiffness with crack on the 8th gear tooth and crack on the 9th gear tooth

Fig. 5.18 – 5.22 compared the cracked ring-planet mesh stiffness with the healthy ring gear tooth and it was found that the stiffness with the crack on different teeth showed diverse variation characteristics and different stiffness reduction through the rotation. More specifically, the healthy ring gear case in Fig. 5.18 showed a modulation effect caused by the pin supports as discussed previously and this mesh stiffness curve will be used to compare with the stiffness with cracks on different teeth. When the crack happened on the 1st ring

gear tooth, the cracked stiffness reduced around 500 kNm/rad and then quickly went back to its normal value, which was identical with the healthy stiffness. When the crack happened on the 2nd ring gear tooth, the reduction of the stiffness can still be observed, but not as large as the one on the 1st tooth. When the crack happened between the 3rd tooth and the 6th tooth, very similar stiffness reduction can be observed except that their stiffness value reduced by different levels and decreased gradually, that is, the second peak was lower than the first peak. Starting from the 7th tooth, the stiffness value began to increase (the second peak was higher than the first peak) and the trend was very similar to that with the 1st tooth. An interesting thing to notice is the large jump on the 9th tooth as the damaged tooth exited the mesh.

5.4 Conclusions

The effect of ring gear rim thickness, the number of pin supports, the flexibility of the pin support, and the crack locations on the ring-planet mesh stiffness has been studied in this chapter. It was shown that the effect of ring gear rim thickness was different with different ring gear boundary conditions. When the boundary condition was fully constrained, the effect on the mesh stiffness was seen as constant and a factor can be assigned to account for the effect. A constant peak-peak value was found through the whole mesh curve, which was around 3600kNm/rad. However, a constant factor cannot be applied when pin-supported conditions are used.

Two different cases were selected to study the effect of the number of supports on the ring-planet mesh stiffness. A very obvious modulation effect was observed when the pin number was 11 and 22 (integer/non-integer ratio relative to number of ring gear teeth) while no such modulation effect was observed when the pin number was 556. It was also found that the thick rim can weaken the pin-support modulation effect.

Three cases were selected to study the effect of the pin flexibility. It was shown that a flexible pin can smooth the ring-planet mesh stiffness curve and the pin flexibility would dominate the mesh stiffness when the pin stiffness was small. Also, the flexible pin can weaken the pin-support modulation effect and potentially reduce the planetary gear vibration.

This result demonstrates that the pin flexibility has great influence on the ring-planet mesh stiffness.

Tooth cracks on different ring gear teeth were modelled to study the effect on the mesh stiffness for various pin support conditions. It was found that the mesh stiffness with the crack on different teeth showed diverse characteristics and different stiffness reductions through the rotation, which can be used to help identify the ring gear crack location. Furthermore, these stiffness curves can be incorporated into the planetary gear dynamic models to help further understanding of the planetary gear dynamic responses under these circumstances.

Chapter 6 Dynamic modelling of planetary gears with flexible ring gear

6.1 Introduction

Mathematical planetary gear models can be used to help understand the complex dynamic response from the gearbox (Kahraman, 1994a, 1994b, 1994c) and the planetary gear system considered in this study is a single-stage planetary gear set, as shown in Fig. 6.1. The system consists of an input motor, one sun gear, three planet gears, one ring gear, one carrier arm and an output load.

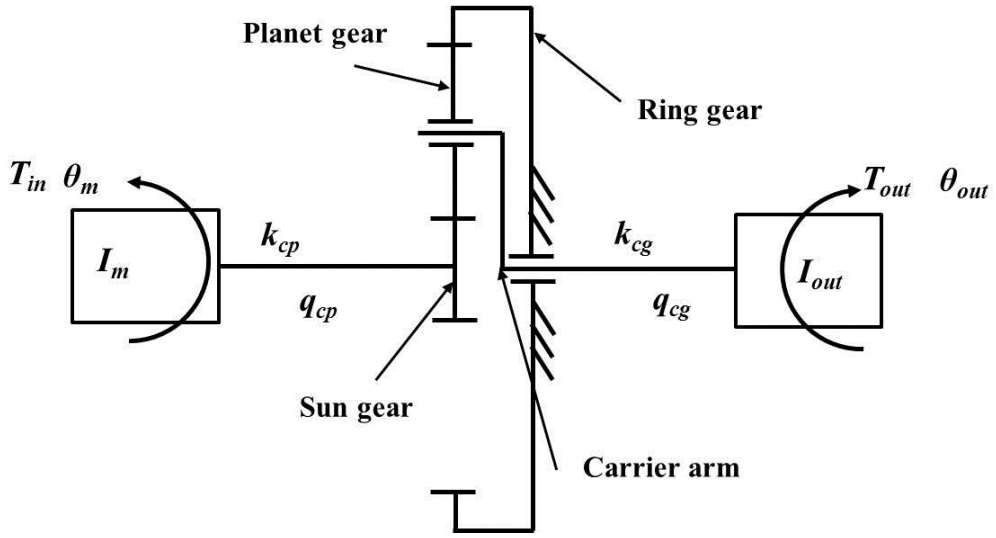

Figure 6.1 Planetary gear train model

In the planetary gear model, the ring gear can be supported by either the uniformly distributed constraint as discussed in chapter 3 or by the pin constraint as discussed in chapter 5. For both scenarios, the casing deflection of the ring gear is included by assuming that the ring gear rim can be modelled as FEA beam elements, whose section dimension can be approximated using the ring gear parameters. The number of the beam elements can be set to be equal to the ring gear teeth number in order to associate every beam element with a tooth, as shown in Fig. 6.2. The motivation for considering a flexible ring is that a stationary transducer on the ring gear is used as a common method for the planetary gear fault

diagnosis (Mark, 2009; Mark & Hines, 2009; McFadden, 1991; McFadden & Smith, 1985b; McNames, 2002) and it is hoped the method described in this study can be used to help further understanding of the vibration response from the stationary transducer mounted on the planetary gear casing.

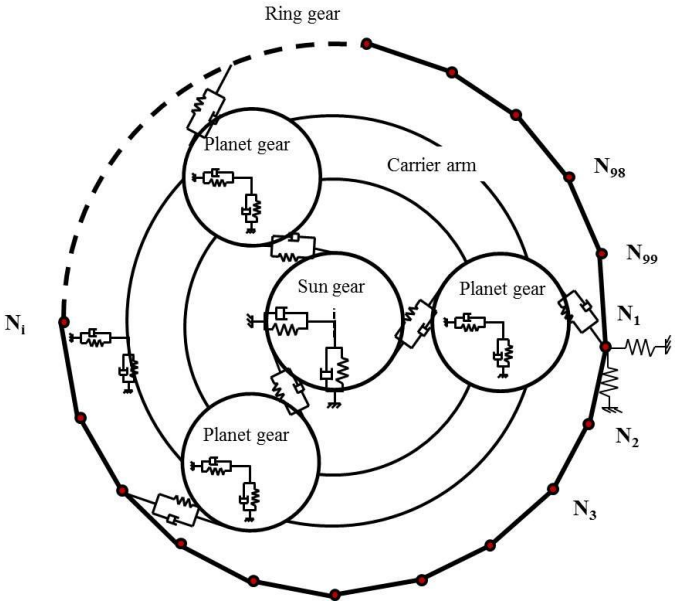

Figure 6.2 Planetary gear with flexible ring gear

For a planetary gear set, the main internal excitations come from the variation of the sun-planet mesh stiffness and the variation of the ring-planet mesh stiffness. The variation of these stiffnesses has been studied previously in chapter 3 and special care has been given to the effect of the boundary condition on the ring-planet mesh stiffness, which has been studied in chapter 5. With the help of the planetary gear mathematical model, the vibration of each component in the planetary gear system can be obtained directly and the resultant ring-planet dynamic forces are found to be the only direct internal excitation from the gear system. As a result, an additional calculation procedure can be developed using FEA methods to calculate the ring gear casing vibration once the ring-planet force was obtained.

6.2 The dynamic modelling of the planetary gear system

6.2.1 Lumped-parameter modelling of the planetary gear system

In this section, a two dimensional lumped-parameter planetary gear mathematical model was created to study the dynamic response and to obtain the dynamic mesh force in the gear system, as shown in Fig. 6.3. The subscript *s* represent the sun gear, *r* stands for the ring gear, c means carrier arm and p1, p2, p3 are the subscript for the 1st, 2nd, 3rd planet gear respectively. Each of these components has three DOFs: transverse motions in the x-axis and y-axis, and rotation. The transverse motions of the sun, planet, ring and carrier (xj, yj, j=s, r, c, p1, p2, p3) were measured with respect to a rotating frame of reference fixed to the carrier (Liang et al., 2015). The major assumptions in this lumped-parameter model are the following,

(1). The gear only vibrates in the 2 dimensional plane;

(2). Unloaded transmission errors in the gears are ignored;

(3). The friction forces between sun-planet and ring-planet are ignored;

(4). The backlash was ignored;

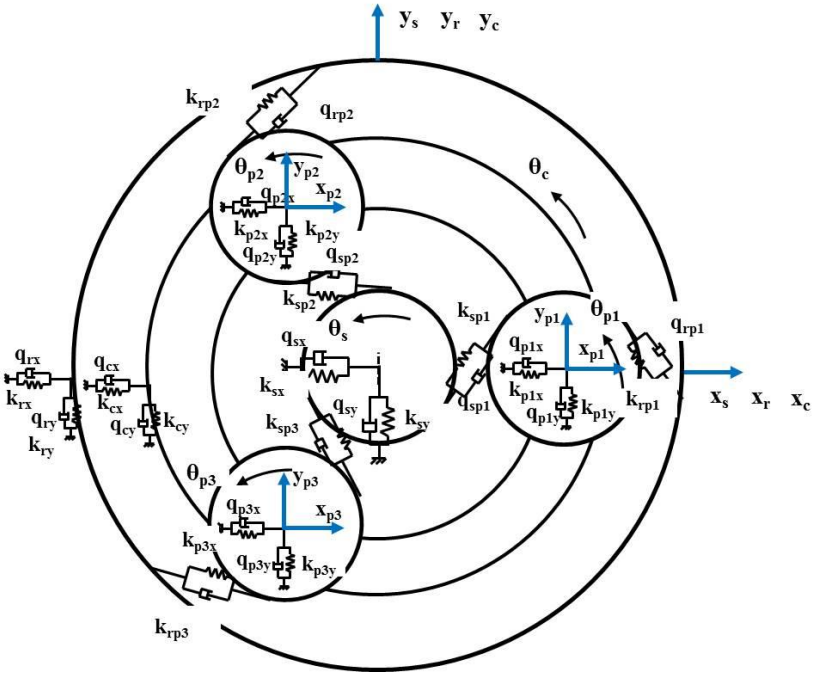

Figure 6.3 Lumped-parameter planetary gear model (Liang et al., 2015)

The resulting equations of motion for this planetary gear system are shown as follows.

For the rotary motion of the motor, the motion equation is,

$$I_m\ddot{\theta}_m = T_{in} - T_s,$$

$$T_s = k_{cp}(\theta_m - \theta_s) + q_{cp}\left(\dot{\theta}_m - \dot{\theta}_s\right). \tag{6.1}$$

For the motion of the sun gear, the motion equation is,

$$m_s\ddot{x}_s + k_{sx}x_s + q_{sx}\dot{x}_s + \sum_{i=1}^{3}\left[F_{spi}\cos\left(\varphi_{spi}\right)\right] = m_s x_s\Omega^2 + 2m_s\dot{y}_s\Omega + m_s y_s\dot{\Omega},$$

$$m_s\ddot{y}_s + k_{sy}y_s + q_{sy}\dot{y}_s + \sum_{i=1}^{3}\left[F_{spi}\sin\left(\varphi_{spi}\right)\right] = m_s y_s\Omega^2 - 2m_s\dot{x}_s\Omega - m_s x_s\dot{\Omega},$$

$$(I_s/r_s)\ddot{\theta}_s + \sum_{i=1}^{3}F_{spi} = T_s/r_s, \tag{6.2}$$

where F_{spi} is the normal contact force between sun gear and the ith planet,

$$F_{spi} = k_{spi}\delta_{spi} + q_{spi}\dot{\delta}_{spi},$$

$$\delta_{spi} = \left(x_s - x_{pi}\right)\cos\varphi_{spi} + \left(y_s - y_{pi}\right)\sin\varphi_{spi} + r_s\theta_s + r_p\theta_{pi} - r_c\theta_c\cos\alpha_{sp},$$

$$\varphi_{spi} = \frac{\pi}{2} - \alpha_{sp} + \varphi_i,$$

$$\varphi_i = \frac{2\pi(i-1)}{3}; i = 1, 2, 3$$

For the motion of the carrier arm, the motion equation is,

$$m_c\ddot{x}_c + k_{cx}x_c + q_{cx}\dot{x}_c - \sum_{i=1}^{3}F_{cpix} = m_c x_c\Omega^2 + 2m_c\dot{y}_c\Omega + m_c y_c\dot{\Omega},$$

$$m_c\ddot{y}_c + k_{cy}y_c + q_{cy}\dot{y}_c + \sum_{i=1}^{3}F_{cpiy} = m_c y_c\Omega^2 - 2m_c\dot{x}_c\Omega - m_c x_c\dot{\Omega},$$

$$(I_c/r_c)\ddot{\theta}_c + \sum_{i=1}^{3}F_{cpix}\sin\varphi_i - \sum_{i=1}^{3}F_{cpiy}\cos\varphi_i = T_c/r_c,$$

$$T_c = k_{cg}(\theta_c - \theta_{out}) + k_{cg} \cdot (\dot{\theta}_c - \dot{\theta}_{out}), \tag{6.3}$$

where F_{cpix} and F_{cpiy} describe the planet bearing forces between the carrier and the i-th planet in the x and y directions:

$$F_{cpix} = k_{pix}(x_{pi} - x_c) + q_{pix}(\dot{x}_{pi} - \dot{x}_c),$$

$$F_{cpiy} = k_{piy}(y_{pi} - y_c) + q_{piy}(\dot{y}_{pi} - \dot{y}_c),$$

For the motion of the planet gears:

$$\begin{aligned} m_{pi}\ddot{x}_{pi} + F_{cpix} - F_{spi}\cos\varphi_{spi} - F_{rpi}\cos\varphi_{rpi} \\ = m_{pi}x_{pi}\Omega^2 + 2m_{pi}\dot{y}_{pi}\Omega + m_{pi}y_{pi}\dot{\Omega} + m_{pi}r_c\Omega^2\cos\varphi_i, \end{aligned}$$

$$\begin{aligned} m_{pi}\ddot{y}_{pi} + F_{cpiy} - F_{spi}\sin\varphi_{spi} - F_{rpi}\sin\varphi_{rpi} \\ = m_{pi}y_{pi}\Omega^2 - 2m_{pi}\dot{x}_{pi}\Omega - m_{pi}x_{pi}\dot{\Omega} + m_{pi}r_c\Omega^2\sin\varphi_i, \end{aligned}$$

$$(I_{pi}/r_p)\ddot{\theta}_{pi} + F_{spi} - F_{rpi} = 0, \tag{6.4}$$

where F_{rpi} is the normal contact force between ring gear and the *i*th planet,

$$F_{rpi} = k_{rpi}\delta_{rpi} + q_{rpi}\dot{\delta}_{rpi},$$

$$\delta_{rpi} = (x_r - x_{pi})\cos\varphi_{rpi} + (y_r - y_{pi})\sin\varphi_{rpi} + r_r\theta_r - r_p\theta_{pi} - r_c\theta_c\cos\alpha_{rp},$$

$$\varphi_{rpi} = \frac{\pi}{2} + \alpha_{rp} + \varphi_i.$$

For the motion of the ring gear, the motion equation is,

$$m_r\ddot{x}_r + k_{rx}x_r + q_{rx}\dot{x}_r + \sum_{i=1}^{3} F_{rpi}\cos\varphi_{rpi} = m_r x_r\Omega^2 + 2m_r\dot{y}_r\Omega + m_r y_r\dot{\Omega},$$

$$m_r\ddot{y}_r + k_{ry}y_r + q_{ry}\dot{y}_r + \sum_{i=1}^{3} F_{rpi}\sin\varphi_{rpi} = m_r y_r\Omega^2 - 2m_r\dot{x}_r\Omega - m_r x_r\dot{\Omega},$$

$$(I_r/r_r)\ddot{\theta}_r + (q_{rt}/r_r)\dot{\theta}_r + (k_{rt}/r_r)\theta_r + \sum_{i=1}^{3} F_{rpi} = 0. \tag{6.5}$$

For the rotary motion of the load, the motion equation is,

$$I_{out}\ddot{\theta}_{out} = -T_{out} + T_c, \tag{6.6}$$

The following nomenclatures were used in the gear system,

I_m, I_s, I_{pi}, I_c, I_r, I_{out}: mass inertia of the motor, sun gear, planet gear, carrier arm, ring gear, output load;

m_s, m_{pi}, m_c, m_r: mass of the sun, planet gear, carrier and ring;

θ_m, θ_s, θ_{pi}, θ_c, θ_r, θ_{out}: angular displacement of the motor, sun gear, planet gear, carrier arm, ring gear, output load;

x_j (j= s, pi, c, r): linear displacement in the horizontal direction measured in the rotating frame;

y_j (j= s, pi, c, r): linear displacement in the vertical direction measured in the rotating frame;

k_{cp}, k_{cg}: stiffness of the input coupling and shaft and the output coupling and shaft;

q_{cp}, q_{cg}: damping of the input coupling and shaft and the output coupling and shaft;

k_{sx}, k_{sy}: bearing radial stiffness of the sun gear;

q_{sx}, q_{sy}: bearing radial damping of the sun gear;

k_{rx}, k_{ry}: bearing radial stiffness of the ring gear;

q_{rx}, q_{ry}: bearing radial damping of the ring gear;

k_{cx}, k_{cy}: bearing radial stiffness of the carrier arm;

q_{cx}, q_{cy}: bearing damping of the carrier arm;

k_{pix}, k_{piy}: bearing stiffness of the planet gear;

q_{pix}, q_{piy}: bearing damping of the planet gear;

k_{spi}, k_{rpi}: mesh stiffness of the i-th sun-planet, ring-planet;

q_{spi}, q_{rpi}: mesh damping of the i-th sun-planet, ring-planet;

k_{rt}, q_{rt}: stiffness and damping of ring gear in the torsional direction;

r_s, r_p, r_r: base radius of the sun gear, planet gear, ring gear;

r_c: radius of the circle passing through planet gear centres;

T_{in}, T_{out}: input motor torque and output load torque;

δ_{spi}, δ_{rpi}: relative displacement on the lines of action of i-th sun-planet, ring-planet;

φ_i: circumferential angle of i-th planet;

Ω: carrier arm rotation speed.

As the transverse motion of the planetary gear component are measured with respect to the rotating carrier arm, the corresponding displacement/velocity/acceleration response from these transverse motions need to be transformed back to the global coordinate that was fixed with the ground. As shown in Fig. 6.4, X−O−Y is the global coordinate that connects with the ground and x−o−y is the rotating coordinate that connects with the carrier arm.

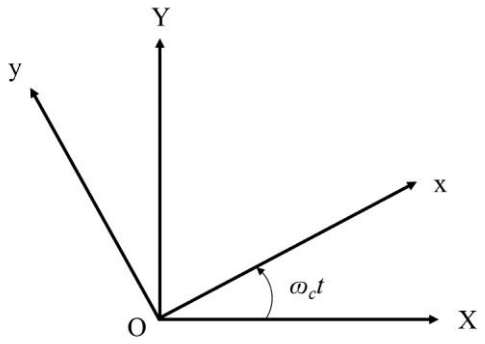

Figure 6.4 Rotating coordinate and global coordinate

To get the displacement reactions in the global coordinate, the following relation can be derived (Amirouche, 2007),

$$\begin{pmatrix} x \\ y \end{pmatrix} = \begin{pmatrix} \cos(\Omega t) & \sin(\Omega t) \\ -\sin(\Omega t) & \cos(\Omega t) \end{pmatrix} \begin{pmatrix} X \\ Y \end{pmatrix}, \tag{6.7}$$

The rotating velocity Ω is the carrier arm angular velocity as the rotating coordinate was connected with the carrier arm. When the planetary gear system reaches stable motion, the rotating velocity Ω can be assumed as constant and the velocity/acceleration reactions in the fixed coordinate can be simplified as (Amirouche, 2007),

$$\begin{pmatrix} \dot{x} \\ \dot{y} \end{pmatrix} = \begin{pmatrix} \cos(\Omega t) & \sin(\Omega t) \\ -\sin(\Omega t) & \cos(\Omega t) \end{pmatrix} \begin{pmatrix} \dot{X} \\ \dot{Y} \end{pmatrix} + \begin{pmatrix} -\Omega\sin(\Omega t) & \Omega\cos(\Omega t) \\ -\Omega\cos(\Omega t) & -\Omega\sin(\Omega t) \end{pmatrix} \begin{pmatrix} X \\ Y \end{pmatrix}, \tag{6.8}$$

$$\begin{pmatrix}\ddot{x}\\ \ddot{y}\end{pmatrix}=\begin{pmatrix}\cos(\Omega t) & \sin(\Omega t)\\ -\sin(\Omega t) & \cos(\Omega t)\end{pmatrix}\begin{pmatrix}\ddot{X}\\ \ddot{Y}\end{pmatrix}+\begin{pmatrix}-2\Omega\sin(\Omega t) & 2\Omega\cos(\Omega t)\\ -2\Omega\cos(\Omega t) & -2\omega_c\sin(\Omega t)\end{pmatrix}\begin{pmatrix}\dot{X}\\ \dot{Y}\end{pmatrix}+$$

$$\begin{pmatrix}-\Omega^2\cos(\Omega t) & -\Omega^2\sin(\Omega t)\\ \Omega^2\sin(\Omega t) & -\Omega^2\cos(\Omega t)\end{pmatrix}\begin{pmatrix}X\\ Y\end{pmatrix}.$$

(6.9)

6.2.2 Mesh stiffness summarized and evaluation

The FEA method mentioned in chapter 3 and chapter 5 will be summarized here to represent the sun-planet and ring-planet mesh stiffness with or without the cracked tooth. The mesh stiffness in each of these mesh pairs will be presented and furthermore, the variation of the mesh stiffness in one carrier arm revolution will also be presented. Overall, there are four cases considered in this study: a tooth crack in the sun gear, a tooth crack in the planet gear (sun side), a tooth crack in the planet gear (ring side) and a tooth crack in the ring gear (with different boundary conditions).

If the sun gear has a crack, the cracked tooth will mesh with each of the planet gears successively and therefore, the mesh stiffness of all sun-planet pairs will be affected (Liang et al., 2014). The variation of the sun-planet mesh stiffness in each of the mesh pairs should share the same characteristics except that they are not necessarily in the same phase and the phase relationship can be calculated in equation (3.35). Here, the phase is calculated as 0 degrees in chapter 3. Fig. 6.5 shows the mesh stiffness of the three sun-planet gear pairs with the impact of the cracked sun gear tooth. The mesh phase is also considered in these curves. The curves k_{sp1}, k_{sp2}, k_{sp3} represent the sun-planet mesh stiffness in the 1st, 2nd, 3rd mesh pairs respectively. The variation of the ring-planet mesh stiffness is assumed to be in perfect condition. In the figure, one full sun gear shaft rotation was considered, which was corresponding to 76.6 degrees of carrier arm rotation.

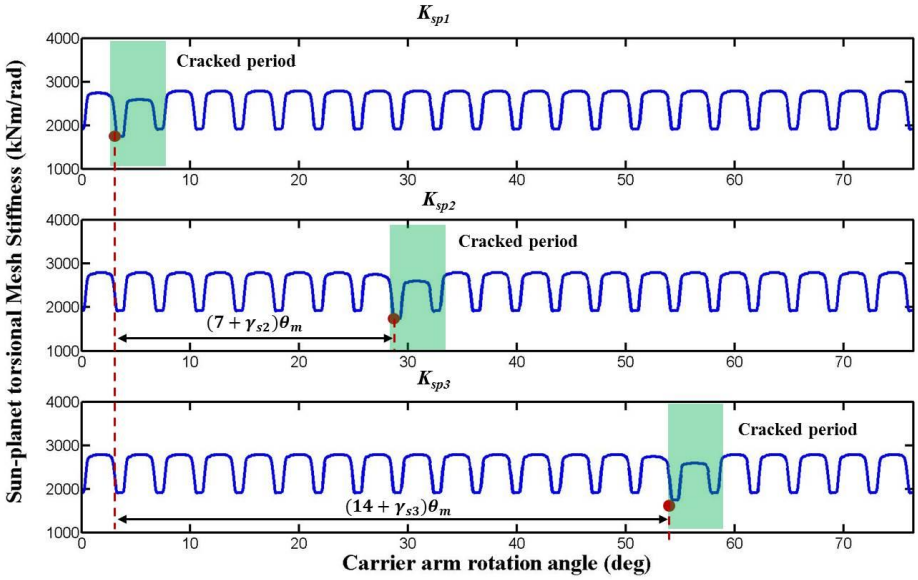

Figure 6.5 Sun-planet mesh stiffness variation with the crack on a sun gear tooth

As shown in Fig. 6.5, the time intervals of the crack period can be evaluated analytically using equation (3.35). The time interval between the cracked period on the 1st sun-planet stiffness curve and the cracked period on the 2nd mesh stiffness curve is (7+γs2)θm, in which γs2 is 0 as calculated in equation (3.16) and θm is the carrier arm rotation angle covering all the sun gear teeth in one sun gear shaft rotation and is equal to 360°/Zr (3.6°). The time interval between the cracked period on the 1st sun-planet stiffness curve and the cracked period on the 3rd mesh stiffness curve is (14+γs3)θm and the parameters can be calculated correspondingly.

Fig. 6.6 described the variation of the sun-planet mesh stiffness curve k_{sp1} over one carrier arm rotation with the impact of the sun gear crack. As shown in the figure, the impact of the crack will appear five times in one carrier arm rotation which agrees with the sun-carrier speed ratio, which is 5.71.

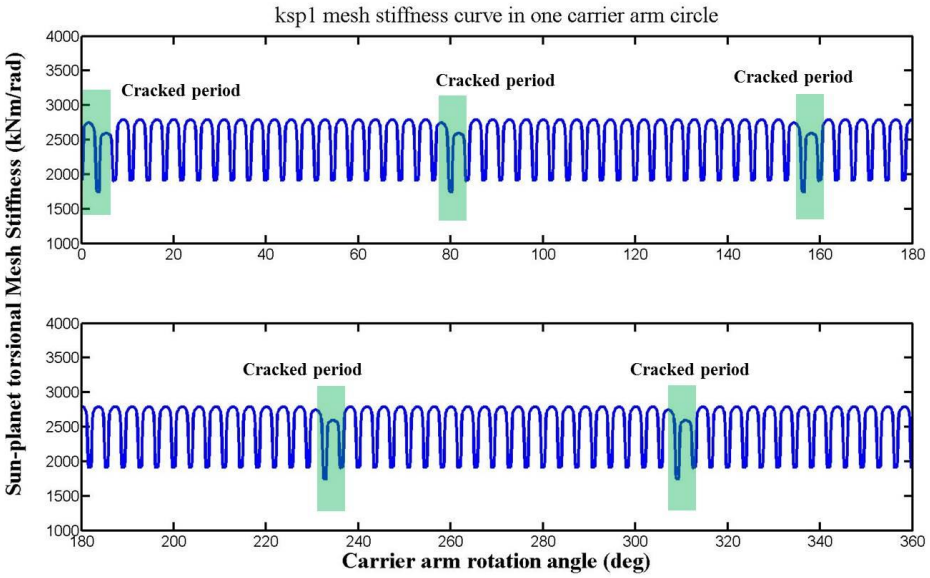

Figure 6.6 Sun-planet mesh stiffness of the 1st pair over one carrier arm revolution

If a cracked tooth occured on one of the planet gears and the crack is on the meshing side with the sun gear, only one pair of sun-planet gears will be affected by the planet gear crack. The ring-planet mesh stiffness is assumed to be in perfect condition as the cracked planet gear tooth can still bear the compressive stiffness as if no crack exists (Liang et al., 2014). Fig. 6.7 presents the mesh stiffness of the three sun-planet gear pairs with the cracked planet gear tooth effect on the 1st sun-planet mesh pair. The variation of the K_{sp2} and K_{sp3} mesh stiffness curves will not be affected by the impact of the crack. In the figure, one full planet gear shaft rotation was considered, which was corresponding to 144 degrees of carrier arm rotation. Fig. 6.8 describes the variation of the sun-planet mesh stiffness curve k_{sp1} in one carrier arm rotation.

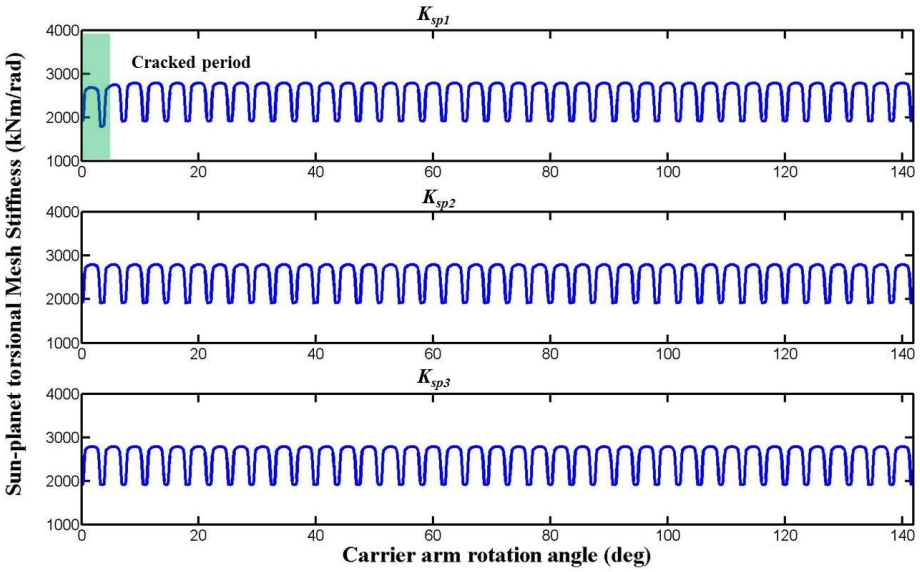

Figure 6.7 Sun-planet mesh stiffness with crack on the 1st sun-planet mesh pair

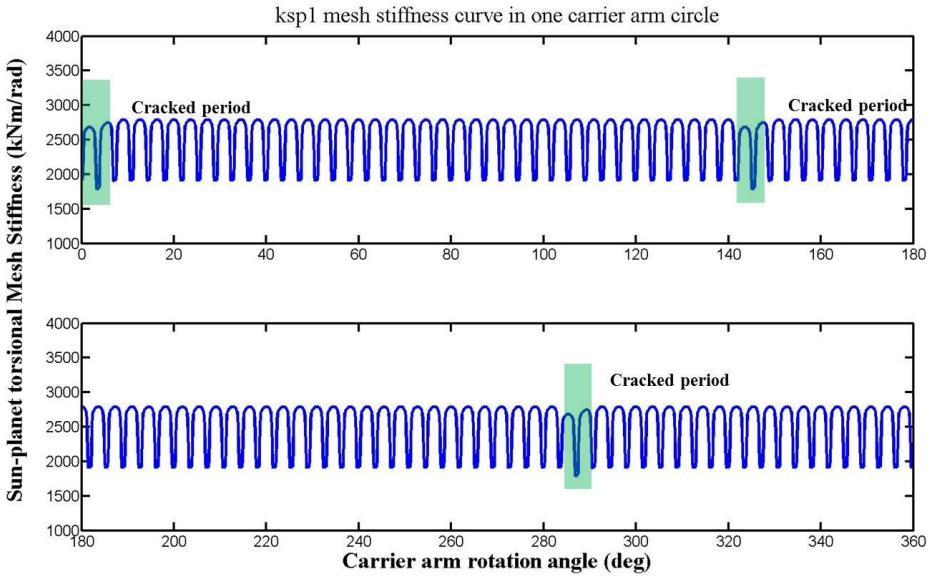

Figure 6.8 Mesh stiffness of 1st sun-planet pairs over one carrier arm revolution

If the planet gear has a crack on the ring gear side, only one pair of ring-planet gears will be affected by the planet tooth crack. However, the sun-planet mesh stiffness is still assumed not to be affected as the cracked planet tooth can still bear the compressive stiffness from the sun-planet mesh as if no crack exists (Liang et al., 2014). Fig. 6.9 shows the three ring-planet gear mesh stiffnesses with the effect of the crack on the 1st ring-planet mesh pair. The ring gear in these curves is assumed to be uniformly constrained and no modulation effect due to

the support was included. In the figure, one full planet gear shaft rotation was considered, which was corresponding to 144 degrees of carrier arm rotation. Fig. 6.10 described the variation of the ring-planet mesh stiffness curve krp1 for one carrier arm rotation.

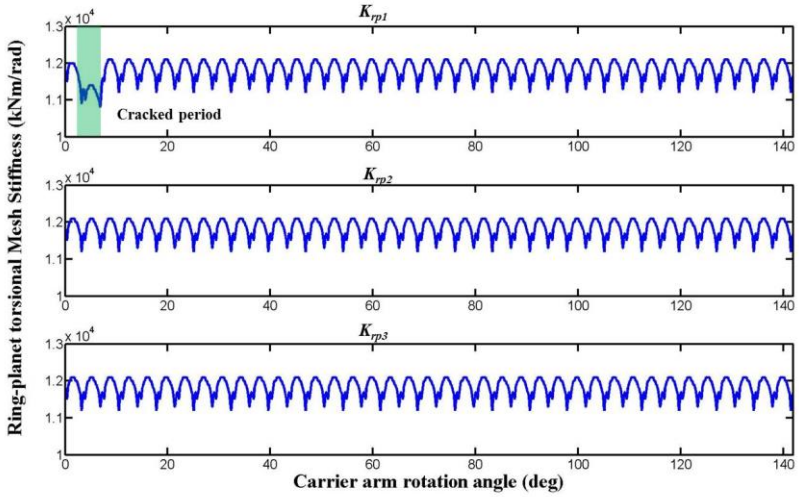

Figure 6.9 Ring-planet mesh stiffness with crack on the 1st ring-planet mesh pair

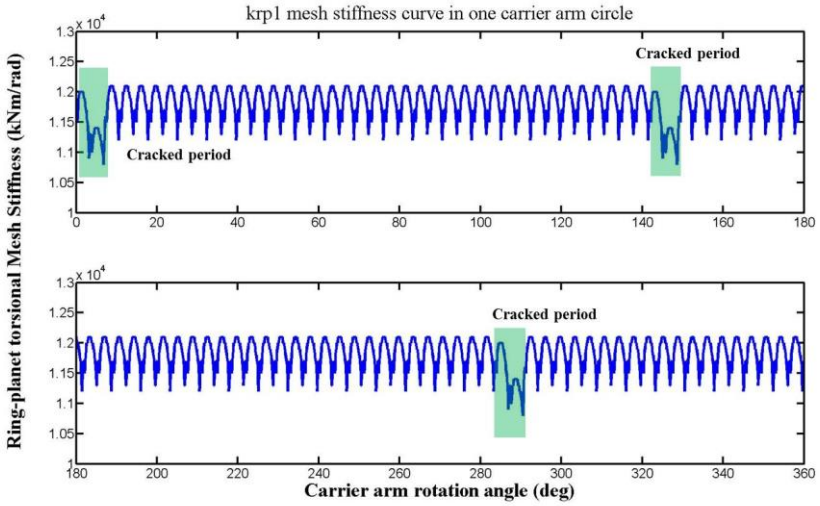

Figure 6.10 Mesh stiffness of the 1st planet-ring over one carrier arm revolution

If the ring gear has a crack, the cracked ring gear tooth will mesh with each of the planet gears successively as the sun gear did and therefore, all the ring-planet mesh stiffnesses will be affected (Liang et al., 2014). The variation of the three ring-planet mesh stiffness should share the same characteristics except that their phases are not necessary identical to each other and the phase relationship can be calculated in equation (3.35). Fig. 6.11 shows the

mesh stiffness of the three ring-planet gear pairs with the impact of the ring gear tooth crack. The ring gear in these curves is assumed to be uniformly constrained and no modulation effect due to the support was included.

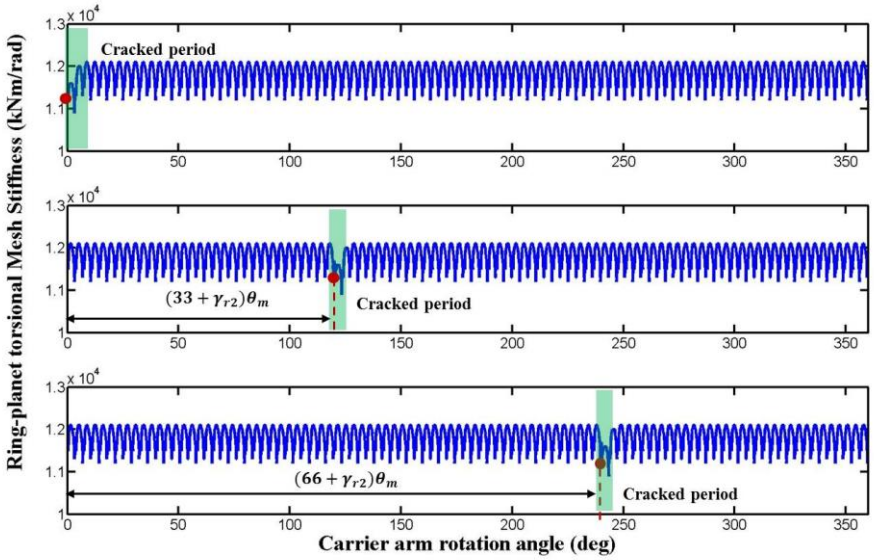

Figure 6.11 Ring-planet mesh stiffness with crack on ring gear

As shown in Fig. 6.11, the time intervals of the crack period on the stiffness curve can be evaluated analytically using equation (3.35). The time interval of the cracked period between the 1st ring-planet stiffness curve and the 2nd ring-planet stiffness curve is (33+γr2)θm, in which γr2 is 0 as calculated in equation (3.16) and θm is the carrier arm rotation angle and is equal to 360°/Zr (3.6°). The time interval of the cracked period between the 1st ring-planet stiffness curve and the 3rd ring-planet stiffness curve is (14+γr3)θm and the parameters can be calculated correspondingly.

If the pin-supported modulation effect (discussed in chapter 5) was considered in the ring-planet mesh, all the ring-planet mesh stiffnesses can also be obtained. The mesh stiffness curve of the sun-planet pairs was assumed to be identical with those shown in Fig. 6.5–Fig. 6.8. Fig. 6.12 presents the ring-planet mesh stiffness k_{rp1} with the influence of the pin-supported as well as the crack on tooth number 6.

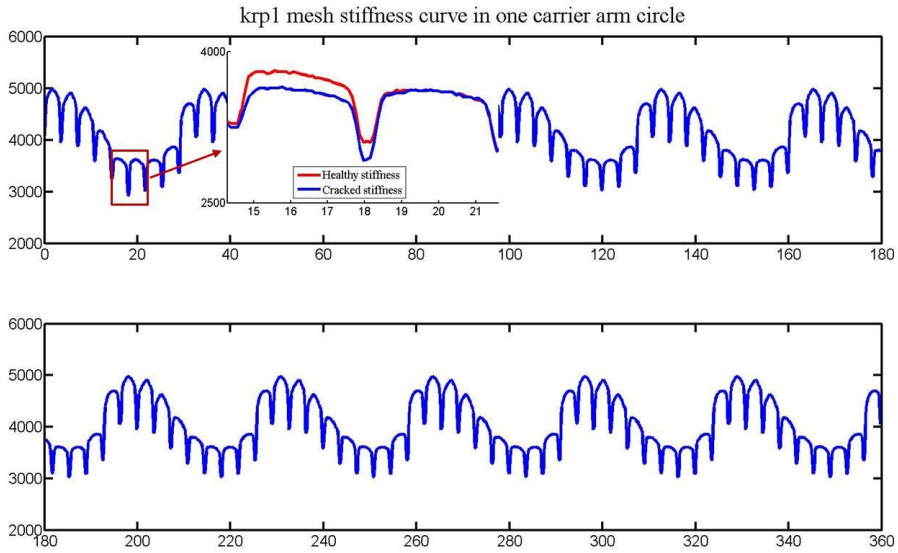

Figure 6.12 Mesh stiffness of planet-ring with pin support modulation

The MATLAB ode solver was used to solve the equation (6.1) to simulate the vibration response in this research. A constant input torque of 100 Nm was assumed to be provided by the input motor and a time-varying output load having a form of $T_{out} = 0.75\dot{\theta}_{out}^2$ was assumed to be provided by the output load. From the ode solver, the planetary gearbox system was simulated with the incorporation of sun-planet and ring-planet mesh stiffnesses summarized above. The simulation results were obtained after the initial transient start-up stage had decayed away and the steady-state conditions were achieved (Howard et al., 2001). A nominal carrier arm angular rotating speed of 27.6 rad/s was obtained and the nominal sun gear angular rotating speed of 157.7 rad/s can also be obtained.

6.3 FEA modelling of the ring gear

6.3.1 FE ring gear beam modelling with moving load

In practical applications, transducers tend to be mounted on the ring gear or on its housing as a common monitoring method for the planetary gear system and the vibration response of the transducer experiences an amplitude modulation as each planet passes through this fixed transducer location (Inalpolat & Kahraman, 2009, 2010). The vibration source of the transducer is the summation of the sun gear vibration, ring gear vibration and planet gear vibration, each of which can be weighted by different Hanning window functions (Inalpolat

& Kahraman, 2009, 2010). Some recent publications on how to model these weighted window functions and the resultant vibration can be found in Ref. (Liu et al., 2016; Feng & Zuo, 2012).

However, these publications indicated that a proper consideration of these effects would require a deformable-body dynamic model that can represent the transmission path between a given gear mesh and the transducer (Feng & Zuo, 2012; Inalpolat & Kahraman, 2009, 2010; Liu et al., 2016). As a result, the ring gear with its support is modelled as a moving load problem on the FE beam in this research to formulate the vibration signal caused by the carrier arm rotation in this research (Forbes & Randall, 2008). The ring gear was represented using classical two-node beam elements whose cross-section parameters can be determined by the ring gear parameters. The number of beam elements is set to be the number of teeth on the ring gear in order to associate a node with every tooth (Abousleiman & Velex, 2006). Each node has three degrees of freedom, namely the axial, radial and torsional motions.

If there is a concentrated load P moving along the beam, the force on all beam nodes are equal to zero except the beam nodes that are subjected to the concentrated force P. For an instance, one concentrated ring-planet force is on element j, as shown in Fig. 6.13. The shape function for a straight beam element can be defined as (Smith et al, 2013),

$$N_1 = 1 - \xi,$$

$$N_2 = 1 - 3\xi^2 + 2\xi^3,$$

$$N_3 = (\xi - 2\xi^2 + \xi^3)L,$$

$$N_4 = \xi,$$

$$N_5 = 3\xi^2 - 2\xi^3,$$

$$N_6 = (-\xi^2 + \xi^3)L,$$

$$\xi = \frac{x}{L}, \tag{6.10}$$

where L is the beam element length and x is the distance along the element to the point of concentrated force P.

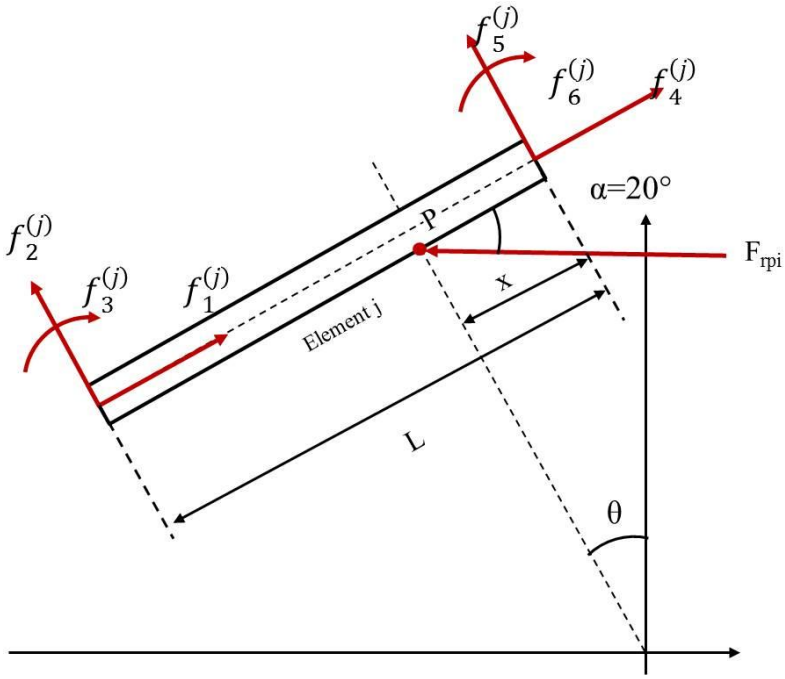

Figure 6.13 Ring gear FE beam model

At any instance, t=rΔt (r=1 to m, time step), the position of the moving load Frpi, relative to the starting position is given by (Wu et al., 2000),

$$x_t = Vr\Delta t = \Omega r_r r\Delta t \tag{6.11}$$

where Ω is the carrier arm angular rotating speed and r_r is the ring gear base radius. The element number, j, that the moving concentrated force is applied to at any time t can be found from (Wu et al., 2000),

$$\text{j = (the integer part of } \quad (x/L)\ ) + 1. \tag{6.12}$$

The node number of the j-th beam element is j and j+1 and then, the following equations for nodal forces and moments can be obtained when the moving concentrated force is on the j-th beam element at any time,

$$f_1^{(j)}(t) = \left(F_{rpi}\cos\alpha\right)N_1,$$

$$f_2^{(j)}(t) = \left(F_{rpi}\sin\alpha\right)N_2,$$

$$f_3^{(j)}(t) = \left(F_{rpi}\sin\alpha\right)N_3,$$

$$f_4^{(j+1)}(t) = \left(F_{rpi}\cos\alpha\right)N_4,$$

$$f_5^{(j+1)}(t) = \left(F_{rpi}\sin\alpha\right)N_5,$$

$$f_6^{(j+1)}(t) = \left(F_{rpi}\sin\alpha\right)N_6. \tag{6.13}$$

Noting that the nodal force $f_n^{(s)}$ (n =1−6; s is the node number except j and j+1) at this instance. The symbol ξ can also be presented in terms of the global displacement x_t instead of local displacement x,

$$\xi = \frac{x_t - (j-1)L}{L}. \tag{6.14}$$

For a planetary gear with three planets, there are three concentrated forces moving with the carrier arm simultaneously. The method mentioned above can still be used to evaluate the contribution of the moving ring-planet forces from the 2nd and 3rd except that the global displacement needs to be modified,

$$x_t 2 = \Omega_c r_r r\Delta t + \frac{2\pi}{3} r_r,$$

$$x_t 3 = \Omega_c r_r r\Delta t + \frac{4\pi}{3} r_r, \tag{6.15}$$

where x_t2 and x_t3 are the global displacements describing the positions of the second and third moving ring-planet force. The element number that the second and third ring-planet forces is on at any time t can be obtained,

$$\text{j2} = (\text{the integer part of } {x_t 2}/{L}\ ) + 1,$$

$$\text{j3} = (\text{the integer part of } {x_t 3}/{L}\ ) + 1. \tag{6.16}$$

The effect of all the force and movement due to the three moving load can now be obtained by considering all the contributions from the three ring-planet forces. Fig. 6.14 shows the FEA model with the moving ring-planet mesh forces along the ring gear. The transient analysis in ANSYS was used for analysing the effect of the moving load on the ring gear beam and the moving speed was assumed to be constant.

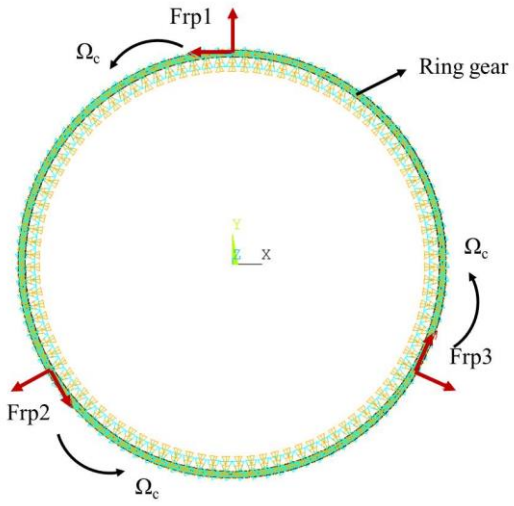

Figure 6.14 FEA ring gear beam model with moving load

6.3.2 Ring-planet mesh force summary

The acceleration signal at the transducer location was caused by the dynamic mesh force from the sun-planet pair and the dynamic mesh force from the ring-planet pair (Wu et al., 2000). With some weighting functions, the resultant force applied on the ring gear can be evaluated with the availability of the sun-planet force and ring-planet force. When the sun-planet mesh force is transmitted to the transducer, it has to pass through the planet gear and the planet bearing and therefore the sun-planet mesh force would have been attenuated during this process. In this research, it was assumed that only the ring-planet mesh force was applied on the ring gear while the sun-planet mesh force has been attenuated to zero. It is expected that the ring-planet mesh force will contain the fault information from the gear mesh, even the sun-planet meshes. This section will summarize the ring-planet mesh force from the planetary gear lumped parameter model with different situations.

Fig. 6.15 shows the resultant ring-planet mesh forces for the healthy planetary gear system. No cracks were present either on the sun-planet pair or on the ring-planet pair. The ring gear was uniformly supported and the original data was resampled into equi-spaced phase data using 2^{10} points per carrier arm revolution.

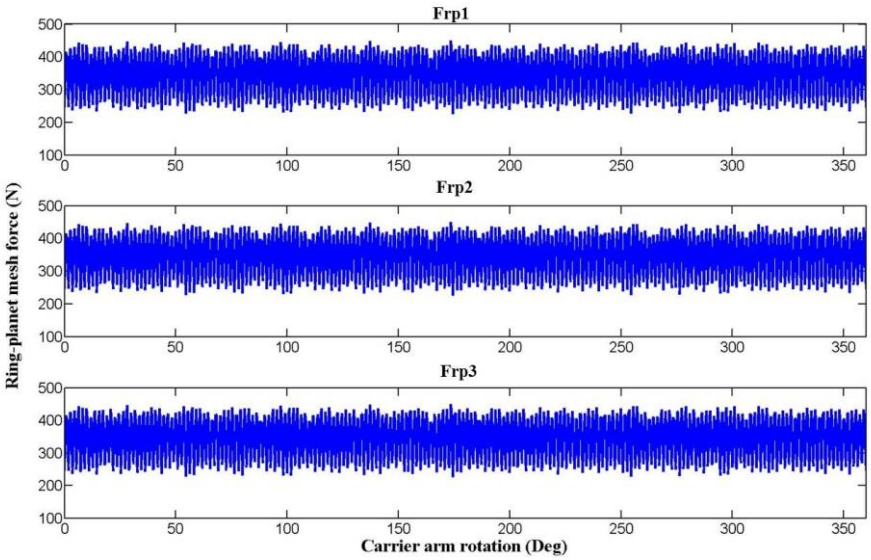

Figure 6.15 Resultant ring-planet mesh forces for the healthy planetary gear with uniformly supported ring gear

Fig. 6.16 shows the resultant ring-planet mesh forces for the planetary gear system with sun gear cracks. The data was also interpolated into equi-spaced phase data using 2^{10} points per carrier arm revolution. By comparing with Fig. 6.15, Fig. 6.16 clearly shows the impact of the sun gear crack on each of the ring-planet mesh forces.

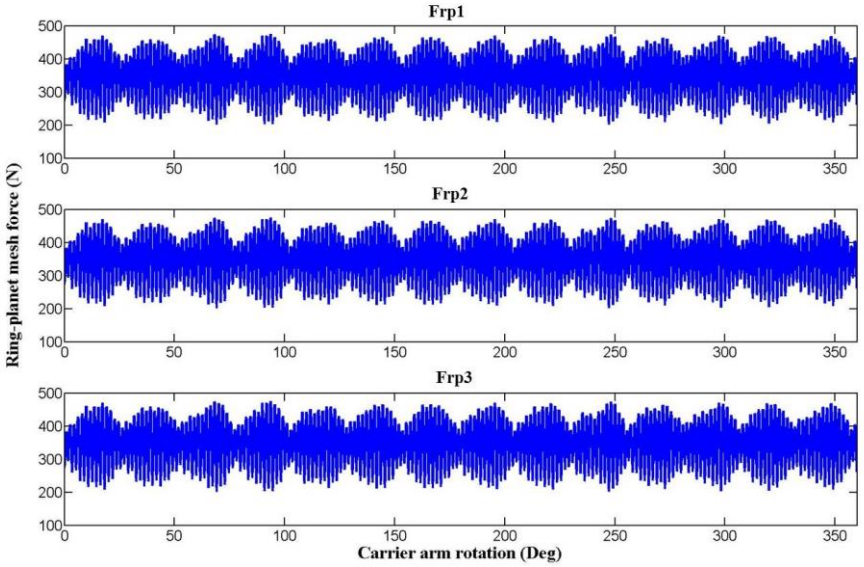

Figure 6.16 Resultant ring-planet mesh forces for the cracked sun gear with uniformly supported ring gear

Fig. 6.17 shows the results of the ring-planet mesh forces for the cracked planet gear on the sun gear mesh side. The original data was resampled into equi-spaced phase data using 2^{10} points per carrier arm revolution and it showed that the impact of the planet crack can be observed only in the F_{rp1} curve while minimal impact can be observed in the other curves.

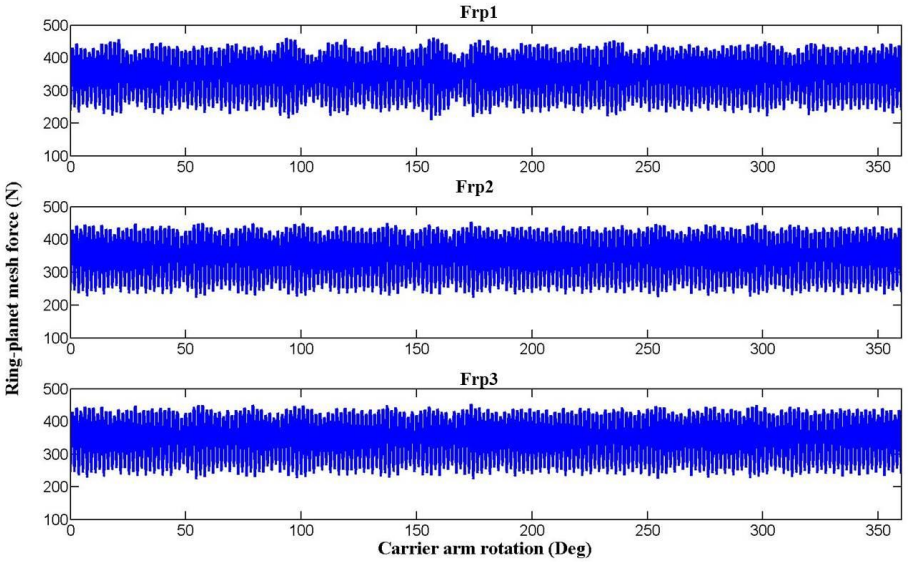

Figure 6.17 Resultant ring-planet mesh forces for the cracked planet gear on the sun gear mesh side with uniformly supported ring gear

Fig. 6.18 shows the results of the ring-planet mesh forces for the cracked planet gear on the ring gear mesh side. The crack was assumed to be on the 1st ring-planet mesh pair. The original data was resampled into equi-spaced phase data using 2^{10} points per carrier arm revolution. By comparing with Fig. 6.15, no significant difference can be observed from the force curve compared with the health ones.

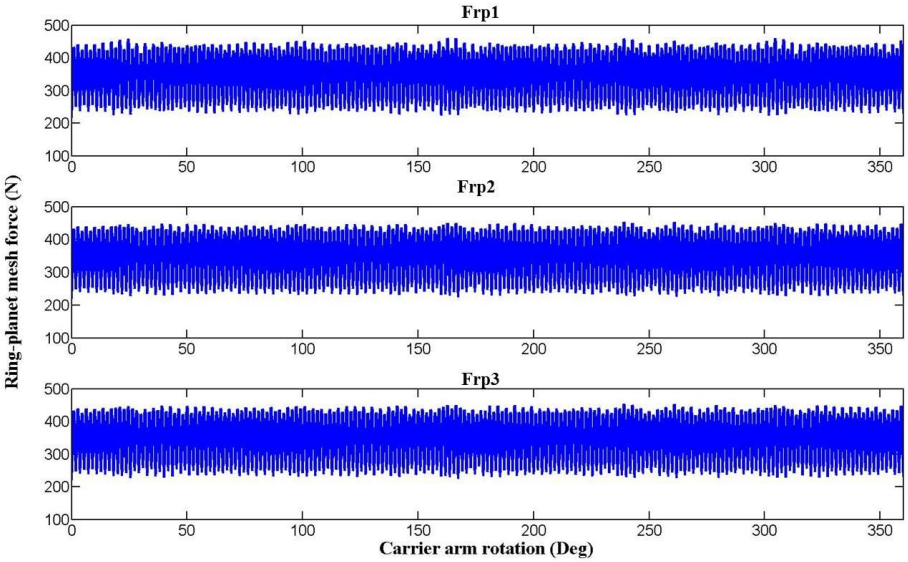

Figure 6.18 Resultant ring-planet mesh forces for cracked planet gear on the ring gear mesh side with uniformly supported ring gear

Fig. 6.19 shows the results of the ring-planet mesh forces for the cracked ring gear system. The ring gear was assumed to be uniformly supported and only one ring gear tooth was created with a crack. The original data was resampled into equi-spaced phase data using 2^{10} points per carrier arm revolution. No significant difference can be observed from the force curve compared with the health ones.

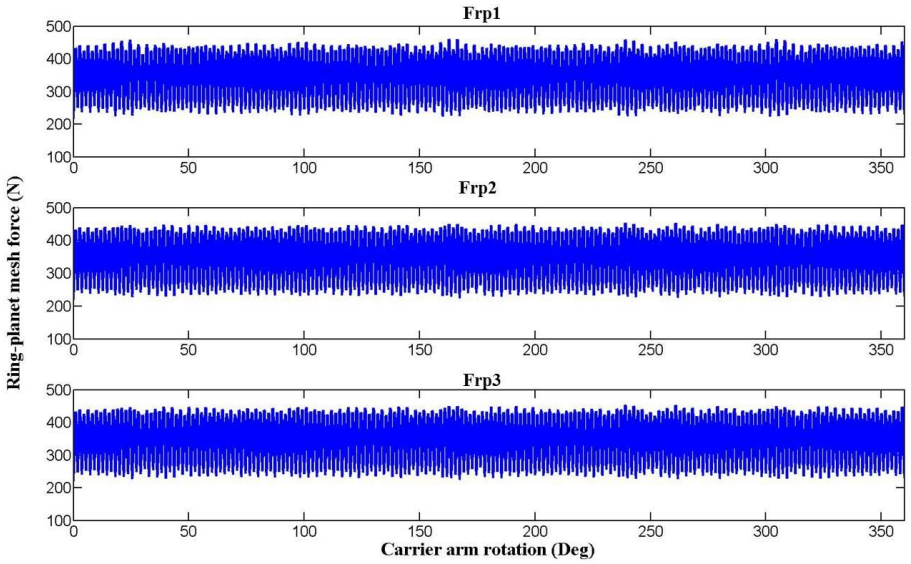

Figure 6.19 Resultant ring-planet mesh forces for cracked ring gear side with uniformly supported ring gear

Fig. 6.15–Fig.6.19 present the summaries for the ring-planet mesh force in a planetary gear system that is uniformly supported on the ring gear. All these forces were calculated from the lump-parameter models and overall, these results suggest that the cracks on the sun-planet mesh, no matter if it is the sun crack or the planet tooth crack on the sun gear side, have greater impact on the ring-planet forces even though the sun-planet force is not directly applied on the ring gear rim. On the other hand, the crack on the ring-planet mesh pair exhibits minimal difference between the cracked case and the healthy case. All these forces will be incorporated into the ring FE beam model as the moving load to study the ring casing vibration with uniformly supported ring gear.

Fig. 6.20 shows the results of the ring-planet mesh forces for the healthy planetary gear system with pin supported ring gear. No cracks were placed on either the sun-planet pair or the ring-planet pair. The original data was resampled into equi-spaced phase data using 2^{10} points per carrier arm revolution.

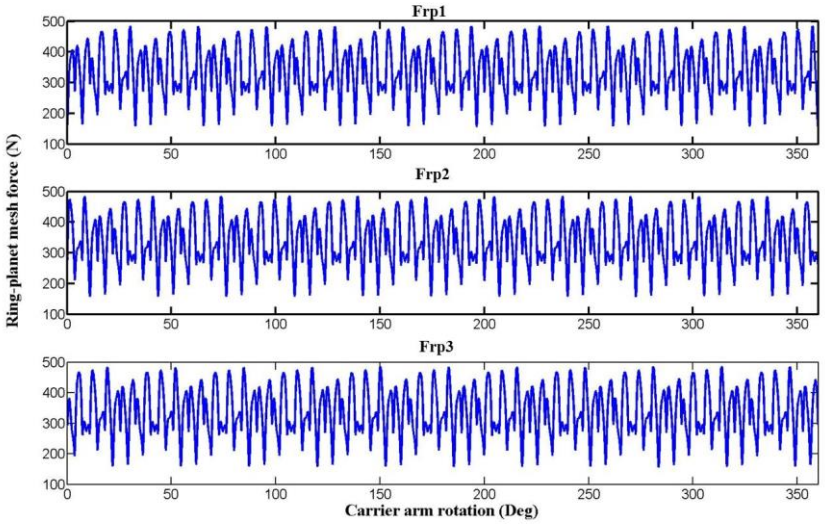

Figure 6.20 Resultant ring-planet mesh forces for healthy planetary gear teeth with pin supported ring gear

Fig. 6.21 shows the results of the ring-planet mesh force for the case of sun gear crack tooth with the pin supported ring gear. The sun-planet mesh stiffness with the impact of the sun gear tooth crack was shown in Fig. 6.5 and it was assumed that the pin support has negligible effect on the sun-planet mesh. The ring-planet mesh stiffness with pin support was shown in Fig. 6.12 and has been discussed in chapter 5. The original data was resampled into equi-spaced phase data using 2^{10} points per carrier arm revolution.

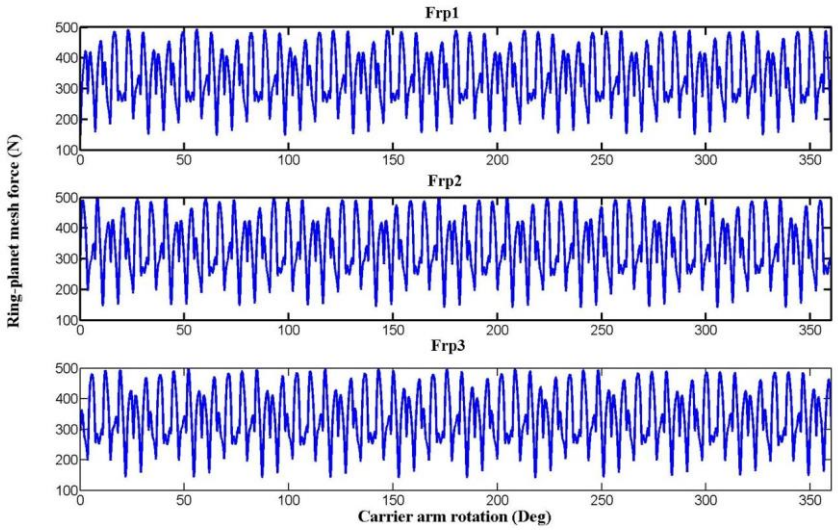

Figure 6.21 Resultant ring-planet mesh forces for cracked sun gear tooth with pin supported ring gear

Fig. 6.22 shows the results of the ring-planet mesh forces for the case of the planet gear tooth crack with the pin supported ring gear. The sun-planet mesh stiffness with the impact of planet gear tooth crack was shown in Fig. 6.8 and it was assumed that the pin support has negligible effect on the sun-planet mesh. The ring-planet mesh stiffness was shown in Fig. 6.12. The original data was resampled into equi-spaced phase data using 2^{10} points per carrier arm revolution.

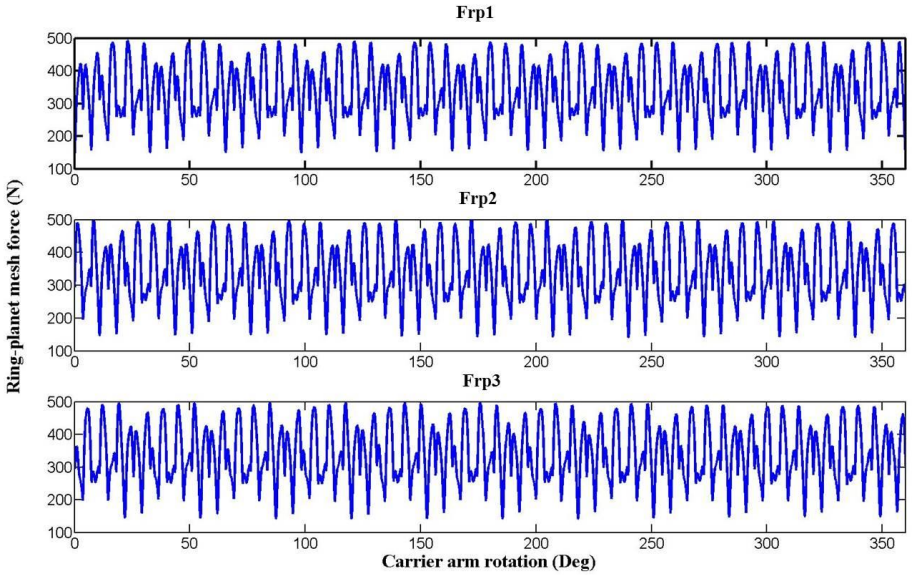

Figure 6.22 Resultant ring-planet mesh forces for cracked planet gear tooth with pin supported ring gear

Fig. 6.23 shows the results of the ring-planet mesh force for the case of the ring gear tooth crack with the pin support. The sun-planet mesh stiffness was assumed to be healthy and it has been discussed in chapter 3. The ring-planet mesh stiffness with the impact of the ring gear tooth crack was shown in Fig. 6.12. The original data was resampled into equi-spaced phase data using 2^{10} points per carrier arm revolution.

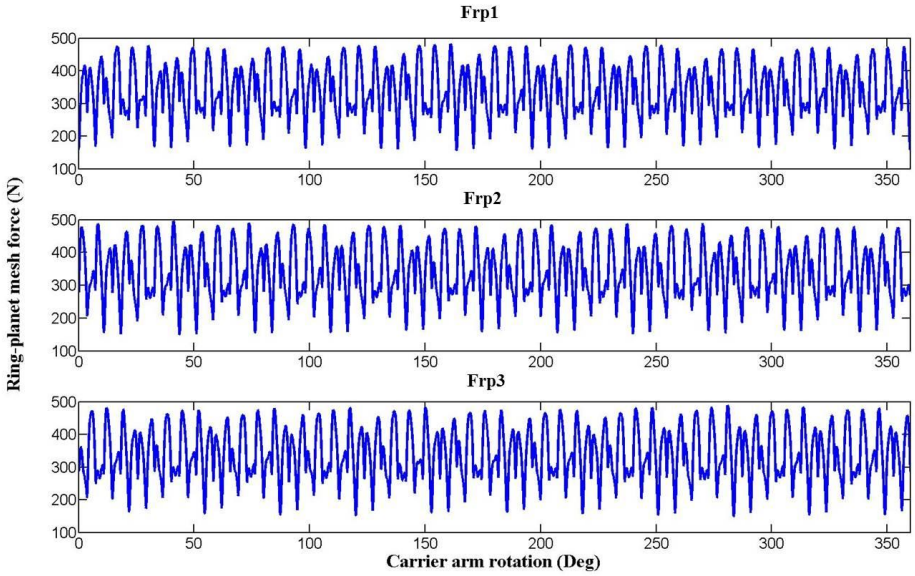

Figure 6.23 Resultant ring-planet mesh forces for cracked ring gear tooth with pin supported ring gear

6.4 Conclusion

This chapter has investigated methods for creating the mathematical planetary gear models, including a Finite Element (FE) beam model for the ring gear. The mathematical model used in this research includes two parts: the lumped-parameter model and the FE beam model with moving load. The internal excitations, sun-planet and ring-planet mesh stiffness, with the impact of cracks have been previously discussed in chapter 3 and chapter 5 and were also summarised in this chapter. With these internal excitations, the lumped-parameter model can be used to simulate the planetary gear torsional and translation vibration. With the availability of the ring-planet mesh force, the ring gear FE beam model can be used to simulate the ring casing vibration with different boundary conditions. All these vibration results with some basic signal processing are presented and analysed in the next chapter.

Chapter 7 Planetary gear fault diagnostic result analysis

7.1 Introduction

The planetary gear vibration generation mechanism has been discussed in the previous chapters and it indicates that sun-planet and ring-planet meshes are the main internal vibration source for the planetary gear system. Once a crack has occurred, the subsystem mesh stiffness will deteriorate and consequently cause changes in the overall dynamic system responses. The vibration signals discussed in this chapter have all been based on the model shown in chapter 6.

When analysing the vibration spectrum of the planetary gear, the first property of interest in a planetary gear system is the tooth meshing frequency, f_m. In this research, the ring gear is stationary and the sun gear, planet gear and the carrier arm rotate with respect to their own axes. Under this case, the tooth mesh frequency of the planetary gear can be calculated as (Howard, 1991),

$$f_m = Z_r f_c = Z_p(f_p + f_c) = Z_s(f_s - f_c), \tag{7.1}$$

where f_c is the carrier arm rotational frequency, f_p is the planet gear rotational frequency and f_s is the sun gear rotational frequency. Therefore, the rotational frequencies of the planet and sun gear are given by (Howard, 1991; McFadden, 1991),

$$f_p = \frac{f_c(Z_r - Z_p)}{Z_p},$$

$$f_s = \frac{f_c(Z_r + Z_s)}{Z_s}, \tag{7.2}$$

and the relative rotational frequencies of the planet and sun gears with respect to the planet carrier are given by (Howard, 1991; McFadden, 1991),

$$f_p^c = f_p + f_c = f_c\frac{Z_r}{Z_p},$$

$$f_s^c = f_s - f_c = f_c\frac{Z_r}{Z_s}. \tag{7.3}$$

If a crack occurs on one of the sun gear teeth, this type of fault can be classified as a localized defect, which tends to create a dynamic response modulation of a short pulse of the length of the order of the tooth-mesh period (Feng & Zuo, 2012, 2013). For the local sun gear damage case, in one relative rotation cycle with respect to the carrier arm, the characteristic fault rotational frequency is given by (Feng & Zuo, 2012, 2013),

$$f_{sf}^{c} = N\frac{f_m}{Z_s} = N\frac{Z_r}{Z_s}f_c, \tag{7.4}$$

where f_{sf}^{c} is the faulty sun gear rotation frequency with respect to the carrier arm. N is the number of planet gears in the system. Similarly, for the local planet gear damage case, in one relative rotation cycle with respect to the carrier arm, the characteristic fault rotational frequency is given by (Feng & Zuo, 2012, 2013),

$$f_{pf}^{c} = \frac{f_m}{Z_p} = \frac{Z_r}{Z_p}f_c, \tag{7.5}$$

where f_{pf}^{c} is the faulty planet gear rotation frequency with respect to the carrier arm. For the local ring gear damage case, in one relative rotation cycle with respect to the carrier arm, the characteristic fault rotational frequency is given by (Feng & Zuo, 2012, 2013),

$$f_{rf}^{c} = N\frac{f_m}{Z_r} = Nf_c, \tag{7.6}$$

where f_{rf} is the faulty ring gear rotation frequency with respect to the carrier arm.

Normally, the planetary gear vibration was measured with a stationary transducer mounted on the ring gear and the transducer would record all the vibration signals when the carrier arm passed by. Numerous publications have been focused on explaining the vibration spectrum caused by this carrier arm passing modulation (McFadden & Smith, 1985b; McNames, 2002; Inalpolat & Kahraman, 2009, 2010) and it indicates that the sidebands will appear in the position of $f_m \pm nf_c$ (n= 1, 2, 3,…), with sideband spacing equal to the carrier arm rotation frequency f_c. Furthermore, Kahraman classified all the possible modulation sidebands into five different conditions based on the assembly condition and parameters of the planetary gear system (Inalpolat & Kahraman, 2009). In this research, the planetary gear parameter can be found in table 3.1 and this gear system belongs to Kahraman's case (i):

equally spaced planets and in-phase gear meshes. As a consequence, the resultant frequency spectrum of the healthy planetary gear will have gear mesh components at mesh frequency f_m and two symmetric sidebands at half-amplitude as the mesh harmonic at frequency f_m+Nf_c and f_m−Nf_c. For the planetary gear system with a localized sun gear fault, the sidebands will appear in the position of $f_m \pm kf_s \pm nf_{sf}^c = f_m \pm kf_c \pm (k/N \pm n)f_{sf}^c$, with sideband spacing equal to the faulty sun gear rotational frequency f_{sf}^c, which has been calculated in equation (7.4). For the planetary gear system with a faulty planet gear, the sidebands will appear in the position of $f_m \pm kf_c \pm nf_{pf}^c$, with sideband spacing equal to the faulty planet gear rotation frequency f_{pf}^c, which has been calculated in equation (7.5). For the planetary system with a faulty ring gear, the sidebands will appear in the position of $f_m \pm nf_{rf}^c$, with sideband spacing equal to the faulty ring gear rotation frequency f_{rf}^c, which has been calculated in equation (7.6).

The planetary gear torsional vibration signals are theoretically free from the modulation effect caused by the time variant vibration transfer paths due to the rotation of the carrier arm and therefore, the torsional vibration is an effective gear diagnostic method with a simple vibration spectrum. For the planetary gear system with a localized sun gear fault, the sidebands of the torsional vibration signal will appear in the position of $f_m \pm nf_{sf}^c$, with sideband spacing equal to the faulty sun gear rotational frequency f_{sf}^c. For the planetary gear system with a faulty planet gear, the sidebands of the torsional vibration signal will appear in the position of $f_m \pm nf_{pf}^c$, with sideband spacing equal to the faulty planet gear rotation frequency f_{pf}^c. For the planetary system with a faulty ring gear, the sidebands will appear in the position of $f_m \pm nf_{rf}^c$, with sideband spacing equal to the faulty ring gear rotation frequency f_{rf}^c.

This chapter mainly analysed the planetary gear torsional vibration, which can be obtained from the planetary gear mathematical model in chapter 6. However, some transverse vibration, especially the ring gear transverse vibration, was also discussed. This transverse vibration can be calculated using the FE ring beam model with moving load as described in chapter 6. The vibration separation method was used for the transverse vibration to obtain the vibration signal for the sun gear and the planet gear.

7.2 Fault diagnostic results for uniformly supported planetary gear

7.2.1 Fault diagnostic results for torsional vibration

After the initial transient start-up was observed to have decayed away, the carrier arm angular velocity has been selected to diagnosis the planetary gear faults. Some common diagnostic algorithms can be used to analysis the fault result, such as RMS spectrum, residual signal narrow band envelop, amplitude and phase modulation, analytical signal plots, and time-frequency analysis.

The carrier arm angular velocity was chosen in this research to analyse the fault diagnostic results because the torsional vibration signals are naturally free from the modulation effect caused by the transfer path and it was also demonstrated by Zhongwei in his thesis that the torsional vibration signal is far superior than the transverse signals for frequency analysis for all rotating components of planetary gearboxes (Wang, 2010). Fig. 7.1 shows the results of the carrier arm angular velocity signal, which has been resampled into equispaced phase data over one carrier arm revolution. There are five plots shown in the figure and corresponding to the condition of the healthy planetary gear, planetary gear with cracked sun gear, planetary gear with cracked planet gear on sun gear side, planetary gear with cracked planet gear on ring gear side as well as planetary gear with cracked ring gear separately. All these signals are obtained under the assumption that the ring gear is uniformly supported and no modulation effect was found on the ring-planet mesh stiffness.

As shown in Fig. 7.1, the presence of the crack on difference components can be identified by visually looking at these waveforms as several repetitive impacts on the carrier arm torsional velocity curves can be observed, especially with the crack on the sun-planet mesh pair. Under the same crack length assumption, the crack on the sun-planet mesh pair tends to be more easily identified than the crack on the ring-planet mesh pair. This has been consistent with the findings in Fig. 3.46 in chapter 3 when analysing the crack sensitivity of different mesh pairs. The impacts are caused by the mesh stiffness reduction due to the crack and the number of these impacts corresponds to the number of the cracked periods within one carrier arm revolution shown in Fig. 6.6, Fig. 6.8, Fig. 6.10 and Fig. 6.11. A closer look

at the simulation results can be achieved by using some statistical indicators, which has been summarized in table 7.1.

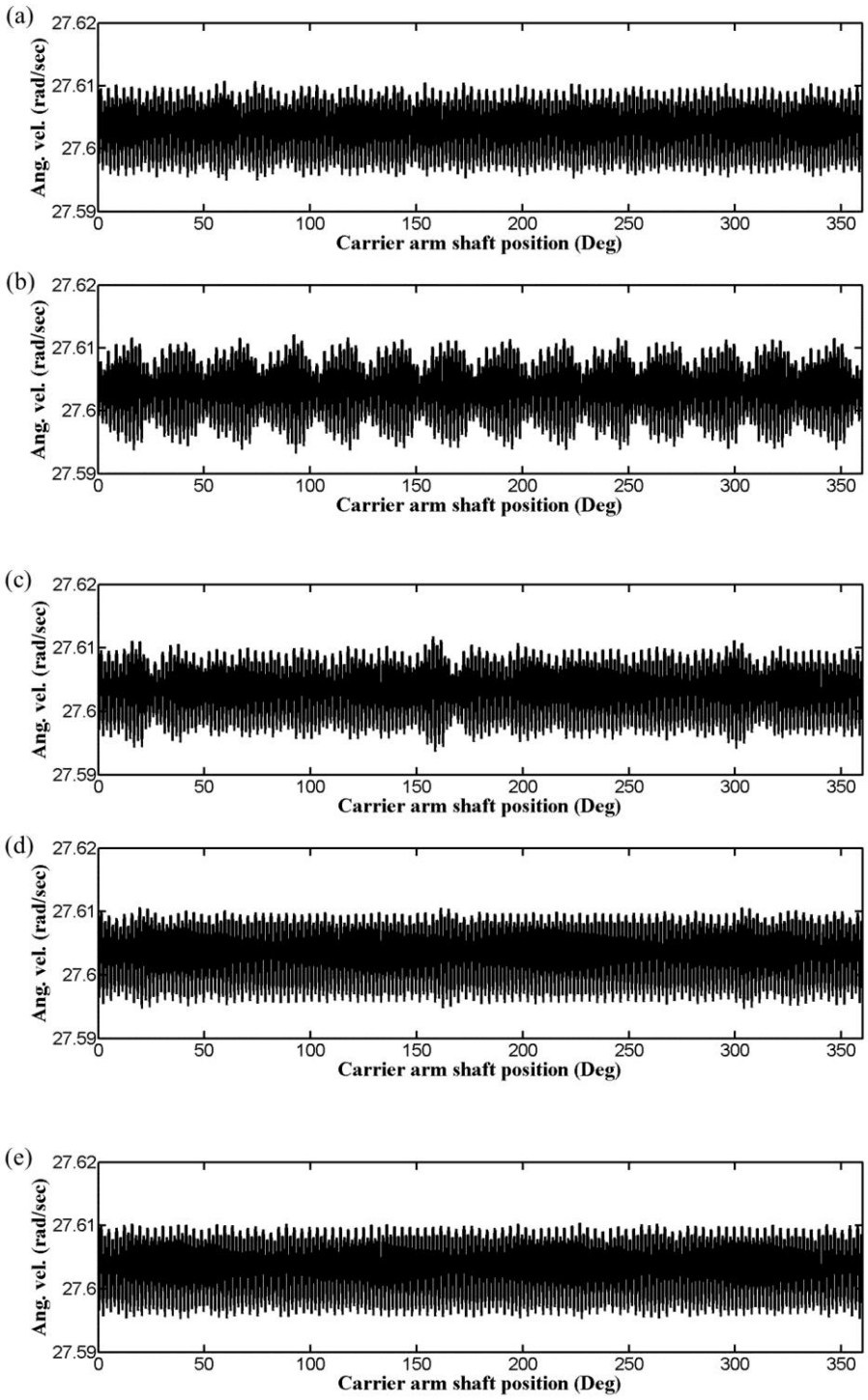

Figure 7.1 Carrier arm angular velocity over one complete revolution with uniformly supported ring gear. (a) healthy planetary gear case; (b) planetary gear with cracked sun gear case; (c) planetary gear with cracked planet gear on the sun gear side case; (d) planetary gear with cracked planet gear on the ring gear side case; (e) planetary gear with cracked ring gear case.

Table 7.1 Comparison of the statistical indicators of the diagnostic results

	Healthy	Cracked sun gear	Cracked planet gear sun gear side	Cracked planet gear ring gear side	Cracked ring gear
Mean	27.60	27.60	27.60	27.60	27.60
STD	0.0043	0.0046	0.0044	0.0045	0.0045
Skew	0.07	0.04	0.06	0.03	0.04
Kurtosis	1.62	1.81	1.67	1.59	1.58
Crest Factor	3.65	4.11	4.17	3.52	3.37

Fig. 7.2 shows the results of the RMS spectra and because the signals cover exactly one carrier arm revolution, the RMS spectral results are presented in terms of carrier arm order or shaft order. The first observation from the figure is that the RMS spectra have gear mesh components at order 99 and its harmonics, like 198, 297 and so on. This observation has been consistence with the analysis in equation (7.1), where the mesh frequency is the carrier arm frequency times the ring gear tooth number. A close look at these mesh component can be made to check the amplitude of the mesh component and the second harmonic was chosen as it appears as the strongest component in the spectrum. The amplitude for the healthy case was around −23.73 dB and the amplitude for the other four cases were −23.69 dB, −23.744 dB, −23.52 dB, and −23.55 dB respectively.

As discussed previously, the faults on different components have their own characteristic frequency and their positions can be identified. The amplitude on these positions could also be used for fault diagnostics. For the planetary gear with the sun gear fault, the position of the sun gear characteristic frequency in Fig. 7.2 (b) is $k \cdot Z_r \pm n \cdot N \cdot (Z_r/Z_s)$. For example, the amplitude of the frequency component at position 170 (for the case of 2×99–2×3×99/21) could be checked and it was found to be −38.654 dB compared with the value of −47.85 dB in the healthy condition. The amplitude of the frequency component at position 184 (for the case of 2×99–1×3×99/21) could be checked and it was found to be −35.39 dB compared with the value of −40.23 dB in the healthy condition. The amplitude of the frequency component at position 212 (for the case of 2×99+ 1×3×99/21) could be checked and it was found to be

−36.897 dB compared with the value of −54.0559 dB in the healthy condition. For the planetary gear with the planet gear fault, the position of the planet gear characteristic frequency in Fig. 7.2 (c) is $k \cdot Z_r \pm n \cdot (Z_r/Z_p)$. For example, the amplitude of the frequency component at position 201 (for the case of 2×99+ 1×99/39) could be checked and it was found to be −42.457 dB compared with the value of −46.7171 dB in the healthy conditions. The same position in Fig. 7.2 (d) could be checked and the amplitude was found to be −44.2651 dB compared with the value of −46.7171 dB in the healthy condition. For the planetary gear with the ring gear fault, the position of the ring gear characteristic frequency in Fig. 7.2 (e) is $k \cdot Z_r \pm n \cdot N$. For example, the amplitude of the frequency component at position 201 (for the case of 2×99+ 3) could be checked and it was found to be −41.7633 dB compared with the value of −46.6229 dB in the healthy condition. As indicated by the results, checking the amplitude of the characteristic faulty frequency components was more effective than checking the amplitude of the gear mesh frequency components in detecting the planetary gear faults. However, the big challenge of using this method is that there are so many faulty characteristic frequencies and it becomes hard to determine which frequency component is the best choice.

Another interesting finding in Fig. 7.2 is that all these spectrum plots were dominated by strong gear mesh sidebands and equations (7.4) − (7.6) suggested that the information of the characteristic faulty frequencies due to the crack on different components was hidden in these sidebands. As shown in the figure, the sideband of each of these conditions exhibited different structure around the mesh frequency. The 'residual signal' can be obtained by removing the regular mesh frequency components, which can be achieved by subtracting the known gear mesh harmonics from the spectrum or by using the linear prediction technique (Randall, 2011).

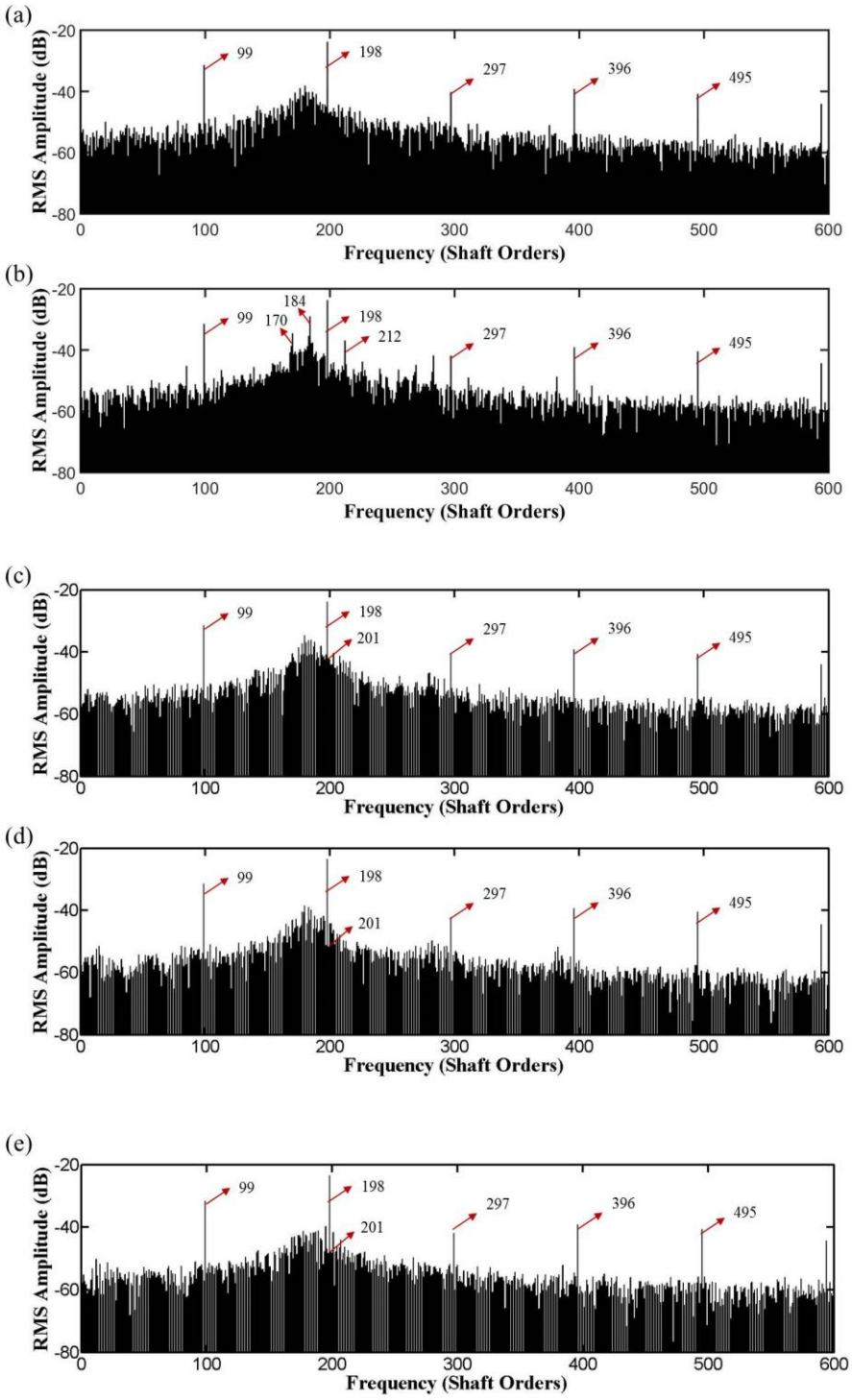

Figure 7.2 RMS spectrum amplitude results. (a) healthy planetary gear case; (b) planetary gear with cracked sun gear case; (c) planetary gear with cracked planet gear on the sun gear side case; (d) planetary gear with cracked planet gear on the ring gear side case; (e) planetary gear with cracked ring gear case.

Fig. 7.3 shows the results of the residual signal and the presence of the crack on different components can be noted. The residual signal significantly enhances the detectability of the gear fault in the signal and some abnormal signals can be easily found in the wave form. Theoretically, within one carrier arm rotation, there should be 15 impacts in the vibration provided there was a cracked sun tooth and there should be 3 impacts in the signal provided if there was a cracked planet gear (Liang et al., 2014). The parameter FM4, defined as the kurtosis of the residual signal, can be used to further quantify the wave form (Howard, 1994). The FM4 for all the cases, from the healthy case to the cracked ring gear case, are 3.3385, 1.86, 5.5591, 4.0157, and 3.1065 respectively. From the result, it was found that the FM4 parameter here was not as powerful as it was when used in the fixed axis gear system. As a result, the statistical indicators used in table 7.1 will be used again to show which statistic parameter is better for the detection in this research, as shown in table 7.2.

Table 7.2 Comparison of the statistical indicators of the diagnostic results

	Healthy	Cracked sun gear	Cracked planet gear sun gear side	Cracked planet gear ring gear side	Cracked ring gear
Mean	4.2×10^{-4}	4.2×10^{-4}	4.2×10^{-4}	4.2×10^{-4}	4.2×10^{-4}
STD	6.15×10^{-9}	2.21×10^{-8}	1.617×10^{-8}	5.02×10^{-9}	4.58×10^{-9}
Skew	-0.03	-0.01	-0.04	-0.01	-0.03
Kurtosis	3.34	1.86	5.56	4.02	3.11
Crest Factor	7.47	4.42	8.69	6.42	6.32

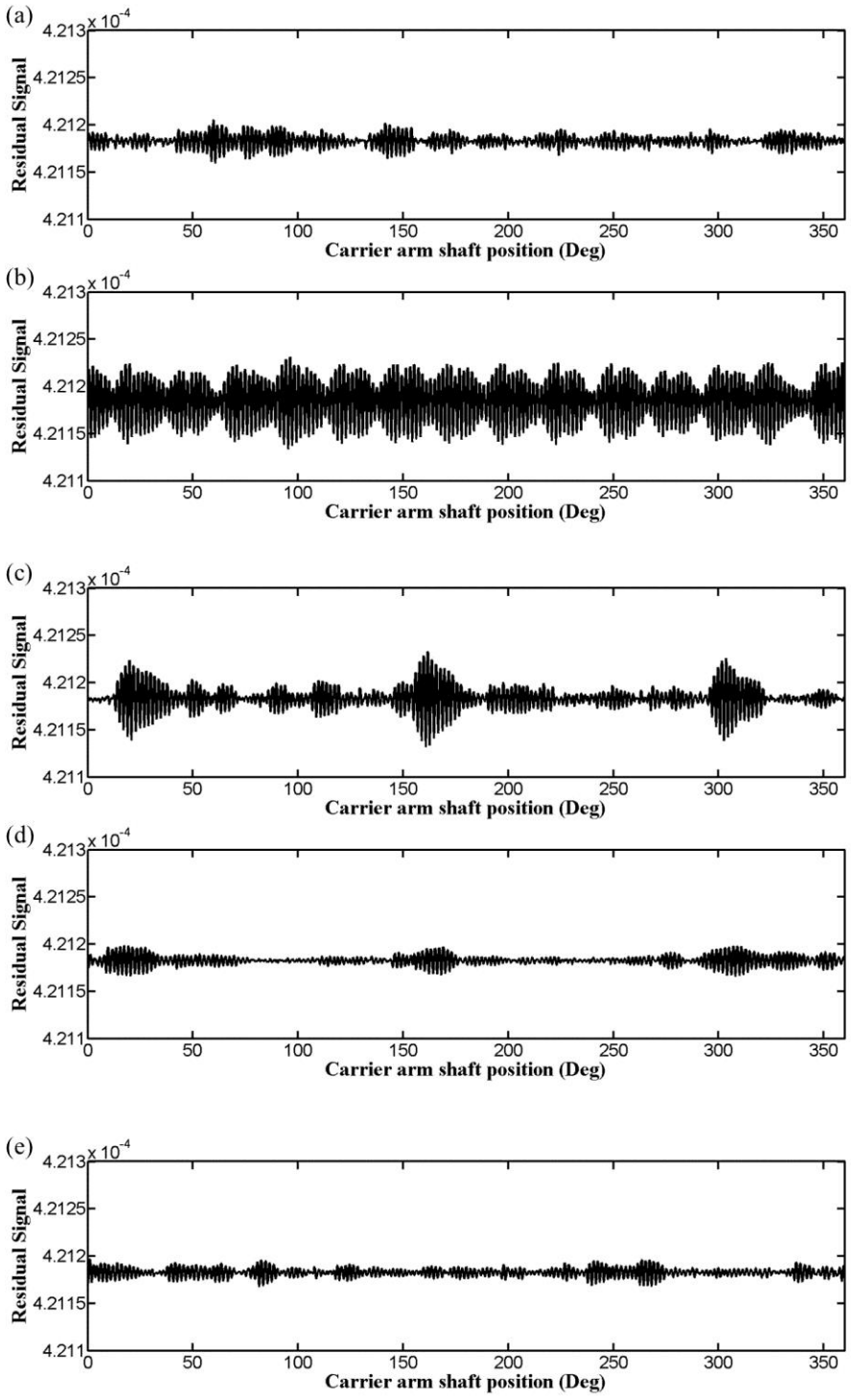

Figure 7.3 Residual signal results. (a) healthy planetary gear case; (b) planetary gear with cracked sun gear case; (c) planetary gear with cracked planet gear on the sun gear side case; (d) planetary gear with cracked planet gear on the ring gear side case; (e) planetary gear with cracked ring gear case.

The narrow band envelope analysis has been developed in the early 1970's and has become one of the prominent vibration signal processing techniques for detection and diagnosis of

the incipient mechanical failure (Howard, 1994). In this study, the second mesh harmonic was chosen for the demodulation process and a bandwidth of 98 shaft orders (±49) was used for the analysis. Fig. 7.4 shows the results of the narrow band envelope for the healthy gear case, cracked sun gear case, cracked planet gear cases on both its mesh side and cracked ring gear cases. The visual impression from the figures reveals the presence of the crack on the sun gear and the planet gear, even though some variations can be observed in the healthy case. For example, there should be three impulses within one carrier arm rotation when the crack occurs on the planet gear and as clearly shown in Fig. 7.4 (c) & (d), the presence of the planet crack can be identified close to 30°, 170° and 300° rotation of the carrier shaft. However, it is interesting to note that the presence of the ring gear crack seems hard to detect using this technique as its variation is almost identical with the healthy gear variation.

Another effective technique to detect the cracks in gear teeth is by amplitude and phase demodulation of the vibration signal (McFadden, 1986) and it can be described in terms of the Hilbert transform and the analytic signal. The amplitude of the analytic signal represents the amplitude modulation and the phase of the analytic signal represents the phase modulation. In this study, the second mesh harmonic was chosen for the demodulation process and a bandwidth of 98 shaft orders (±49) was used for the analysis. Fig. 7.5 shows the results of the amplitude modulation and phase modulation from the carrier arm angular velocity. The left column shows the results of the amplitude modulation and the right column shows the results of the phase modulation. Similarly, the visual impression from the figures can reveal the presence of the crack. For example, the amplitude modulation and phase modulation in Fig. 7.5(c) clearly reflects the presence of the crack on the planet gear as the perturbations are visible. The phase modulation undergoes a reduction of 30-deg shift. There are three perturbations, but they are caused by the same crack as the crack on the planet would contact three times with the sun gear within one carrier arm rotation. However, the presence of the ring gear crack in Fig. 7.5(e) was still difficult to be distinguished from the healthy case as no obvious perturbation can be observed in the amplitude modulation and in the phase modulation.

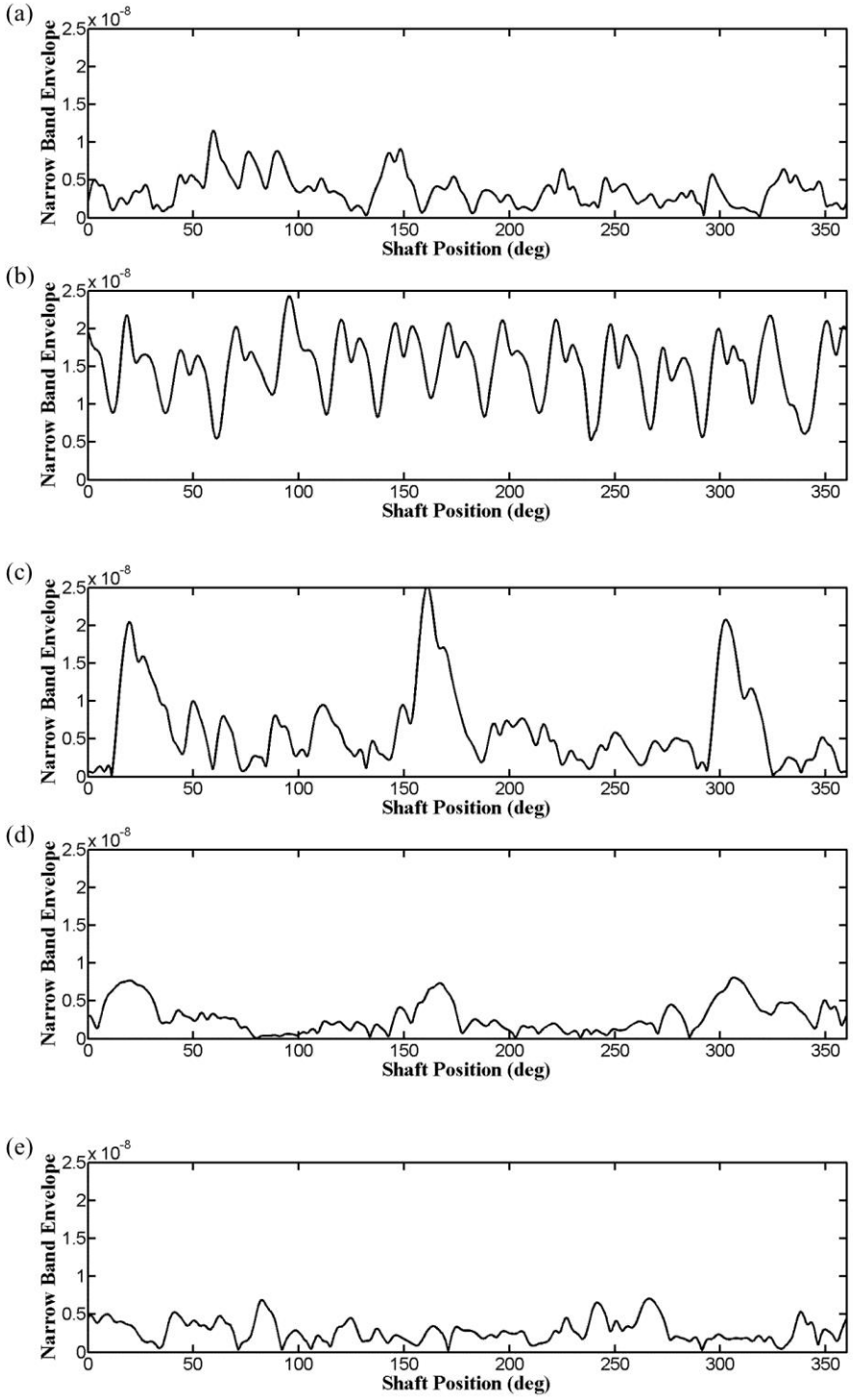

Figure 7.4 Narrowband envelope results. (a) healthy planetary gear case; (b) planetary gear with cracked sun gear case; (c) planetary gear with cracked planet gear on the sun gear side case; (d) planetary gear with cracked planet gear on the ring gear side case; (e) planetary gear with cracked ring gear case.

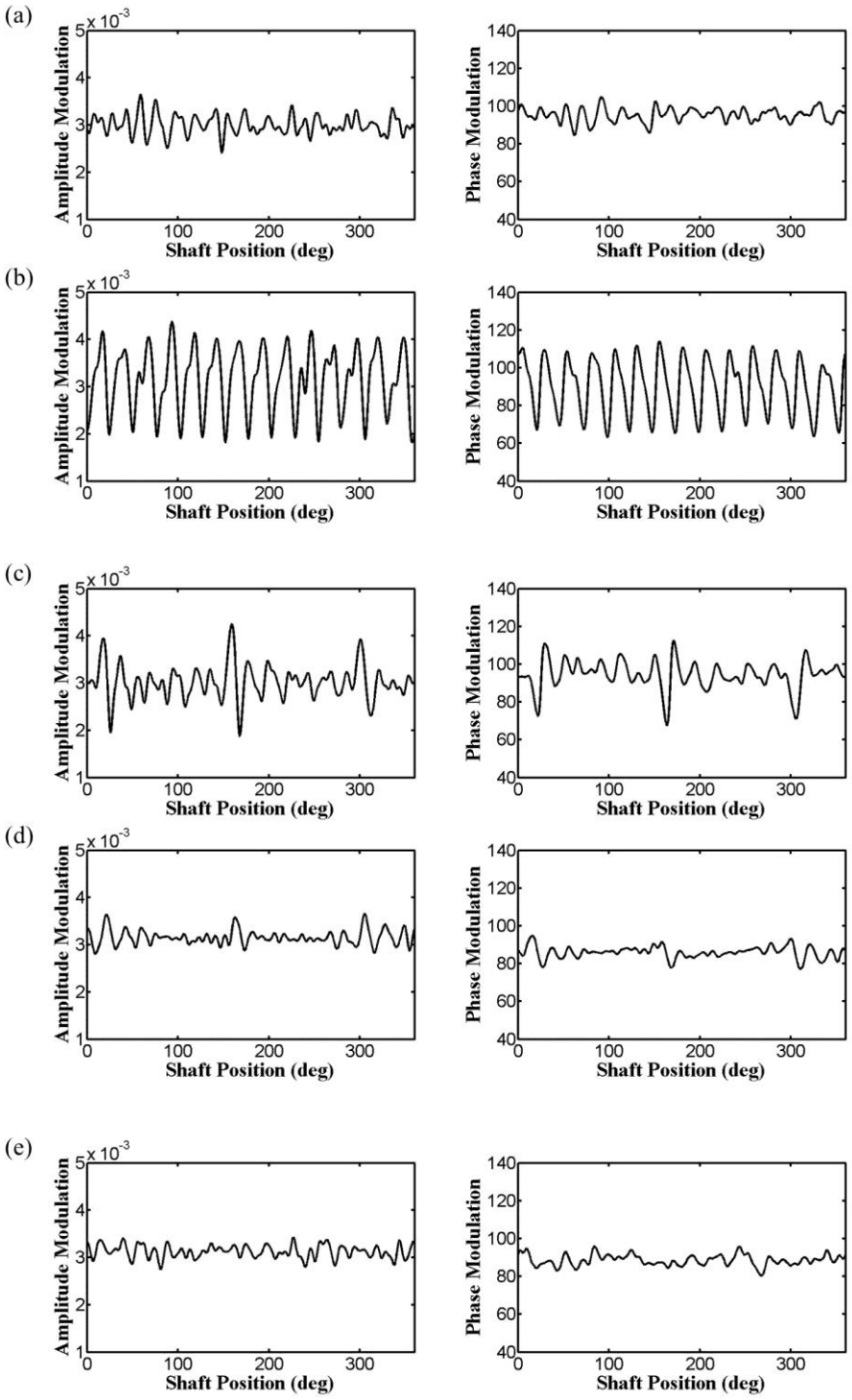

Figure 7.5 Amplitude modulation and phase modulation results. (a) healthy planetary gear case; (b) planetary gear with cracked sun gear case; (c) planetary gear with cracked planet gear on the sun gear side case; (d) planetary gear with cracked planet gear on the ring gear side case; (e) planetary gear with cracked ring gear case.

The Wigner-Ville distribution (WVD) is one of the well know time-frequency analysis methods and its application to the detection of the gear damage has been widely described recently. However, the cross-terms in the WVD have limited its application and by applying a suitable window function in the time domain, the so-called pseudo Wigner−Ville distribution (PWVD) can be obtained, which can attenuate the cross-term. Fig. 7.6 shows the PWVD of the carrier arm angular velocity residual signal.

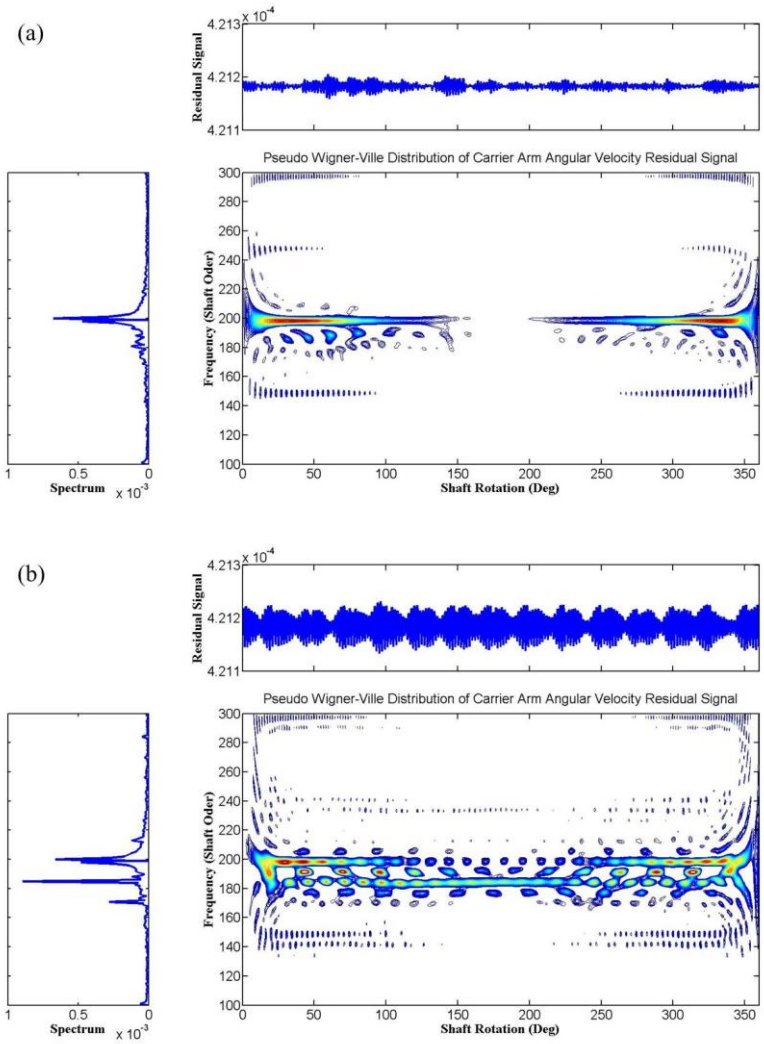

Figure 7.6 Pseudo Wigner−Ville distribution (PWVD) of the carrier arm angular velocity residual results. (a) healthy planetary gear case; (b) planetary gear with cracked sun gear case; (c) planetary gear with cracked planet gear on the sun gear side case; (d) planetary gear with cracked planet gear on the ring gear side case; (e) planetary gear with cracked ring gear case.

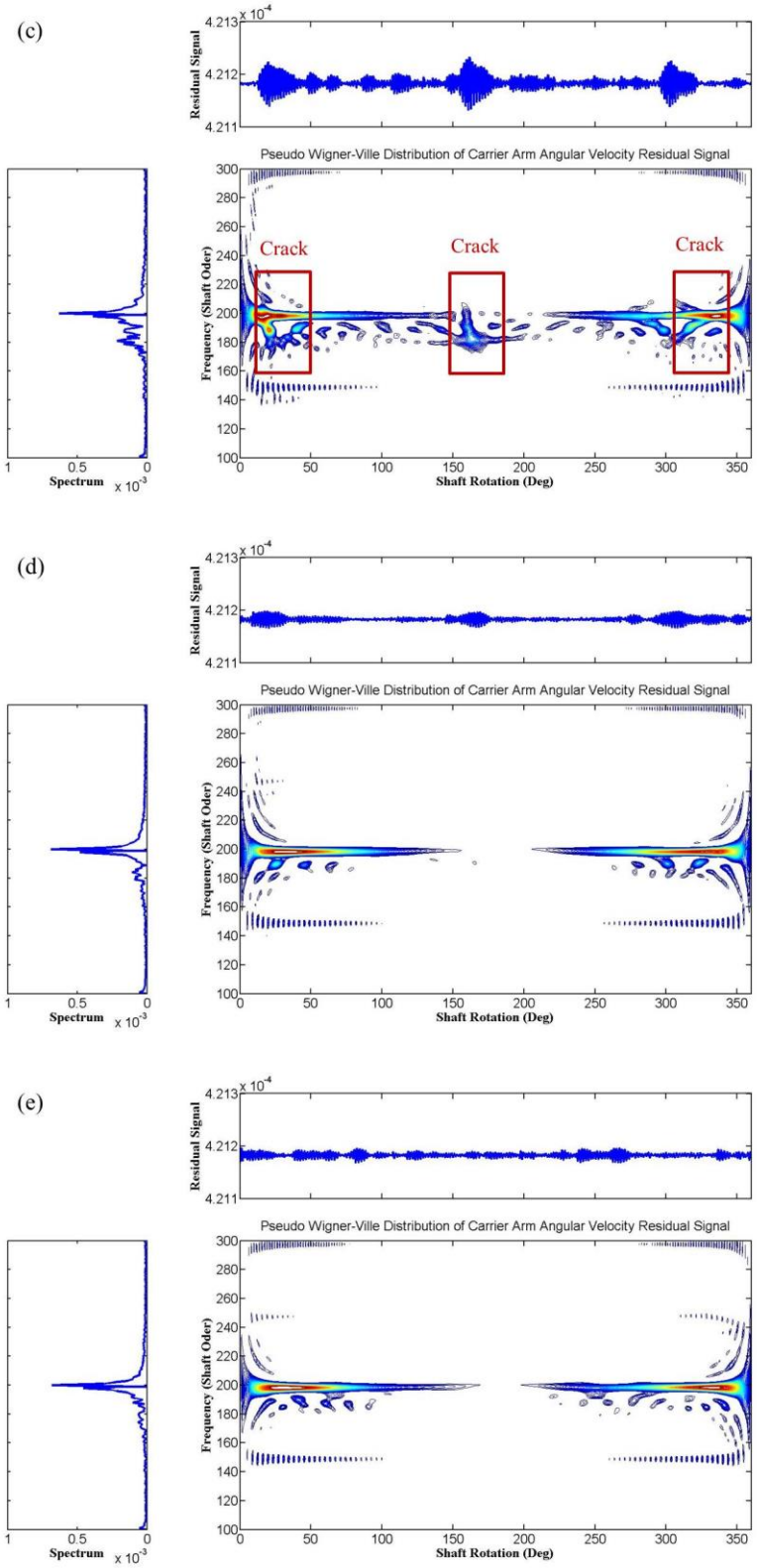

Figure 7.6 (Continued) Pseudo Wigner–Ville distribution (PWVD) of the carrier arm angular velocity residual results. (a) healthy planetary gear case; (b) planetary gear with cracked sun gear case; (c) planetary gear with cracked planet gear on the sun gear side case; (d) planetary gear with cracked planet gear on the ring gear side case; (e) planetary gear with cracked ring gear case.

As shown in Fig. 7.6, the residual signal instead of the original signal was used here because removing the components at the meshing harmonics can increases the sensitivity to energy changes related to the gear damage and a much clearer energy distribution pattern can be observed in the figure. Compared with the healthy case in Fig. 7.6 (a), the energy distribution related to the damage can be observed in Fig. 7.6 (b) and Fig. 7.6 (c), corresponding to the sun gear damage and the planet gear damage. If the crack occurred on the sun gear, the PWVD pattern tends to show a uniform distribution along its mesh component. This is largely because the sun gear crack repeats itself 15 times within one carrier arm rotation and these impacts are occurring uniformly during the rotation. Similarly, if the crack occurred on the planet gear, the PWVD energy patterns tend to be concentrated on three positions, corresponding to the moment when the cracked tooth was in contact, as shown in Fig. 7.6 (c). However, no obvious PWVD energy pattern can be found in Fig. 7.6 (d) and Fig. 7.6(e).

7.2.2 Fault diagnostic results for stationary transducer on ring gear

The FEA model developed in chapter 6 (section 6.3) was used to simulate the dynamic response from the ring gear. It was assumed that a transducer was mounted on the ring gear and that the ring gear was supported by a uniformly distributed flexible spring support. ANSYS transient analysis was used to obtain the dynamic response, as shown in Fig. 7.7. The carrier arm rotation speed was 27.6 rad/s requiring 0.2277 s to finish one carrier revolution. There are three planet gears in the system and it is obvious that when the planets pass through this fixed transducer location, three peaks can be observed in Fig. 7.7(a). Once the displacement history data is recorded, the corresponding vibration data can be easily obtained as well, as shown in Fig. 7.7(b). As this planetary gear system has equally spaced planets and in-phase gear meshes, the corresponding frequency spectrum will be expected to have mesh component at mesh frequency f_m and the sidebands are symmetrical about the gear mesh component (Inalpolat & Kahraman, 2009, 2010) with spacing $f_m \pm N f_c$. Fig. 7.7(c) shows the frequency spectra of the ring gear vibration. It can be observed that the mesh component is the strongest in the spectra and the sideband spacing equal to 3, which has been consistence with the analysis in (Inalpolat & Kahraman, 2009, 2010).

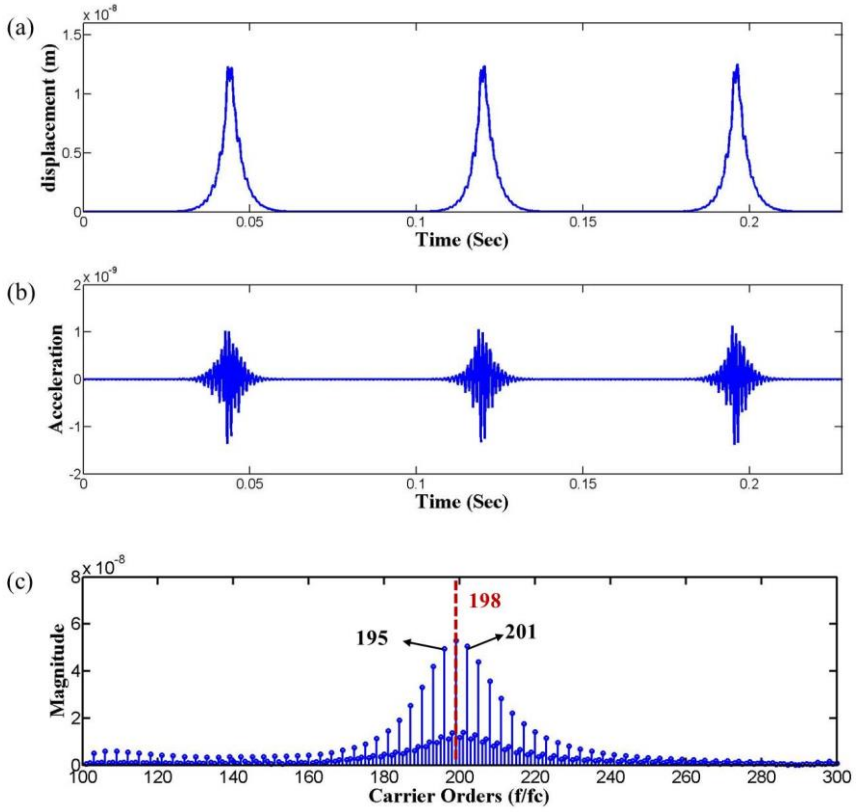

Figure 7.7 Ring gear dynamic motion. (a) displacement data, (b) acceleration data, (c) frequency spectra.

Traditionally, only one transducer on the ring gear was used in the planetary gear condition monitoring and by applying some window function, the transducer can capture the vibration from the tooth that is in mesh nearest to the transducer. From the numbers of teeth on the gears, it can be determined which teeth is nearest to the transducer and by repeating the process for Z_p revolutions of the carrier arm, the vibration data can be divided into Z_p segments, which can be re-assembled into one shaft rotation. Jong M. Ha (Ha et al., 2016) developed a meshing tooth matrix to determine the tooth that is in mesh, as shown in Fig. 7.8.

M_r	1	2	3	20	21	22	38	39	40	98	99	1
M_p	1	2	3	20	21	22	38	39	1	20	21	22
M_s	1	2	3	20	21	1	17	18	19	14	15	16

Figure 7.8 Meshing tooth matrix of the sun gear, the planet gear and the ring gear.

From the matrix, it can be observed that when the sun gear finishes one revolution, the 1st tooth of the sun gear will be in mesh with the 22nd tooth of the planet gear and the 22nd tooth of the ring gear. When the planet gear finishes one revolution, the 1st tooth of the planet gear will be in mesh with the 40th tooth of the ring gear and the 18th tooth of the sun gear. When the carrier arm finishes one revolution, the 1st tooth of the ring gear will be in mesh with the 22nd–tooth of the planet gear and the 16th tooth of the sun gear.

If the sun gear is of interest and is to be monitored using this method, then the vibration data from the 1st ring gear tooth position to the 21st tooth position can be recorded. In other words, it was assumed that there are 21 transducers mounted on the ring gear and each transducer will record the vibration data that is nearest to its position. This method will reduce the simulation time instead of repeating the process for Z_s revolutions of the carrier arm. Fig. 7.9 shows the vibration data of the ring gear teeth from the 21 transducers, being 21 vibration records in total. However, it is found that the overlap between the data makes it hard to distinguish which data set is for which tooth. As a result, a window function can be applied to each tooth vibration data to divide the data and then they can be re-assembled into one shaft rotation. There are numerous window functions available and in this research, the narrow-range rectangular window function was used. The angle for one ring gear tooth is 2pi/99=0.063 rad and the carrier arm speed is 27.6 rad/s. Therefore, the time duration for one ring gear tooth is 0.0023s. Fig. 7.10 shows the window function used to obtain the vibration data within one tooth duration.

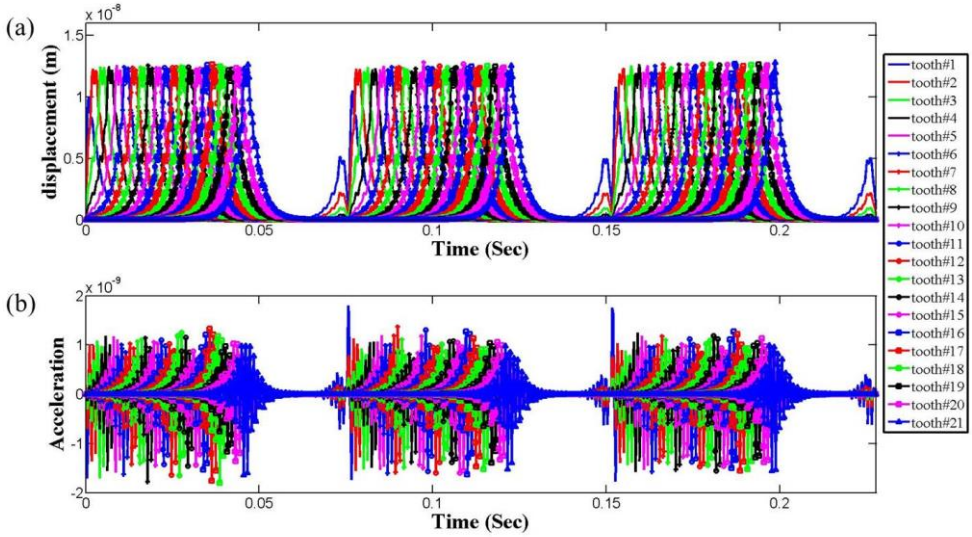

Figure 7.9 Ring gear dynamic motion from the 1st tooth to the 21st tooth. (a) displacement data, (b) acceleration data.

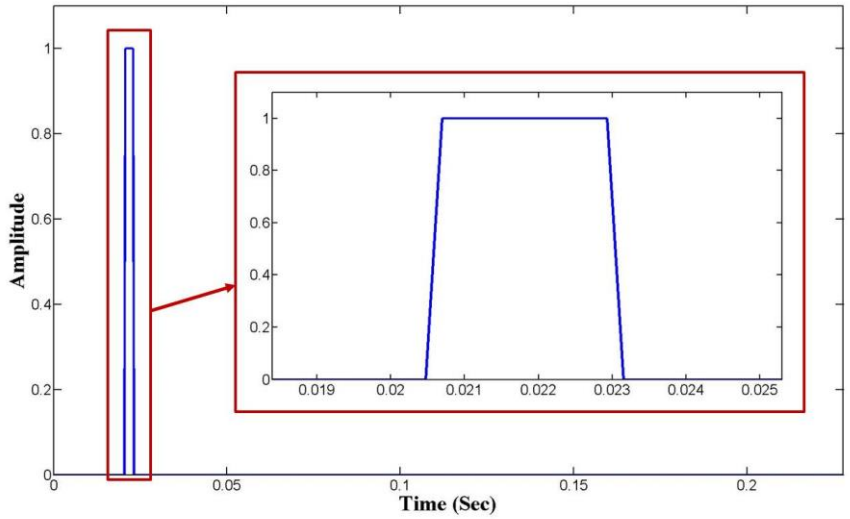

Figure 7.10 Example of the window function for the 10th ring gear tooth

By applying the corresponding window function to the ring gear teeth vibration data, one can reduce the data overlap and then re-arrange the data to be assembled for one sun gear shaft rotation. It was assumed here that there was no profile error on the gear teeth and that all the planet gears are identical to each other except when a crack occurs on one of the planet gears.

As a result, even though there are three planets passing through each tooth, only the data when the 1st planet passes was processed with the rectangular window.

Fig. 7.11 shows the results of the signal for one sun gear shaft rotation with perfect teeth. Fig. 7.12(a) shows the corresponding results of the RMS frequency spectrum and the components at the sun gear shaft order and its harmonic can be easily identified. Fig. 7.12 (b) shows the corresponding results of the narrow band envelope from the ring gear casing vibration signal. The second mesh harmonic was chosen and a bandwidth of 20 shaft orders (±10) was used for the narrow band analysis.

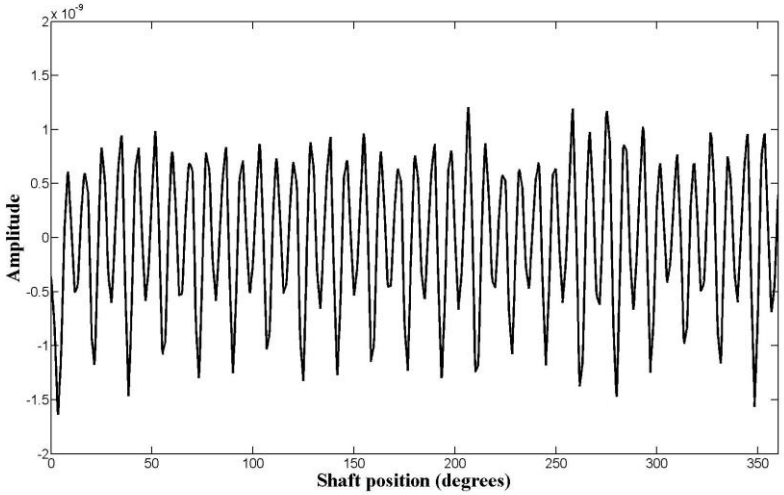

Figure 7.11 Sun gear signal obtained from the ring gear casing with perfect tooth

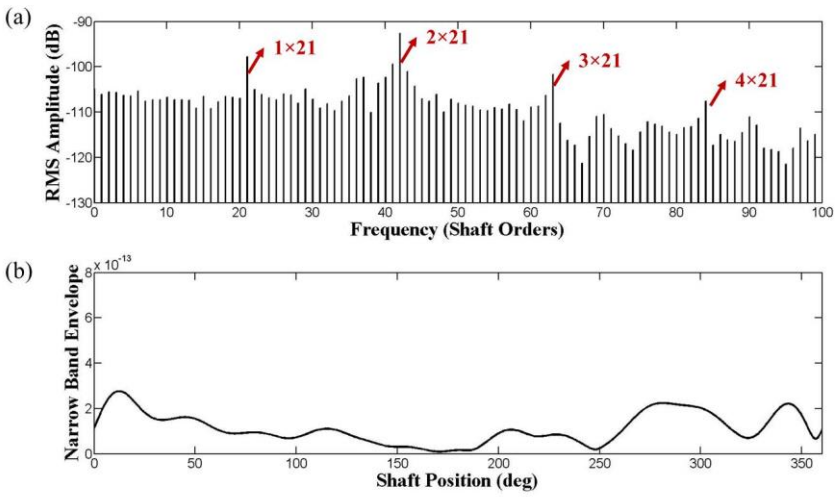

Figure 7.12 Sun gear signal with perfect tooth, (a) RMS frequency spectrum, (b) narrow band envelope

Fig. 7.13 shows the results of the amplitude modulation and phase modulation. The second mesh harmonic was chosen and a bandwidth of 20 shaft orders (±10) was used for the demodulation process.

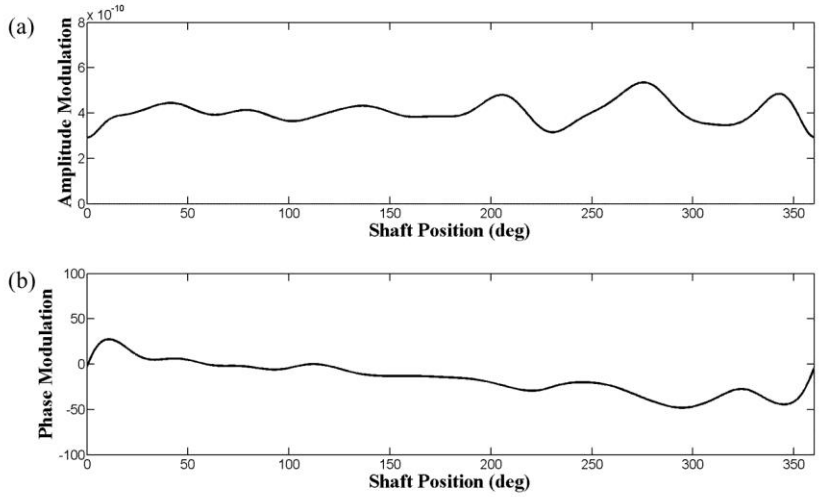

Figure 7.13 Sun gear signal with perfect tooth, (a) amplitude modulation, (b) phase modulation

Fig. 7.14 shows the results of the signal for one sun gear shaft rotation with a cracked sun gear tooth. The damage can be visually observed in the signal where the damaged tooth meshes with the planet gears at around 0°, 120°, and 240° as there are three planet gears in the system.

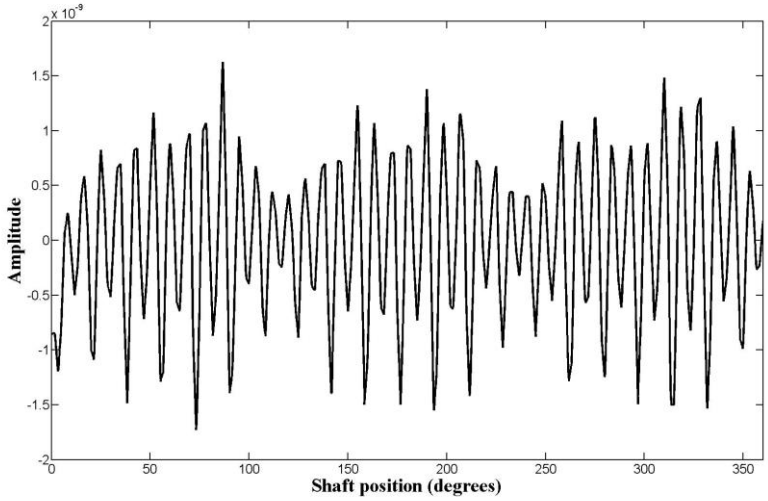

Figure 7.14 Sun gear signal obtained from the ring gear casing with cracked tooth

Fig. 7.15(a) shows the results of the RMS frequency spectrum and the narrow band envelope, which are based on the signal in Fig. 7.14. The sun gear shaft order can still be observed in the figure and the amplitude at the second mesh harmonic was around −92.72 dB compared with that (−92.63dB) at the second mesh harmonic in healthy condition. Fig. 7.15(b) shows the results of the narrow band envelope for the second mesh harmonic. Compared with that in Fig. 7.12 (b), no obvious peak can be observed in the narrow band result except that the overall value increased slightly.

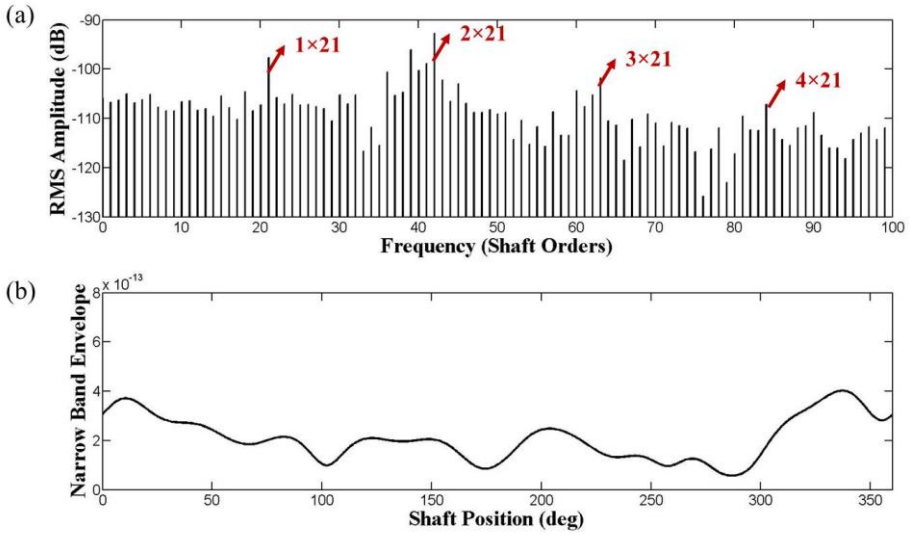

Figure 7.15 Sun gear signal with cracked sun gear tooth, (a) RMS frequency spectrum, (b) narrow band envelope

Fig. 7.16 shows the results of the amplitude modulation and phase modulation. The second mesh harmonic was chosen and a bandwidth of 20 shaft orders (±10) was used for the demodulation process. The presence of the sun gear crack can be noted at the position 90°, 200°, and 320°, which corresponded to the positions where the cracked tooth meshes with the planet gear separately. The kurtosis value of the cracked sun gear amplitude modulation was 2.73, compared with the value of 3.28 in the healthy condition. The kurtosis value of the cracked sun gear phase modulation was 2.57, compared with the value of 2.48 in the healthy condition. These results suggested that the kurtosis value, which worked very well in the fixed axis gear in chapter 4, was not very effective for the cracked sun gear in planetary gear.

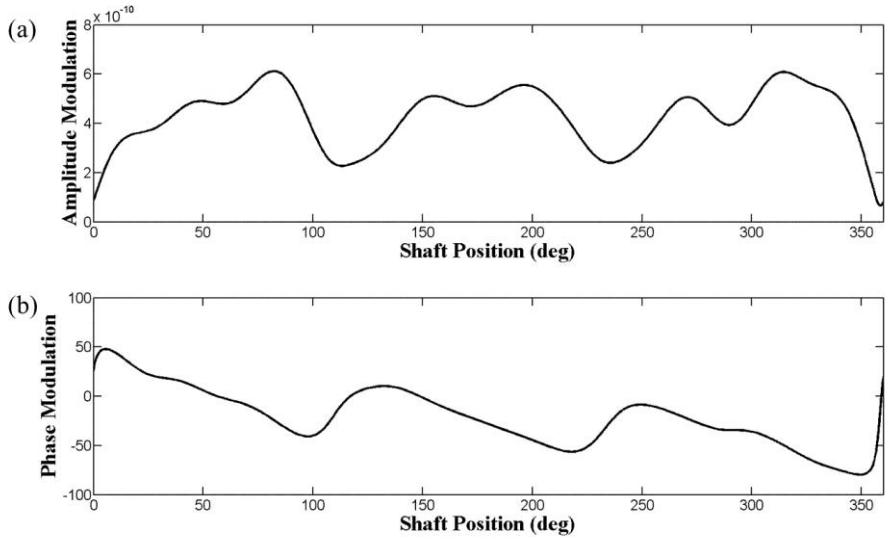

Figure 7.16 Sun gear signal with cracked sun gear tooth, (a) amplitude modulation, (b) phase modulation

Fig. 7.17 shows the results of the signal for one planet gear shaft rotation with a cracked planet gear tooth on the sun gear side. The same procedure mentioned for obtaining the sun gear vibration was used to obtain the vibration data for the detection of the planet gear vibration. The damage can be visually observed in the signal at around 70º.

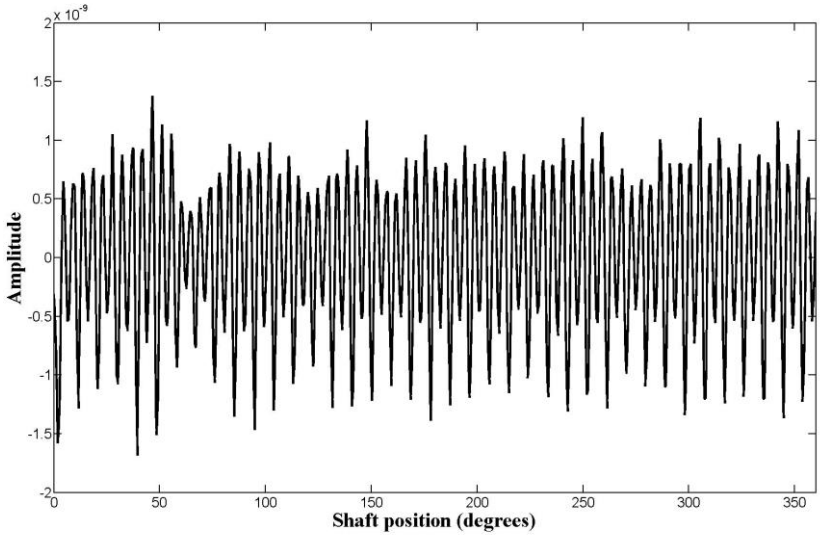

Figure 7.17 Planet gear signal obtained from the ring gear casing with cracked planet gear tooth meshing with the sun gear

Fig. 7.18 shows the results of the RMS frequency spectrum and the narrow band envelope, which are based on the signal in Fig. 7.17. The planet gear shaft order can be observed in the figure and the amplitude at the second mesh harmonic was around −92.51 dB. Fig. 7.18(b) shows the results of the narrow band envelop for the second mesh harmonic. A bandwidth of 38 shaft orders (±19) was used for the narrow band analysis.

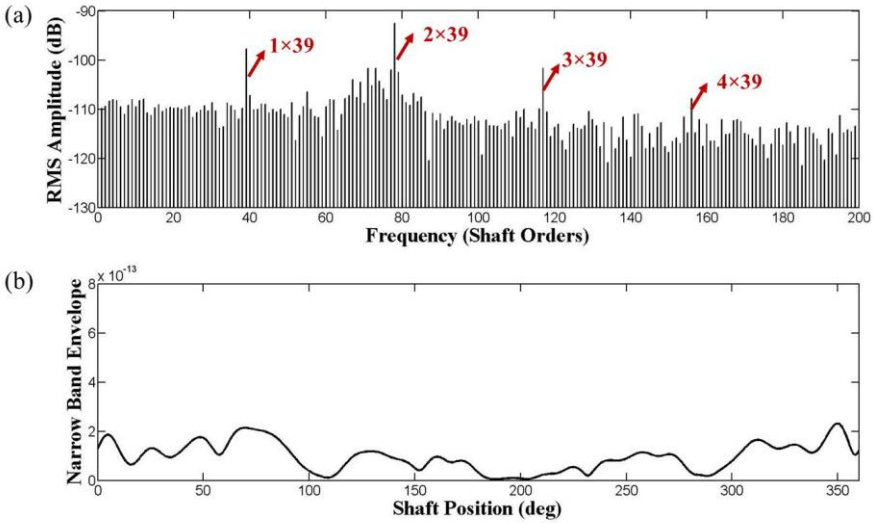

Figure 7.18 Planet gear signal with cracked planet tooth on the sun gear mesh side, (a) RMS frequency spectrum, (b) narrow band envelope

Fig. 7.19 shows the results of the amplitude modulation and phase modulation. The second mesh harmonic was chosen and a bandwidth of 38 shaft orders (±19) was used for the demodulation process. The presence of the planet gear crack can be noted at the position 70°. The kurtosis value of the cracked planet gear amplitude modulation was 3.77. The kurtosis value of the cracked planet gear phase modulation was 2.70. It should be noted that there is only one peak caused by the cracked planet gear tooth during the whole shaft rotation, compared with the three peaks caused by the cracked sun gear tooth during one shaft rotation. This is because the cracked planet gear tooth was created only on one planet and it only meshed once with the sun gear during this whole rotation.

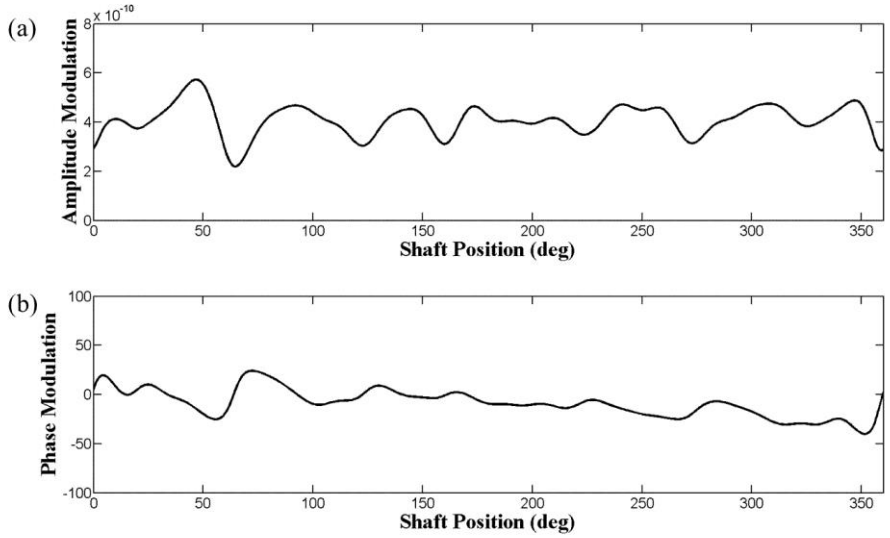

Figure 7.19 Planet gear signal with cracked planet tooth on the sun gear mesh side, (a) amplitude modulation, (b) phase modulation

Fig. 7.20 shows the results of the signal for one planet gear shaft rotation with the cracked planet gear tooth meshing on the ring gear side. The same procedure mentioned for obtaining the sun gear vibration was used to obtain the vibration data for the detection of the planet gear. No obvious evidence can be found for the presence of the crack.

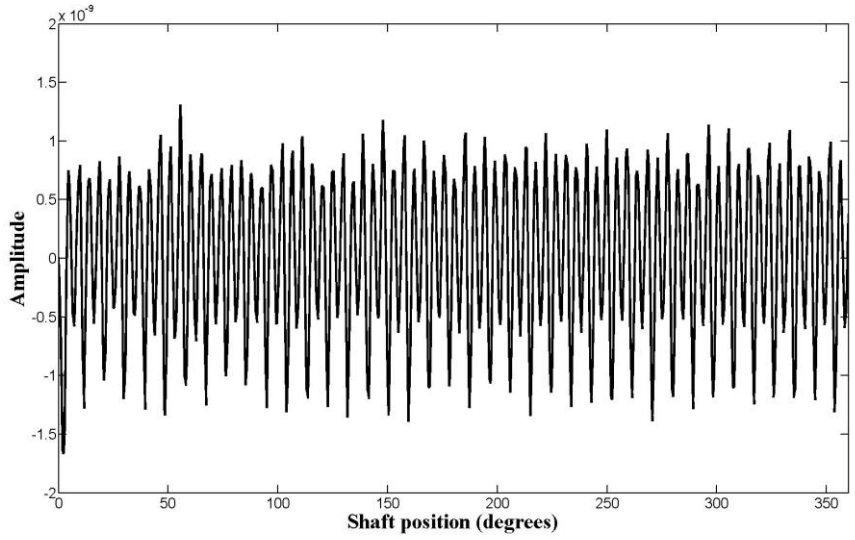

Figure 7.20 Planet gear signal obtained from the ring gear casing with cracked planet gear tooth meshing with the ring gear

Fig. 7.21 shows the results of the RMS frequency spectrum and the narrow band envelope, which are based on the signal in Fig. 7.20. The planet gear shaft order can be observed in the figure and the amplitude at the second mesh harmonic was around −92.31 dB. Fig. 7.21(b) shows the results of the narrow band envelop for the second mesh harmonic. A bandwidth of 38 shaft orders (±19) was used for the narrow band analysis. An insignificant peak can be found at the shaft position 50º.

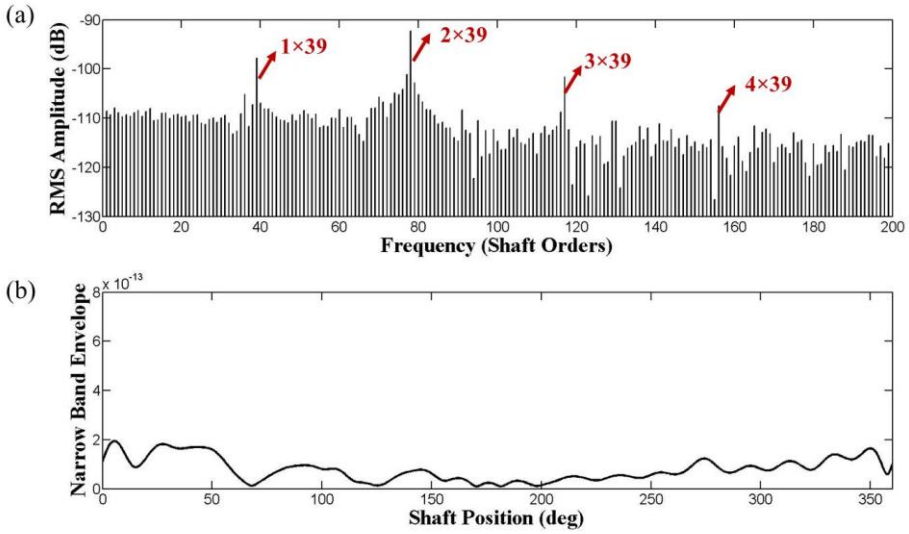

Figure 7.21 Planet gear signal with cracked planet tooth on the ring gear mesh side, (a) RMS frequency spectrum, (b) narrow band envelope

Fig. 7.22 shows the results of the amplitude modulation and phase modulation. The second mesh harmonic was chosen and a bandwidth of 38 shaft orders (±19) was used for the demodulation process. The evidence for the presence of the planet gear crack can be noted at the position 50° with a small peak at the amplitude modulation. The kurtosis value of the cracked planet gear amplitude modulation was 2.99. The kurtosis value of the cracked planet gear phase modulation was 2.41.

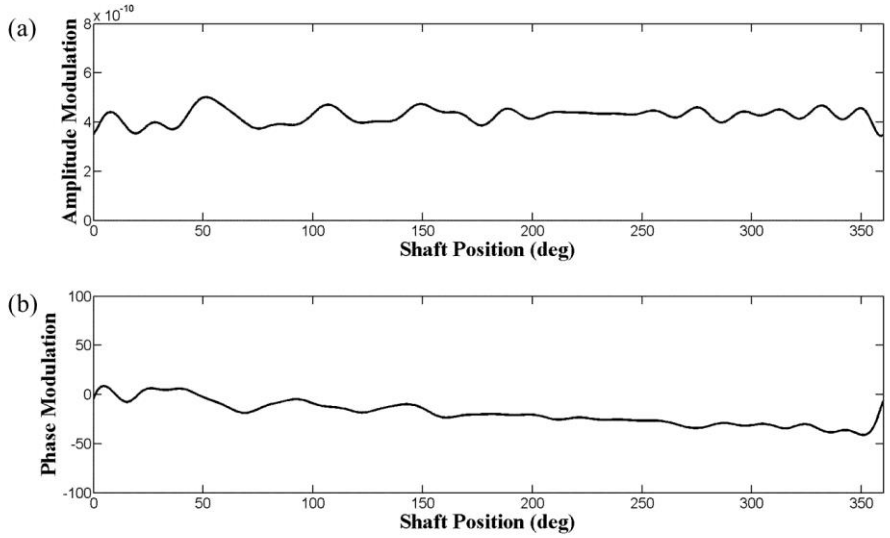

Figure 7.22 Planet gear signal with cracked planet tooth on the ring gear mesh side, (a) amplitude modulation, (b) phase modulation

7.3 Fault diagnostic results for pin supported planetary gear

7.3.1 Fault diagnostic results for torsional vibration

After the initial transient start-up was observed to have decayed away, the carrier arm angular velocity was chosen to diagnose the planetary gear response with the pin supported ring gear. The same diagnostic algorithms used for the uniformly supported ring gear were used again in order to compare the difference. These algorithms include RMS spectrum, residual signal, narrow band envelop, amplitude and phase modulation and time-frequency analysis.

The sun-planet mesh stiffness used in this situation was assumed to be not affected by the change of the ring gear support and all the sun-planet stiffnesses with or without a crack were summarized in chapter 6. However, the ring-planet mesh stiffness used in this pin situation was significantly affected by the change of the ring gear support and all the ring-planet stiffnesses with or without a crack were also summarized in chapter 6.

Fig. 7.23 shows the results of the carrier arm angular velocity signal over one carrier arm revolution, which has been resampled into equispaced phase data over one carrier arm revolution. There are four plots shown in the figure corresponding to the condition of the

healthy planetary gears, the planetary gear with a cracked sun gear, the planetary gear with a cracked planet gear as well as the planetary gear with a cracked ring gear. It was noted that there was no obvious evidence for the presence of the crack, even for the cracked sun gear, whose effect has been shown to be very significant in the uniformly supported conditions.

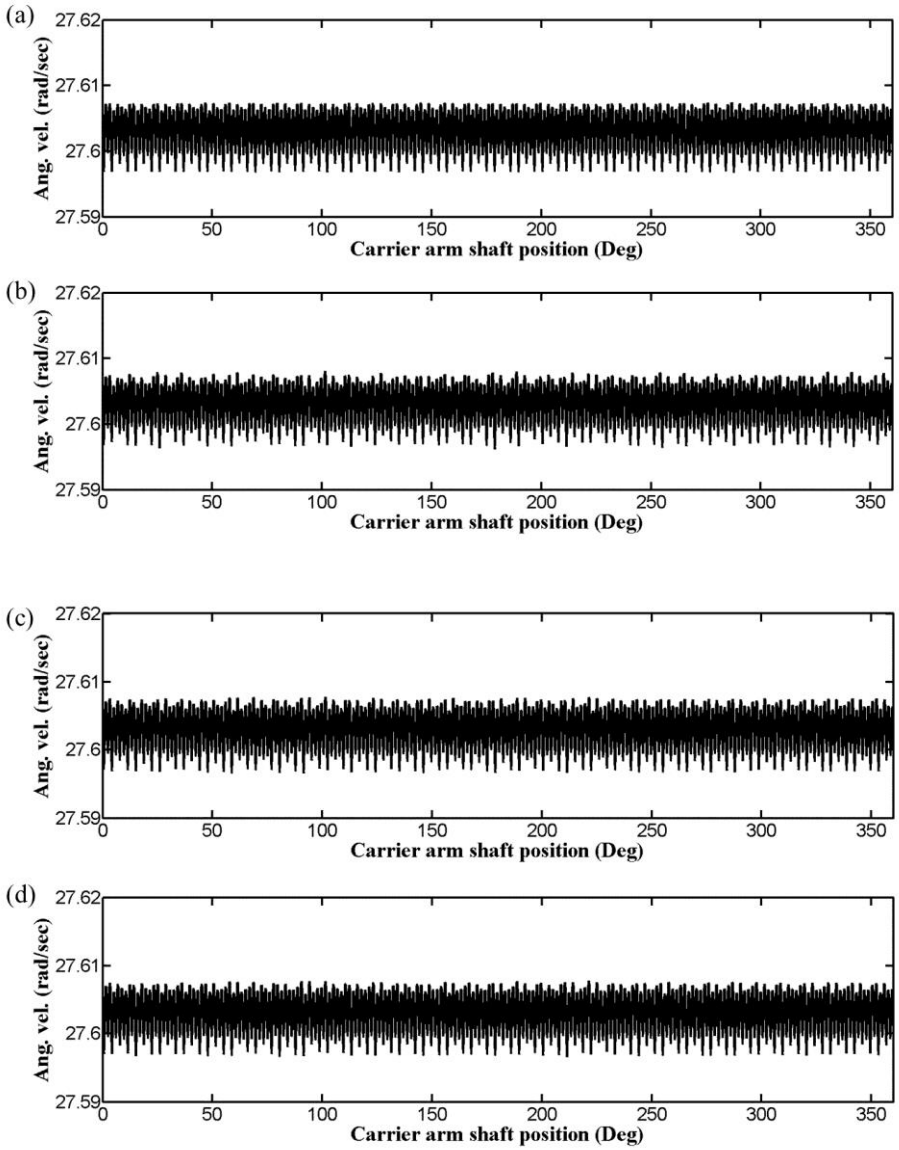

Figure 7.23 Carrier arm angular velocity over one complete revolution with pin supported ring gear. (a) healthy planetary gear case; (b) planetary gear with cracked sun gear case; (c) planetary gear with cracked planet gear on the sun gear side case; (d) planetary gear with cracked ring gear case.

Fig. 7.24 shows the results of the RMS spectra, which are based on the signal obtained in Fig. 7.23, for the pin supported ring gear situation. As the signals cover one carrier arm revolution, the RMS spectra results are presented in terms of carrier arm order. The first observation from the figure was that the RMS spectra still have the gear mesh components at order 99 and its harmonics as it did in the uniformly supported situation. However, besides all these gear mesh components, another interesting finding was that several strong components from the sidebands appeared, whose magnitude was obviously larger and very close to the magnitude of the mesh components, can be observed at 33 shaft orders and its harmonics. These strong sideband components can be identified in all situations, no matter if it was a healthy case or a cracked tooth on the sun gear (Fig. 7.24(b)), planet gear (Fig. 7.24(c)), or ring gear (Fig. 7.24(d)).

Checking the amplitude of the mesh components is a common method for gear fault diagnosis and the amplitude of the first mesh component was chosen. The amplitudes for the corresponding four cases in Fig. 7.24 were −31.9559 dB, −33.0369 dB, −32.8358 dB, and −32.8673 dB respectively. The amplitude of the characteristic frequency positions could also be used for the fault diagnosis. For the planetary gear system with the sun gear fault, the position of the sun gear characteristic frequency in Fig. 7.24 (b) is $k \cdot Z_r \pm n \cdot N \cdot (Z_r/Z_s)$. For example, the amplitude of the frequency component at position 113 (for the case of 99+ 1×3×99/21) could be checked and it was found to be −45.7252 dB compared with the value of −56.9269 dB in the healthy condition. For the planetary gear system with the planet gear fault, the position of the planet gear characteristic frequency in Fig. 7.24 (c) is $k \cdot Z_r \pm n \cdot (Z_r/Z_p)$. For example, the amplitude of the frequency component at position 101 (for the case of 99+ 1×99/39) could be checked and it was found to be −58.2498 dB compared with the value of −48.6849 dB in the healthy condition. For the planetary gear system with the ring gear fault, the position of the ring gear characteristic frequency in Fig. 7.24 (d) is $k \cdot Z_r \pm n \cdot N$. For example, the amplitude of the frequency component at position 201 (for the case of 99 − 18×3) could be checked and it was found to be −50.3383 dB compared with the value of −58.0438 dB in the healthy condition.

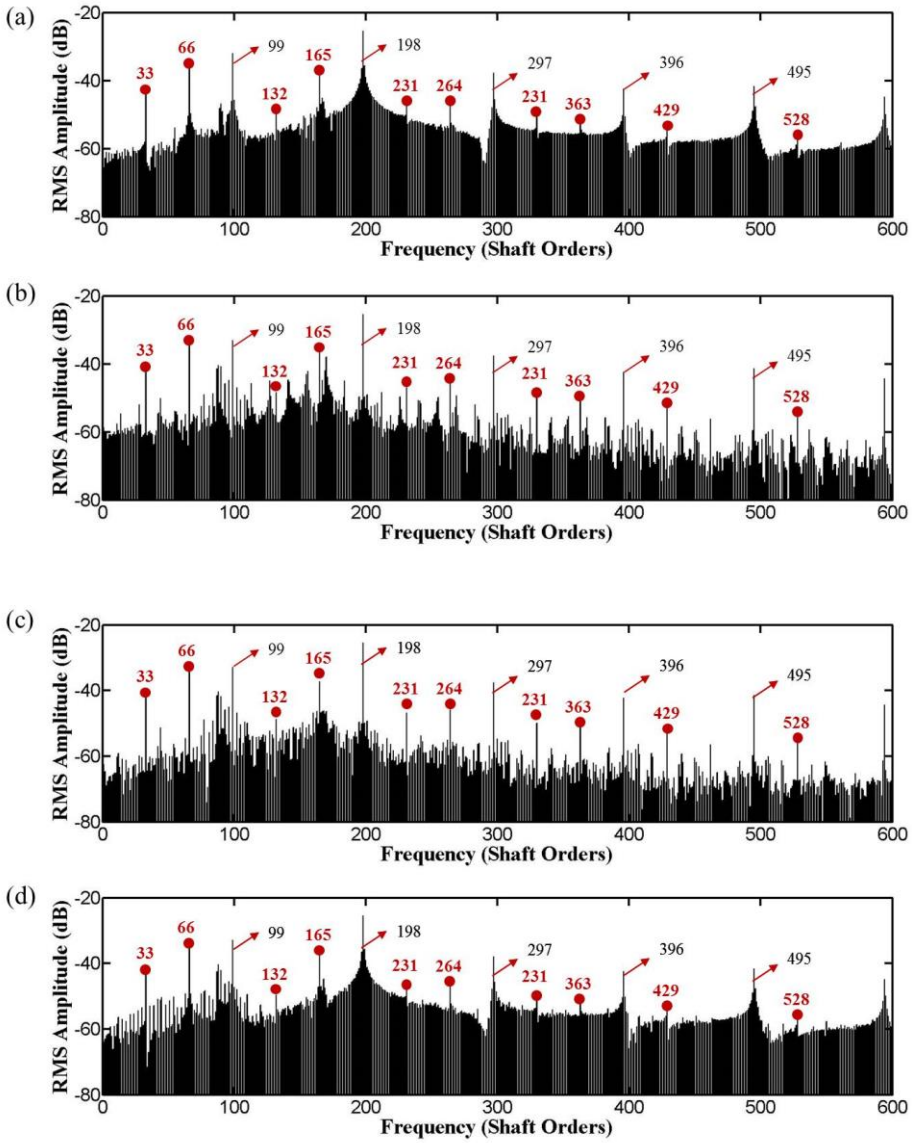

Figure 7.24 RMS spectrum amplitude results with pin supported ring gear. (a) healthy planetary gear case; (b) planetary gear with cracked sun gear case; (c) planetary gear with cracked planet gear on the sun gear side case; (d) planetary gear with cracked ring gear case.

As the sidebands tend to contain important information of the characteristic faulty frequencies, the residual signal can be obtained by removing the mesh components and its harmonics, as shown in Fig. 7.25. It was found that the detectability of the gear fault was not enhanced significantly as expected and it was still hard to diagnose the fault in the system. As a result, the statistical indicators were not used here to further analysis the results in Fig. 7.25.

However, as analysed in the frequency spectra in Fig. 7.24, there were also several strong components observed at shaft order 33 and its harmonics, which were largely due to the modulation effect in the ring-planet mesh stiffness with the pin supported ring gear. There were 11 pins in this system and each of the ring-planet mesh stiffness was significantly modulated by these pin supports. Therefore, these components were caused by the pin support instead of any fault in the system and as a result, the residual signal can be further simplified by removing the components at 11 and its harmonics, as shown in Fig. 7.26. It was found that the difference between the cracked case and the healthy case can be observed in this further simplified residual signal, but the problem was that the signal became insignificant. This method of enhancing the fault detection also had a negative effect on the signal and too much information was removed by this method.

Another compromising method of obtaining a reasonable residual signal was in removing the gear mesh components and the components at 33 orders and its harmonics instead of 11 orders and its harmonics. This result was shown in Fig. 7.27. It was found that the signal strength has been enhanced while it was still able to distinguish the difference between the healthy case and the faulty case.

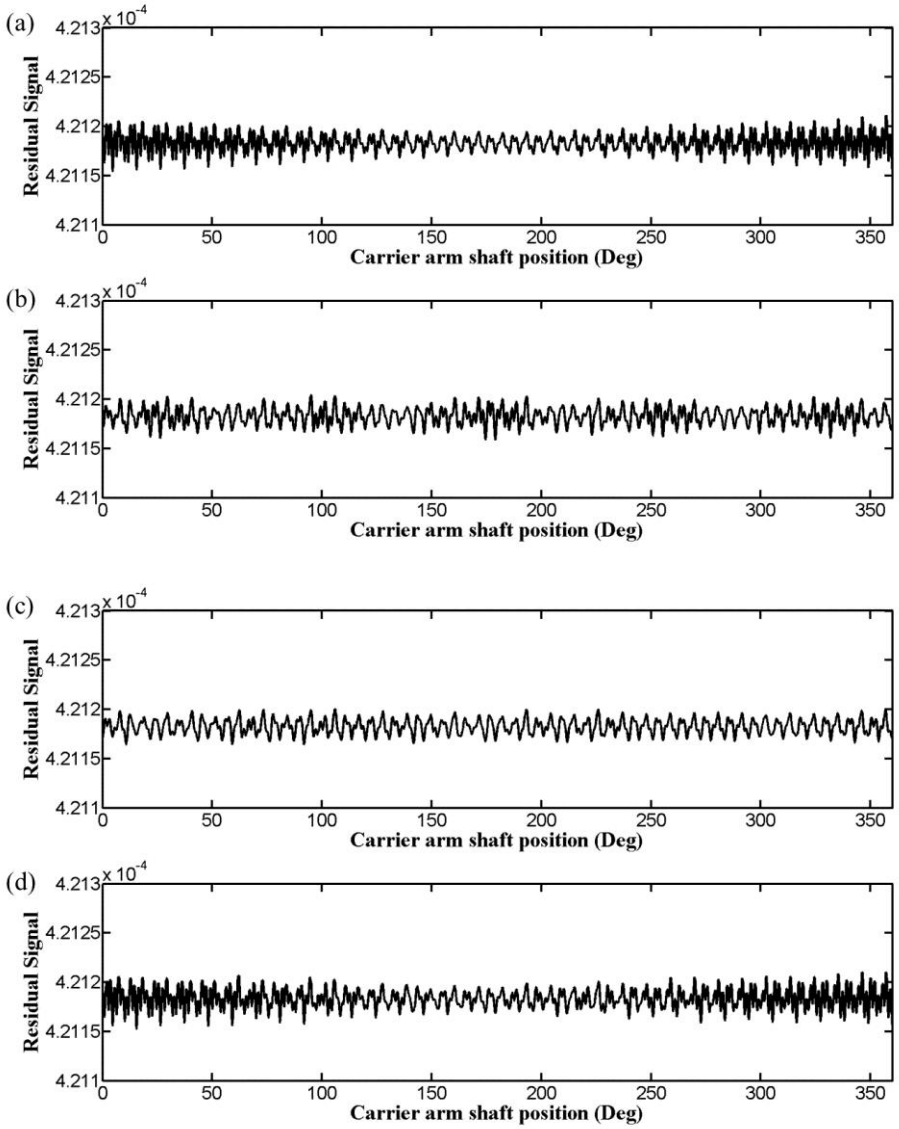

Figure 7.25 Residual signal results with pin supported ring gear. (a) healthy planetary gear case; (b) planetary gear with cracked sun gear case; (c) planetary gear with cracked planet gear on the sun gear side case; (d) planetary gear with cracked ring gear case.

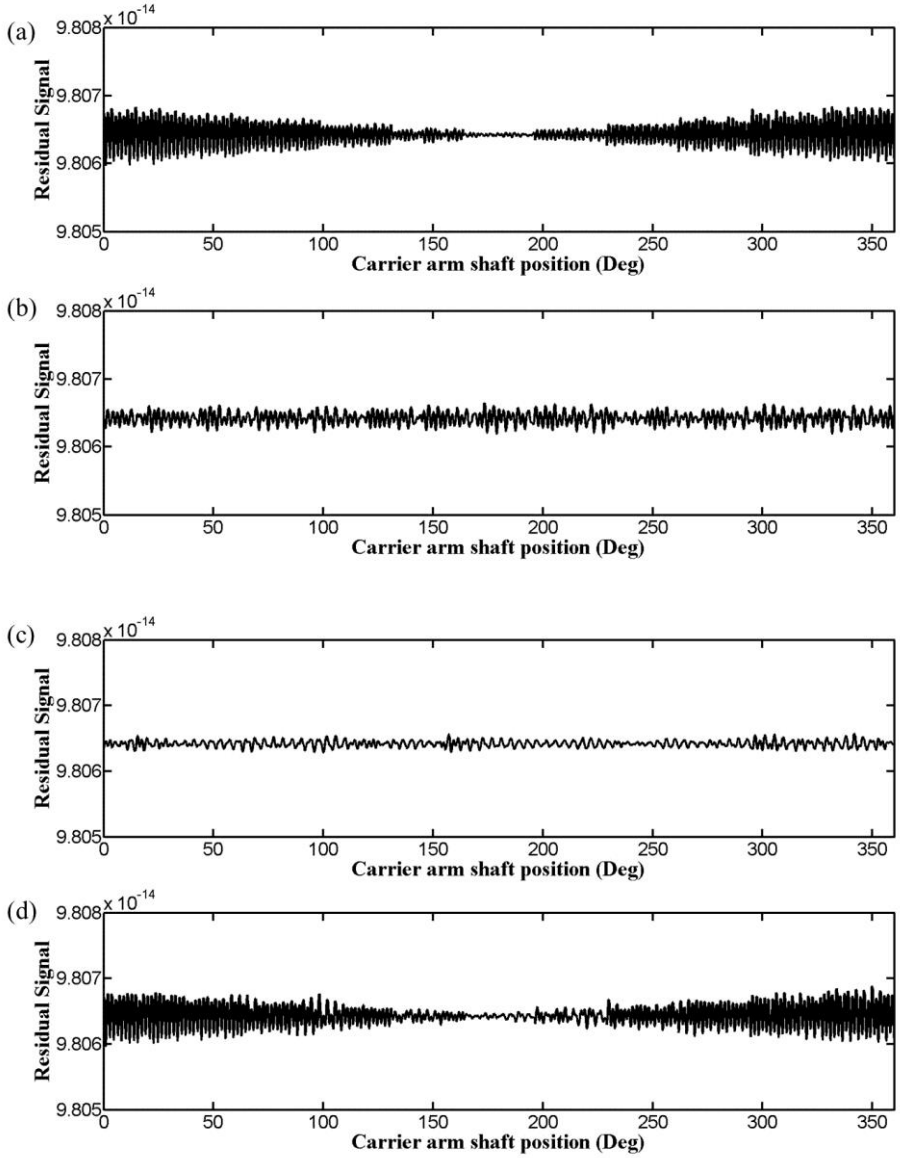

Figure 7.26 Residual signal results by removing the component at 11 orders and its harmonics with pin supported ring gear. (a) healthy planetary gear case; (b) planetary gear with cracked sun gear case; (c) planetary gear with cracked planet gear on the sun gear side case; (d) planetary gear with cracked ring gear case.

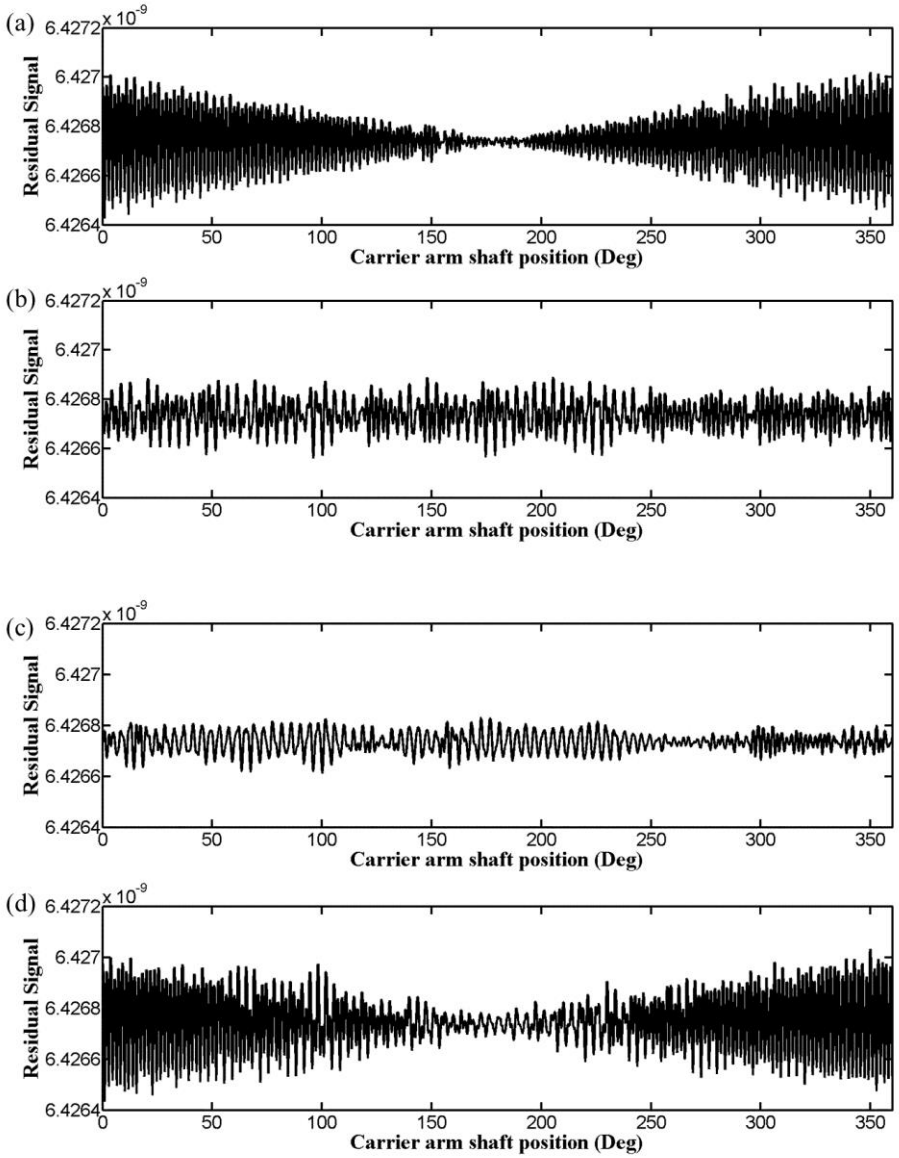

Figure 7.27 Residual signal results by removing the component at 33 orders and its harmonics with pin supported ring gear. (a) healthy planetary gear case; (b) planetary gear with cracked sun gear case; (c) planetary gear with cracked planet gear on the sun gear side case; (d) planetary gear with cracked ring gear case.

Fig. 7.28 shows the results for the narrowband envelope results and the second mesh harmonic was chosen for the demodulation process and a bandwidth of 98 shaft orders (±49) was used for the analysis. The first observation of this result was that the crack on the sun gear and the planet gear can be identified even though they were not as obvious as they were in the uniformly supported ring situations. However, the effect of the modulation from the pin supports can be observed in all the figures.

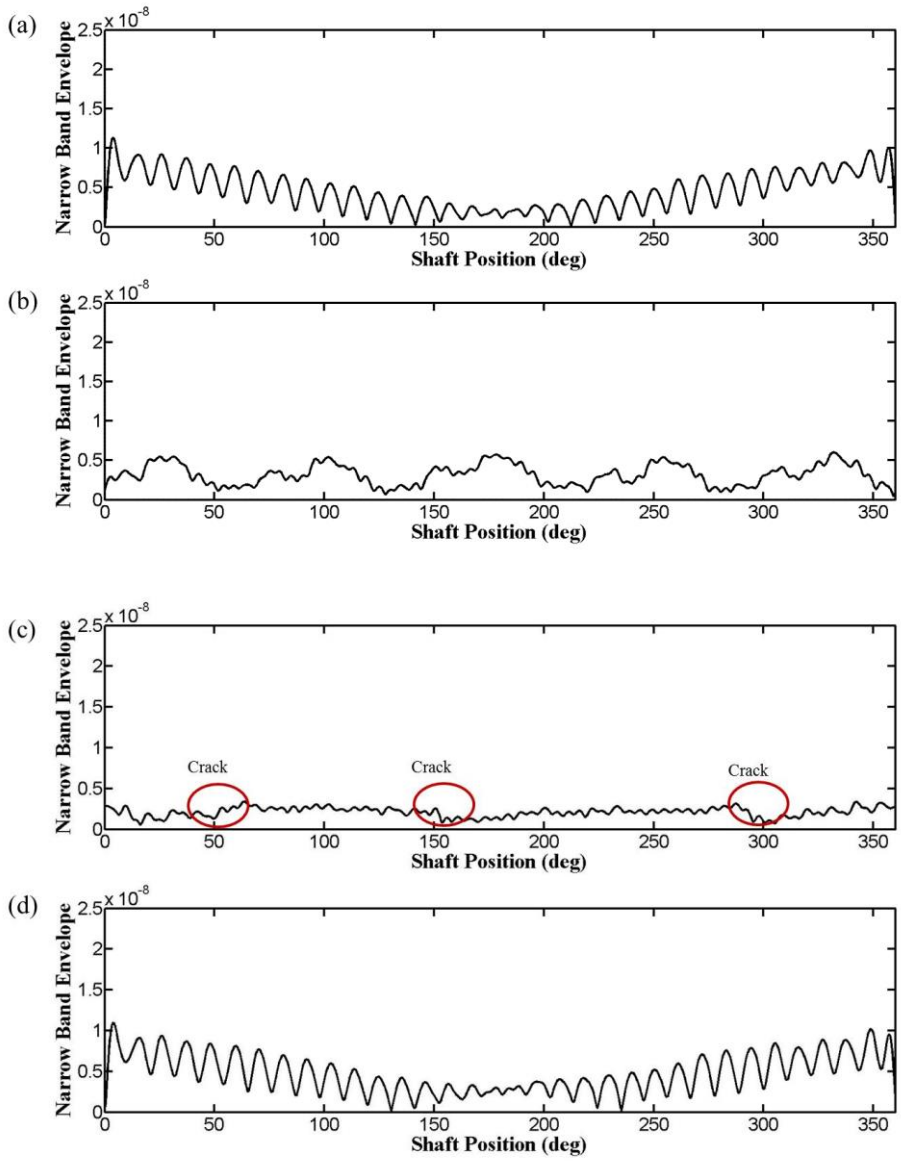

Figure 7.28 Narrowband envelope results with pin supported ring gear. (a) healthy planetary gear case; (b) planetary gear with cracked sun gear case; (c) planetary gear with cracked planet gear on the sun gear side case; (d) planetary gear with cracked ring gear case.

Fig. 7.29 shows the results of the amplitude and phase demodulation of the gear signal. The second mesh harmonic was chosen for the demodulation process and a bandwidth of 98 shaft order (±49) was used for the analysis. It was found that the effect of the modulation from the pin support can still be observed in the modulation graph, especially the healthy case. Even though there was no fault in the healthy case, the amplitude and phase modulation still experienced some fluctuation through the shaft rotation. However, the impulses caused by

the gear fault in the system were still able to be identified visually except in the cracked ring gear case. Another important finding was that the number of the impulses in the cracked sun gear case that can be visually identified was only 5, which was quite different compared with that in the uniformly supported ring gear situation.

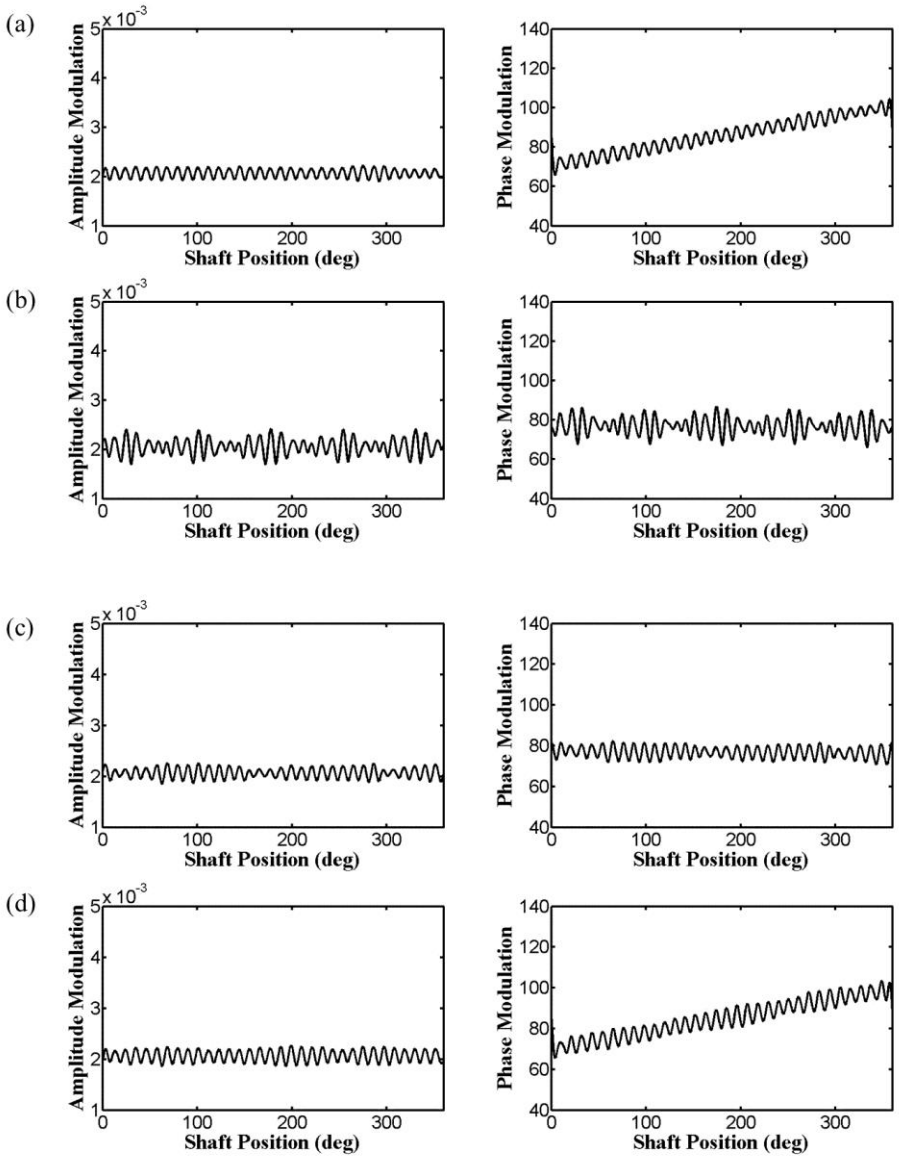

Figure 7.29 Amplitude modulation and phase modulation results with pin supported ring gear. (a) healthy planetary gear case; (b) planetary gear with cracked sun gear case; (c) planetary gear with cracked planet gear on the sun gear side case; (d) planetary gear with cracked ring gear case.

7.3.2 Fault diagnostic results for stationary transducer on ring gear

The FEA model developed in chapter 6 (section 6.3) was used to simulate the dynamic response from the ring gear and instead of having a uniformly supported ring, the ring gear was supported by pins, as shown in Fig. 7.30. In the uniformly supported ring, each ring teeth was under identical support situation and therefore, no matter where the sensor location is, the spectrum of the vibration data recorded by the sensor should be identical if there was no crack occurring in the gear system. However, in the pin supported condition, the boundaries for each of the ring gear teeth between the supports was different and as a result, the spectrum of the vibration data recorded by the sensor located on different teeth was expected to be different. For example, in a 11−pin supported ring condition, there were 9 teeth between the pins and the vibration data recorded by sensors on location 1, 3, 5, and 8, as shown in Fig. 7.30, should be different. Sensor 1 was located on the pin support. Sensor 3 was located on the third tooth counting from sensor 1. Sensor 5 was located in the middle of the two pins. Sensor 8 was located on the eighth tooth counting from sensor 1. ANSYS transient analysis was used to obtain the dynamic response and as the carrier arm speed was 27.6 rad/s, around 0.2277 s was needed to finish one carrier revolution.

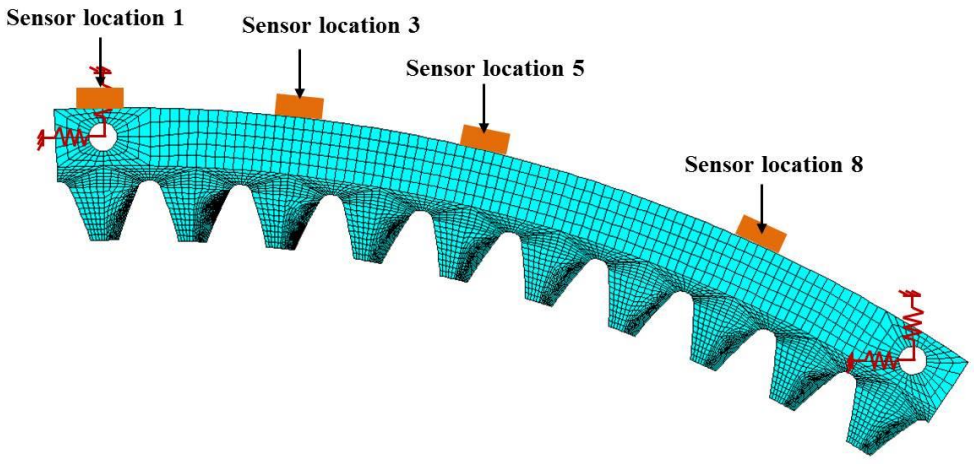

Figure 7.30 Pin supported ring gear with different sensor location

Fig. 7.31 shows the displacement history data for the sensors located on different teeth. The first observation was that each sensor experienced the modulation effect from the carrier arm

rotation. There were three planet gears in the system and therefore, three peaks can be observed in the history data. Another interesting finding was that the displacement curves were not as smooth as those in the uniformly supported ring gear, as one example shown in Fig. 7.7 (a). This is largely because the pin supports cause modulation to the stiffness and then further modulation effect to the ring-planet mesh forces. The last observation was that the amplitude of the displacement data was found to be different from each, for example, the amplitude of the displacement data of sensor 8 was around 10×10^{-8} m, which was twice of that from the 1st sensor.

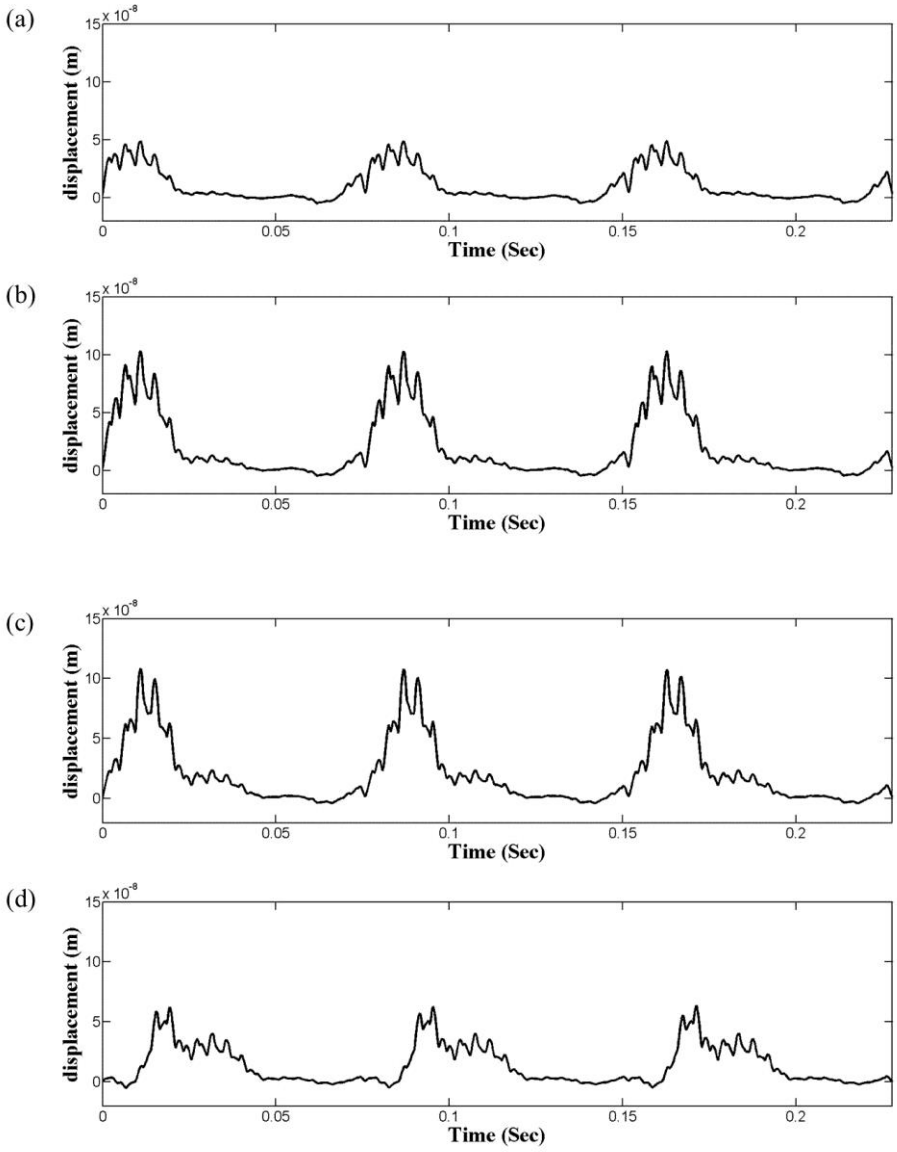

Figure 7.31 The displacement data recorded by sensors located on different teeth. (a) sensor 1; (b) sensor 3; (c) sensor 5; (d) sensor 8.

The displacement data from each ring gear tooth can be recorded and the amplitude plotted to study the effect of the sensor location on the vibration amplitude. Fig. 7.32 shows the maximum displacement data recorded from 20 ring gear sensors, which were located between three pin supports. It was obvious that the vibration data recorded by different sensors can be different in terms of their amplitude and the amplitude of the sensor on the fourth ring gear tooth, counted from the pin support, was found to be a maximum. This phenomenon repeated again in the process between the next two pins.

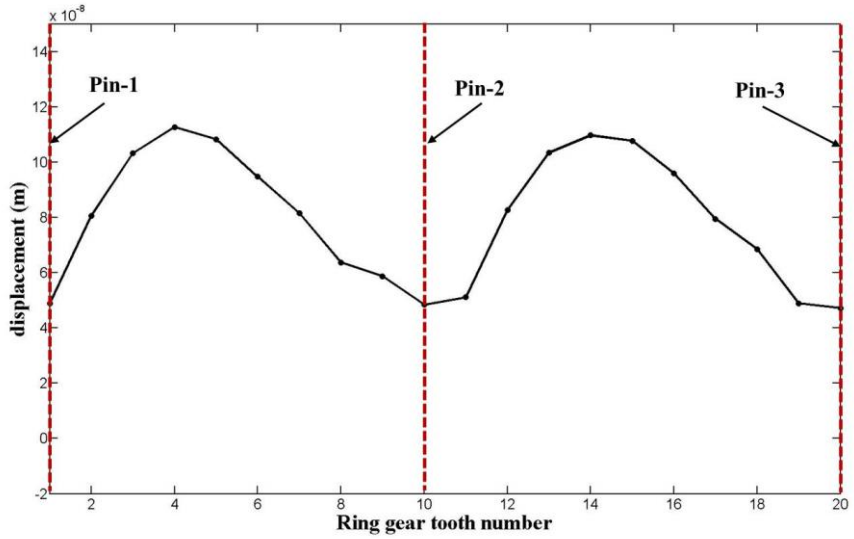

Figure 7.32 The maximum displacement data recorded by sensors located on different teeth.

Fig. 7.33 shows the results of the acceleration data obtained from the displacement data. As expected, the amplitude of the acceleration data from the sensors were different, which means that when a stationary transducer was mounted on the ring gear with pin support for the fault detection, the selection of the transducer location has to be taken into consideration with special care if a strong vibration signal with large amplitude is desired. Once the location was chosen, the same procedure for capturing the vibration data described in the uniformly supported ring gear can be used again to detect the fault. The only difference was that as the boundary condition for each ring gear tooth was different, the method of recording the data from the 1st ring gear tooth to the 21st tooth as a short cut for carrier arm rotating 21 revolutions cannot be used. Instead, if the sun gear is under interest, 21 carrier

arm revolutions has to be modelled and then the data can be recorded at one particular location with the stationary transducer and finally these data can be reassembled for the sun gear fault detection.

Fig. 7.34 shows the results of the frequency spectra of the acceleration data. As there was no fault involved, the spectra would be expected to be symmetrical about the mesh component (Inalpolat & Kahraman, 2009, 2010). The spectra in the uniformly supported ring gear case has been kept consistence with Kahraman's discussion, as shown in Fig. 7.7. However, it was interesting to see that the spectra in this situation lost its symmetric property and components at the shaft order of 11 and its harmonics began to emerge in the spectra, especially the component at 55 orders. Another interesting finding was that the amplitudes at location 96 and 102 should be equal to each other in the analytical analysis (Inalpolat & Kahraman, 2009, 2010), but this situation was only found in the spectra of the 1st sensor, even though the component in the spectra of the 8th sensor appeared to be the same. The corresponding components in the spectra of the 3rd sensor and 5th sensor obviously had different amplitude and more specifically, the amplitude at 102 was larger than that at 96. All these results suggested that the vibration data recorded by transducers on different locations can be quite different even in the healthy case and special care has to be taken when selecting the transducer location. Also, it indicated that the sensor that was closest to the pin support would give the best vibration data in terms of the symmetrical spectra.

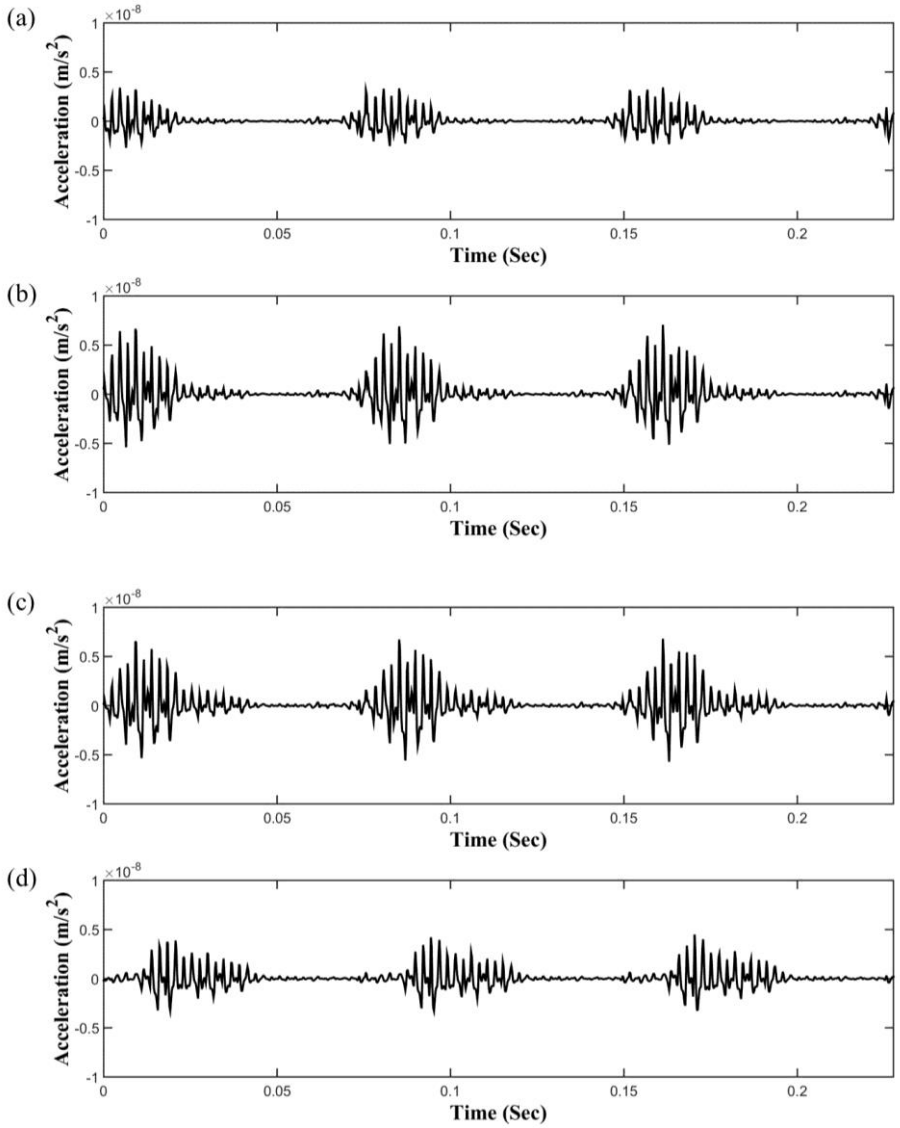

Figure 7.33 The acceleration data recorded by sensors located on different teeth. (a) sensor 1; (b) sensor 3; (c) sensor 5; (d) sensor 8.

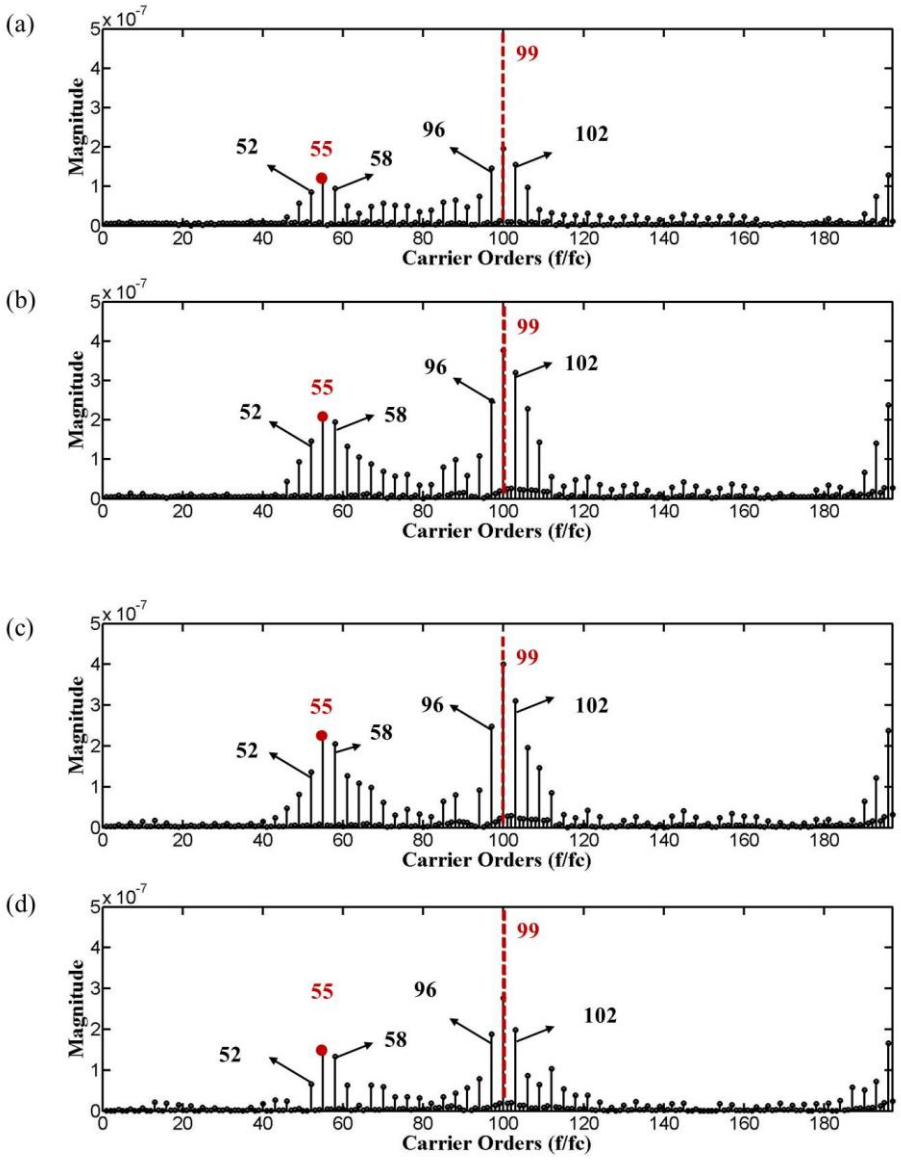

Figure 7.34 The frequency spectra of the acceleration data recorded by sensors located on different teeth. (a) sensor 1; (b) sensor 3; (c) sensor 5; (d) sensor 8.

In this stationary transducer with a pin supported ring gear analysis, no fault has been discussed here. As discussed previously, the similar procedure for capturing the vibration data described in the uniformly supported ring gear can be used and then the common diagnostic method, like the RMS spectrum, narrow band analysis, amplitude and phase modulation can be used to detect the fault. The only difference was that, if the sun gear is under interest, 21 carrier arm revolutions of data will be required to re-assemble the vibration data for the stationary transducer.

7.4 Investigation of other sensor options for ring gear fault detection

7.4.1 Probe sensor for measuring the sun gear displacement

As shown previously, using the carrier arm torsional vibration to detect the ring gear fault was not as successful as using it for detecting the sun gear and planet gear faults. As a result, this section focused on ring gear fault detection analysis. Fig. 7.35 shows the displacement signal of the sun gear in the x direction using data recorded over 1 second in total. During this period, there were 4 carrier arm revolutions and in each carrier arm revolution, the fault impulse can be identified. As the fault was created on the ring gear and there were three planet gears, when each planet gear was in mesh with the fault on the ring, it would generate one fault impulse and therefore, there were three fault impulses in each carrier arm revolution in total.

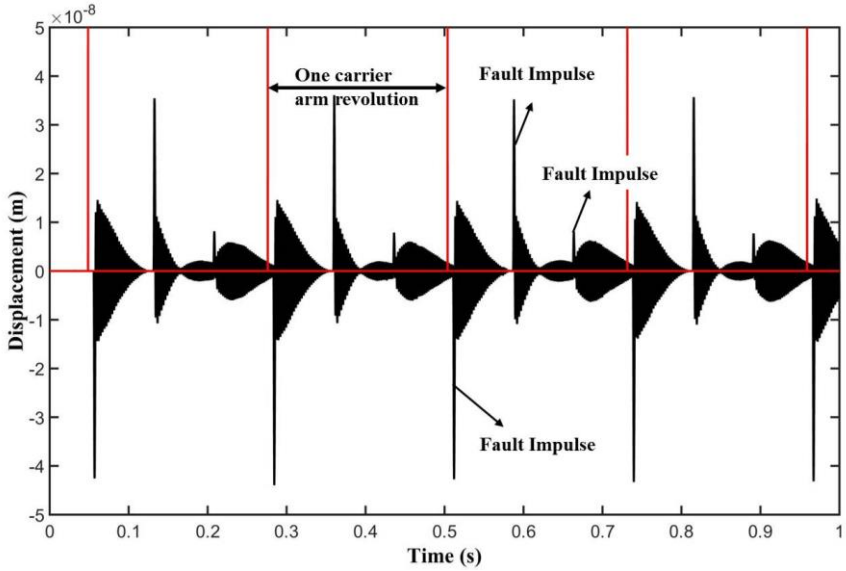

Figure 7.35 Displacement of the sun gear in the x-direction.

Fig. 7.36 shows the absolute displacement squared of the sun gear. This displacement signal was calculated by $(d_x^2 + d_y^2)$, where d_x is the displacement of the sun gear in the x direction and d_y is the displacement of the sun gear in the y direction. It was found that the fault impulse has been reinforced in this way and the three fault impulses during one carrier arm revolution can be clearly identified. These results indicated that the ring gear fault seemed more sensitive to the signal in the transverse direction instead of the carrier arm torsional

signal. The advanced signal processing could be used to detect the ring gear fault based on this transverse displacement signal, but it will be discussed more in future work.

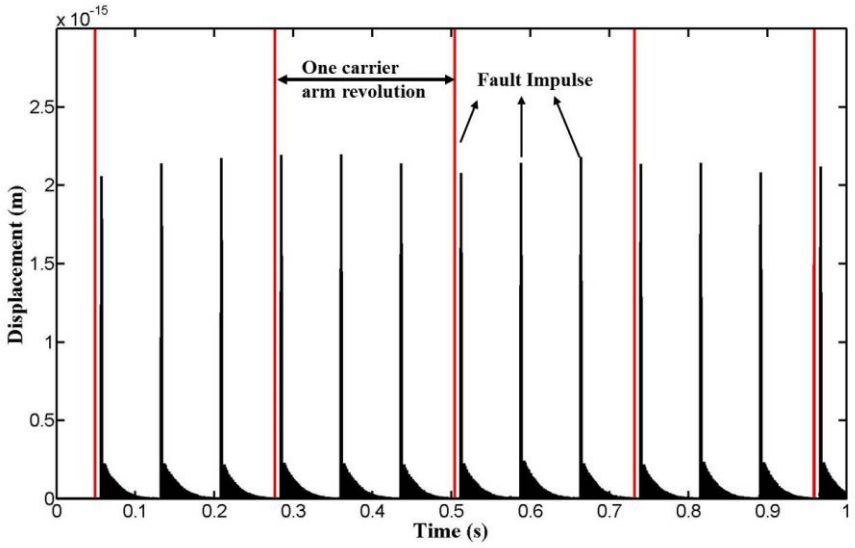

Figure 7.36 Absolute displacement squared of the sun gear.

Fig. 7.37 shows the centre locus of the sun gear in just one carrier arm revolution with the impact of the ring gear fault. The x axis is the displacement signal of the sun gear in the x direction and the y axis is the displacement signal of the sun gear in the y direction. If no fault occurred, there should be 99 spikes corresponding to 99 ring gear teeth meshes. When the fault occurs, however, even larger spikes caused by the ring gear could be observed in the locus, which provided another potentially effective way to detect the ring gear fault.

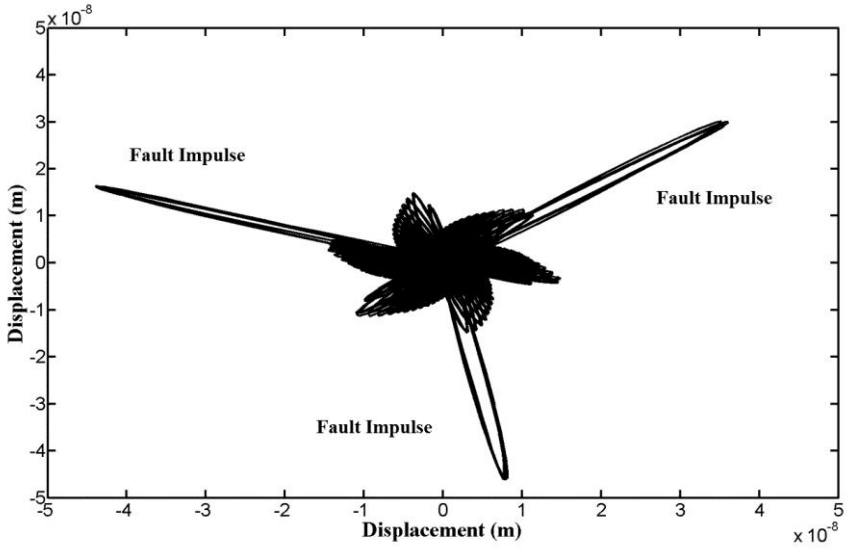

Figure 7.37 Centre locus of the sun gear

7.4.2 Strain gauge for measuring the ring gear stress

Beside the vibration methods mentioned above, stress can also be measured to detect the gear fault, especially for the ring gear fault in the pin supported situation. For a constant input load, the stress variation in the gear was found to change with the meshing position. The significant change would occur when the meshing of the teeth changes from the single pair to double pair. Fig. 7.39 shows the ring gear FEA model with the stress sensors. The stress at two positions has been obtained, that is, the rims of the ten teeth and the tooth root of the ten teeth. The von Mises stress in the FEA model can be plotted for the healthy ring gear and the ring gear with the cracks on different teeth.

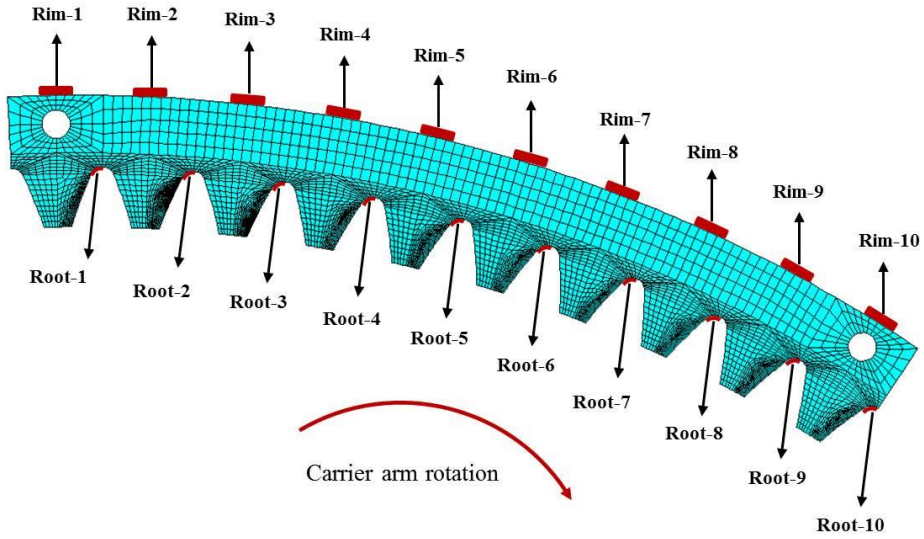

Figure 7.38 Ring gear FEA model with stress sensors

Fig. 7.40 shows the ring gear rim stress history data, which only included the data when one planet gear passes from one pin to the next pin. The rim position was selected because it is convenient to install the strain gauges to measure the stress without opening the gear system and stoping the operation. The left column shows the whole stress data with the healthy system during the whole rotation and the right column shows zoomed-in healthy data with comparison with the crack on different teeth. From the left column, it was found that the rim stress reached the maximum value when the planet gear passed except the stress at location Rim−1. Another observation was that the single contact zone and double contact zone can be clearly identified when the planet meshes with the ring gear. Moreover, the stress at the double contact zone tended to be smaller than that at the single contact zone. From the right column, when comparing the healthy gear with the cracked gear using the rim stress, no significant difference can be observed except for the stresses at Rim−1 and Rim−10, which were located right at the pin support. All these results suggested that measuring the stress at the rim was not an effective way to detect the fault in the ring gear with the pin supports.

Fig. 7.41 shows the ring gear tooth root stress history data. The crack was assumed to occur at the tooth root location and as a result, measuring the stress at the tooth root was the most direct way to detect the fault. However, the shortcoming will be that the gear system needs to be opened and the stress cannot be measured during normal operation. The left column

shows the stress data with healthy assumption during the whole rotation and the right column shows the zoomed-in healthy data with comparison with the crack on different teeth. From the left column, it was found that all the root stress reached its maximum value when the planet gear passed and the double contact zone and single contact zone can be clearly identified during this process. From the right column, significant differences could be observed between the healthy root stress data compared with the cracked root stress data no matter where the crack was located. The stress at the crack position almost reduced to half in the double contact zone. All these results indicated that measuring the stress at the tooth root was an effective way to detect the fault in the ring gear, but it required numerous strain gauges to be installed at every ring gear tooth root if the crack location was not known in advance. As a result, this method of detecting the ring gear fault was more suitable for monitoring the progression of the crack, whose location was already known.

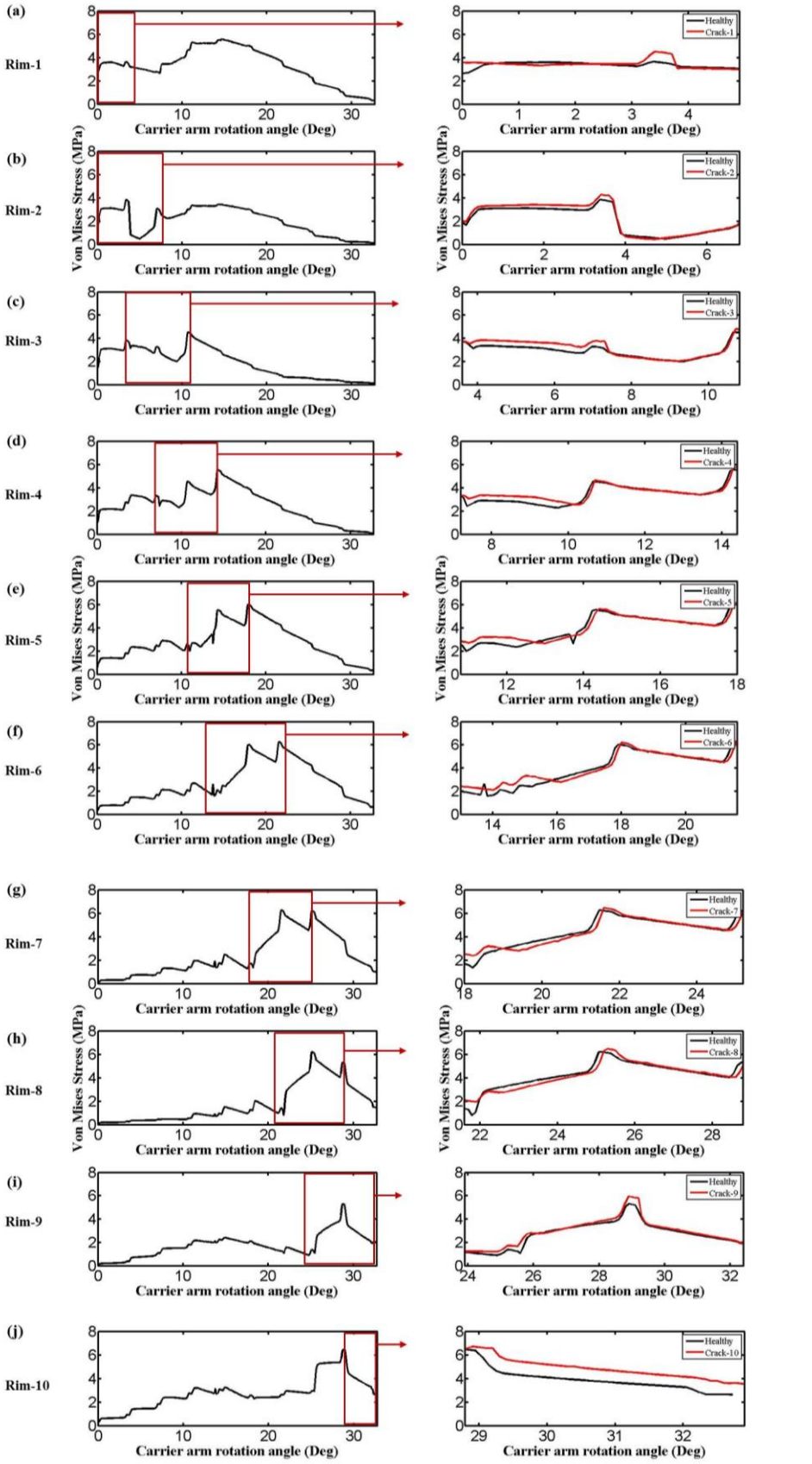

Figure 7.39 Ring gear rim stress. (a) rim–1, (b) rim–2, (c) rim–3, (d) rim–4, (e) rim–5, (f) rim–6, (g) rim–7, (h) rim–8, (i) rim–9, (j) rim–10.

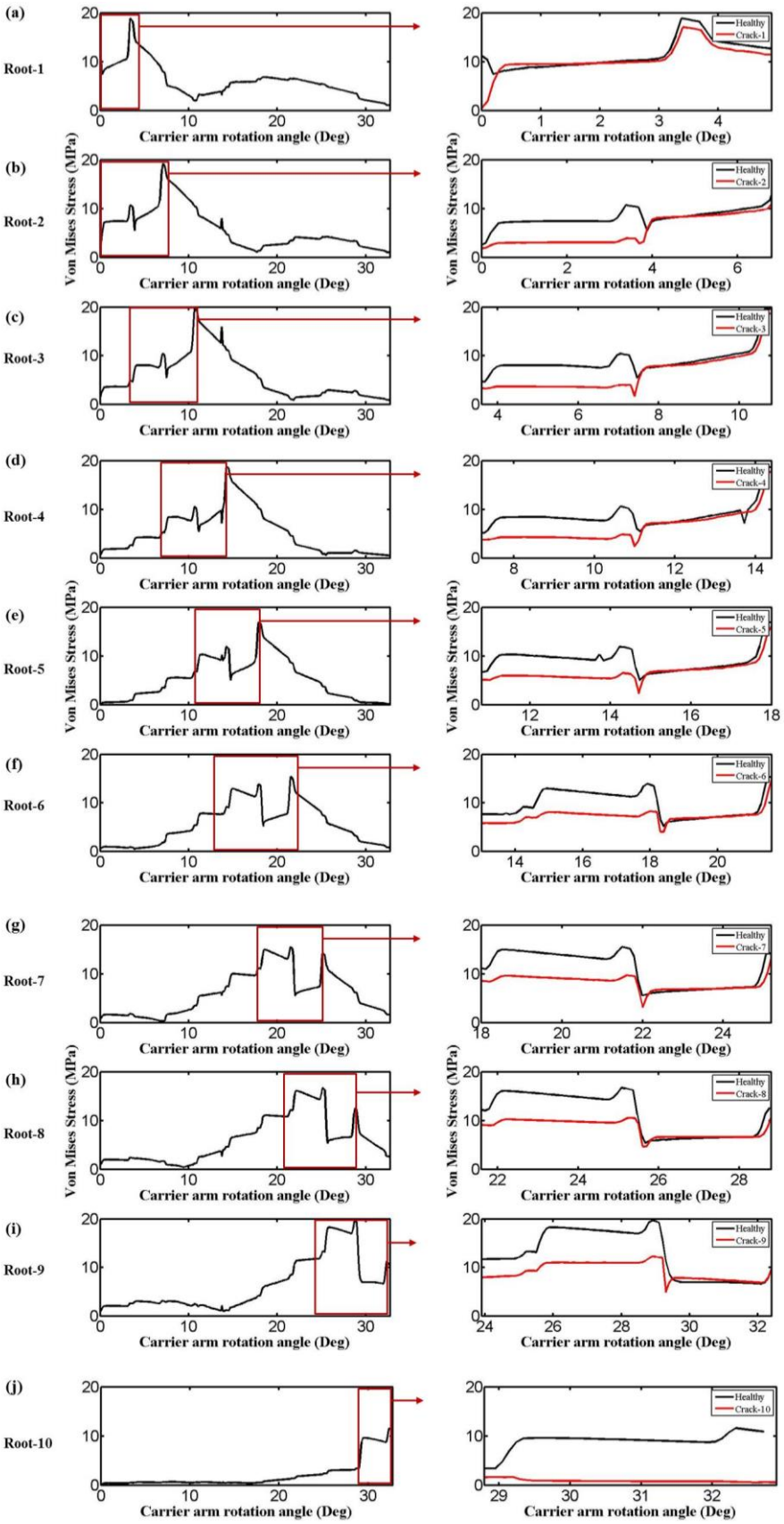

Figure 7.40 Ring gear tooth root stress. (a) root–1, (b) root –2, (c) root –3, (d) root –4, (e) root –5, (f) root –6, (g) root –7, (h) root –8, (i) root –9, (j) root –10.

7.5 Conclusions

This chapter has discussed the planetary gear fault diagnostic results using different types of vibration data. As the torsional vibration signals are free from the modulation effect caused by the rotation of the carrier arm, they have much simpler spectral structure than the transverse vibration signals. Different diagnostic methods were used in this chapter and showed that measurement of the torsional gear vibration could be an effective way for fault detection and diagnosis to distinguish the fault in the planetary gear system, especially in the uniformly supported situation. This work has provided a potential new method for extracting the planetary gear fault symptoms.

Chapter 8 Discussion, conclusion and recommendations

8.1 Discussion

8.1.1 The planetary gear mesh stiffness

The subsystem mesh stiffness, like the sun-planet (Fig. 3.16) and ring-planet mesh stiffnesses (Fig. 3.21), can be incorporated into the planetary dynamic models (Kahraman, 1994; Lin & Parker, 1999) separately to study the dynamic response with or without gear cracks. In other words, there are two internal vibration generation sources in the planetary gear system. Different crack sizes and crack angles can be created to estimate their influence on the subsystem stiffness (Chen & Shao, 2013) and then these resultant stiffnesses can be used as input in the planetary gear system to obtain the time domain response or the frequency domain response.

The calculated sun-planet-ring mesh stiffness for one branch, as shown in Fig. 3.26, provided a way to combine all the subsystem stiffnesses together. By this way, the sun-planet and ring-planet stiffness behave as if they are in an in-series connection, as shown in Fig. 3.23 and Fig. 3.36, and they can be replaced with an equivalent stiffness, which has been widely used in planetary load sharing analytical models (Singh, 2010). Another way of using this equivalent stiffness is to predict the sun gear radial orbit of a planetary gear set (Banerjee, 2012). With the inclusion of the crack analysis in section 4, the sun gear orbiting motion with cracks can be predicted to help further identification of the fault in the planetary system (Sheng & Guo, 2015).

The predictive model for the overall planetary gear, as shown in Fig. 3.34 and Fig. 3.38, provided an easier way to estimate the overall mesh stiffness, which can also be extended to include multiple gearbox trains because it is independent of the gear arrangement and only the gear speed ratio is needed. One application of this method is that it can be used in wind turbine dynamic modelling to estimate the overall mesh stiffness of the gearbox stage. Usually, the gearbox modelling involves detailed gear dynamic equations (Ozguven & Houser, 1988; Ma et al., 2015), which have also been introduced into the wind turbine

modelling analysis (Zhao & Ji, 2015; Shi et al., 2013). However, the wind turbine includes multiple components, like the rotor, shaft, generator and tower beside the gearbox. When the whole structure of the wind turbine was considered, the gearbox stage tends to be simplified as a constant stiffness (Girsang et al., 2014) or even as rigid (Hall & Chen, 2013; Dinh & Basu, 2015). The predictive model developed in this thesis can provide a reasonable estimation of the gearbox stage stiffness as long as the subsystem stiffness and the gear ratio are known. As a result, the variation of the gearbox stage can be considered in wind turbine dynamic modelling to help understand the overall wind turbine responses while avoiding the use of detailed gear dynamic equations.

The FE planetary gear model developed in this research can also be extended to study the effect of the unequal planet-to-planet load sharing due to the manufacturing errors. Bodas (Bodas & Kahraman, 2004) employed a contact mechanics model of a planetary gear set to study the effect of a number of manufacturing and assembly related carrier and gear errors on the load sharing amongst the planets in the quasi-static conditions. The manufacturing errors and assembly related errors included, (1) time-invariant, assembly-independent errors such as carrier planet pinhole position errors, (2) time-invariant, assembly-dependent errors such as planet tooth thickness errors, and (3) time-varying, assembly-dependent errors such as gear run-out errors (Bodas & Kahraman, 2004). All these errors could be considered in the overall planetary gear model, as shown in Fig. 3.27 and then the resultant overall planetary torsional stiffness could be studied correspondingly.

The fault sensitivity analysis mentioned in this research is focused on the gear root crack, which is a type of local fault. This local fault type causes the gear mesh stiffness and gear transmission error to change in a limited range. Another local fault type is pitting, which can occur on the pitch point of the gear tooth as discussed in chapter 2. The pitting would also cause the gear mesh stiffness and the resultant gear transmission error to change in a limited range, but with different form compared with the gear root crack. A number of researches have been conducted to study and compare the characteristics of the two local gear faults (Jia & Howard, 2006; Endo et al., 2009). Another common gear failure is the wear, which belongs to the distributed gear fault. This type of gear fault normally happens in the micro

scale and multiple gear teeth will be affected. The shape and the value of the gear mesh stiffness can hardly be affected by the gear wear due to the small scale, but the resultant transmission error can be affected. Some vibration based methods were used to detect the gear wear (Randall, 2011).

8.1.2 Dynamic modeling of flexibly supported gears

This thesis has presented a method for improving the theoretical modelling of flexibly supported gears in mesh by including the gear centre distance variation effect, which has a significant influence on the gear mesh stiffness. The theoretical model has been kept simple in order to clearly show the effect of the gear centre distance variation and therefore there are several major assumptions in the theoretical model itself, as geometrical pitch, profile errors and eccentricity effects were neglected and the friction force between the teeth was neglected. The account of any of these effects would change the resulting vibration response presented here, as has been demonstrated by many authors (Jia et al., 2003; Inalpolat et al., 2015) while excluding these effects assists in focusing only on the gear centre distance variation. Another major assumption was that the gear has been arranged in a way such that the translational motion is restricted in the direction along the line of action. As a result, only the motion along the line of action was included in the gear model. As demonstrated in section 4.2.2, the gear centre distance can also have influence on the pressure angle and this effect has been discussed by (Kim et al., 2010).

The Newmark method has been used to solve for the time domain responses and an inspection at the end of each time step was inserted to check the convergence of the system response. The important outcome of the inspection was to improve the accuracy of the calculation. As this study has been focused on the impact of the gear centre distance variation, the convergence criteria was based on the comparison of the gear centre distances obtained from the previous and the current time step separately. A tolerance of 0.1μm was used for the convergence criteria and by showing the iteration number at each time step, it was noted that the mesh stiffness during the handover region as well as in the cracked region experienced modification by the iteration loop. This was to be expected, as the mesh

stiffness varies considerably with centre distance, as shown in Fig. 4.5 and Fig. 4.9. For a rigid bearing supported gear model where the gear centre distance only varies in a small range (for example, less than 0.1μm), this inspection does not necessarily improve the accuracy of the calculation, unless some transient event was introduced to affect the gear centre distance.

The FEA method has been used to study the gear mesh stiffness curve by considering both the tooth root crack and the gear centre distance changes. The reason for using the FEA method was that it was reported to be most suitable for capturing the extended tooth contact phenomenon (Ma et al., 2015) as well as for modelling the gear tooth mesh stiffness with larger gear tooth crack size (Mohammed et al., 2013). As shown in Fig. 4.5 and Fig. 9, the FEA model was shown to have very good ability to capture both the root crack effect and the gear centre distance change effects.

The resultant gear vibration has been examined using some common gear diagnostic techniques in the time, frequency and the joint time-frequency domain. Comparisons have been made between model I and model II in these domains to investigate the effect of gear centre distance in the presence of the crack. In all cases, the diagnostic techniques were able to clearly detect the presence of the crack in both models but with differences in the magnitude and pattern. In the time domain, the properties of the time synchronous averaged results were almost identical in both models as shown in table 4.4, except for the skewness parameter. In the frequency domain, both spectrums are dominated by strong gear mesh harmonics and sidebands, though differences were observed in the amplitudes of several of the gear mesh harmonics from the spectrum figure. However, a notable difference can be observed in the kurtosis value of the residual signals if the gear mesh harmonics were eliminated and only the gear mesh sidebands were considered. It can be found that the kurtosis values of model II were all slightly smaller than those of model I, which suggested the residual distribution of model I was sharper and this can also be observed directly from the figure. This observation was as expected, because the inclusion of the gear centre distance would introduce extra stiffness reduction when the tooth with the crack went through the mesh, and so the system in model II at this moment should momentarily speed

up more and induce a larger vibration response. In the time-frequency domain, it was found both models have similar behaviour with the PWVD results in (Forrester, 1990). However, different energy distribution patterns were found in the presence of the localised tooth cracks. As pattern recognition (Staszewski et al., 1997) or image processing techniques (Wang & McFadden, 1993) were often used to interpret the PWVD for detection of gear failure, the inclusion of the gear centre distance is expected to provide a more precise distribution, which can help better identify the failure. Significant phase modulation, which was very similar to the results in (McFadden, 1986), was found to occur when the crack was present in the simulation. From the analytic signal plot, it can be found that the inclusion of the gear centre distance introduced a completely different phase response in the signal compared with the phase response in model I. This is to be expected as the inclusion of the gear centre distance can change the gear contact ratio and subsequently change the length of the single and double contact zones, and so the system should change the speed-up duration in the single contact zone and then the slowdown duration as the tooth enters the double contact zone.

The iterative convergence of tooth mesh stiffness method of dealing with the gear centre distance change can also be extended into the planetary gear system. Due to the floating of central members (typically carrier or sun gear), out-of-roundness of the ring gear, as well as the eccentricities or runout errors of the sun and planet gears, the theoretical sun-planet gear centre distance and ring-planet gear centre distance will also be affected during the gear operation. However, it should be noticed that if either of the meshing pairs, no matter if it is the sun-planet mesh pair or the ring-planet mesh pair, changes its design gear centre distance, it would also affect the other mesh pair. In other words, the sun-planet and ring-planet gear centre distances in the planetary gear would change simultaneously. As a result, when analysing the gear centre distance variation in the planetary gear system, all these mesh pairs should be included in the iterative convergence of tooth mesh stiffness method.

8.1.3 The effect of ring gear boundary conditions

The planetary gear system can be supported by different structures with different applications in the various industries. This research has put great effort on one type of the

supporting structure, which is the pin support. As shown in chapter 5, this type of supporting structure will affect the mesh stiffness, especially the ring-planet mesh stiffness, with some modulation effect. The other type of supporting structures, for example, the spline teeth, can also affect the ring-planet mesh stiffness in a different way. To study this effect, a FE model can be created in a similar way as shown in chapter 5 with the desired supporting situations. The corresponding resultant ring-planet mesh stiffness could be obtained afterwards. However, it has to be pointed out that this resultant mesh stiffness not only includes the teeth mesh stiffness, but also includes the stiffness from the supporting structures.

A number of researchers have already been focused on the ring-planet mesh stiffness calculation with an assumption that the supporting structure has no effect on the mesh stiffness (Kahraman, 1994; Lin & Parker, 1999; Chen & Shao, 2013; Chen & Shao 2013; Liang et al., 2014). Even though this ring-planet mesh stiffness was incorporated into the dynamic model, it was hard to reflect the real interaction between the gear system and the supporting structure and there were always some discrepancy between the theoretical modelling and the experimental work (Inalpolat & Kahraman, 2009). The results in this research showed that the supporting structure could modify the mesh stiffness and it revealed one of the mechanisms that affect more complex gear system responses compared with the results from the theoretical modelling. The results obtained here have been consistence with the analytical analysis (Chen & Shao, 2013; Chen et al., 2015) and could provide further support for (Forbes & Randall, 2008). The crack locations created in this research has covered the location from one pin support to its adjacent pin support. Different stiffness reduction could be observed on these locations, which was very different with the previous researches (Chen & Shao, 2013; Liang et al., 2014). However, this difference came from the inclusion of the supporting structures, which means the results could further improve the accuracy of the gear fault detection.

8.1.4 Overall planetary gear dynamic modelling

There were several major assumptions in the mathematical planetary gear dynamic model itself, as geometrical pitch, profile errors and eccentricity effects were neglected and the

friction force between the teeth was ignored. The account of any of these effects would change the resultant planetary gear response as well as the diagnostic results presented in this thesis. Another assumption was that all the planet gears were identical, which means the resultant sun-planet mesh stiffnesses and ring-planet mesh stiffnesses in all the branches were all the same except if a crack occurred on any of these components.

The mesh stiffness summarized in chapter 6 was presented in a way that its period covered exactly one carrier arm revolution. This was helpful as this research utilized the carrier arm torsional vibration as the main method to detect the planetary gear fault. With the presence of the gear crack, it clearly showed the number of the crack impulses within one carrier arm revolution. This feature has been used to distinguish the crack position in chapter 7.

With the rotation of the carrier arm, the planet gears will rotate along and mesh with the ring gear at the same time. This phenomenon was treated as a moving load problem in this research, which has been commonly used in the dynamics of bridges in civil engineering (Fryba, 1972; Yang et al., 2004; Chatterjee et al., 1994). The successful application of the moving load theory in civil engineering could be found in (Yang et al., 2004) and it could be solved by either the analytical method or the FE method (Fryba, 1972). The flexibility of the ring gear was represented using FE beam elements in this research and the mesh force obtained from the lumped parameter model was used as excitation for the beam element. Here, only the ring-planet mesh force was used as it was assumed the sun-planet mesh force has been isolated. Some other researchers (Inalpolat & Kahraman, 2010) have included the sun-planet mesh impact by assigning a constant factor (chosen between 0 and 1), but there is no accurate value for this factor as it depends on the characteristics of the sun-planet transfer path, like the property of the planet gear bearings.

8.1.5 The planetary gear diagnostic results

Section 7.2 focused on the uniformly supported situations, which has been discussed by numerous researchers (Feng & Zuo, 2013; Feng & Zuo, 2012; Wang, 2010; Liang et al., 2014). An important task of this section was to use the planetary gear torsional vibration to detect gear faults on different components because the torsional vibration was found to be

free from the modulation caused by the carrier arm passing effect (Feng & Zuo, 2013). The results of several diagnostic methods have been discussed in section 7.2.1. The amplitude and phase modulation results were impressive as they not only successfully showed the presence of the fault, but also indicated the location of the fault. If the fault occurred on the sun gear, it showed 15 twists in the modulation results while if the fault occurred on the planet gear, it showed 3 twists in the modulation results. The transverse vibration from the ring gear was also discussed in section 7.2.2 using the method mentioned in (Howard, 1991; McFadden, 1991). It was found that the presence of the fault on the sun gear and planet gear can also be identified, however, not as clearly as in the torsional vibration. Section 7.3 focused on the pin supported situations, which has not been previously intensively discussed (Chen et al., 2015). The torsional vibration was also used to detect the gear faults on different components. Some evidence can be observed in the diagnostic results for the presence of the cracks, however, it was not as obvious as it was in the uniformly supported situation because of the modulation caused by the pin supports. The transverse vibration from the ring gear was also discussed and it indicated that the sensor that was closest to the pin support would give the best vibration response if a symmetrical vibration spectrum is desired.

Since the detection of the ring gear fault was not as satisfactory as the detection of the sun gear and planet gear faults, section 7.4 was added to investigate other potential sensor options for the ring gear fault detection. Two types of sensors have been considered. One was a probe sensor measuring the sun gear displacements in the transversal directions and another was a strain gauge measuring the ring gear stress change. Both sensor options were found to be effective in detecting the ring gear faults, but some short comings were also found in how to obtain these diagnostic data. For example, the planetary gearbox needs to be opened if the stress data was required and this would result in stopping the normal operation of the gearbox, where the strain gauge sensors were pre-installed.

8.1.6 Discussion of computational effort

There were two professional simulation softwares used in this research, one was ANSYS and the other was MATLAB. Both softwares require great computational resources. Precision workstation T5000, with 8GB memory and 1TB hard drive, from DELL Company was used in this research. The operation system was Window 7 Professional, 64bit with the processor Intel® Xeon® Processor E5-1603 v3. The availability of this high performance computer made the simulation run faster. In this research, ANSYS requires much more computational resources than MATLAB. There were four types of finite element models in this research, which are sun-planet subsystem (Fig. 3.14), ring-planet subsystem (Fig. 3.19), sun-planet-ring subsystem (Fig. 3.25) and the overall planetary gear system (Fig. 3.27). Each model has different element number and node number and therefore, they require different computation time. All the models in chapter 3 have been calculated at 72 positions, which will cover two mesh cycles. Table 8.1 shows the computation time of each position for all the models in chapter 3.

Table 8.1 Computational time for the finite element models

Models	Element number	Node number	Computation time for one position	Total computation time
Sun-planet subsystem	15,600	50,520	3 mins	3.6 hours
Ring-planet subsystem	36,870	119,364	6 mins	7.2 hours
Sun-planet-ring subsystem	42,330	137,046	12 mins	14.4 hours
Overall planetary gear system	62,610	202,722	30 mins	36 hours

As one can see, it is quite time consuming to use finite element models, especially for the overall planetary gear system. It should also be noticed that if multiple input load levels are desired, this computational time will increase as well. Some effort was made in chapter 4 and chapter 5 to decrease the number of the elements and nodes in the models based on some reasonable assumptions and it was found the computational time decreased significantly. For the sun-planet subsystem, the model in Fig. 4.4 reduced the element number and it required only 1 min per position. For the ring-planet subsystem, the model in Fig. 5.2 reduced the element number and it required only 3 mins per position.

All in all, this research is based on a high computational resource requirement, especially in chapter 3 when initially starting this research. If one would like to follow this research, it is recommended that some effort should be made to control the element number, as shown in chapter 4 and chapter 5. The other alternative way to reduce the computational time would be to use the parallel computing or the supercomputing.

8.1.7 Discussion of experimental work

There are a number of published experimental data for spur gear systems, but it is still hard to find related experimental data for the planetary gear system from the literature. To conduct the experimental work for the planetary gear system, it is very time consuming and expensive as you not only need the planetary gear system itself, but also the motor, the load, the control system as well as the data acquisition system. Due to the time limit for the current research work and limited funding to support this research, it was not possible to establish a high quality planetary gear experimental test rig. Due to these reasons, this research constitutes a solely theoretical study, however the results in this research can still be compared with some limited planetary gear experimental work done by the other researchers. In 1970s, Hidaka published a series of experimental work on the dynamic behaviour of the planetary gear and there were a total of 7 reports. It included the study of the load sharing of the planetary gear (Hidaka & Terauchi, 1976), the study of the displacement of sun and ring gear (Hidaka et al., 1976), the study of the displacement of ring gear in the direction of line action (Hidaka et al., 1977), the influence of the transmitted tooth load on the dynamic

increment load (Hidaka et al., 1979), the dynamic increment of torque (Hidaka et al., 1979), the influence of the mesh phase (Hidaka et al., 1979), the influence of the thickness of the ring gear (Hidaka et al., 1979). The influence of the thickness of the ring gear has been studied in chapter 3 and chapter 5 in this research with different boundary conditions. It was found in his research that for a ring gear with a thin rim, the tensile fillet stress decreases with a decreasing rim thickness. The stress level in the tooth is closely related with the tooth mesh stiffness and the result in Fig. 6.3 was consistence with Hidaka's finding. More recently, Kahraman carried out a series of studies on the influence of ring gear rim thickness using both the contact mechanics model and the experimental test rig (Kahraman et al., 2010). Strain gauges were used to measure the ring gear deflections. The variation of the deflection was found to be weakened with a thicker ring gear rim, which has been consistence with the findings in chapter 6. The results in section 7.4.2 were also consistence with his data. Kahraman also carried out a series of experimental work on the sun gear orbit motion and the planet load sharing ratio by measuring the stress variation (Boguski & Kahraman, 2012).

All the experimental work mentioned above was focused on the gear design aspects. With regard to the planetary gear condition monitoring experimental work, the most famous experimental work on this aspect was the work conducted in the Defence Science and Technology Organisation (DSTO) in Australia. Peter McFadden, David Forrester and Ian Howard investigated the vibration signal averaging of individual components in the planetary gearbox (Howard, 1991). They used a stationary sensor to capture the vibration signal when the planet gear passed by. Later on, National Aeronautics and Space Administration (NASA) continued the related experimental work and they called it the vibration separation technique (Samuel & Pines, 2000). The results in the section 7.2.2 and section 7.3.2 were compared with DSTO's data and they showed good agreement. Zhipeng used intensive experimental work to valid his theoretical model. In his experimental, the damaged sun gear, the damaged planet gear and the damaged ring gear were included and corresponding frequency spectrum were analysed (Feng & Zuo, 2012, 2013; Feng et al.,

2014). The results in section 7.2.1 and section 7.3.2 were in good agreement with Zhipeng's work.

From the results of this research, some recommendations can be given for the future experimental work. First, some experimental work on the effect of the ring gear boundary condition could be conducted with the inclusion of the pin support. The number of 11 pin supports is recommended to show a clear modulation effect. The strain gauge could be used to measure the stress levels to estimate the stiffness. This method has been used to measure the stiffness of the spur gear (Pandya & Parey, 2013). The vibration signal modulation caused by the ring gear boundary condition could also be conducted and a thin ring gear rim was recommended. Second, the alternative condition monitoring method was proposed in chapter 7. With the development of the new method of measuring the torsional motion (Kang & Kahraman, 2012), it is expected more planetary gear torsional vibration data could be recorded to confirm the results in this research. The carrier arm torsional vibration was recommended and it could be measured within one carrier arm revolution and then be expressed in terms of angle, just like the shaft domain in the spur gear. Different gear faults, both the local gear fault and distributed gear fault, could be created and then the corresponding vibration data could be analysed.

8.2 Conclusions

This thesis has presented the improvement of numerical approaches for analysing the characteristics of tooth cracks for both the parallel spur gear and the planetary gear. The numerical models include FE models and lumped parameter models. In the FE models, parallel gear pairs with various meshing distance and tooth crack, sun-planet mesh pair with and without tooth crack, ring-planet mesh pairs with and without tooth crack, sun-planet-ring mesh pairs as well as the overall planetary gear system were created to study the resultant gear mesh stiffness. In the lumped parameter models, the fixed axis gear differential equations were solved using iterative gear mesh stiffness as the gear centre distance could affect the mesh stiffness significantly and the planetary gear differential equations was also solved numerically, where the ring gear flexibility was considered. All these models

developed in this research were aimed to make contributions to improve the understanding of the gear fault mechanism as well as to improve the gear fault diagnostic method. The main findings of this study are summarized as follows,

1. The overall torsional mesh stiffness of a planetary gear and the individual sun-planet, ring-planet and carrier arm stiffness could be combined together via the squared of the gear speed ratios between the various components.

2. The overall planetary gear mesh stiffness was most sensitive to the crack on the sun-planet mesh and a stiffer carrier arm could be helpful to improve the detection of the crack on both the sun-planet and ring-planet meshes.

3. The gear centre distance significantly changes the behaviour of the gear mesh stiffness curve in terms of the stiffness value and length of the single and double contact zones.

4. The iterative process using the convergence of tooth mesh stiffness was proven to be effective to solve the dynamic response for flexibly supported gears.

5. The effect of the gear centre distance variation has a significant effect on the detection of the gear fault for the flexible supported gear. More specifically, the variation of the gear centre distance tends to weaken the gear fault diagnostic results.

6. The boundary conditions of the ring gear have to be considered when studying the planetary gear dynamic response. When the boundary condition is fully constrained, the ring gear rim thickness effect could be treated as a constant factor. When the boundary condition is pin supported, a modulation effect was observed in the ring-planet mesh stiffness. However, a thicker ring gear rim can weaken this modulation effect. The flexibility of the pin supports have also to be considered as they can potentially change the stiffness curve and the tooth load sharing ratio.

7. Lumped parameter mathematical modelling was shown to be an effective tool to simulate the gear fault dynamics and to understand the gear fault mechanism.

8. The planetary gear torsional vibration was found to be an effective alternative approach for planetary gear condition monitoring. Traditional signal processing techniques, like residual signal, amplitude and phase modulation, were also found effective to process these signals to extract the gear fault features.

8.3 Recommendations for future work

The following areas have been noted as being worthy of further research,

1. Further investigation and study should be conducted on the incorporation of the effect of tooth crack plasticity in the FE model and studies on its effect on the gear dynamic responses.

2. Further investigation and study should be conducted on the transient analysis of the gear in mesh with and without cracked teeth, surface pitting and wear using the finite element method.

3. Further investigation and study should be conducted on the effect of the shaft behaviour on the gear fault diagnostic results.

4. Further investigation and study should be conducted on the effect of the variation of the input load. As the mesh stiffness is found to be load dependent, the resultant mesh stiffness due to the input load variation should be worthy of studying. It would also be interesting to see the resultant gear dynamics due to the load variation.

5. Further investigation and study should be conducted on the formation and growth of gear faults using both the simulation method and experimental method.

6. Further investigation and study should be conducted on the dynamic behaviour of simple gear pairs and planetary gear simulation models with rolling element bearing effects.

7. Further investigation and study should be conducted on the consideration of the more complicated loading conditions in the gear dynamic model. The wind-turbine gearbox often experiences sudden wind gusts and with the consideration of more realistic gearbox operating conditions, it would be helpful to further improve the gear fault detection.

8. Further investigation and study should be conducted on the development of the advanced signal processing techniques for the time varying operation conditions. Time-frequency method is able to capture the transient event in the time varying operation conditions, but its application is limited by the cross-term and the readability of the instantaneous frequency. Some methods, like iterative generalized synchrosqueezing transform, were developed recently, but it needs continuous effort in this area.

Reference

Abousleiman, V., & Velex, P. (2006). A hybrid 3D finite element/lumped parameter model for quasi-static and dynamic analyses of planetary/epicyclic gear sets. *Mechanism and Machine Theory*, *41*(6), 725-748.

Abousleiman, V., Velex, P., & Becquerelle, S. (2007). Modeling of spur and helical gear planetary drives with flexible ring gears and planet carriers. *Journal of Mechanical Design*, *129*(1), 95-106.

Ambarisha, V. K., & Parker, R. G. (2007). Nonlinear dynamics of planetary gears using analytical and finite element models. *Journal of sound and vibration*, *302*(3), 577-595.

Amiri Rad, A., Forouzan, M. R., & Sadeghi Dolatabadi, A. (2014). Three‐dimensional fatigue crack growth modelling in a helical gear using extended finite element method. *Fatigue & Fracture of Engineering Materials & Structures*, *37*(6), 581-591.

Amirouche, F. (2007). *Fundamentals of multibody dynamics: theory and applications*. Springer Science & Business Media.

Antoniadou, I., Manson, G., Staszewski, W. J., Barszcz, T., & Worden, K. (2015). A time–frequency analysis approach for condition monitoring of a wind turbine gearbox under varying load conditions. *Mechanical Systems and Signal Processing*, *64*, 188-216.

August, R. (1984). *Dynamics of planetary gear trains* (Vol. 3793). National Aeronautics and Space Administration, Scientific and Technical Information Branch.

Banerjee, A. (2012). *A model to predict sun gear radial orbit of a planetary gear set having manufacturing er-rors*, Master thesis, The Ohio State University, Columbus, United States.

Bartelmus, W. (2001). Mathematical modelling and computer simulations as an aid to gearbox diagnostics. *Mechanical Systems and Signal Processing*, *15*(5), 855-871.

Bartelmus, W. (2008). Root cause and vibration signal analysis for gearbox condition monitoring, *Insight*, 50(4).

Bartelmus, W., & Zimroz, R. (2009). A new feature for monitoring the condition of gearboxes in non-stationary operating conditions. *Mechanical Systems and Signal Processing*, *23*(5), 1528-1534.

Bartelmus, W. (2011). Gearbox damage process. In *Journal of Physics: Conference Series* (Vol. 305, No. 1, p. 012029). IOP Publishing.

Bartelmus, W. (2014). New focus on gearbox condition monitoring for failure prevention technology. In *Key Engineering Materials* (Vol. 588, pp. 184-191). Trans Tech Publications.

Bartelmus, W., Chaari, F., Zimroz, R., & Haddar, M. (2010). Modelling of gearbox dynamics under time-varying nonstationary load for distributed fault detection and diagnosis. *European Journal of Mechanics-A/Solids*, *29*(4), 637-646.

Bodas, A., & Kahraman, A. (2004). Influence of carrier and gear manufacturing errors on the static load sharing behavior of planetary gear sets. *JSME International Journal Series C*, *47*(3),

908-915.

Boguski, B., Kahraman, A., & Nishino, T. (2012). A new method to measure planet load sharing and sun gear radial orbit of planetary gear sets. *Journal of Mechanical Design*, *134*(7), 071002.

Botman, M. (1976). Epicyclic Gear Vibrations. *Journal of Manufacturing Science and Engineering*, *98*(3), 811-815.

Braun, S. (1975). The extraction of periodic waveforms by time domain averaging. *Acta Acustica united with Acustica*, *32*(2), 69-77.

Braun, S. G., & Seth, B. B. (1979). On the extraction and filtering of signals acquired from rotating machines. *Journal of Sound and Vibration*, *65*(1), 37-50.

Brie, D., Tomczak, M., Oehlmann, H., & Richard, A. (1997). Gear crack detection by adaptive amplitude and phase demodulation. *Mechanical Systems and Signal Processing*, *11*(1), 149-167.

Chaari, F., Baccar, W., Abbes, M. S., & Haddar, M. (2008). Effect of spalling or tooth breakage on gearmesh stiffness and dynamic response of a one-stage spur gear transmission. *European Journal of Mechanics-A/Solids*,*27*(4), 691-705.

Chaari, F., Fakhfakh, T., & Haddar, M. (2006). Dynamic analysis of a planetary gear failure caused by tooth pitting and cracking. *Journal of Failure Analysis and Prevention*, *6*(2), 73-78.

Chaari, F., Fakhfakh, T., & Haddar, M. (2009). Analytical modelling of spur gear tooth crack and influence on gearmesh stiffness. *European Journal of Mechanics-A/Solids*, *28*(3), 461-468.

Chaari, F., Zimroz, R., Bartelmus, W., & Haddar, M. (2014, December). Advances in Condition Monitoring of Machinery in Non-Stationary Operations. In *Proceedings of the Fourth International Conference on Condition Monitoring of Machinery in Non-Stationary Operations, Lyon, France* (Vol. 1517, p. 314).

Chatterjee, P. K., Datta, T. K., & Surana, C. S. (1994). Vibration of suspension bridges under vehicular movement. *Journal of Structural Engineering*, *120*(3), 681-703.

Chen, X., & Feng, Z. (2016). Iterative generalized time–frequency reassignment for planetary gearbox fault diagnosis under nonstationary conditions. *Mechanical Systems and Signal Processing*. *80*, 429-444.

Chen, Z., & Shao, Y. (2011). Dynamic simulation of spur gear with tooth root crack propagating along tooth width and crack depth. *Engineering Failure Analysis*, *18*(8), 2149-2164.

Chen, Z., & Shao, Y. (2013a). Dynamic features of a planetary gear system with tooth crack under different sizes and inclination angles. *Journal of Vibration and Acoustics*, *135*(3), 031004.

Chen, Z., & Shao, Y. (2013b). Mesh stiffness calculation of a spur gear pair with tooth profile modification and tooth root crack. *Mechanism and Machine Theory*, *62*, 63-74.

Chen, Z., & Shao, Y. (2013c). Dynamic simulation of planetary gear with tooth root crack in ring gear. *Engineering Failure Analysis*, *31*, 8-18.

Chen, Z., & Shao, Y. (2013d). Mesh stiffness of an internal spur gear pair with ring gear rim deformation. *Mechanism and Machine Theory*, *69*, 1-12.

Chen, Z., Shao, Y., & Su, D. (2013). Dynamic simulation of planetary gear set with flexible spur ring gear. *Journal of Sound and Vibration*, 332(26), 7191-7204.

Chen, Z., Zhu, Z., & Shao, Y. (2015). Fault feature analysis of planetary gear system with tooth root crack and flexible ring gear rim. *Engineering Failure Analysis*, *49*, 92-103.

Cohen, L. (1995). *Time-frequency analysis*, first ed., Prentice-Hall PTR, New Jersey.

Cooley, C. G., & Parker, R. G. (2014). A Review of Planetary and Epicyclic Gear Dynamics and Vibrations Research. Applied Mechanics Reviews, 66(4), 040804-040804.

Cornell, R. W. (1981). Compliance and stress sensitivity of spur gear teeth. *Journal of Mechanical Design*, *103*(2), 447-459.

Cunliffe, F., Smith, J. D., & Welbourn, D. B. (1974). Dynamic tooth loads in epicyclic gears. *Journal of Engineering for Industry*, *96*(2), 578-584.

Dalpiaz, G., Rubini, R., D'Elia, G., Cocconcelli, M., Chaari, F., Zimroz, R., & Haddar, M. (2013). Advances in condition monitoring of machinery in non-stationary operations. In *Proceedings of the third International Conference on Condition Monitoring of Machinery in Non-Stationary Operations CMMNO*.

Davies, A. (Ed.). (2012). *Handbook of condition monitoring: techniques and methodology*. Springer Science & Business Media.

Del Rincon, A. F., Iglesias, M., De-Juan, A., & Viadero, F. (2010). Defect simulation in a spur gear transmission model. In *New Trends in Mechanism Science* (pp. 191-198). Springer Netherlands.

Del Rincon, A. F., Viadero, F., Iglesias, M., de-Juan, A., Garcia, P., & Sancibrian, R. (2012). Effect of cracks and pitting defects on gear meshing. *Proceedings of the Institution of Mechanical Engineers, Part C: Journal of Mechanical Engineering Science*, *226*(11), 2805-2815.

De Silva, C. W. (Ed.). (2007). *Vibration monitoring, testing, and instrumentation*. CRC Press.

Dinh, V. N., & Basu, B. (2015). Passive control of floating offshore wind turbine nacelle and spar vibrations by multiple tuned mass dampers. *Structural Control and Health Monitoring*, *22*(1), 152-176.

Dooner, D. B. (2012). Kinematics Geometry of Gearing (2nd ed.): Wiley.

Du, S. (1997). *Dynamic modelling and simulation of gear transmission error for gearbox vibration analysis*. Ph.D Thesis, University of New South Wales, Sydney, Australia.

Endo, H. (2005). *Simulation of gear faults and its application to the development of differential diagnostic technique*. University of New South Wales. Ph.D Thesis, University of New South Wales, Sydney, Australia.

Endo, H., Randall, R. B., & Gosselin, C. (2009). Differential diagnosis of spall vs. cracks in the gear tooth fillet region: Experimental validation. *Mechanical Systems and Signal Processing*, *23*(3), 636-651.

Ericson, T. M., & Parker, R. G. (2013). Natural Frequency Clusters in Planetary Gear Vibration. Journal of Vibration and Acoustics, 135(6), 061002-061002.

Eritenel, T., & Parker, R. G. (2009). Modal properties of three-dimensional helical planetary gears. Journal of Sound and Vibration, 325(1–2), 397-420.

Fakhfakh, T., Bartelmus, W., Chaari, F., Zimroz, R., & Haddar, M. (2012). Condition Monitoring of Machinery in Non-Stationary Operations. In*Proceedings of the Second International Conference Condition Monitoring of Machinery in Non-Stationary Operations CMMNO'2012*.

Feng, Z., Chen, X., & Liang, M. (2015). Iterative generalized synchrosqueezing transform for fault diagnosis of wind turbine planetary gearbox under nonstationary conditions. *Mechanical Systems and Signal Processing*, *52*, 360-375.

Feng, Z., & Liang, M. (2014). Fault diagnosis of wind turbine planetary gearbox under nonstationary conditions via adaptive optimal kernel time–frequency analysis. *Renewable Energy*, *66*, 468-477.

Feng, Z., & Zuo, M. J. (2012). Vibration signal models for fault diagnosis of planetary gearboxes. *Journal of Sound and Vibration*, *331*(22), 4919-4939.

Feng, Z., & Zuo, M. J. (2013). Fault diagnosis of planetary gearboxes via torsional vibration signal analysis. *Mechanical Systems and Signal Processing*, *36*(2), 401-421.

Forbes, G. L., & Randall, R. B. (2008). Resonance phenomena of an elastic ring under a moving load. *Journal of Sound and Vibration*, *318*(4), 991-1004.

Forrester, B. D. (1990). Gear fault detection using the Wigner-Ville distribution. In *Australian Vibration and Noise Conference 1990: Vibration and Noise-measurement Prediction and Control; Preprints of Papers* (p. 296). Institution of Engineers, Australia.

Forrester, B. D. (1996). *Advanced vibration analysis techniques for fault detection and diagnosis in geared transmission systems*. Ph.D Thesis, Swinburne University of Technology, Melbourne, Australia.

Frýba, L. (1973). *Vibration of solids and structures under moving loads*. Springer Science & Business Media.

Ghaffari, M. A., Pahl, E., & Xiao, S. (2015). Three dimensional fatigue crack initiation and propagation analysis of a gear tooth under various load conditions and fatigue life extension with boron/epoxy patches. *Engineering Fracture Mechanics*, *135*, 126-146.

Giner, E., Sukumar, N., Tarancon, J. E., & Fuenmayor, F. J. (2009). An Abaqus implementation of the extended finite element method. *Engineering fracture mechanics*, *76*(3), 347-368.

Girsang, I. P., Dhupia, J. S., Muljadi, E., Singh, M., & Pao, L. Y. (2014). Gearbox and drivetrain models to study dynamic effects of modern wind turbines. *IEEE Transactions on Industry Applications*, *50*(6), 3777-3786.

Glodež, S., Šraml, M., & Kramberger, J. (2002). A computation model for determination of service life of gears. *International Journal of Fatigue*, *24*(10), 1013-1020.

Goldman, S. (1999). *Vibration spectrum analysis: a practical approach*. Industrial Press Inc..

Gu, X., & Velex, P. (2012). A dynamic model to study the influence of planet position errors in planetary gears. *Journal of Sound and Vibration*, *331*(20), 4554-4574.

Gu, X., & Velex, P. (2013). On the dynamic simulation of eccentricity errors in planetary gears. *Mechanism and Machine Theory*, *61*, 14-29.

Guilbault, R., Lalonde, S., & Thomas, M. (2015). Modeling and monitoring of tooth fillet crack growth in dynamic simulation of spur gear set. *Journal of Sound and Vibration*, *343*, 144-165.

Ha, J. M., Youn, B. D., Oh, H., Han, B., Jung, Y., & Park, J. (2016). Autocorrelation-based time synchronous averaging for condition monitoring of planetary gearboxes in wind turbines. *Mechanical Systems and Signal Processing*, *70*, 161-175.

Haastrup, M., Hansen, M. R., & Ebbesen, M. K. (2011). Modeling of wind turbine gearbox mounting. *Modeling, Identification and Control*, *32*(4), 141.

Hao, D. S. (2012). Research on Numerical Analysis Modeling Method for Gear Meshing and its Applications. Ph.D Thesis, Dalian University of Technology, Dalian, China.

Hall, J. F., & Chen, D. (2013). Dynamic Optimization of Drivetrain Gear Ratio to Maximize Wind Turbine Power Generation—Part 1: System Model and Control Framework. *Journal of dynamic systems, measurement, and control*, *135*(1), 011016.

Helsen, J., Vanhollebeke, F., Marrant, B., Vandepitte, D., & Desmet, W. (2011). Multibody modelling of varying complexity for modal behaviour analysis of wind turbine gearboxes. *Renewable Energy*, *36*(11), 3098-3113.

Hidaka, T., & Terauchi, Y. (1976). Dynamic Behavior of Planetary Gear: 1st Report Load Distribution in Planetary Gear. *Bulletin of JSME*, *19*(132), 690-698.

HIDAKA, T., TERAUCHI, Y., & ISHIOKA, K. (1976). Dynamic Behavior of Planetary Gear: 2nd Report, Displacement of Sun Gear and Ring Gear. *Bulletin of JSME*, *19*(138), 1563-1570.

HIDAKA, T., TERAUCHI, Y., NOHARA, M., & OSHITA, J. I. (1977). Dynamic behavior of planetary gear: 3rd report, Displacement of ring gear in direction of line of action. *Bulletin of JSME*, *20*(150), 1663-1672.

HIDAKA, T., TERAUCHI, Y., & ISHIOKA, K. (1979). Dynamic Behavior of Planetary Gear: 4th Report, Influence of the Transmitted Tooth Load on the Dynamic Increment Load. *Bulletin of JSME*, 22(168), 877-884.

HIDAKA, T., TERAUCHI, Y., & NAGAMURA, K. (1979). Dynamic Behavior of Planetary Gear: 5th report, Dynamic Increment of Torque. *Bulletin of JSME*, *22*(169), 1017-1025.

HIDAKA, T., TERAUCHI, Y., & Nagamura, K. (1979). Dynamic Behavior of Planetary Gear: 6th Report, Influence of Meshing-Phase. *Bulletin of JSME*,*22*(169), 1026-1033.

HIDAKA, T., TERAUCHI, Y., & NAGAMURA, K. (1979). Dynamic behavior of planetary gear: 7th report, Influence of the Thickness of the Ring Gear. *Bulletin of JSME*, *22*(170), 1142-1149.

Hong, L., Dhupia, J. S., & Sheng, S. (2014). An explanation of frequency features enabling detection of faults in equally spaced planetary gearbox. *Mechanism and Machine Theory*, *73*, 169-183.

Howard, I. M. (1991). *An investigation of vibration signal averaging of individual components in an epicyclic gearbox* (No. ARL-PROP-R-185). AERONAUTICAL RESEARCH LABS

MELBOURNE (AUSTRALIA).

Howard, I. M. (1994). *A Review of Rolling Element Bearing Vibration'Detection, Diagnosis and Prognosis.* (No. DSTO-RR-0013). DEFENCE SCIENCE AND TECHNOLOGY ORGANIZATION CANBERRA (AUSTRALIA).

Howard, I. M., Jia, S., & Wang, J. (2001). The dynamic modelling of a spur gear in mesh including friction and a crack. *Mechanical systems and signal processing*, *15*(5), 831-853.

Hwang, J. F. (1986). Advanced Computer-Aided Design Method on the Stress Analysis of Internal Spur Gears. Master Thesis, The Ohio State University, Colombia, United States.

Inalpotat, M. (2009). *A theoretical and experimental investigation of modulation sidebands of planetary gear sets*. Ph. D Thesis, The Ohio State University, Colombia, United States.

Inalpolat, M., Handschuh, M., & Kahraman, A. (2015). Influence of indexing errors on dynamic response of spur gear pairs. *Mechanical Systems and Signal Processing*, *60*, 391-405.

Inalpolat, M., & Kahraman, A. (2009). A theoretical and experimental investigation of modulation sidebands of planetary gear sets. *Journal of Sound and Vibration*, *323*(3), 677-696.

Inalpolat, M., & Kahraman, A. (2010). A dynamic model to predict modulation sidebands of a planetary gear set having manufacturing errors. *Journal of Sound and Vibration*, *329*(4), 371-393.

ISO. (2014). Wind turbines -- Part 4: Design requirements for wind turbine gearboxes.

Jia, S., Howard, I., & Wang, J. (2003). The dynamic modeling of multiple pairs of spur gears in mesh, including friction and geometrical errors. *International Journal of Rotating Machinery*, *9*(6), 437-442.

Jia, S., & Howard, I. M. (2006). Comparison of localised spalling and crack damage from dynamic modelling of spur gear vibrations. *Mechanical Systems and Signal Processing*, *20*(2), 332-349.

Kahraman, A. (1994a). Natural Modes of Planetary Gear Trains. *Journal of Sound and Vibration*, 173(1), 125-130.

Kahraman, A. (1994b). Planetary Gear Train Dynamics. *Journal of Mechanical Design*, 116(3), 713-720.

Kahraman, A. (1994c). Load sharing characteristics of planetary transmissions. *Mechanism and Machine Theory*, *29*(8), 1151-1165.

Kahraman, A. (1999). *Static load sharing characteristics of transmission planetary gear sets: Model and experiment* (No. 1999-01-1050). SAE Technical Paper.

Kahraman, A., Kharazi, A. A., & Umrani, M. (2003). A deformable body dynamic analysis of planetary gears with thin rims. *Journal of sound and vibration*, *262*(3), 752-768.

Kahraman, A., Ligata, H., & Singh, A. (2010). Influence of ring gear rim thickness on planetary gear set behavior. *Journal of Mechanical Design*, *132*(2), 021002.

Kahraman, A., & Vijayakar, S. (2001). Effect of internal gear flexibility on the quasi-static behavior of a planetary gear set. *Journal of Mechanical Design*, *123*(3), 408-415.

Kang, M. R., & Kahraman, A. (2012). Measurement of vibratory motions of gears supported by compliant shafts. *Mechanical Systems and Signal Processing*, *29*, 391-403.

Kiekbusch, T., Sappok, D., Sauer, B., & Howard, I. (2011). Calculation of the combined torsional mesh stiffness of spur gears with two-and three-dimensional parametrical FE models. *Strojniški vestnik-Journal of Mechanical Engineering*, *57*(11), 810-818.

Kim, W., Lee, J. Y., & Chung, J. (2012). Dynamic analysis for a planetary gear with time-varying pressure angles and contact ratios. *Journal of Sound and Vibration*, *331*(4), 883-901.

Kim, W., Yoo, H. H., & Chung, J. (2010). Dynamic analysis for a pair of spur gears with translational motion due to bearing deformation. *Journal of Sound and Vibration*, *329*(21), 4409-4421.

Kirov, V. & Wang, Y. Y. (2013). Finite element analysis of a floating planetary ring gear with external splines. *AGMA 13FTM07-2013*.

Kohnme, P. (2003). ANSYS help documentation. *ANSYS, Inc. Theory Release*, *8*.

Krantz, T. L. (1992, September). Gear tooth stress measurements of two helicopter planetary stages. *International Power Transmission and Gearing Conference*, Phoeniz, United States.

Lewicki, D. G., & Ballarini, R. (1997). Effect of rim thickness on gear crack propagation path. *Journal of mechanical design*, *119*(1), 88-95.

Lewicki, D. G., Handschuh, R. F., Spievak, L. E., Wawrzynek, P. A., & Ingraffea, A. R. (2001). Consideration of moving tooth load in gear crack propagation predictions. *Journal of Mechanical Design*, *123*(1), 118-124.

Lewicki, D. G., Sane, A. D., Drago, R. J., & Wawrzynek, P. A. (1998). *Three-dimensional gear crack propagation studies* (No. NASA-E-11436). NATIONAL AERONAUTICS AND SPACE ADMINISTRATION CLEVELAND OH LEWIS RESEARCH CENTER.

Li, S. (2007). Finite element analyses for contact strength and bending strength of a pair of spur gears with machining errors, assembly errors and tooth modifications. *Mechanism and Machine Theory*, *42*(1), 88-114.

Liang, X., Zuo, M. J., & Hoseini, M. R. (2015). Vibration signal modeling of a planetary gear set for tooth crack detection. *Engineering Failure Analysis*, *48*, 185-200.

Liang, X., Zuo, M. J., & Pandey, M. (2014). Analytically evaluating the influence of crack on the mesh stiffness of a planetary gear set. *Mechanism and Machine Theory*, *76*, 20-38.

Liang, X., Zuo, M. J., & Patel, T. H. (2013). Evaluating the time-varying mesh stiffness of a planetary gear set using the potential energy method. *Proceedings of the Institution of Mechanical Engineers, Part C: Journal of Mechanical Engineering Science*, 0954406213486734.

Ligata, H., Kahraman, A., & Singh, A. (2008). An experimental study of the influence of manufacturing errors on the planetary gear stresses and planet load sharing. *Journal of Mechanical Design*, *130*(4), 041701.

Ligata, H., Kahraman, A., & Singh, A. (2009). A closed-form planet load sharing formulation for planetary gear sets using a translational analogy. *Journal of Mechanical Design*, *131*(2), 021007.

Lin, H. H., & Liou, C. H. (1998). *A parametric study of spur gear dynamics*. (No. NASA/CR-1998-206598). NATIONAL AERONAUTICS AND SPACE ADMINISTRATION CLEVELAND OH LEWIS RESEARCH CENTER.

Lin, H. H., Liou, C. H., & Townsend, D. P. (1996). *Balancing Dynamic Strength of Spur Gears Operated at Extended Center Distance* (No. NASA-E-10255). NATIONAL AERONAUTICS AND SPACE ADMINISTRATION CLEVELAND OH LEWIS RESEARCH CENTER.

Lin, J., & Parker, R. G. (1999a). Sensitivity of planetary gear natural frequencies and vibration modes to model parameters. *Journal of Sound and Vibration*, *228*(1), 109-128.

Lin, J., & Parker, R. G. (1999b). Analytical characterization of the unique properties of planetary gear free vibration. *Journal of vibration and acoustics,121*(3), 316-321.

Link, H., Keller, J., Guo, Y., & McNiff, B. (2013). *Gearbox reliability collaborative phase 3 gearbox 2 test plan* (No. NREL/TP-5000-58190). National Renewable Energy Laboratory (NREL), Golden, CO..

Litak, G., & Friswell, M. I. (2005). Dynamics of a gear system with faults in meshing stiffness. *Nonlinear Dynamics*, *41*(4), 415-421.

Litvin, F. L. (1997). *Development of Gear Technology and Theory of Gearing* (No. NASA-E-10679). NATIONAL AERONAUTICS AND SPACE ADMINISTRATION CLEVELAND OH LEWIS RESEARCH CENTER.

Liu, L., Liang, X., & Zuo, M. J. (2016). Vibration signal modeling of a planetary gear set with transmission path effect analysis. *Measurement*, *85*, 20-31.

Ma, H., Pang, X., Feng, R., Song, R., & Wen, B. (2015). Fault features analysis of cracked gear considering the effects of the extended tooth contact. *Engineering Failure Analysis*, *48*, 105-120.

Ma, H., Pang, X., Zeng, J., Wang, Q., & Wen, B. (2015). Effects of gear crack propagation paths on vibration responses of the perforated gear system. *Mechanical Systems and Signal Processing*, *62*, 113-128.

Ma, H., Song, R., Pang, X., & Wen, B. (2014). Time-varying mesh stiffness calculation of cracked spur gears. *Engineering Failure Analysis*, *44*, 179-194.

Ma, H., Zeng, J., Feng, R., Pang, X., Wang, Q., & Wen, B. (2015). Review on dynamics of cracked gear systems. *Engineering Failure Analysis*, *55*, 224-245.

Ma, P., & Botman, M. (1985). Load sharing in a planetary gear stage in the presence of gear errors and misalignment. *Journal of Mechanisms, Transmissions, and Automation in Design*, *107*(1), 4-10.

Ma, R., & Chen, Y. (2012). Research on the dynamic mechanism of the gear system with local crack and spalling failure. *Engineering Failure Analysis*, *26*, 12-20.

Maheswari, R. U., & Umamaheswari, R. (2017). Trends in non-stationary signal processing techniques applied to vibration analysis of wind turbine drive train–A contemporary survey. *Mechanical Systems and Signal Processing*, *85*, 296-311.

Mark, W. D. (2009). Stationary transducer response to planetary-gear vibration excitation II: effects of

torque modulations. *Mechanical Systems and Signal Processing*, *23*(7), 2253-2259.

Mark, W. D., & Hines, J. A. (2009). Stationary transducer response to planetary-gear vibration excitation with non-uniform planet loading. *Mechanical Systems and Signal Processing*, *23*(4), 1366-1381.

Mark, W. D., Lee, H., Patrick, R., & Coker, J. D. (2010). A simple frequency-domain algorithm for early detection of damaged gear teeth. *Mechanical Systems and Signal Processing*, *24*(8), 2807-2823.

MathWorks, Inc. (2005). *MATLAB: the language of technical computing. Desktop tools and development environment, version 7* (Vol. 9). MathWorks.

Meltzer, G., & Ivanov, Y. Y. (2003). Fault detection in gear drives with non-stationary rotational speed-part II: the time-quefrency approach. *Mechanical Systems and Signal Processing*, *17*(2), 273-283.

McFadden, P. D. (1986). Detecting fatigue cracks in gears by amplitude and phase demodulation of the meshing vibration. *Journal of vibration, acoustics, stress, and reliability in design*, *108*(2), 165-170.

McFadden, P. D. (1987a). A revised model for the extraction of periodic waveforms by time domain averaging. *Mechanical Systems and Signal Processing*, *1*(1), 83-95.

McFadden, P. D. (1987b). Examination of a technique for the early detection of failure in gears by signal processing of the time domain average of the meshing vibration. *Mechanical systems and signal processing*, *1*(2), 173-183.

McFadden, P. D. (1991). A technique for calculating the time domain averages of the vibration of the individual planet gears and the sun gear in an epicyclic gearbox. *Journal of Sound and vibration*, *144*(1), 163-172.

McFadden, P. D. (1994). Window functions for the calculation of the time domain averages of the vibration of the individual planet gears and sun gear in an epicyclic gearbox. *Journal of Vibration and Acoustics*, *116*(2), 179-187.

McFadden, P. D., & Smith, J. D. (1984). Vibration monitoring of rolling element bearings by the high-frequency resonance technique—a review. *Tribology international*, *17*(1), 3-10.

McFadden, P. D., & Smith, J. D. (1985a). A signal processing technique for detecting local defects in a gear from the signal average of the vibration. *Proceedings of the Institution of Mechanical Engineers, Part C: Journal of Mechanical Engineering Science*, *199*(4), 287-292.

McFadden, P. D., & Smith, J. D. (1985b). An explanation for the asymmetry of the modulation sidebands about the tooth meshing frequency in epicyclic gear vibration. *Proceedings of the Institution of Mechanical Engineers, Part C: Journal of Mechanical Engineering Science*, *199*(1), 65-70.

McNames, J. (2002). Fourier series analysis of epicyclic gearbox vibration. *Journal of Vibration and Acoustics*, *124*(1), 150-153.

Mohammed, O. D., Rantatalo, M., & Aidanpää, J. O. (2013). Improving mesh stiffness calculation of

cracked gears for the purpose of vibration-based fault analysis. *Engineering Failure Analysis*, *34*, 235-251.

Mohammed, O. D., Rantatalo, M., Aidanpää, J. O., & Kumar, U. (2013). Vibration signal analysis for gear fault diagnosis with various crack progression scenarios. *Mechanical systems and signal processing*, *41*(1), 176-195.

Mohammed, O. D., Rantatalo, M., & Aidanpää, J. O. (2015). Dynamic modelling of a one-stage spur gear system and vibration-based tooth crack detection analysis. *Mechanical Systems and Signal Processing*, *54*, 293-305.

Mohammed, O. D., Rantatalo, M., & Kumar, U. (2012). Analytical crack propagation scenario for gear teeth and time-varying gear mesh stiffness.*World Academy of Science, Engineering and Technology*, *68*.

Nair, D. (2005). Gear Modelling by Simulating the Fabrication Process. Master Thesis, University of Cincinnati, Cincinnati, United States.

Neale, M. J. (1995). *The tribology handbook*. Butterworth-Heinemann.

Özgüven, H. N., & Houser, D. R. (1988). Mathematical models used in gear dynamics—a review. *Journal of sound and vibration*, *121*(3), 383-411.

Pandya, Y., & Parey, A. (2013a). Simulation of crack propagation in spur gear tooth for different gear parameter and its influence on mesh stiffness.*Engineering Failure Analysis*, *30*, 124-137.

Pandya, Y., & Parey, A. (2013b). Failure path based modified gear mesh stiffness for spur gear pair with tooth root crack. *Engineering Failure Analysis*,*27*, 286-296.

Pandya, Y., & Parey, A. (2013c). Crack behavior in a high contact ratio spur gear tooth and its effect on mesh stiffness. *Engineering Failure Analysis*, *34*, 69-78.

Pandya, Y., & Parey, A. (2013d). Failure path based modified gear mesh stiffness for spur gear pair with tooth root crack. *Engineering Failure Analysis*, *27*, 286-296.

Pandya, Y., & Parey, A. (2013). Experimental investigation of spur gear tooth mesh stiffness in the presence of crack using photoelasticity technique. *Engineering Failure Analysis*, *34*, 488-500.

Parey, A., El Badaoui, M., Guillet, F., & Tandon, N. (2006). Dynamic modelling of spur gear pair and application of empirical mode decomposition-based statistical analysis for early detection of localized tooth defect. *Journal of sound and vibration*, *294*(3), 547-561.

Parker, R. G., Agashe, V., & Vijayakar, S. M. (2000). Dynamic response of a planetary gear system using a finite element/contact mechanics model. *Journal of Mechanical Design*, *122*(3), 304-310.

Parker, R. G., & Lin, J. (2004). Mesh Phasing Relationships in Planetary and Epicyclic Gears. *Journal of Mechanical Design*, *126*(2), 365-370.

Parker, R. G., Vijayakar, S. M., & Imajo, T. (2000). Non-linear dynamic response of a spur gear pair: modelling and experimental comparisons. *Journal of Sound and vibration*, *237*(3), 435-455.

Parker, R. G., & Wu, X. (2010). Vibration modes of planetary gears with unequally spaced planets and an elastic ring gear. *Journal of Sound and Vibration*, *329*(11), 2265-2275.

Prueter, P. E., Parker, R. G., & Cunliffe, F. (2011, January). A study of gear root strains in a multi-stage planetary wind turbine gear train using a three dimensional finite element/contact mechanics model and experiments. In*ASME 2011 International Design Engineering Technical Conferences and Computers and Information in Engineering Conference* (pp. 621-633). American Society of Mechanical Engineers.

Radzevich, S. P. (2012). *Theory of gearing: kinematics, geometry, and synthesis*. CRC Press.

Randall, R. B. (2011). *Vibration-based condition monitoring: industrial, aerospace and automotive applications*. John Wiley & Sons.

Samuel, P. D., & Pines, D. J. (2000, June). Vibration separation methodology for planetary gear health monitoring. In *SPIE's 7th Annual International Symposium on Smart Structures and Materials* (pp. 250-260). International Society for Optics and Photonics.

Savage, M., Rubadeux, K. L., & Coe, H. H. (1995). *Bending Strength Model for Internal Spur Gear Teeth* (No. NASA-E-9797). NATIONAL AERONAUTICS AND SPACE ADMINISTRATION CLEVELAND OH LEWIS RESEARCH CEN TER.

Shao, Y., & Chen, Z. (2013). Dynamic features of planetary gear set with tooth plastic inclination deformation due to tooth root crack. *Nonlinear Dynamics*, *74*(4), 1253-1266.

Sheng, G. (2012). Vehicle noise, vibration, and sound quality. SAE International.

Sheng, S., & Guo, Y. (2015, March). An Integrated Approach Using Condition Monitoring and Modeling to Investigate Wind Turbine Gearbox Design. In*ASME Turbo Expo* (pp. 15-19).

Sheng, S., Link, H., LaCava, W., Van Dam, J., McNiff, B., Veers, P., & Oyague, F. (2011). Wind turbine drivetrain condition monitoring during GRC phase 1 and phase 2 testing. *Contract*, *303*, 275-3000.

Shi, W., Kim, C. W., Chung, C. W., & Park, H. C. (2013). Dynamic modeling and analysis of a wind turbine drivetrain using the torsional dynamic model. *International Journal of Precision Engineering and Manufacturing*, *14*(1), 153-159.

Singh, A. (2005). Application of a system level model to study the planetary load sharing behavior. *Journal of Mechanical Design*, *127*(3), 469-476.

Singh, A. (2010). Load sharing behavior in epicyclic gears: Physical explanation and generalized formulation. *Mechanism and Machine Theory*, *45*(3), 511-530.

Singh, A., Kahraman, A., & Ligata, H. (2008). Internal Gear Strains and Load Sharing in Planetary Transmissions: Model and Experiments. *Journal of Mechanical Design*, *130*(7), 072602-072602.

Sirichai, S. (1999). Torsional properties of spur gears in mesh using nonlinear finite element analysis. Ph.D Thesis, Curtin University, Perth, Australia.

Smith, I. M., Griffiths, D. V., & Margetts, L. (2013). *Programming the finite element method*. John Wiley & Sons.

Smith, J. D. (2003). *Gear noise and vibration*. CRC Press.

Staszewski, W. J., Worden, K., & Tomlinson, G. R. (1997). Time–frequency analysis in gearbox fault

detection using the Wigner–Ville distribution and pattern recognition. *Mechanical systems and signal processing*, *11*(5), 673-692.

Stephen, P. R. (2012). *Handbook of Practical Gear Design and Manufacture*. CRC press.

Stewart, R. M. (1977). *Some useful data analysis techniques for gearbox diagnostics*. University of Southampton.

Struggl, S., Berbyuk, V., & Johansson, H. (2015). Review on wind turbines with focus on drive train system dynamics. *Wind Energy*, *18*(4), 567-590.

Sun, T., & Hu, H. (2003). Nonlinear dynamics of a planetary gear system with multiple clearances. *Mechanism and Machine Theory*, *38*(12), 1371-1390.

Tamminana, V. K., Kahraman, A., & Vijayakar, S. (2007). A study of the relationship between the dynamic factors and the dynamic transmission error of spur gear pairs. *Journal of Mechanical Design*, *129*(1), 75-84.

Townsend, D. P. (1991). *Dudley's Gear Handbook*: Mcgraw-Hill.

Ural, A., Heber, G., Wawrzynek, P. A., Ingraffea, A. R., Lewicki, D. G., & Neto, J. B. (2005). Three-dimensional, parallel, finite element simulation of fatigue crack growth in a spiral bevel pinion gear. *Engineering Fracture Mechanics*, *72*(8), 1148-1170.

Ural, A., Wawrzynek, P. A., Ingraffea, A. R., & Lewicki, D. G. (2003, January). Simulating Fatigue Crack Growth in Spiral Bevel Gears Using Computational Fracture Mechanics. In *ASME 2003 International Design Engineering Technical Conferences and Computers and Information in Engineering Conference* (pp. 195-199). American Society of Mechanical Engineers.

Urbanek, J., Barszcz, T., & Antoni, J. (2013). A two-step procedure for estimation of instantaneous rotational speed with large fluctuations.*Mechanical Systems and Signal Processing*, *38*(1), 96-102.

Valco, M. J. (1992). Planetary gear train ring gear and support structure investigation. Ph.D. Thesis, Cleveland State University, Cleveland, United States.

Velex, P., & Flamand, L. (1996). Dynamic response of planetary trains to mesh parametric excitations. *Journal of Mechanical Design*, *118*(1), 7-14.

Wan, Z., Cao, H., Zi, Y., He, W., & He, Z. (2014). An improved time-varying mesh stiffness algorithm and dynamic modeling of gear-rotor system with tooth root crack. *Engineering Failure Analysis*, *42*, 157-177.

Wang, J. (2003). Numerical and experimental analysis of spur gears in mesh. Ph.D. Thesis, Curtin University, Perth, Australia.

Wang, J., & Howard, I.M. (2004). The torsional stiffness of involute spur gears. *Proceedings of the Institution of Mechanical Engineers, Part C: Journal of Mechanical Engineering Science*, *218*(1), 131-142.

Wang, J. D., & Howard, I. M. (2006). Error analysis on finite element modeling of involute spur gears. *Journal of Mechanical Design*, *128*(1), 90-97.

Wang, W. (2001). Early detection of gear tooth cracking using the resonance demodulation technique. *Mechanical Systems and Signal Processing*, *15*(5), 887-903.

Wang, W., & Wong, A. K. (2002). Autoregressive model-based gear fault diagnosis. *Journal of vibration and acoustics*, *124*(2), 172-179.

Wang, W. J. & McFadden, P. D. (1993a). Early detection of gear failure by vibration analysis—I. calculation of the time-frequency distribution. *Mechanical System and Signal Processing*, *7*(3), 193–203.

Wang, W. J. & McFadden, P. D. (1993b). Early detection of gear failure by vibration analysis—II. Interpretation of the time-frequency distribution using image processing techniques. *Mechanical System and Signal Processing*, *7*(3), 205–215.

Wang, Z. (2010). Dynamic modelling of planetary gear systems for gear tooth fault. Master Thesis, Curtin University, Perth, Australia.

Wu, J. J., Whittaker, A. R., & Cartmell, M. P. (2000). The use of finite element techniques for calculating the dynamic response of structures to moving loads. *Computers & Structures*, *78*(6), 789-799.

Wu, S., Zuo, M. J., & Parey, A. (2008). Simulation of spur gear dynamics and estimation of fault growth. *Journal of Sound and Vibration*, *317*(3), 608-624.

Wu, X., & Parker, R. G. (2008). Modal properties of planetary gears with an elastic continuum ring gear. *Journal of Applied Mechanics*, *75*(3), 031014.

Xue, S., Entwistle, R., Mazhar, I. & Howard, I. M. (2014). The torsional mesh stiffness of spur planetary gear. *9th IFToMM International Conference on Rotordynamics, Milano*.

Yang, D. C. H., & Lin, J. Y. (1987). Hertzian damping, tooth friction and bending elasticity in gear impact dynamics. *Journal of mechanisms, transmissions, and automation in design*, *109*(2), 189-196.

Yang, Y. B., Yau, J. D., & Wu, Y. S. (2004). *Vehicle-bridge interaction dynamics*. World Scientific Publishing Company.

Yin, J., Wang, W., Man, Z., & Khoo, S. (2013). Modeling and analysis of gear tooth crack growth under variable-amplitude loading. *Mechanical Systems and Signal Processing*, *40*(1), 105-113.

Zhao, F., Tian, Z., & Zeng, Y. (2013). Uncertainty quantification in gear remaining useful life prediction through an integrated prognostics method. *IEEE Transactions on Reliability*, *62*(1), 146-159.

Zhao, M., & Ji, J. C. (2015). Nonlinear torsional vibrations of a wind turbine gearbox. *Applied Mathematical Modelling*, *39*(16), 4928-4950.

Zhonghe, Y., Zhaohui, L., & Smith, M. R. (2001). *Mechanisms and machine theory*. Beijing: Higher Education Press.

Zimroz, R., Bartelmus, W., Barszcz, T., & Urbanek, J. (2014). Diagnostics of bearings in presence of strong operating conditions non-stationarity—a procedure of load-dependent features processing with application to wind turbine bearings. *Mechanical Systems and Signal Processing*, *46*(1), 16-27.

Appendix A

This appendix includes the APDL program for generating the geometry of the planetary gear.

```
/clear
/filename,planetary gear
/prep7
pi=acos(-1)
csys,0
n_planet=3
! sun gear geometry*
m1=10
z1=21
ang1=20
n1=150
n2=50
ha_c1=1
c_c1=0.25
ha1=ha_c1*m1
hf1=(ha_c1+c_c1)*m1
x1=0
d1=m1*z1
db1=d1*cos(ang1*pi/180)
da1=d1+2*ha1
df1=d1-2*hf1
s1=pi*m1/2+2*x1*m1*tan(ang1*pi/180)
theta_s1=tan(ang1*pi/180)-ang1*pi/180
fai_s1=s1/d1
alfa_a1=acos(db1/da1)*180/pi
deata_ang1=360/z1
pesai_kong1=0.4
rp1=c_c1*m1/(1-sin(ang1*pi/180))
a1=hf1-rp1
b1=pi*m1/4+ha1*tan(ang1*pi/180)+
rp1*cos(ang1*pi/180)
alf1=acos(db1/(2*sqrt(d1*d1/4+(a1/sin(ang1*pi/
180)+rp1)*(a1/sin(ang1*pi/180)+rp1)-d1*(a1/sin
(ang1*pi/180)+ rp1)*cos(pi/2-ang1*pi/180))))
!*involute curve equations*
*dim,alfa1,array,n1
*dim,rk1,array,n1
*dim,w1,array,n1
*dim,y1,array,n1
*dim,theta1,array,n1
*do,i,1,n1
alfa1(i)=(alfa_a1-((alfa_a1-alf1*180/pi)/(n1-1))*
(i-1))*pi/180
*enddo
*do,i,1,n1
rk1(i)=(db1/2)/cos(alfa1(i))
theta1(i)=tan(alfa1(i))-alfa1(i)
*enddo
*do,i,1,n1
w1(i)=rk1(i)*cos(pi/2-fai_s1
+(theta1(i)-theta_s1))
y1(i)=rk1(i)*sin(pi/2-fai_s1
+(theta1(i)-theta_s1))
*enddo
*do,i,1,n1
k,,w1(i),y1(i)
*enddo
BSPLIN,ALL
KDELE,2,n1-1,1
nummrg,all
numcmp,all
!*fillet curve equations*
*dim,al1,array,n2
*dim,thet1,array,n2
*dim,g1,array,n2
*dim,u1,array,n2
*do,i,1,n2
al1(i)=(ang1+((90-ang1)/(n2-1))*(i-1))*pi/180
*enddo
aa1=a1-x1*m1
*do,i,1,n2
thet1(i)=(2/d1)*(aa1/tan(al1(i))+b1)
*enddo
*do,i,1,n2
g1(i)
=(d1/2)*sin(thet1(i))-(aa1/sin(al1(i))+rp1)*cos(al
1(i)-thet1(i))
u1(i)
=(d1/2)*cos(thet1(i))-(aa1/sin(al1(i))+rp1)*sin(al
1(i)-thet1(i))
k,,g1(i),u1(i)
```

```
*enddo
CSYS,0
ksel,u,,,1,2,1,
BSPLIN,ALL
ksel,all
KDELE,4,2+n2-1,1
nummrg,all
numcmp,all
LSYMM,x,1,2,,,0,0
allsel,all
nummrg,all
numcmp,all
csys,1
K,30000
larc,1,4,30000,da1/2
kdele,30000
csys,0
k,30000,0,0,0
k,30001,(da1/2)*sin(pi/z1),(da1/2)*cos(pi/z1),0
l,30000,30001
k,30002,0,0,10
lrotat,3,,,,,,30000,30002,-45
lsbl,7,6,sepo,delete,delete
ldele,8,,,1
kdele,30002
allsel,all
nummrg,all
numcmp,all
LSYMM,x,6,,,,0,0
allsel,all
nummrg,all
numcmp,all
/replot

csys,0
k,30000,0,0,0
lstr,7,30000
lstr,8,30000
circle,30000,d1/2*pesai_kong1
lsbl,10,8,sepo,delete,keep
lsbl,11,9,sepo,delete,keep
lsbl,8,14,sepo,delete,keep
lsbl,9,10,sepo,delete,keep
ldele,12,13
ldele,15,18,1,1
kdele,9
kdele,11,12,1,1
nummrg,all
numcmp,all
al,all
allsel,all
!*planet gear geometry*
m2=10
z2=39
ang2=20
n1=150
n2=50
ha_c2=1
c_c2=0.25
ha2=ha_c2*m2
hf2=(ha_c2+c_c2)*m2
x2=0
d2=m2*z2
db2=d2*cos(ang2*pi/180)
da2=d2+2*ha2
df2=d2-2*hf2
s2=pi*m2/2+2*x2*m2*tan(ang2*pi/180)
theta_s2=tan(ang2*pi/180)-ang2*pi/180
fai_s2=s2/d2
alfa_a2=acos(db2/da2)*180/pi
deata_ang2=360/z2
pesai_kong2=0.4
rp2=c_c2*m2/(1-sin(ang2*pi/180))
a2=hf2-rp2
b2=pi*m2/4+ha2*tan(ang2*pi/180)+
rp2*cos(ang2*pi/180)
alf2=acos(db2/(2*sqrt(d2*d2/4+(a2/sin(ang2*pi/
180)+rp2)*(a2/sin(ang2*pi/180)+rp2)-d2*(a2/sin
(ang2*pi/180)+ rp2)*cos(pi/2-ang2*pi/180))))
local,11,0,0,(d1+d2)/2,0
csys,11
!*involutes curve*
*dim,alfa2,array,n1
*dim,rk2,array,n1
*dim,w2,array,n1
*dim,y2,array,n1
*dim,theta2,array,n1
*do,i,1,n1
```

```
alfa2(i)=(alfa_a2-((alfa_a2-alf2*180/pi)/(n1-1))*
(i-1))*pi/180
*enddo
*do,i,1,n1
rk2(i)=(db2/2)/cos(alfa2(i))
theta2(i)=tan(alfa2(i))-alfa2(i)
*enddo
*do,i,1,n1
w2(i)=rk2(i)*cos(pi/2-fai_s2
+(theta2(i)-theta_s2))
y2(i)=rk2(i)*sin(pi/2-fai_s2
+(theta2(i)-theta_s2))
*enddo
*do,i,1,n1
k,,w2(i),y2(i)
*enddo
ksel,u,,,1,11 ,1
bsplin,all
kdele,13,160,1
nummrg,all
numcmp,all
!*fillet curve*
*dim,al2,array,n2
*dim,thet2,array,n2
*dim,g2,array,n2
*dim,u2,array,n2
*do,i,1,n2
al2(i)=(ang2+((90-ang2)/(n2-1))*(i-1))*pi/180
*enddo
aa2=a2-x2*m2
*do,i,1,n2
thet2(i)=(2/d2)*(aa2/tan(al2(i))+b2)
*enddo
*do,i,1,n2
g2(i)
=(d2/2)*sin(thet2(i))-(aa2/sin(al2(i))+rp2)*cos(al
2(i)-thet2(i))
u2(i)
=(d2/2)*cos(thet2(i))-(aa2/sin(al2(i))+rp2)*sin(al
2(i)-thet2(i))
k,,g2(i),u2(i)
*enddo
ksel,u,,,1,13,
BSPLIN,ALL
KDELE,15,62,1
ksel,all
nummrg,all
numcmp,all
LSYMM,x,12,13,,,0,0
local,12, 1,0,(d1+d2)/2,0
csys,12
K,30000
larc,12,15,30000,da2/2
kdele,30000
csys,11
k,30000,0,0,0
k,30001,0,0,10
k,30002,(da2/2)*sin(pi/z2),(da2/2)*cos(pi/z2),0
l,30000,30002
lrotat,14,,,,,,30000,30001,-45
lsbl,18,17,sepo,delete,delete
ldele,19,,,1
nummrg,all
numcmp,all
LSYMM,x,17,,,,0,0
nummrg,all
numcmp,all
csys,11
k,30000,0,0,0
lstr,18,30000
lstr,20,30000
circle,30000,d2/2*pesai_kong2
lsbl,21,19,sepo,delete,keep
lsbl,22,20,sepo,delete,keep
lsbl,19,25,sepo,delete,keep
lsbl,20,21,sepo,delete,keep
ldele,23,24
ldele,26,29,1,1
kdele,21
kdele,23,24,1,1
nummrg,all
numcmp,all
lsel,u,,,1,11,1
al,all
lsel,all
csys,0
ldiv,8,0.2,,,0
ldiv,10,0.2,,,0
```

```
k,30000,0,0,0
larc,5,2,30000,(db1/2)/cos(alfa1)
larc,24,25,30000,(df1/2-d1/2*pesai_kong1)*(4/5
)+d1/2*pesai_kong1
kdele,30000
ldiv,5,0.5,,,0
ldiv,25,0.5,,,0
ldiv,26,0.5,,,0
lstr,26,27
lstr,27,28
lstr,28,10
allsel,all
nummrg,all
numcmp,all
csys,12
ldiv,19,0.2,,,0
ldiv,21,0.2,,,0
k,30000,0,0
larc,16,13,30000,(db2/2)/cos(alfa2)
larc,29,30,30000,(df2/2-d2/2*pesai_kong2)*(4/5
)+d2/2*pesai_kong2
kdele,30000
ldiv,16,0.5,,,0
ldiv,35,0.5,,,0
ldiv,36,0.5,,,0
lstr,31,32
lstr,32,33
lstr,33,22
allsel,all
nummrg,all
numcmp,all
adele,1
adele,2
allsel,all
nummrg,all
numcmp,all
al,1,5,30,28
al,30,27,3,25
al,6,2,28,31,29,10
al,7,4,25,31,26,8
al,24,29,32,11
al,23,26,32,9
allsel,all
nummrg,all
numcmp,all
al,12,16,40,38
al,37,14,35,40
al,18,15,35,41,36,19
al,17,13,38,41,39,21
al,20,33,36,42
al,22,42,39,34
allsel,all
nummrg,all
numcmp,all
number1=10
number2=5
number3=10
number4=1
number5=5
!
lesize,1,,,number1
lesize,5,,,number2
lesize,28,,,number2
lesize,30,,,number1
lesize,3,,,number1
lesize,27,,,number2
lesize,25,,,number2

lesize,6,,,number4
lesize,2,,,number3
lesize,10,,,number2

lesize,7,,,number4
lesize,4,,,number3
lesize,8,,,number2
lesize,26,,,number2

lesize,24,,,number5
lesize,32,,,number5

lesize,23,,,number5
allsel,all
nummrg,all
numcmp,all

lesize,12,,,number1
lesize,16,,,number2
lesize,38,,,number2
```

```
lesize,40,,,number1
lesize,14,,,number1
lesize,37,,,number2
lesize,35,,,number2
lesize,18,,,number4
lesize,15,,,number3
lesize,36,,,number2
lesize,17,,,number4
lesize,13,,,number3
lesize,39,,,number2
lesize,33,,,number5
lesize,42,,,number5
lesize,34,,,number5

mp,ex,1,2.06e5
mp,prxy,1,0.3
et,1,plane82
type,1
asel,s,,,1,,,,
mshape,0,2d
mshkey,1
amesh,1,,,
allsel,all
nummrg,all
numcmp,all

asel,s,,,2,,,,
mshape,0,2d
mshkey,1
amesh,2,,,

allsel,all
nummrg,all
numcmp,all

asel,s,,,3,,,,
lccat,2,6
lccat,31,29
mshape,0,2d
mshkey,1
amesh,3,,,
ldele,43,44

allsel,all
nummrg,all
numcmp,all

asel,s,,,4,,,,
lccat,4,7
lccat,31,26
mshape,0,2d
mshkey,1
amesh,4,,,
ldele,43,44

allsel,all
nummrg,all
numcmp,all
asel,s,,,5,,,,
mshape,0,2d
mshkey,1
amesh,5,,,

allsel,all
nummrg,all
numcmp,all

asel,s,,,6,,,,
mshape,0,2d
mshkey,1
amesh,6,,,
allsel,all
nummrg,all
numcmp,all

et,2,plane82
type,2
asel,s,,,7,,,,
mshape,0,2d
mshkey,1
amesh,7,,,

allsel,all
nummrg,all
numcmp,all

asel,s,,,8,,,,
mshape,0,2d
```

```
mshkey,1
amesh,8,,,

allsel,all
nummrg,all
numcmp,all

asel,s,,,9,,,,
lccat,18,15
lccat,41,36
mshape,0,2d
mshkey,1
amesh,9,,,
ldele,43,44

allsel,all
nummrg,all
numcmp,all

asel,s,,,10,,,,
lccat,17,13
lccat,41,39
mshape,0,2d
mshkey,1
amesh,10,,,
ldele,43,44

allsel,all
nummrg,all
numcmp,all

asel,s,,,11,,,,
mshape,0,2d
mshkey,1
amesh,11,,,

allsel,all
nummrg,all
numcmp,all

asel,s,,,12,,,,
mshape,0,2d
mshkey,1
amesh,12,,,
```

```
allsel,all
nummrg,all
numcmp,all

!*ring gear geometry*
m3=10 !ring gear tooth module
z3=99 !ring gear tooth number
ang3=20*pi/180 !ring gear tooth pressure angle
inv_ang3=tan(ang3)-ang3
d3=m3*z3
r3=d3/2
rb3=r3*cos(ang3) !ring gear basic radius
hadd3=0.849
hroot3=1.25
rr3=r3+hroot3*m3
ra3=r3-hadd3*m3
rf3=0.38*m3
psai_kong3=1.2
rout3=psai_kong3*rr3
tp3=pi*m3/2
anga3=acos(rb3/ra3)
inv_anga3=tan(anga3)-anga3
alpha3=tp3/(2*r3)+inv_anga3-inv_ang3
sigma31=acos(rb3/(rr3-rf3))
d3=rb3*tan(sigma31)
sigma32=atan((d3+rf3)/rb3)
rqf3=(d3+rf3)/sin(sigma32)
phi3=tan(sigma32)-sigma32-inv_anga3
sigma3=alpha3+phi3+sigma32

csys,1
section31=(rqf3-ra3)/n1
*do,rq3,ra3,rqf3,section31
angq3=acos(rb3/rq3)
inv_angq3=tan(angq3)-angq3
thetaq3=alpha3+inv_angq3-inv_anga3
k,,rq3,thetaq3*180/pi
*enddo

angqf3=acos(rb3/rqf3)
inv_angqf3=tan(angqf3)-angqf3
thetaqf3=alpha3+inv_angqf3-inv_anga3
k,,rqf3,thetaqf3*180/pi
```

```
nummrg,all
numcmp,all
section32=(pi/2-sigma31)/n2
*do,thetas3,0,pi/2-sigma31,section32
xs3=(rr3-rf3)*sin(sigma3-sigma31)-rf3*cos(sig
ma3+thetas3)
ys3=(rr3-rf3)*cos(sigma3-sigma31)+rf3*sin(sig
ma3+thetas3)
rs3=sqrt(xs3**2+ys3**2)
sigmas3=asin(xs3/rs3)
k,,rs3,sigmas3*180/pi
*enddo

xsf3= (rr3-rf3)*sin(sigma3-sigma31)
-rf3*cos(sigma3+pi/2-sigma31)
ysf3=(rr3-rf3)*cos(sigma3-sigma31)
+rf3*sin(sigma3+pi/2-sigma31)

rsf3= sqrt(xsf3**2+ysf3**2)
sigmasf3=asin(xsf3/rsf3)
k,,rsf3,sigmasf3*180/pi
nummrg,all
numcmp,all
ksel,s,,,34,184,,
bsplin,all
KDELE,35,183,1
ksel,s,,,all
ksel,s,,,184,234,,
bsplin,all
KDELE,185,233,1
ksel,all
nummrg,all
numcmp,all
csys,0
lsymm,y,43,44,,,,0,0
csys,1
k,30000
larc,34,37,30000,ra3
kdele,30000
csys,0
k,30000,0,0,0
k,30001,rr3*cos(pi/z3),rr3*sin(pi/z3),0
l,30000,30001
k,30002,0,0,10
lrotat,36,,,,,,30000,30002,45
lsbl,49,48,sepo,delete,delete
ldele,50,,,1
kdele,30002
allsel,all
nummrg,all
numcmp,all
lsymm,y,48,,,,0,0
allsel,all
nummrg,all
numcmp,all
/replot
!*
csys,0
k,30000,0,0,0
lstr,40,30000
lstr,41,30000

circle,30000,rout3
LEXTND,50,40,200,1
LEXTND,51,41,200,1
LSBL,56,52,,,KEEP
lsbl,59,48,,,keep
ldele,60,,,1
LDELE,50,,,1
ldele,58,,,1
lsbl,57,55,,,keep
lsbl,58,49,,,keep
ldele,59,,,1
ldele,51,,,1
ldele,50,,,1
lsbl,52,56,,,keep
lsbl,55,57,,,keep
ldele,51,,,1
ldele,53,,,1
ldele,54,,,1
ldele,58,,,1
allsel,all
nummrg,all
numcmp,all

LSEL,s,,,43,53,,
al,all
allsel,all
```

```
nummrg,all
numcmp,all

csys,1
agen,,13,,,,90,,,,1
save
asel,s,,,13
csys,1
ldiv,52,0.2,,,0
ldiv,53,0.2,,,0
k,30000,0,0,0
larc,35,38,30000,rqf3
larc,45,46,30000, (rout3-rr3)*(1/5)+rr3
kdele,30000

ldiv,47,0.5,,,0
ldiv,56,0.5,,,0
ldiv,57,0.5,,,0
lstr,47,48
lstr,48,49
lstr,49,42
allsel,all
nummrg,all
numcmp,all
adele,13
allsel,all
nummrg,all
numcmp,all
al,43,47,61,56
al,45,58,61,59
al,48,44,56,62,57,52
al,49,46,59,62,60,53
al,54,57,63,50
al,55,60,63,51
allsel,all
nummrg,all
numcmp,all

lesize,43,,,number1
lesize,47,,,number2
lesize,56,,,number2
lesize,61,,,number1
lesize,45,,,number1
lesize,58,,,number2
lesize,59,,,number2

lesize,48,,,number4
lesize,44,,,number3
lesize,52,,,number2
lesize,62,,,number2
lesize,49,,,number4
lesize,46,,,number3
lesize,53,,,number2
lesize,60,,,number3+number4-number2
lesize,54,,,number5
lesize,63,,,number5
lesize,55,,,number5

allsel,all
nummrg,all
numcmp,all
et,3,plane82
type,3
asel,s,,,13,,,,
mshape,0,2d
mshkey,1
amesh,13,,,
allsel,all
nummrg,all
numcmp,all
asel,s,,,14,,,,
mshape,0,2d
mshkey,1
amesh,14,,,
allsel,all
nummrg,all
numcmp,all

asel,s,,,15,,,,
lccat,48,44
lccat,57,62
mshape,0,2d
mshkey,1
amesh,15,,,
ldele,64,65
allsel,all
nummrg,all
numcmp,all
```

```
asel,s,,,16,,,,
lccat,49,46
lccat,60,62
mshape,0,2d
mshkey,1
amesh,16,,,
ldele,64,65
allsel,all
nummrg,all
numcmp,all

asel,s,,,17,,,,
mshape,0,2d
mshkey,1
amesh,17,,,
allsel,all
nummrg,all
numcmp,all
asel,s,,,18,,,,
mshape,0,2d
mshkey,1
amesh,18,,,
allsel,all
nummrg,all
numcmp,all
save
asel,s,,,1,6,,
csys,1
agen,z1,all,,,,360/z1,,,,
allsel,all
nummrg,all
numcmp,all

asel,s,,,7,12,,
csys,12 agen,z2,all,,,,360/z2,,,,
allsel,all
nummrg,all
numcmp,all

csys,1
asel,s,,,13,18,,
csys,1
agen,z3,all,,,,360/z3,,,,
allsel,all
nummrg,all
numcmp,all
save

asel,s,,,1,6,,
asel,a,,,19,138,,,
cm,sungear,area
allsel,all
asel,s,,,7,12,,,
asel,a,,,139,366,,,
cm,planetgear1,area
allsel,all
asel,s,,,13,18,,
asel,a,,,367,954
cm,ringgear,area

allsel,all
cmsel,,sungear,,
csys,1
agen,,all,,,,360/(4*z1),,,,1
allsel,all
cmsel,,planetgear1,,
csys,12
agen,,all,,,,-360/(4*z2),,,,1
allsel,all
cmsel,,ringgear,,
csys,1
agen,,all,,,,360/(4*z3),,,,1
allsel,all
!*
cmsel,,planetgear1,,
csys,1
agen,2,all,,,,360/n_planet,,,,
cmsel,u,planetgear1,
cm,planetgear2,area
cmsel,,planetgear2,,
csys,1
agen,2,all,,,,360/n_planet,,,,
cmsel,u,planetgear2,
cm,planetgear3,area
allsel,all
csys,0
local,13,1,-(d1+d2)/2*cos(30*pi/180),-(d1+d2)/2
```

```
*sin(30*pi/180),0
local,14,1,
(d1+d2)/2*cos(30*pi/180),-(d1+d2)/2*sin(30*pi/
180),0

cmsel,,planetgear2,,
csys,13
agen,,all,,,,-z3/z2*360/n_planet,,,,1
allsel,all

cmsel,,planetgear3,,
csys,14
agen,,all,,,,-z3/z2*360/n_planet-z3/z2*360/n_pla
net,,,,1
allsel,all

csys,1
lsel,s,loc,x,d1/2*pesai_kong1
cm,line_sungearhub,line
nsll,s,1
cm,node_sungearhub,node
allsel,all

csys,12
lsel,s,loc,x,d2/2*pesai_kong2
cm,line_planetgear1hub,line
nsll,s,1
cm,node_planetgear1hub,node
allsel,all
csys,13
lsel,s,loc,x,d2/2*pesai_kong2
cm,line_planetgear1hub,line
nsll,s,1
cm,node_planetgear2hub,node
allsel,all

csys,14
lsel,s,loc,x,d2/2*pesai_kong2
cm,line_planetgear1hub,line
nsll,s,1
cm,node_planetgear3hub,node
allsel,all

csys,1
lsel,s,loc,x,rout3
cm,line_ringgearhub,line
nsll,s,1
cm,node_ringgearhub,node
allsel,all

kdele,19
nummrg,all
numcmp,all
Eplot
SAVE,PLANETARYGEAR
```

Appendix B

This appendix includes the APDL program for calculating the resultant planetary gear mesh stiffness.

```
/GST,on

!*Define the rolling angle for sun gear, planet gear and ring gear*
*DIM,ANG_CARRIER,,75
!
ANG_CARRIER(1) =0,0.1,0.2,0.3,0.4
ANG_CARRIER(6) =0.5,0.6,0.7,0.8,0.9
ANG_CARRIER(11)=1,1.1,1.2,1.3,1.4
ANG_CARRIER(16)=1.5,1.6,1.7,1.8,1.9
ANG_CARRIER(21)=2,2.1,2.2,2.3,2.4
ANG_CARRIER(26)=2.5,2.6,2.7,2.8,2.9
ANG_CARRIER(31)=3,3.1,3.2,3.3,3.4
ANG_CARRIER(36)=3.5,3.6,3.7,3.8,3.9
ANG_CARRIER(41)=4,4.1,4.2,4.3,4.4
ANG_CARRIER(46)=4.5,4.6,4.7,4.8,4.9
ANG_CARRIER(51)=5,5.1,5.2,5.3,5.4
ANG_CARRIER(56)=5.5,5.6,5.7,5.8,5.9
ANG_CARRIER(61)=6,6.1,6.2,6.3,6.4
ANG_CARRIER(66)=6.5,6.6,6.7,6.8,6.9
ANG_CARRIER(71)=7,7.1,7.2,7.3,7.4

FNAM=1
PARSAV,ALL,ANGLE_A
:DOLOOP
RESUME,PLANETARYGEAR,DB,,0,0
!
PARRES,,ANGLE_A,,,,
/prep7
!

TOQ=-300000
toq_weak=-1000
B=60
!
allsel,all
csys,12
wpcsys,,12
k,,0,0        ! Key point # is 3082
CSYS,13
WPCSYS,,13
K,,0,0        ! Key point # is 3083

CSYS,14
WPCSYS,,14
K,,0,0        ! Key point # is 3084

csys,1
wpcsys,1
k,,0,0       ! Key point # is 3085

lstr,3082,3085
lstr,3083,3085
lstr,3084,3085
lsel,s,,,4504,4506

CM,carrierarm,LINE

CSYS,1
lgen,,all,,,,-ANG_CARRIER(%FNAM%),,,,1
ALLSEL,ALL
lsel,s,,,4504,4506
cm,carrierarm,line
allsel,all

CSYS,1
CMSEL,,PLANETGEAR1,,
AGEN,,ALL,,,,-ANG_CARRIER(%FNAM%),,,,1
KWPAVE,3082
CSYS,4
CSWPLA,20,1
CSYS,20
AGEN,,ALL,,,,
(-z3/z2)*ANG_CARRIER(%FNAM%),,,,1
CSDELE,20,,,
ALLSEL,ALL
```

```
CSYS,1
CMSEL,,PLANETGEAR2,,
AGEN,,ALL,,,,-ANG_CARRIER(%FNAM%),,,,1
KWPAVE,3083
CSYS,4
CSWPLA,21,1
CSYS,21
AGEN,,ALL,,,,
(-z3/z2)*ANG_CARRIER(%FNAM%),,,,1
CSDELE,21,,,
ALLSEL,ALL

CSYS,1
CMSEL,,PLANETGEAR3,,
AGEN,,ALL,,,,-ANG_CARRIER(%FNAM%),
,,,1
KWPAVE,3084
CSYS,4
CSWPLA,22,1
CSYS,22
AGEN,,ALL,,,,
(-z3/z2)*ANG_CARRIER(%FNAM%),,,,1
CSDELE,22,,,
ALLSEL,ALL

CSYS,1
CMSEL,,SUNGEAR,,
AGEN,,ALL,,,,
-(1+z3/z1)* ANG_CARRIER(%FNAM%),,,,1
ALLSEL,ALL

ET,2,beam188
SECTYPE,2,BEAM,RECT,,0
SECOFFSET,CENT
SECDATA,B,B,0,0,0,0,0,0,0,0,0,0

lesize,4504,,,10,,,,,1
type,2
mat,1
esys, 0
secnum,2
lmesh,4504

lesize,4505,,,10,,,,,1
type,2
mat,1
esys, 0
secnum,2
lmesh,4505

lesize,4506,,,10,,,,,1
type,2
mat,1
esys, 0
secnum,2
lmesh,4506

ET,10,MASS21
KEYOPT,10,1,0
KEYOPT,10,2,0
KEYOPT,10,3,3
R,6,1e-6,1e-6,
TYPE,10
MAT, 1
REAL, 6
ESYS, 0
SECNUM, ,
TSHAP,PILO
E,202724

nkpt,,3082
et,3,mpc184,6
csys,0
sectype,3,joint,revo,arm1
KWPAVE,3082
CSYS,4
wprota,,,-90
CSWPLA,15,0
CSYS,15
secjoint,,15
type,3
secnum,3
e,202723,202754

nkpt,,3083
et,3,mpc184,6
csys,0
sectype,4,joint,revo,arm2
```

```
KWPAVE,3083
CSYS,4
CSWPLA,16,0
CSYS,16
secjoint,,16
type,3
secnum,3
e,202734,202755

nkpt,,3084
csys,0
sectype,5,joint,revo,arm3
KWPAVE,3084
CSYS,4
CSWPLA,17,0
CSYS,17
secjoint,,17
type,3
secnum,3
e,202744,202756

/COM, CONTACT PAIR CREATION - START
CM,_NODECM,NODE
CM,_ELEMCM,ELEM
CM,_KPCM,KP
CM,_LINECM,LINE
CM,_AREACM,AREA
CM,_VOLUCM,VOLU
/GSAV,cwz,gsav,,temp
! Define surface-based constraint type of pair
MAT,1
R,7
REAL,7
ET,11,169
ET,12,175
KEYOPT,12,12,5
KEYOPT,12,4,0
KEYOPT,12,2,2
KEYOPT,11,2,0
KEYOPT,11,4,111
TYPE,11
! Create a pilot node
TSHAP,PILO
E,202754
NSEL,S,,,202754
CM,planet1centrenode,NODE
CMSEL,S,_NODECM
! Generate the contact surface
NSEL,S,,,NODE_PLANETGEAR1HUB
CM,_CONTACT,NODE
TYPE,12
ESLN,S,0
ESURF
ALLSEL
ESEL,ALL
ESEL,S,TYPE,,11
ESEL,A,TYPE,,12
ESEL,R,REAL,,7
/PSYMB,ESYS,1
/PNUM,TYPE,1
/NUM,1
EPLOT
ESEL,ALL
ESEL,S,TYPE,,11
ESEL,A,TYPE,,12
ESEL,R,REAL,,7
CMSEL,A,_NODECM
CMDEL,_NODECM
CMSEL,A,_ELEMCM
CMDEL,_ELEMCM
CMSEL,S,_KPCM
CMDEL,_KPCM
CMSEL,S,_LINECM
CMDEL,_LINECM
CMSEL,S,_AREACM
CMDEL,_AREACM
CMSEL,S,_VOLUCM
CMDEL,_VOLUCM
/GRES,cwz,gsav
CMDEL,_TARGET
CMDEL,_CONTACT
/COM, CONTACT PAIR CREATION - END
! CARRIER ARM FINISHED

! Create rigid constraints between the node on the edge of the planet gear 2 hub and the node in the centre of the node
/COM, CONTACT PAIR CREATION - START
```

```
CM,_NODECM,NODE
CM,_ELEMCM,ELEM
CM,_KPCM,KP
CM,_LINECM,LINE
CM,_AREACM,AREA
CM,_VOLUCM,VOLU
/GSAV,cwz,gsav,,temp
! Define surface-based constraint type of pair
MAT,1
R,8
REAL,8
ET,13,169
ET,14,175
KEYOPT,14,12,5
KEYOPT,14,4,0
KEYOPT,14,2,2
KEYOPT,13,2,0
KEYOPT,13,4,111
TYPE,13
! Create a pilot node
TSHAP,PILO
E,202755
NSEL,S,,,202755
CM,PLANET2CENTRENODE,NODE
CMSEL,S,_NODECM
! Generate the contact surface
NSEL,S,,,NODE_PLANETGEAR2HUB
CM,_CONTACT,NODE
TYPE,14
ESLN,S,0
ESURF
ALLSEL
ESEL,ALL
ESEL,S,TYPE,,13
ESEL,A,TYPE,,14
ESEL,R,REAL,,8
/PSYMB,ESYS,1
/PNUM,TYPE,1
/NUM,1
EPLOT
ESEL,ALL
ESEL,S,TYPE,,13
ESEL,A,TYPE,,14
ESEL,R,REAL,,8
CMSEL,A,_NODECM
CMDEL,_NODECM
CMSEL,A,_ELEMCM
CMDEL,_ELEMCM
CMSEL,S,_KPCM
CMDEL,_KPCM
CMSEL,S,_LINECM
CMDEL,_LINECM
CMSEL,S,_AREACM
CMDEL,_AREACM
CMSEL,S,_VOLUCM
CMDEL,_VOLUCM
/GRES,cwz,gsav
CMDEL,_TARGET
CMDEL,_CONTACT
/COM, CONTACT PAIR CREATION - END
! CARRIER ARM FINISHED

/COM, CONTACT PAIR CREATION - START
CM,_NODECM,NODE
CM,_ELEMCM,ELEM
CM,_KPCM,KP
CM,_LINECM,LINE
CM,_AREACM,AREA
CM,_VOLUCM,VOLU
/GSAV,cwz,gsav,,temp
! Define surface-based constraint type of pair
MAT,1
R,9
REAL,9
ET,15,169
ET,16,175
KEYOPT,16,12,5
KEYOPT,16,4,0
KEYOPT,16,2,2
KEYOPT,15,2,0
KEYOPT,15,4,111
TYPE,15
! Create a pilot node
TSHAP,PILO
E,202756
NSEL,S,,,202756
CM,PLANET3CENTRENODE,NODE
CMSEL,S,_NODECM
```

```
! Generate the contact surface
NSEL,S,,,NODE_PLANETGEAR3HUB
CM,_CONTACT,NODE
TYPE,16
ESLN,S,0
ESURF
ALLSEL
ESEL,ALL
ESEL,S,TYPE,,15
ESEL,A,TYPE,,16
ESEL,R,REAL,,9
/PSYMB,ESYS,1
/PNUM,TYPE,1
/NUM,1
EPLOT
ESEL,ALL
ESEL,S,TYPE,,15
ESEL,A,TYPE,,16
ESEL,R,REAL,,9
CMSEL,A,_NODECM
CMDEL,_NODECM
CMSEL,A,_ELEMCM
CMDEL,_ELEMCM
CMSEL,S,_KPCM
CMDEL,_KPCM
CMSEL,S,_LINECM
CMDEL,_LINECM
CMSEL,S,_AREACM
CMDEL,_AREACM
CMSEL,S,_VOLUCM
CMDEL,_VOLUCM
/GRES,cwz,gsav
CMDEL,_TARGET
CMDEL,_CONTACT
/COM, CONTACT PAIR CREATION - END
! CARRIER ARM FINISHED

csys,0
L_weakspring=1000
*afun,deg
alpha5=atan(41.883/3.1387)
theta5=asin(d1/2*pesai_kong1/L_weakspring)
fai5=90-theta5-(alpha5-(-ang_sun(%FNAM%))
)
x5=L_weakspring*cos(fai5)
y5=L_weakspring*sin(fai5)
k,,x5,y5
nkpt,,3086
et,31,combin14
keyopt,31,1,0
KEYOPT,31,2,0
KEYOPT,31,3,2
R,31,10,0,0, , ,0,
RMORE, ,

TYPE,31
MAT,1
REAL,31
ESYS, 0
SECNUM,
TSHAP,LINE
!*
FLST,2,2,1
FITEM,2,704
FITEM,2,202757
E,P51X

!constraint the freedom of the weak spring
d,202757,ux,0
d,202757,uy,0

!start the mesh adaptation on the sun gear surface

!create component for the S_P contact area
FLST,5,138,5,ORDE,138
FITEM,5,1
…… ! SELECT THE AREA
FITEM,5,1417
ASEL,S, , ,P51X
CM,S_Pcontactarea,AREA
ALLSEL,ALL

!create component for the P1_R contact area
FLST,5,216,5,ORDE,216
FITEM,5,8
…… ! SELECT THE AREA
FITEM,5,1418
```

```
ASEL,S, , ,P51X
CM,P_Rcontactarea,AREA

!create adaptive mesh between sun gear and planet 1 gear
cmsel,s,S_Pcontactarea
aclear,all
FLST,2,276,4,ORDE,276
FITEM,2,1
……! SELECT THE AREA
FITEM,2,4490
LESIZE,P51X, , ,-1, ,1

TYPE,      1
MAT,           1
ESYS,           0
MSHKEY,0
ESIZE,0.4
SMRTSIZE, ,0.2,1,2,7,15,1.5,1,1,4,0
!*
FLST,5,138,5,ORDE,138
FITEM,5,1
……!SELECT THE AREA
FITEM,5,1417
CM,_Y,AREA
ASEL, , , ,P51X
CM,_Y1,AREA
CHKMSH,'AREA'
CMSEL,S,_Y
AMESH,_Y1
!*
CMDELE,_Y
CMDELE,_Y1
CMDELE,_Y2
allsel,all
! create adaptive mesh between Planet 1 gear and ring gear
cmsel,s,P_Rcontactarea
aclear,all
FLST,2,432,4,ORDE,432
FITEM,2,14
……!SELECT THE AREA
FITEM,2,-4492
LESIZE,P51X, , ,-1, ,1

TYPE,1
MAT,1
ESYS,0
SECNUM, ,
ESIZE,0.4
SMRTSIZE, ,0.2,1,2,7,15,1.4,1,1,4,0
FLST,5,216,5,ORDE,216
FITEM,5,8
……!SELECT THE AREA
FITEM,5,1418
CM,_Y,AREA
ASEL, , , ,P51X
CM,_Y1,AREA
CHKMSH,'AREA'
CMSEL,S,_Y
AMESH,_Y1
CMDELE,_Y
CMDELE,_Y1
CMDELE,_Y2
allsel,all
! Create contact pair in this model
MPTEMP,,,,,,,,
MPTEMP,1,0
MPDATA,MU,2,,0.2
/COM, CONTACT PAIR CREATION - START
CM,_NODECM,NODE
CM,_ELEMCM,ELEM
CM,_KPCM,KP
CM,_LINECM,LINE
CM,_AREACM,AREA
CM,_VOLUCM,VOLU
/GSAV,cwz,gsav,,temp
MP,MU,2,0.2
MAT,2
R,34
REAL,34
ET,36,169
ET,37,172
KEYOPT,37,9,0
KEYOPT,37,10,2
R,34,
RMORE,
RMORE,,0
```

```
RMORE,0
! Generate the target surface
……! SELECT THE AREA
CM,_TARGET,LINE
TYPE,36
NSLL,S,1
ESLN,S,0
ESURF
CMSEL,S,_ELEMCM
! Generate the contact surface
……! SELECT THE AREA
CM,_CONTACT,LINE
TYPE,37
NSLL,S,1
ESLN,S,0
ESURF
ALLSEL
ESEL,ALL
ESEL,S,TYPE,,36
ESEL,A,TYPE,,37
ESEL,R,REAL,,34
/PSYMB,ESYS,1
/PNUM,TYPE,1
/NUM,1
EPLOT
ESEL,ALL
ESEL,S,TYPE,,36
ESEL,A,TYPE,,37
ESEL,R,REAL,,34
CMSEL,A,_NODECM
CMDEL,_NODECM
CMSEL,A,_ELEMCM
CMDEL,_ELEMCM
CMSEL,S,_KPCM
CMDEL,_KPCM
CMSEL,S,_LINECM
CMDEL,_LINECM
CMSEL,S,_AREACM
CMDEL,_AREACM
CMSEL,S,_VOLUCM
CMDEL,_VOLUCM
/GRES,cwz,gsav
CMDEL,_TARGET
CMDEL,_CONTACT
/COM, CONTACT PAIR CREATION - END
!*??sun gear hub nodal coordinates*
csys,1
cmsel,s,node_sungearhub
nrotat,all
allsel,all

csys,12
cmsel,s,node_planetgear1hub
nrotat,all
allsel,all

csys,13
cmsel,s,node_planetgear2hub
nrotat,all
allsel,all

csys,14
cmsel,s,node_planetgear3hub
nrotat,all
allsel,all

csys,1
cmsel,s,node_ringgearhub
nrotat,all
allsel,all

cmsel,s, node_sungearhub
CP,1,UY,all
d,all,ux,0
allsel,all

cmsel,s, node_ringgearhub
d,all,ux,0,
d,all,uy,0
allsel,all

nsel,s,,,202724,,,
d,all,ux,0,
d,all,uy,0,
d,all,uz,0,
d,all,rotx,0,
d,all,roty,0,
```

```
d,all,rotz,0,
allsel,all

!the first step solution
FINISH
/SOL
cmsel,s, node_sungearhub
f,all,fy,toq_weak
allsel,all
ANTYPE,0
NLGEOM,1
OUTRES,ERASE
OUTRES,ALL,ALL
TIME,1
/STATUS,SOLU
SOLVE

!the second step solution
FINISH
/SOL
ANTYPE,,REST,1, ,0
cmsel,s, node_sungearhub
f,all,fy,TOQ
allsel,all
!kill the weak spring element
ekill,65383
TIME,2
/STATUS,SOLU
SOLVE
FINISH

! POSTPROCESS THE RESULT AND GET
THE MASS ELEMENT ROLLING ANGLE
/POST1
set,2,last,1,
RSYS,1

*CFOPEN,202723rotation%TOQ/1000%NM,L
IS,,APPEND
*CFWRITE,,%-ANG_CARRIER(FNAM)%,Ro
tz%FNAM%,rotz(202723)
*cfclose

*CFOPEN,202734rotation%TOQ/1000%NM,L
IS,,APPEND
*CFWRITE,,%-ANG_CARRIER(FNAM)%,Ro
tz%FNAM%,rotz(202734)
*cfclose

*CFOPEN,202744rotation%TOQ/1000%NM,L
IS,,APPEND
*CFWRITE,,%-ANG_CARRIER(FNAM)%,rot
z%FNAM%,rotz(202744)
*cfclose

*CFOPEN,704%TOQ/1000%NM,LIS,,APPEN
D
*CFWRITE,,%-ANG_CARRIER(FNAM)%,uy
%FNAM%,uy(704)
*cfclose

SAVE,2dsungearinput%TOQ/1000%NM%-AN
G_CARRIER(FNAM)%,DB,
FINISH
FNAM=FNAM+1
*IF,FNAM,GT,37,:ENDLOOP
PARSAV,ALL,ANGLE_A,,
*GO,:DOLOOP
:ENDLOOP
FINISH
```

Appendix C

This appendix includes the matlab procedure for calucating the dynamic responses of the flexibly supported gear.

```
clear ;clc ;
ti = 0;          % initial time step
tf = 0.1;      % final time step
dt = 0.00001 ;      % size of the time step
nt = fix((tf-ti)/dt)+1;           % number of time steps
[depl12_p,vel12_p,accl12_p] = newmarknew(ti,tf,dt,nt) ;
t=linspace(ti,tf,nt);
figure(1)
plot(t,vel12_p(4,:)) ;

function [depl, vel, accl] = newmarknew(ti,tf,dt,nt)
% Newmark step-by-step time integration scheme
%                [R]    : External applied load                                  %
%                [m]    : Assembeled Mass Matrix                                   %
%                [k]    : Assembeled Stiffness MAtrix                            %
%                [c]    : Damping Matrix                                           %
%                                                                                      %
% OUTPUT :                                                                          %
%                depl : Displacement Response                                    %
%                vel    : Velocity                                                   %
%                accl : Acceleration                                              %
%                                                                                      %

%gear mesh stiffness from FEA calculation
[ang,dis,kp,kp0,kp10] = stiffness12_p;

%gear design parameters
mod=0.006; %module, m
zg=23;
zp=zg;
rg = mod*zg*cos(20*pi/180)/2; % base circle radii, m
rp = rg;

ha=1;
rga = zg*mod/2+ha*mod; %addendum circle radii, m
rpa = zp*mod/2+ha*mod;

mp = 0.7;
mg = 0.7; % mass of the pinion and gear and part of the shaft, kg
```

```
ip = 0.0025;
ig = 0.0025; % Mass moment of inertia of pinion and gear    and associated shafts, kg m^2

%parameter for motor and load
im = 0.07;
iout = 0.07;
%parameter for shaft and coupling
kcp = 500; %estimate shaft&couplings torsional stiffness Nm/rad
kcg = kcp;
qcp = 20;    %estimate shaft&couplings torsional damping Nms/rad
qcg = qcp;

%parameter for bearing
kxp = 1e6; % bearing support stiffness, N/m
kyp = 1e6;
kxg = kxp;
kyg = kyp;

qxp = 100; % vertical viscous damping of bearing Ns/m
qyp = 100;
qxg = qxp;
qyg = qyp;
qstp = 0.01; %torsional viscous damping of bearing Ns/m
qstg = qstp;

%mass matrix
m=[im 0 0 0 0 0;...
      0 mp 0 0 0 0;...
      0 0 ip 0 0 0;...
      0 0 0 mg 0 0;...
      0 0 0 0 ig 0;...
      0 0 0 0 0 iout];
% initializing the displacement, velocity matrices
%depl=[0;0;0;0;0;0];
%vel=[0;0;0;0;0;0];
depl=[1.128678460096995e+03;-0.001525203063789;1.128478437051381e+03;0.001525203064240
;1.128431001019016e+03;1.128235543748530e+03];
vel=[1.141377926748764e+02;0.007531290898960;1.141791906680401e+02;0.007531291091795;1
.141096366326829e+02;1.141510438643724e+02];

%initial gear centre distance
cd(1)=sqrt((rp+rg)^2+((rp+rg)*tan(20*pi/180)+(depl(4,1)-depl(2,1)))^2);
save('cd12_p.txt','cd','-ascii')
cdc(1)=sqrt((rp+rg)^2+((rp+rg)*tan(20*pi/180)+(depl(4,1)-depl(2,1)))^2)-(rg+rp)/cos(20*pi/180);
```

```
save('cdc12_p.txt','cdc','-ascii')
%initial gear pressure angle
preang(1)=acos((rp+rg)/cd(1))*180/pi;
save('preang12_p.txt','preang','-ascii')
%initial contact ratio
ARC(1)=
(sqrt(rga^2-rg^2)+sqrt(rpa^2-rp^2)-(rp/cos(preang(1)*pi/180)+rg/cos(preang(1)*pi/180))*sin(preang(
1)*pi/180))/cos(preang(1)*pi/180);
ctr(1)=ARC(1)/(pi*mod);
save('ctr12_p.txt','ctr','-ascii')
%initial gear mesh deformation
gmd(1)=depl(2,1)+rp*depl(3,1)-depl(4,1)-rg*depl(5,1);
save('gmd12_p.txt','gmd','-ascii')
if gmd(1)>=0
      h=1;
else
      h=0;
end
%gear dynamic transmission error
te(1)=rp*depl(3,1)-rg*depl(5,1);
save('te12_p.txt','te','-ascii')
% calculate initial acceleration
tin = 100; %input torque
tout=0.0075*vel(6,1)^2; %output torque
%external force matrix
R=[tin;0;0;0;0;-tout];
%gear mesh stiffness
[km]=vmesh2(depl(3,1),ang,kp,dis,cdc(1));
kmb=km/rg^2; %calcualte linear mesh stiffness
%gear mesh damping
sg=0.03;
qmb=2*sg*sqrt(kmb*rp^2*rg^2*ip*ig/(rp^2*ip+rg^2*ig)); %proporsional gear mesh damping
%stiffness matrix
k=[kcp 0 -kcp 0 0 0;...
    0 kyp+h*kmb h*kmb*rp -h*kmb -h*kmb*rg 0;...
    -kcp h*kmb*rp h*kmb*rp^2+kcp -h*kmb*rp -h*kmb*rp*rg 0;...
    0 -h*kmb -h*kmb*rp kyg+h*kmb h*kmb*rg 0;...
    0 -h*kmb*rg -h*kmb*rp*rg h*kmb*rg h*kmb*rg^2+kcg -kcg;...
    0 0 0 0 -kcg kcg];
%damping matrix
c=[qcp 0 -qcp 0 0 0;...
      0 qyp+h*qmb h*qmb*rp -h*qmb -h*qmb*rg 0;...
      -qcp h*qmb*rp h*qmb*rp^2+qcp+qstp -h*qmb*rp -h*qmb*rp*rg 0;...
      0 -h*qmb -h*qmb*rp qyg+h*qmb h*qmb*rg 0;...
```

```
    0 -h*qmb*rg -h*qmb*rp*rg h*qmb*rg h*qmb*rg^2+qcg+qstg -qcg;...
    0 0 0 0 -qcg qcg];
% Solve for initial accelerations
accl(:,1) = inv(m)*(R-c*vel(:,1)-k*depl(:,1));

% Parameters for Newmark time integration
alpha = 0.25 ;delta = 0.5 ;
% Calculating integration constants
a0 = 1/(alpha*dt^2) ; a1 = delta/(alpha*dt) ; a2 = 1/(alpha*dt) ;
a3 = (1/(2*alpha))-1 ; a4 = (delta/alpha)-1 ;a5 = (dt/2)*(delta/alpha-2) ;
a6 = dt*(1-delta) ; a7 = delta*dt ;

% time step starts
for i = 1:nt-1
    %i
    %input load and output load
    tin = 100;
    tout=0.0075*vel(6,i)^2;
    %external force matrix
    R=[tin;0;0;0;0;-tout];

    [km]=vmesh2(depl(3,i),ang,kp,dis,cdc(i));
    kmb=km/rg^2;
    kcdc(i)=km;
    save('kcdc10_p.txt','kcdc','-ascii')%save the mesh stiffness that been used
   %gear mesh damping
    qmb=2*sg*sqrt(kmb*rp^2*rg^2*ip*ig/(rp^2*ip+rg^2*ig));
  %stiffness matrix
k=[kcp 0 -kcp 0 0 0;...
   0 kyp+h*kmb h*kmb*rp -h*kmb -h*kmb*rg 0;...
   -kcp h*kmb*rp h*kmb*rp^2+kcp -h*kmb*rp -h*kmb*rp*rg 0;...
   0 -h*kmb -h*kmb*rp kyg+h*kmb h*kmb*rg 0;...
   0 -h*kmb*rg -h*kmb*rp*rg h*kmb*rg h*kmb*rg^2+kcg -kcg;...
   0 0 0 0 -kcg kcg];
%damping matrix
c=[qcp 0 -qcp 0 0 0;...
    0 qyp+h*qmb h*qmb*rp -h*qmb -h*qmb*rg 0;...
    -qcp h*qmb*rp h*qmb*rp^2+qcp+qstp -h*qmb*rp -h*qmb*rp*rg 0;...
    0 -h*qmb -h*qmb*rp qyg+h*qmb h*qmb*rg 0;...
    0 -h*qmb*rg -h*qmb*rp*rg h*qmb*rg h*qmb*rg^2+qcg+qstg -qcg;...
    0 0 0 0 -qcg qcg];

    % calculating effectvie stiffness matrix
    keff = k+a0*m+a1*c ;
```

```
        %calculating effective external force matrix
        Reff(:,i) = R+m*(a0*depl(:,i)+a2*vel(:,i)+a3*accl(:,i))+c*(a1*depl(:,i)+a4*vel(:,i)+a5*accl(:,i));
        % solving for displacements at time (i+dt)
        depl(:,i+1)= keff\Reff(:,i);
        %calculate the gear centre distance change at step i+1
cdc(i+1)=sqrt((rp+rg)^2+((rp+rg)*tan(20*pi/180)+(depl(4,i+1)-depl(2,i+1)))^2)-(rg+rp)/cos(20*pi/18
0);
        n=1;
        %initialization of the displacement, velocity and acceleration for
        %interation
        eps=1e-7;
        depln(:,n)=depl(:,i+1);
        kmn=km;
        b1 = cdc(i);
        b2 = cdc(i+1);
      while abs(b1-b2)>eps

            %output i to determine time step
            n = n+1;
            cdc(i)=cdc(i+1);% rechoose the center distance change

            b1=cdc(i);
            [kmn]=vmesh2(depl(3,i),ang,kp,dis,cdc(i));
            kmbn=kmn/rg^2;%rechoose the mesh stiffness based on the new gear centre distance
change
        %gear mesh damping
        qmbn=2*sg*sqrt(kmbn*rp^2*rg^2*ip*ig/(rp^2*ip+rg^2*ig));
      %stiffness matrix
kn=[kcp 0 -kcp 0 0 0;...
      0 kyp+h*kmbn h*kmbn*rp -h*kmbn -h*kmbn*rg 0;...
      -kcp h*kmbn*rp h*kmbn*rp^2+kcp -h*kmbn*rp -h*kmbn*rp*rg 0;...
      0 -h*kmbn -h*kmbn*rp kyg+h*kmbn h*kmbn*rg 0;...
      0 -h*kmbn*rg -h*kmbn*rp*rg h*kmbn*rg h*kmbn*rg^2+kcg -kcg;...
      0 0 0 0 -kcg kcg];
%damping matrix
cn=[qcp 0 -qcp 0 0 0;...
        0 qyp+h*qmbn h*qmbn*rp -h*qmbn -h*qmbn*rg 0;...
        -qcp h*qmbn*rp h*qmbn*rp^2+qcp+qstp -h*qmbn*rp -h*qmbn*rp*rg 0;...
        0 -h*qmbn -h*qmbn*rp qyg+h*qmbn h*qmbn*rg 0;...
        0 -h*qmbn*rg -h*qmbn*rp*rg h*qmbn*rg h*qmbn*rg^2+qcg+qstg -qcg;...
        0 0 0 0 -qcg qcg];
            % recalculating effectvie stiffness matrix
            keffn = kn+a0.*m+a1.*cn;
```

```
            %recalculating effective external force matrix
            Reffn(:,n)=
R+m*(a0*depl(:,i)+a2*vel(:,i)+a3*accl(:,i))+c*(a1*depl(:,i)+a4*vel(:,i)+a5*accl(:,i));
            % resolving for displacements at time (i+dt)
            depln(:,n)= inv(keffn)*Reffn(:,n);
            %recalculating gear center distance change
cdc(i+1)=sqrt((rp+rg)^2+((rp+rg)*tan(20*pi/180)+(depln(4,n)-depln(2,n)))^2)-(rg+rp)/cos(20*pi/180)
;
            b2=cdc(i+1);
     end
      %save iteration number at each time step
      ite(i)=n;
      save('ite.txt','ite','-ascii')
      %assign the displacement
      depl(:,i+1)=depln(:,n);
      % calculating velocities at time (i+dt)
      accl(:,i+1) = a0*(depl(:,i+1)-depl(:,i))-a2*vel(:,i)-a3*accl(:,i) ;
      %calculating accelerations at time (i+dt)
      vel(:,i+1) = vel(:,i)+a6*accl(:,i)+a7*accl(:,i+1);
      %save the centre distance in each time step
      cd(i+1)=sqrt((rp+rg)^2+((rp+rg)*tan(20*pi/180)+(depl(4,i+1)-depl(2,i+1)))^2);
      save('cd12_p.txt','cd','-ascii')
      %save the pressure angle in each time step
      preang(i+1)=acos((rp+rg)/cd(i+1))*180/pi;
      save('preang12_p.txt','preang','-ascii')
      %save contact ratio in each time step
     ARC(i+1)=
(sqrt(rga^2-rg^2)+sqrt(rpa^2-rp^2)-(cd(i+1))*sin(preang(i+1)*pi/180))/cos(preang(i+1)*pi/180);
     ctr(i+1)=ARC(i+1)/(pi*mod);
     save('ctr12_p.txt','ctr','-ascii')
     %save gear mesh deformation
   gmd(i+1)=depl(2,i+1)+rp*depl(3,i+1)-depl(4,i+1)-rg*depl(5,i+1);
   save('gmd12_p.txt','gmd','-ascii')
   if gmd(i+1)>=0
      h=1;
   else
      h=0;
   end
%gear dynamic transmission error
te(i+1)=rp*depl(3,i+1)-rg*depl(5,i+1);
save('te12_p.txt','te','-ascii')
end
function [km] = vmesh(theta2,angl,K,dis,a1)
%
```

```
% this function is used for the gear dynamic modelling
% simulation to calculate the variable mesh stiffness at any angle of rotation of the gear.
% convert radians to degrees relative to the start of the simulation
theta2= theta2 - 2*pi*fix(theta2/(2*pi));
theta = theta2*180/pi;

% calculate desired angle for interpolation in terms of the mesh stiffness cycle

a=(theta/(360/23)-fix(theta/(360/23)))*360/23;

km = interp2(angl,dis,K,a,a1,'spline');
```

Appendix D

This appendix includes the APDL program for generating the pin supports in the planetary gear finite element model.

```
PINHOLE=5

FLST,5,4,5,ORDE,4
FITEM,5,287
FITEM,5,293
FITEM,5,-294
FITEM,5,300
ASEL,S, , ,P51X
ALLSEL,BELOW,AREA
!PICK UP THE 1ST PIN AREA

ACLEAR,293,294
ACLEAR,287
ACLEAR,300

FLST,2,3,4,ORDE,3
FITEM,2,853
FITEM,2,872
FITEM,2,874
LESIZE,P51X, , ,-1, ,1

LDIV,874,0.5
LDIV,872,0.5
LDIV,853,0.5
!GENERATE LINE2387 AND LINE874, AND KEYPOINT 1559

ADELE,293
ADELE,294
ADELE,287
ADELE,300

KWPAVE,1559 !MOVE WORKING PLANE TO 1559
WPSTYL,,,,,,1

CSYS,4

CIRCLE,1559,PINHOLE

LGEN,2,2390,2393,1,,360/(4*Z3),,,,1
```

```
LDELE,2387,,,1
LDELE,874,,,1

L,582,1563
L,578,1565
L,1560,1564
L,1561,1562

AL,873,874,2391,2394,2388
AL,872,865,2387,2392,2394
AL,875,874,2390,2395,2389
AL,853,869,2387,2393,2395

AL,894,2388,872,888,893
AL,854,855,846,853,2389

!1st pin area
lesize,872,,,3
lesize,2392,,,8
lesize,2387,,,3
lesize,2394,,,3

TYPE,1
MAT,1
REAL,1
ESYS,0
SECNUM,
FLST,2,2,4,ORDE,2
FITEM,2,865
FITEM,2,872
LCCAT,P51X
CM,_Y,AREA
ASEL, , , ,          293
CM,_Y1,AREA
CHKMSH,'AREA'
CMSEL,S,_Y
!*
AMESH,_Y1
!*
CMDELE,_Y
CMDELE,_Y1
CMDELE,_Y2
!*
```

```
ldele,2396

!2nd pin area
lesize,873,,,5
lesize,2388,,,2
lesize,2391,,,7
lesize,2394,,,3
lesize,874,,,3

TYPE,1
MAT,1
REAL,1
ESYS,0
SECNUM,
FLST,2,2,4,ORDE,2
FITEM,2,873
FITEM,2,2388
LCCAT,P51X
CM,_Y,AREA
ASEL, , , ,287
CM,_Y1,AREA
CHKMSH,'AREA'
CMSEL,S,_Y
!*
AMESH,_Y1
!*
CMDELE,_Y
CMDELE,_Y1
CMDELE,_Y2
!*

ldele,2396

!3rd pin area
lesize,2395,,,3
lesize,2387,,,3
lesize,2393,,,8
lesize,853,,,3

TYPE,1
MAT,1
REAL,1
ESYS,0
```

```
SECNUM,
FLST,2,2,4,ORDE,2
FITEM,2,853
FITEM,2,869
LCCAT,P51X
CM,_Y,AREA
ASEL, , , ,300
CM,_Y1,AREA
CHKMSH,'AREA'
CMSEL,S,_Y
!*
AMESH,_Y1
!*
CMDELE,_Y
CMDELE,_Y1
CMDELE,_Y2
!*

ldele,2396

!4th pin area
lesize,875,,,5
lesize,2389,,,2
lesize,2390,,,7
lesize,2395,,,3
lesize,874,,,3

TYPE,1
MAT,1
REAL,1
ESYS,0
SECNUM,
FLST,2,2,4,ORDE,2
FITEM,2,875
FITEM,2,2389
LCCAT,P51X
CM,_Y,AREA
ASEL, , , ,294
CM,_Y1,AREA
CHKMSH,'AREA'
CMSEL,S,_Y
!*
AMESH,_Y1
!*
```

```
CMDELE,_Y
CMDELE,_Y1
CMDELE,_Y2
!*

ldele,2396

!5th pin area
TYPE,      1
MAT,             1
REAL,              1
ESYS,             0
SECNUM,
!*
MSHKEY,0
!*
FLST,2,2,4,ORDE,2
FITEM,2,872
FITEM,2,2388
LCCAT,P51X
CM,_Y,AREA
ASEL, , , ,          829
CM,_Y1,AREA
CHKMSH,'AREA'
CMSEL,S,_Y
!*
AMESH,_Y1
!*
CMDELE,_Y
CMDELE,_Y1
CMDELE,_Y2
!*

ldele,2396

!6th pin area
TYPE,      1
MAT,             1
REAL,              1
ESYS,             0
SECNUM,
!*
MSHKEY,0
!*
```

```
FLST,2,2,4,ORDE,2
FITEM,2,853
FITEM,2,2389
LCCAT,P51X
CM,_Y,AREA
ASEL, , , ,         830
CM,_Y1,AREA
CHKMSH,'AREA'
CMSEL,S,_Y
!*
AMESH,_Y1
!*
CMDELE,_Y
CMDELE,_Y1
CMDELE,_Y2
!*
ldele,2396
nummrg,KP
numcmp,KP


csys,4
K,,,, !keypoint number is 1565
NKPT,100000,1565    !GENERATE A NODE IS 23732

/COM, CONTACT PAIR CREATION - START
CM,_NODECM,NODE
CM,_ELEMCM,ELEM
CM,_KPCM,KP
CM,_LINECM,LINE
CM,_AREACM,AREA
CM,_VOLUCM,VOLU
/GSAV,cwz,gsav,,temp
! Define surface-based constraint type of pair
MAT,1
R,3
REAL,3
ET,2,169
ET,3,175
KEYOPT,3,12,5
KEYOPT,3,4,1
KEYOPT,3,2,2
KEYOPT,2,2,0
KEYOPT,2,4,111
```

```
TYPE,2
! Create a pilot node
TSHAP,PILO
E,100000
NSEL,S,,,100000
CM,p1,NODE
CMSEL,S,_NODECM
! Generate the contact surface
LSEL,S,,,2390
LSEL,A,,,2391
LSEL,A,,,2392
LSEL,A,,,2393
CM,_CONTACT,LINE
TYPE,3
NSLL,S,1
ESLN,S,0
ESURF
ALLSEL
ESEL,ALL
ESEL,S,TYPE,,2
ESEL,A,TYPE,,3
ESEL,R,REAL,,3
/PSYMB,ESYS,1
/PNUM,TYPE,1
/NUM,1
EPLOT
ESEL,ALL
ESEL,S,TYPE,,2
ESEL,A,TYPE,,3
ESEL,R,REAL,,3
CMSEL,A,_NODECM
CMDEL,_NODECM
CMSEL,A,_ELEMCM
CMDEL,_ELEMCM
CMSEL,S,_KPCM
CMDEL,_KPCM
CMSEL,S,_LINECM
CMDEL,_LINECM
CMSEL,S,_AREACM
CMDEL,_AREACM
CMSEL,S,_VOLUCM
CMDEL,_VOLUCM
/GRES,cwz,gsav
CMDEL,_TARGET
```

CMDEL,_CONTACT
/COM, CONTACT PAIR CREATION - END
allsel,all

!!!